Geometric and Elastic Properties and Mechanical Phase Separation Phenomena in Self-Assembling Mesoscopic Helical Springs

by

Brice Christopher Smith

Submitted to the Department of Physics
in partial fulfillment of the requirements for the degree of

Doctor of Philosophy

at the

MASSACHUSETTS INSTITUTE OF TECHNOLOGY
[June 2003]
May 2003

Author .....
Department of Physics
May 15, 2003

Certified by .....
George B. Benedek
Alfred H. Caspary Professor of Physics and Biological Physics
Thesis Supervisor

Accepted by .....
Thomas J. Greytak
Professor of Physics
Associate Department Head for Education

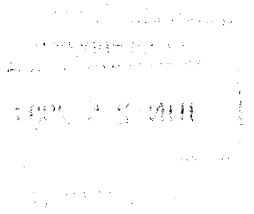

Geometric and Elastic Properties and Mechanical Phase Separation Phenomena in Self-Assembling Mesoscopic Helical Springs

by

Brice Christopher Smith

Submitted to the Department of Physics
on May 15, 2003, in partial fulfillment of the
requirements for the degree of
Doctor of Philosophy

Abstract

Helical ribbons with pitch angles of either 11° or 54° self-assemble in a wide variety of quaternary surfactant-phospholipid/fatty acid-sterol-water systems. In all of the systems studied, the thermodynamically stable state for the sterol is plate like monohydrate crystals. However, the sterol is typically found to pass through a serious of metastable intermediates from filaments to helical ribbons to tubules before reaching the stable crystalline state.

In the present work, we chose to focus on helical ribbons formed in the Chemically Defined Lipid Concentrate (CDLC) system. These helices typically have radii on the order of a few to a few tens of microns and lengths on the order of hundreds of microns. By tethering to these mesoscopic helical ribbons using Devcon 5-Minute Epoxy®, we have been able to elastically deform them, and thus examine their response to uniaxial tension. For small deformations, the low pitch helices behave like linear elastic springs with a spring constant for a typical example measured to be $(4.80 \pm 0.77) \times 10^{-6}$ N/m. From the observed spread in helix dimension, our theory predicts a corresponding range of spring constants for the structures of 10^{-7} to 10^{-4} N/m allowing, in principle, a great range of forces to be examined.

Under larger tensions, both low and high pitch helices have been observed to reversibly separate into a straight domain with a pitch angle of 90° and a helical domain with a pitch angle of $(16.5 \pm 1.3)°$ for the low pitch or $(59.6 \pm 1.7)°$ for the high pitch. Using a newly developed continuum elastic free energy model, we have shown that this phenomena can be understood as a mechanical phase transition of first order. From this analysis, we have also been able to determine all of the parameters within our model, and to show that it is capable of self-consistently and quantitatively explaining all of the observed properties of these self-assembled helices.

Thesis Supervisor: George B. Benedek
Title: Alfred H. Caspary Professor of Physics and Biological Physics

Acknowledgments

No one accomplishes anything of this complexity on their own.

First and foremost I would like to thank my parents for instilling in me a great love of learning and a desire to always search out the truth for myself, no matter where it might take me. However far my education has come, it stands on the foundation they built for me through all their years of support. I would also like to thank my brother and sister who, like any good sibling rivals, always gave me a great many intellectual achievements to try and match, and James Harpel who helped me first discover physics and started me on the path I now walk. In addition, I am greatly indebted to my research advisor, Professor George Benedek. His patience and his guidance has helped me develop from the mere student of science I was upon my arrival into the scientist I am today. His vision and passion for this project was vital to my ability to carry out the work I will present in this thesis. But far beyond that, his knowledge and his support has helped me to develop the tools necessary to tackle new and exciting problems that cross the boundaries of many different fields of study. Whatever my future holds, I know that the lessons I learned in this lab will serve me well.

I would also like to thank Profs. Mehran Kardar and Alexander van Oudenaarden for being on my thesis review committee.

In my time here, I have had the great fortune to benefit from collaborations and interactions with a number of other amazing scientists. In particular, I would like to thank Dr. Yevgenyia Zastavker who, despite being near the end of her graduate career, never failed to take the time to help teach me about this project. My experimental technique grew enormously under her guidance, and our collaborations on the theory and interpretations of what we saw pushed us both far further than would have been possible alone. I would also like to thank Dr. Aleksey Lomakin for his ever ready willingness to offer theoretical guidance. He gave us the original conception of the crystalline model free energy and provided invaluable help throughout the development of our current formalism, keeping us from going down innumerable dead

ends. In addition, I would like to thank Dr. Neer Asherie for his constant willingness to listen as I tried to work though the physical interpretation of our theory out loud. In particular, his assistance was absolutely vital in the formulation of our current treatment of the tension induced straightening transition. I am also very grateful to Dr. Jonathan Selinger for many stimulating discussions about the fundamental similarities and differences between the chiral and achiral models, and those between our experimental observations on the quaternary systems to the observations in other systems which had always been assumed to be simply and directly analogous to ours in the past. Finally, I would like to thank Ms. Winnie Yong for her tireless help in developing the sample preparation protocol and in acquiring the AFM images of helical ribbons reported in this thesis. Her knowledge of chemistry and wet lab technique has become a very important part of the future of this work.

Finally, I would like to thank all of my close friends for keeping me sane in an insane world. Gabrielle, Aimee, Anton, Mike, Saurabh, Julia, Abby, and especially Corrina; in these last five years you helped to make me a better person as well as a better scientist, and for that I am forever grateful.

"It is not enough for a handful of experts to attempt the solution of a problem, to solve it and then to apply it. The restriction of knowledge to an elite group destroys the spirit of society and leads to its intellectual impoverishment."

- Albert Einstein

Contents

1 General Introduction **27**

1.1 Background and History 27

1.2 Thesis Organization 30

2 Experimental Observations, Measurements, and Results **35**

2.1 Introduction 35

2.2 The Formation of Helical Ribbons in Quaternary Systems 37

2.3 The Helix Geometric Properties 43

2.3.1 Measurements Using Optical Microscopy 47

2.3.2 Measurements Using Atomic Force Microscopy 54

2.4 The Helix Elastic Properties 62

2.4.1 Techniques for Measuring Biological Forces 63

2.4.2 Tethering and Manipulating Helical Ribbons in CDLC 70

2.4.3 Calibration of the Helical Ribbon Stiffness 76

2.5 The Tension Induced Straightening Transition 80

2.5.1 Observations of Domain Separation in Low-Pitch Helices Under Tension 83

2.5.2 Observations of Possible Domain Separation in a High-Pitch Helix 85

3 The Generalized Mechanical Theory of Helical Ribbons **91**

3.1 Introduction 91

3.2 Geometric Parameterization of the Helix Free Energy 92
3.3 Incorporation of Externally Applied Stress 95
3.3.1 The Internal Elastic Potential Energy 96
3.3.2 The Work Done by External Stress 97
3.3.3 The Total Energy and Conditions of Mechanical Equilibrium . 100
3.4 Implications of External Constraints on the Applied Stress 102
3.4.1 Case 1 : Zero Tension and Zero Torque 103
3.4.2 Case 2 : Externally Applied Axial Tension with Freely Rotating Helix Ends 105
3.4.3 Case 3 : Externally Applied Axial Tension With Clamped Helix Ends 107
3.4.4 Case 4 : Externally Applied Torque in the Absence of an Axial Tension 114
3.5 The Equilibrium Conditions For a Domain Separated Helix 117
3.5.1 The Conditions of Material Conservation 117
3.5.2 The Conditions of Stability Under Axial Tension 119
3.5.3 The Stability Constraints Under Tension as an Equal Area Construction 121
3.5.4 The Conditions of Stability Under a Pure Torque 126
3.5.5 The Stability Constraints Under Torque as an Equal Area Construction 127
3.6 Conclusion 130

4 Choice of the Model Free Energy **133**
4.1 Introduction 133
4.2 Previous Models For Helix Formation 135
4.2.1 Class One: The Non-Chiral Theories 137
4.2.2 Class Two: The Chiral Theories 141
4.2.3 Successes and Failures of The Chiral Theories 159
4.3 The Crystalline Model 168

4.3.1 Arguments for Positional Order in Helical Ribbons 169
4.3.2 Derivation of the Crystalline Model Free Energy 172
4.3.3 Implications of the Crystalline Model Free Energy 180

5 Analysis of Experimental Results Using the Crystalline Model 185
5.1 Introduction 185
5.2 The Helix Spring Constant 187
5.3 Domain Separation in Low-Pitch Helices
Under Axial Tension 196
5.4 Predictions for Low-Pitch Helices Under Torque 215

6 General Conclusions 231

A Strengths and Limitations of Helical Ribbons as Force Probes 239

B Application of the Generalized Energy Formalism to a Classical Spring and Mass 247

C Application of Our Indirect Method for Imposing External Constraints to an Ideal Gas 253

D Derivation of the Energy Due to a Surface-Tension Imbalance 259

E Domain Separation in a High-Pitch Helix Under Tension 267

List of Figures

2-1 Typical examples of isolated helical ribbons in the CDLC system viewed with a phase contrast microscope (see section 2.3.1). (a) A low pitch helix with a pitch angle of 11 ± 0.5° and radius 9 μm, (b) an intermediate pitch helix with a pitch angle of 40.8 ± 0.5° and radius 15.5 μm, and (c) a high pitch helix with a pitch angle of 54 ± 0.5° and radius 4.2 μm. 42

2-2 Definition of the notation we will adopt for the geometric variables that parameterize the conformation of a general helix of length ℓ formed by wrapping a thin ribbon with total contour length s, width w, and thickness t around a cylinder of radius R at a fixed pitch angle ψ (equal to 11° in this figure), or equivalently at a fixed pitch P. 44

2-3 Two dimensional representation of a wound cylindrical helix used to relate the axial length and pitch to the other geometric parameters. . 45

2-4 Measurements of the radius (R) versus pitch (P) for low-pitch helices in CDLC. The dashed line gives the linear least squares fit to this data which has a slope of 1.241 ± 0.015 and a y-intercept of -0.32 ± 0.41. These values corresponds to a pitch angle of (11.17 ± 0.14)° which is consistent with our expectations from previous work on this system. . 49

2-5 A representative set of measurements for the helix radius (R) versus the ribbon width (w) for the low-pitch helices in CDLC. The shaded area corresponds to a region of the parameter space in which a structure will have closed up into tubule guaranteeing that no helical ribbons could be found by definition. 51

2-6 A representative set of measurements for the radius (R) versus the axial length (ℓ) for low-pitch helices in CDLC. The lightly shaded area in the upper left corresponds to a region where helices would have less than one turn ($n < 1$), while the darkly shaded area to the lower right would correspond to helices of greater than eleven turns ($n > 11$). . . 53

2-7 Two representative Contact mode AFM scans in air of low-pitch helical ribbons laid out on freshly cleaved mica. The colors encode the height information in the scan with a progression from dark brown being zero height above the substrate through yellow to white/pink indicating 10 nm above the substrate for (a) and 5 nm for (b). The scan in (a) was taken over a 10 μm horizontal square while the scan in (b) was taken over a 15 μm square to show as much detail on the ribbon surface as possible. 57

2-8 Two representative Contact mode AFM scans in water of low-pitch helical ribbons laid out on freshly cleaved mica that has been treated with APS to improve the binding of the structures. As before, the colors encode the height information in the scan with the progression from dark brown at zero through yellow to pink/white indicating 300 nm above the substrate for (a) and 500 nm for (b). In order to include as large a number of ribbons as possible, the scan in (a) was taken over a 95 μm horizontal square while the scan in (b) was taken over a 90 μm square. 59

2-9 The measurements of ribbon width (w) versus thickness (t) for the two representative AFM scans of low-pitch helices shown in Figure 2-8. . . 60

2-10 Typical examples of a low pitch helical ribbon with raduis $sim24$ μm (a) and a high pitch helical ribbon with radius $sim9$ μm (b) in CDLC under tension. The thick glass rod at the top of the images is fixed to the bottom of the sample cell while the thin glass needle is attached to the micromanipulator. This combination allows us to have precise control over the deformation of the helices. 72

2-11 A typical low pitch helix with a radius of 22 μm in CDLC free from external stress while attached to the micromanipulator at one end (a), the same helix under compression (b), and under extension (c). . . . 73

2-12 A plot of the experimental results for the fractional change in radius $((R - R_o)/R_o)$ versus the change in pitch angle $(\psi - \psi_o)$ in radians for the low-pitch helix shown in Figure 2-11. The uncertainty in the data in both parameters is represented by the size of the rectangle used at each point. 75

2-13 A cartoon schematic of the typical sequence in the experiments designed to calibrate the helix spring constant (not drawn to scale). (a) One of the softest cantilevers from a set on the silicon wafer is glued to an glass needle attached to the micromanipulator. (b) After allowing the epoxy to cure, the needle is retracted and the cantilever is separated from the block. (c) The cantilever attached to the needle is cross calibrated by bending against the remaining cantilever on the block to insure that its elastic properties have remained the same. (d) With the cantilever placed aside for safekeeping, a glass needle tethers one end of a low-pitch helix to a thick, rigid glass needle attached to the microscope slide. (e) The cantilever is returned to the micromanipulator and tethered to the free end of the helix, and (f) used to deform the helix allowing both the cantilever deflection and the helix extension to be measured simultaneously. 79

2-14 A typical graph of the restoring force versus helix extension measured using the silicon-nitride cantilevers. The slope of the linear curve fit (4.8×10^{-6}) is the spring constant of this helix in N/m. 81

2-15 (a) A low pitch helix with radius 17 μm free from external force attached to a glass rod at one end and surrounded by other free low pitch helices in solution, (b) the same helix attached at both ends and slightly extended, and (c) the helix extended beyond 16.5° and allowed to come to equilibrium with respect to the straightening transition (the helix ends are off screen). 83

2-16 An schematic illustration of an idealized sequence in our pulling experiments. In (a) the helix is free from stress and has a pitch angle of 11°. Under the influence of a pure axial tension, (b) the helix is extended to a pitch angle of 16.5° at which point it is still stable as a single domain. As the tension is increased beyond this point (c) the helix expands metastably until it reaches a pitch angle of 24°. Here the helix will spontaneous separate (d) into two connected domains maintaining the same total axial length as it had before the transition. The two domains will consist of a helical domain with pitch angle 16.5° and a straight domain with pitch angle 90°. The two distinct conformations will be connected by a short crossover region with length on the order of R_o. 86

2-17 (a) The high pitch helix with radius 16.6 μm free from external force while attached to the glass rod at one end, (b) the same helix attached at both ends and slightly extended, and (c) the helix extended beyond 59.6° and allowed to come to equilibrium with respect to the observed domain separation phenomena. 87

2-18 (a) The short high pitch helix with radius 20 μm free from external force while attached to the glass rod at one end, (b) the same helix attached at both ends and slightly extended, and (c) the helix under a large extension showing the same type of "wobble" defect observed for the longer helix in Figure 2-17. 88

3-1 Definition of the geometric state variables that fully parameterize the conformation of a helix and of its underlying ribbon. 93

3-2 Schematic definition of the two types of external forces applied to a helical ribbon that we will consider. Throughout the following analysis, we will be interested not in the perpendicular force, but in the torque. The magnitude of the applied torque (not shown) may be calculated as $|\vec{\tau}^{ext}| = J_{\perp}^{ext} R$ and its direction will follow from the right-hand rule. 98

3-3 Schematic plot of a typical pressure-volume isotherm for a van der Waals gas below the critical temperature T_c. The region of instability (shown as the darkened portion of the curve) corresponds to a volume range where the gas is predicted to have a negative isothermal compressibility, which is not physically allowed. 101

3-4 Schematic illustration of the four external constraints on the applied stress to be considered. Case 1 is a helix free from all forces. Case 2 corresponds to a helix extended by a positive axial tension in the absence of an applied torque. Case 3 is a helix that has been extended by a positive axial tension in addition to a positive torque that holds the azimuthal angle Φ fixed. Case 4 corresponds to a helix that has been unwound by a negative torque in the absence of an applied tension. 104

3-5 Schematic plot of the torque applied to a helix as function of the axial length for extension with clamped ends. The solid line represents the desired path along which Φ remains fixed as the helix is extended. The dashed line shows the proposed two-step path which begins with extending the helix at zero torque allowing the azimuthal angle to change from Φ_o to $\tilde{\Phi}$ followed by winding the helix at constant ℓ until Φ is returned to its initial value. 111

3-6 Illustration of the geometric variables for a helix which are constrained to lay in a restricted region by the finite width of the ribbons. 123

4-1 The local coordinate system for a tilted symmetric bilayer determined by the orthonormal set $\hat{k}$, $\hat{c}$, and $\hat{p}$. In this notation, $\hat{c}$ represents the normalized projection of the molecular tilt ($\hat{d}$) onto the ribbon plane, $\hat{k}$ represents the unit normal to the ribbon, and $\hat{p} = \hat{k} \times \hat{c}$ coincides with the expected axis of ferroelectric polarization. In addition, the molecular tilt angle (ϕ) is defined as the angle in the tangent plane between the projection of the tilt direction ($\hat{c}$) and the equator. . . . 142

4-2 Schematic illustrations of the bilayer geometries considered in the work of Ou-Yang and Liu: (a) a helical ribbon with cylindrical curvature, (b) a twisted strip with non-zero Gaussian curvature, and (c) a spherical vesicle. 144

4-3 Schematic illustration of the physical mechanism responsible for linking tilt modulation to membrane curvature. (a) A splay in the tilt direction ($\nabla \cdot \hat{c} \neq 0$) induces a spontaneous curvature in the membrane (b) in order to keep the molecules more nearly parallel to one another as favored by steric interactions. 149

4-4 A schematic plot of the biased free energy density considered by Selinger *et al.* as a function of the chiral order parameter ζ [25]. (a) The free energy (in arbitrary units) for a positive value of the control parameter $\bar{t}$ corresponding to a single packing state with small effective chiral order. (b) The same function with a negative value of $\bar{t}$, yielding to two inequivalent packing configurations. The bias field favors one state relative to the other based upon the sign of h thus resulting in a membrane with large effective chirality. 157

4-5 An illustrative example of a low-pitch helix formed in a model bile system that exhibits two regions of different width ($w = 6$ or 12 μm) while maintaining a single radius ($R = 16$ μm). 162

4-6 Plot of a typical set of experimental results for the fractional change in radius versus the change in pitch angle in radians for a low pitch helix in CDLC (squares). The theoretical results using a chiral model with uniform tilt (dashed line) are clearly inconsistent with the data. . . . 166

4-7 Schematic representation of the two principle modes of bending for cylindrical deformations of a thin rectangular plate. (a) A deformation which bends all lines parallel to the contour length of the ribbon creating a cylinder equivalent to a helix with zero pitch angle. (b) The complimentary deformation bending lines parallel to the ribbon width which creates a cylinder equivalent to a helix with a 90° pitch angle. [NOTE: the thickness of the ribbon has been greatly exaggerated for clarity.] 176

4-8 Plot of a typical set of experimental results for the fractional change in radius versus the change in pitch angle in radians for a low pitch helix in CDLC (squares). The theoretical result using the crystalline model with an isotropic spontaneous bending energy (solid line) is in good agreement with the data shown. 180

5-1 A schematic plot of the theoretical tension vs. inverse axial density curves for the case of extension with zero external torque (a) and for the case of extensions with clamped helix ends (b). For consistency, the elastic energy constants used to generate these plots have been set to the ratios calculated later in this section (Equation 5.42) while their overall magnitudes have been left arbitrary. The vertical scale in plots (a) and (b) has been set the same in order to allow for more easy comparison of the shape and relative magnitudes of the two tensions. 198

5-2 A plot of $\nu_o f(\nu_0)$ (dashed line) and of $\nu f(\nu)$ (solid line) over the maximum range $\nu \in [0,1]$. The crossings of these two lines define the realistic boundaries for the inverse axial density given the maximum possible width of a low-pitch helical ribbon. As in Figure 5-1, the elastic energy constants used to generate these plots have been set to the ratios given in Equation 5.42 while leaving their overall magnitudes arbitrary. . . 202

5-3 A plot of the theoretical tension in nN vs. ν for a particular low pitch helix in CDLC showing the appropriate equal area stability condition. The figure also labels the free equilibrium value of ν (Point A: ν_o = 0.19), the value of the order parameter in the helical phase (Point B: ν_h = 0.28), and the limit of metastability with respect to the straightening transition (Point C: $\nu_{J_{max}} = 0.42$). The lower bound for ν given the finite width of the helical ribbon used to determine $\tilde{K}_{spring}$ ($\nu_{b,lower}$ = 0.10) is shown for completeness. 206

5-4 A plot of the theoretical tension in nN vs. ν for a typical low pitch helix in CDLC with $w/R_o = 0.15$ showing the appropriate equal area stability condition upon compression for the free (a) and clamped (b) end constraints. The figure also labels the unstressed equilibrium value of ν (Point A: $\nu_o = 0.191$), the value of the order parameter in the helical phase (Point B: $\tilde{\nu}_1 = 0.150$ / $\bar{\nu}_1 = 0.150$), the limit of metastability (Point C: $\tilde{\nu}_{J_{min}} = 0.112$ / $\bar{\nu}_{J_{min}} = 0.112$), and the lower boundary of ν at which point the helix closes up into a tubule (Point D: $\tilde{\nu}_2 = 0.0230$ / $\bar{\nu}_2 = 0.0234$). 211

5-5 (a) A particularly long ($\ell = 243.8 \pm 3$ μm) and narrow (R_o = 21.21 $\pm$ 0.37) low pitch helix free from stress and (b) extended by a positive axial tension. (c) The same helix under a very small compressive force clearly showing the onset of buckling. 214

5-6 A plot of the theoretical ratio of the helix radius ($R^\star$) upon the application of a pure torque to the unstressed equilibrium radius (R_o) using the ratios of the elastic energy constants given in Equation 5.42. As already discussed, the pitch angle of the helix may go beyond 90° for this type of deformation, and therefore we must examine the function over the full range of ψ from 0° to 180°. 216

5-7 A plot of the predicted ratio of the azimuthal angle under a pure torque ($\Phi^\star$) to its unstressed value (Φ_o) for low-pitch helices in CDLC. For generality, the curve is shown over the full range of the pitch angle running from $\psi_{c,lower} = (7.8 \pm 2.4)°$ to $\psi_{c,upper}) = (172.2 \pm 2.4)°$. . . . 219

5-8 A plot of the properly scaled theoretical predictions for the transverse force in nN (a) and the helix torque in nN × μm (b) vs. the azimuthal angle for the typical low-pitch helix used to measure $\tilde{K}_{spring}$. As noted above, the range of Φ is unbounded, and thus we have chosen to cut it off at a reasonable value in order to allow the more interesting features of the curves around the straight configuration to be seen more clearly. 221

5-9 A plot of the theoretically predicted ratios of the stressed to unstressed radii ($R^\star/R_o$) (a) and of the azimuthal angle under a pure torque ($\Phi^\star$) to its unstressed value (Φ_o) (b) using the free energy model of Chung *et al.* In this case we find that there are no lower or upper cutoff values for the allowed range of ψ so the full range from 0° to 180° is shown. 224

5-10 A plot of the predictions from the model of Chung *et al.* for the transverse force in nN (a) and the torque in nN × μm (b) vs. the azimuthal angle for the typical low pitch helix used to measure $\tilde{K}_{spring}$. Again, the range has been cut off in order to allow the region around $\Phi = 0$ to be analyzed more easily. 227

A-1 (a) A cartoon schematic (not drawn to scale) showing the important components that would be associated with using the helical ribbons as force probes. The helix is attached at one end to a glass needle that controls the extension by its connection to a micomanipulator, while the other end is attached to the biomolecule under investigation through the use of a functionalized latex sphere. (b) Shows a similar schematic for the biomembrane force probe developed by Evans *et al.* [103]. In this setup the force is measured by moving the pipette and recording the displacement of the functionalized latex sphere attached to the sample (see section 2.4.1). 240

A-2 A typical example of a characteristically (a) large (radius 24 μm) and (b) small (radius 9 μm) low pitch helix used to determine their response time to a step change in force. The helical ribbons under tension are shown as the inserts on the right-hand side while the plots of their relaxation upon removal of the force approximately 0.08 seconds into the experiment is shown on the left. The large helix (a) corresponds to "Helix Five" in Table A.1 while the small one (b) is the one labeled "Helix Two". 245

B-1 (a) A classical ideal spring with spring constant K connected to a rigid wall and a mass. The spring is at its unstressed length and the block is held in place by an external force not shown. (b) The block is released and the system is allowed to come into static equilibrium in which the restoring force of the spring just balances the weight of the block. . . 248

C-1 (a) Schematic pressure-volume diagram of a typical direct isothermal expansion of a classical ideal gas from the initial state (P_0, V_0, T) to the final state (P_1^a, V_1, T). (b) The conjugate two-step path in which the gas is first expanded at constant pressure from (P_0, V_0, T) to (P_0, V_1, $\tilde{T}$) allowing the temperature to change. The gas is then cooled at constant volume until the temperature is returned to its initial value T with a corresponding pressure P_1^b. 254

D-1 Schematic illustration of a short section of a ribbon that has been bent into a helix with finite pitch. The figure labels the stretched outer surface (top), the compressed inner surface (bottom), and the neutral surface (dashed line) that separates the two regions. [NOTE: the thickness of the ribbon has been greatly exaggerated for clarity.] . 260

E-1 A typical graph of the theoretical tension vs. inverse axial density curves for the case of extensions with zero external torque (a) and for the case of extensions with clamped ends (b) for a high-pitch helix. For consistency with the results of this section, the elastic energy constants used to generate these plots have been set to the ratios calculated in Equation E.11 while their overall magnitudes have been left arbitrary. The vertical scale in plots (a) and (b) has been set the same in order to allow for more easy comparison of the shape and relative magnitudes of the two functions. 269

E-2 A plot of the theoretical tension in arbitrary units vs. ν for the high-pitch helix showing the appropriate equal area stability condition. The figure also labels the free equilibrium value of ν (Point A: $\nu_o = 0.808$), the value of the order parameter in the helical phase (Point B: $\nu_h = 0.863$), and the limit of metastability with respect to the straightening transition (Point C: $\nu_{J_{max}} = 0.898$). 274

E-3 A plot of the theoretical tension in arbitrary units vs. ν for a typical high-pitch helix in CDLC with $w/R_o = 0.603 \pm 0.075$ showing the appropriate equal area stability condition upon compression for the free (a) and clamped (b) end constraints. The figure also labels the unstressed equilibrium value of ν (Point A: $\nu_o = 0.808$), the value of the order parameter in the helical phase (Point B: $\tilde{\nu}_1 = 0.794$ / $\bar{\nu}_1 = 0.748$), the limit of metastability (Point C: $\tilde{\nu}_{J_{min}} = 0.722$ / $\bar{\nu}_{J_{min}} = 0.613$), and the lower boundary of ν at which point the helix closes up into a tubule (Point D: $\tilde{\nu}_2 = 0.0122$ / $\bar{\nu}_2 = 0.0566$). 277

List of Tables

2.1 The composition of the Chemically Defined Lipid Concentrate system manufactured by Gibco/BRL. 40

A.1 The characteristic decay times of various low-pitch helices in CDLC for relaxation from an extended state upon the sudden removal of the axial tension. 246

Chapter 1

General Introduction

1.1 Background and History

Since their discovery in 1984 by Yager and Schoen at the US Naval Research Laboratory [1], self-assembling lipid tubules and helical ribbons have been of rapidly growing interest due to their potential for use in a wide variety of advanced materials applications [2, 3, 4]. One of the most significant advances in this area has been the development of techniques to coat lipid tubules with nickel, copper, gold, and iron [5]. Using these metalization techniques, extremely anisotropic high dielectric materials can be formed which have the potential for many important application such as substantially reducing the size of microwave electronics [6, 7].

A second area of great interest in applying microtubules derives from their ability to be used in the controlled release of drugs and other materials over long times. In order to be effective for chemical delivery, a system must have four essential elements (1) it must allow drug loading without adversely effecting its functionality, (2) it must provide a predictable rate of release over prolonged times, (3) the material must retain activity after release, and finally (4) the suspension must not cause irritation or allergic reactions when introduced into the body [8]. Current techniques for packaging such materials have many important drawbacks, most significantly of which is that the rate of release is not constant over time. This fact arises because most techniques involve packaging the material inside microspheres, and thus con-

trolling the rate of release by controlling the diffusivity of the material through the walls. However, as the solute is released, the osmotic pressure decreases causing the package to shrink. Because the total rate of diffusion depends strongly on the surface area of the sphere, the rate of release thus also varies with time. In addition, many of the current techniques require exposing the drugs to organic solvents [9, 10], which can result in the denaturing of delicate proteins and genetic materials. The use of self-assembled tubules, however, avoids these limitations because they may be removed from any organic solvents required in their manufacture prior to chemical loading, and their high aspect ratio leaves them extremely resistant to shape change as a function of osmotic pressure [2, 4, 8]. In order to demonstrate this potential, microtubules have been used for controlled release of testosterone in living rats [11] while additional in vitro investigations have demonstrated the preservation of protein activity upon packaging and release [8]. In fact, the majority of the present work was carried out under Grant Number N00014-95-1-0871 from the Office of Naval Research whose primary interest in the helical ribbons and tubules formed in the quaternary systems to be described below was their potential for use in antifouling applications. More than a decade ago, Price and co-workers demonstrated quite dramatically that packaging antifouling agents within copper coated lipid tubules and mixing them into paint protected a fiberglass rod for more than six months whereas a similar rod with the agent freely mixed into the paint suffered significant bio-fouling over the same time period [12, 13, 14].

Other, more novel uses for these microstructures have been developed such as using tubules made from specially functionalized lipids as substrates to aid in the crystallization of certain proteins [15, 16]. However, by far the most important remaining application is their connection to the so called "condensation diseases". It was from this context, in fact, that the work on our present helical ribbons was first begun.

In the early 1990's it was discovered that the onset of cholesterol gallstone disease is preceded by the formation of cholesterol monohydrate crystals due to supersaturation of bile in the gallbladder [17]. In the investigation of this phenomena, it was discovered

by Konikoff *et al.* that the evolution of a stable crystalline phase was itself preceded by the formation of a complex sequence of metastable intermediaries that typically progressed from filaments to helical ribbons to closed tubules, and only then to the monohydrate crystals [18]. From a clinical point-of-view, given that an estimated 10% of all adults will develop gallstones [19], it would obviously be very advantageous to have the ability to control the kinetics of this crystallization pathway for cholesterol, and thus to be able to delay or prevent the formation of gallstones.

Native bile, however, is a very complex solution involving a wide range of constituents, and so to allow a clearer picture of the important physics to emerge, Chung *et al.* chose to work instead with various synthetic systems composed of the common bile salt sodium taurocholate, lecithin, cholesterol, and water [20]. Collectively these systems are referred to as the model biles. Prior to the work of Chung *et al.*, self-assembled microstructures had been studied extensively in a variety of other synthetic systems composed of chiral amphiphiles. In all of these previous studies, it was found that the structures within a given system always formed with a single pitch angle, and that that while the radius and length of structures could vary significantly from system to system, the pitch angles were always either 45° [21, 22, 23] or roughly 60° [1, 24] depending on the type of amphiphile used. However, when Chung *et al.* began to investigate the helical ribbons formed in model bile systems, they discovered that instead of having a single pitch, two distinct types of helical ribbons formed. One variety was tightly wound with a pitch angle of $11.1 \pm 0.5°$ while the other was loosely wound with a pitch angle of $53.7 \pm 0.8°$ [20]. This observation raised a number of interesting questions about the nature of their microscopic structure, and prompted several attempts to create a consistent theoretical model capable of explaining the equilibrium geometry of these helices [20, 44, 26]. These previous models all relied explicitly on the chiral elastic properties of the constituent molecules in order to allow for the mechanical stabilization of helical ribbons. This assumption lead to the prediction that structures of only one handedness would form from enantiomerically pure chemical systems in agreement with the observations of Chung *et al.* However, all of these proposed models were later called into question by further experimental

investigations by Zastavker *et al.* [27].

Originally motivated by the desire to determine a means of controlling the morphology of structures formed in the model biles in order to improve their usefulness in the types of materials applications described above, Zastavker *et al.* examined helix formation in more than twenty distinct systems composed of a surfactant or nonionic detergent, a phosphatidylcholine or fatty acid(s), a steroid analog of cholesterol, and water [27]. In these experiments Zastavker *et al.* found that despite a variation in the dimensions and kinetics of helix formation, the pitch angles were always either low ($11 \pm 2°$) or high ($54 \pm 2°$) with a small yield ($< 10\%$) of intermediate structures with pitch angles ranging from approximately $30°$ to $47°$. In addition, they found that while right-handed helical ribbons dominated the distribution, a small yield ($< 5\%$) of left handed helices was also observed in a number of systems composed of purely $L-$ enantiomers. Along with other evidence, these observations lead Zastavker *et al.* to formulate a new model for the helical ribbons based upon crystalline elasticity with an isotropic spontaneous curvature instead of the liquid crystalline mechanics with chiral elasticity that characterized the previous models [28].

It is the goal of the present work to extend these previous investigations and to fully characterize a phenomenological model capable of explaining both the geometry of a helix when free in solution as well as its response to externally applied stress. A brief overview of the organization of this thesis is given in the following section.

1.2 Thesis Organization

The goal of our current work is to further our understanding of the formation and physical properties of metastable helical ribbons in quaternary cholesterol - surfactant - fatty acid / phospholipid - water systems. These helical ribbons are mesoscopic objects on the order of several to several hundreds of microns is size containing billions of particles. Given this consideration, our basic approach to the problem of predicting both the free equilibrium configuration of a helix as well as its response under applied tensions and torques will be to construct a course grained model free

energy with experimentally determined parameters. With this general idea, which is consistent with that adopted in previous investigations, we will divide the thesis into four main sections progressing from a discussion of our experimental observations to a general theory of the free energy formalism then on to a discussion of our choice of a specific model for the helical ribbons followed finally by an analysis of the observed phenomena and our predictions for future experiments. Each of these major topics will be presented in its own separate chapter.

We will begin in Chapter 2 with a discussion of the formation of the helical ribbons in the various quaternary systems (section 2.2) along with a characterization of the geometry of these structures in the Chemically Defined Lipid Concentrate (CDLC) system when free from stress, including measurements using both optical and atomic force microscopy (section 2.3). We will then proceed to discuss the method we have developed for tethering and applying forces to individual helical ribbons in CDLC, as well as our measurements of their response to small tensions including their effective axial spring constant (section 2.4). Finally, we will conclude this chapter with a discussion of our observations of a novel mechanical straightening transition in both low and high pitch helical ribbons in which a helix will reversibly separate into two connected domains with distinctly different pitch angles under the application of an axial tension (section 2.5).

We will proceed in Chapter 3 to present a discussion of the general free energy formalism that will hold true for any specific model chosen. We will begin in section 3.2 with the general parameterization of the elastic free energy as a function of helix geometry, and thus define the state variables for the problem. In section 3.3 we will demonstrate the proper theoretical framework for incorporating a general externally applied tension and torque into our formalism. A previous consideration of the tension term was given by Zastavker *et al.* based on a simple thermodynamic analogy [28], however, our treatment is far more general and conceptually straightforward being based solely upon energy considerations. Continuing with our consideration of forces, we will work out in section 3.4 the consequences of constraining the applied tension or torque in a variety of experimentally interesting ways. These will include

such constraints as applying an axial tension in the absence of a torque, applying tension while holding the orientation of the two helix ends fixed, and applying torque in the absence of an axial tension. Finally, in section 3.5 we will present a fully general theoretical treatment of the stability and material conservation conditions for domain separation under both tension and torque. Our most important result will be the formulation of a equal area condition for the stability of a domain separated helix akin to the Maxwell construction in the thermodynamic treatment of the gas-liquid phase transition [29].

In light of our general formalism for describing a helix, we will present in Chapter 4 a discussion of the experimental evidence that governs our choice of the specific form for the model free energy we will consider. Section 4.2 will review the previous models proposed for the formation of helical ribbons and tubules in a variety of self-assembling systems, as well as the evidence that leads us to conclude that none is capable of providing a self-consistent explanation of the structures formed in the quaternary systems. Instead we find in section 4.3 that, in agreement with the intuitive arguments of Zastavker *et al.* [28], the most appropriate model for the helical ribbons is an achiral model that incorporates an isotropic spontaneous curvature.

Finally, in Chapter 5 we will be able to apply the general formalism to our choice of the model free energy in order to analyze the experimental results discussed in the second chapter. We will begin in section 5.2 with an analysis of the helix spring constant. We will consider both the case of a zero torque extension which is what we actually measured in our current experiments, as well as make predictions for the clamped end boundary condition in which the orientation of the helix ends is held constant upon extension. In section 5.3, we will consider the domain separation phenomena in low-pitch helices and find that, along with measurements of the spring constant and the unstressed radius and pitch angle, a measurement of the pitch angle of the helical domain will allow us to uniquely determine all of the parameters in the model free energy. In addition, we will show that, up to a constant that sets the overall scale, we can determine the proper shape for the free energy of all low pitch helices without knowing the spring constant, and have used this fact to make

a prediction for the maximum possible achievable pitch angle before a helix will undergo domain separation. This value is found to be in excellent agreement with experimental measurements providing a powerful self-consistency check on our model. (A discussion of our observation of domain separation in a particular high-pitch helix is delayed to the appendix.) Finally, in section 5.4 we will make predictions about the expected response of a low pitch helix in CDLC to the application of a torque in the absence of axial tension. This experiment is shown to provide an unambiguous method for distinguishing between chiral and isotropic curvature in the free energy models, and thus would be of great interest to perform as new tethers are developed.

The thesis concludes in Chapter 6 with a brief review of our important findings and general conclusions as well as our sugestions for future work on these self-assembled structures.

Chapter 2

Experimental Observations, Measurements, and Results

2.1 Introduction

We will begin our investigation of the mechanical properties of the helical ribbons formed in quaternary cholesterol - surfactant - fatty acid / phospholipid - water systems with a discussion of our current experimental observations. Starting in section 2.2, we will present a brief review of the empirical data surrounding the self-assembly of helical ribbons in the various types of quaternary systems. This will include the basic chemistry and phase behavior of our multi-component solutions, as well as the kinetic pathway from solublized cholesterol through helical ribbons to stable cholesterol monohydrate crystals. From the work of Dr. Yevgenyia Zastavker [27, 28], we now know how to prepare samples with high yields of long lived helical ribbons that will help to facilitate our investigations of their bulk elastic properties.

Continuing in section 2.3, we will discuss the various visualization techniques used to image the helices including optical phase contrast microscopy and atomic force microscopy (AFM). Using these techniques, we have been able to precisely measure the typical geometric dimensions of the low-pitch helices in the Chemically Defined Lipid Concentrate (CDLC) system when free from external stress. As noted by previous authors [20, 27], the most striking feature of the helical ribbons formed

in the quaternary systems is that despite the wide variety among the systems studied (including variations in the physical and chemical nature of the constituents and even in the number of distinct components) helices form with pitch angles of either $(11 \pm 2)^\circ$ or $(54 \pm 2)^\circ$. It is to explain this rather remarkable observation that is one of the long-term goals of our ongoing experimental and theoretical investigations.

Until recently, experimental observations on these types of self-assembled helical ribbons was limited to only these types of observations on unstressed helices. In order to gain more detailed knowledge of the factors that govern the helix geometry, however, it is necessary to measure their response to externally applied forces and torques. Section 2.4, will therefore discuss our current experimental setup used to tether and manipulate individual helices in light of recent advances in techniques for probing forces on the biologically relevant scale. With this apparatus, we have been able to determine the change in the helix radius upon extension and compression for low pitch helices in CDLC which, in Chapter 4, will help to guide our choice for the most appropriate model for the elastic free energy. In addition, we have been able to determine the effective spring constant for these helices as well as their temporal response to a sudden step change in force. Utilizing these results, Appendix A will provide a comparison of the relative advantages and limitations our helical ribbons would have as force probes when compared to the common techniques currently employed.

Finally, we will close out this chapter in section 2.5 with a description of our observations of a novel tension induced straightening transition in individual helices similar to the "stem-flower" transition observed in collapsed polymers like DNA [30, 31, 120]. In low-pitch CDLC helices, we have found a reversible and highly reproducible type of phenomena in which a helix will spontaneously form a straight domain connected to a helical domain beyond a certain critical extension. Further extension simply changes the amount of material in each domain and the helix will always relax back to its original radius and pitch angle upon the removal of the external force. Interestingly, like the unstressed pitch angle, the pitch angle of the helical domain is always found to be the same $(16.5 \pm 1.3)^\circ$, regardless of helix geometry. In addition, despite

the added complexities of tethering and manipulating high-pitch helices in CDLC, we have been able to observe what appears to be an analogous type of domain separation in a single high-pitch helix. We will conclude this section with a description of these observations as well as the arguments both for and against interpreting it in the same way as for the low-pitch helices.

These experimental results, and those of previous investigators [20, 27, 28], will form the basis of the phenomenological theory for helix elasticity which we will develop throughout the following two chapters. Finally, in Chapter 5 we will show that these results may be made fully consistent with our current crystalline model free energy for the high and low pitch helical ribbons.

2.2 The Formation of Helical Ribbons in Quaternary Systems

The self assembly of tubules, helical ribbons, and twisted strips has been found to occur quite generally in a variety of systems composed of chiral amphiphilic molecules [21, 32, 24, 23, 33, 1, 34] or mixtures of charged achiral surfactants with chiral counterions [35]. In addition, similar types of helical structures have been observed in systems of amphiphilic block copolymers containing a poly(styrene) tail and a charged poly(isocyanide) headgroup [36]. In this section, we will provide an overview of the formation and kinetics of the helical ribbons that self-assemble in the quaternary cholesterol - surfactant - fatty acid / phospholipid - water systems [20, 27]. In particular, we will choose to focus on the specifics of the Chemically Defined Lipid Concentrate system which we used as the primary source of helical ribbons investigated in the current work.

A detailed description of the chemistry governing the quaternary systems has been presented previously by Zastavker *et al.* [27, 28], and will therefore not be repeated here. Instead we will simply note their major findings and how they relate to the manipulation experiments as well as to the assumptions and predictions of the

theoretical models to be developed in Chapter 4.

Following their discovery by Chung *et al.*, it was assumed that the formation of helical ribbons with two distinct pitch angles was a phenomena unique to the model bile systems. It was known that the kinetics of helix formation was dramatically affected by the specific identity of the phosphatidylcholine or bile salt used to prepare the sample, but the pitch angles always remained unchanged [37, 38, 39, 40, 41, 42]. However, in the absence of the phosphatidylcholine only needle-like crystals formed [37, 41], while without the bile salt only stable plate-like crystals were found [43]. In order to more fully explore these requirements for the formation of high and low pitch helical ribbons, Zastavker *et al.* systematically replaced the three components with substances that play an analogous physical and chemical role in the solution. Thus, within the broad class of what we refer to as the quaternary systems, there are actually four main subdivisions that can be drawn based upon the chemical nature of various constituents. There are two types of Quaternary Sterol Systems (QSS1, which include the model biles, and QSS2), the Quaternary Fatty Acid Systems (QFAS), and the Lipid Concentrate Systems (LCS).

In order to investigate the effect that the lipid species has on the formation of helical ribbons in model biles, the QSS1 systems were created using the common bile salt sodium taurocholate (NaTC), one of the following phosphatidylcholines: DOPC, SOPC, DEPC, POPC, OSPC, OPPC, DZPC, DMPC, DPPC, and DLPC[1], and cholesterol in a molar ratio of 97.5:0.8:1.7. Complimenting these investigations, the role of the sterol in helix formation was probed by the QSS2 systems which were

[1]Synthetic *L*-enantiomers of phosphatidylcholine used to prepare QSS1 were: 1,2-dioleoyl-glycero-3-phosphocholine (DOPC, sn-1-18:1-sn-2-18:1), 1-stearoyl-2-oleoyl-glycero-3-phosphocholine (SOPC, sn-1-18:0-sn-2-18:1), 1,2-dielaidoyl-glycero-3-phosphocholine (DEPC, sn-1-trans18:1-sn-2-trans18:1), 1-palmitoyl-2-oleoyolglycero-3-phosphocholine (POPC, sn-1-16:0-sn-2-18:1), 1-oleoyl-2-stearoyl-glycero-3-phosphocholine (OSPC, sn-1-18:1-sn-2-18:0), 1-oleoyl-2-palmitoyl-glycero-3-phosphocholine (OPPC, sn-1-18:1-sn-2-16:0), dipalmitoleoyl phosphatidylcholine (DZPC, sn-1-16:1-sn-2-16:1), 1,2-dimyristoyl-glycero-3-phosphocholine (DMPC, sn-1-14:0-sn-2-14:0), 1,2-dipalmitoyl-glycero-3-phosphocholine (DPPC, sn-1-16:0-sn-2-16:0), and 1,2-dilauroyl-glycero-3-phosphocholine (DLPC, sn-1-12:0-sn-2-12:0).

made from sodium taurocholate, DOPC, and one of the following sterols: cholesterol, coprostanol, epicoprostanol, cholestanol, 7-dehydrocholesterol, ergosterol, and lanosterol[2] in the same molar ratios used in the QSS1.

In addition, one of the most important questions surrounding the formation of helical ribbons from a theoretical point of view has been to what extent the molecular chirality of the constituents influence the macroscopic chirality of the overall structure [20, 28, 44, 25, 26, 45]. In order to investigate this question, the Quaternary Fatty Acid System (QFAS) was created by replacing the chiral phosphatidylcholine used in the model biles with an achiral fatty acid. In particular, the QFAS studied by Zastavker *et al.* contained sodium taurocholate, oleic acid, and cholesterol in the standard molar ratio 97.5 to 0.8 to 1.7. In addition, the two Lipid Concentrate Systems (LCS) were formed by replacing not only the phospholipid, but also the bile salt with achiral analogs. Both the Lipid Concentrate and Chemically Defined Lipid Concentrate systems replace the bile salt with a combination of the anionic surfactants Tween™ 80 and Pluronic® F-68, while keeping cholesterol as the sterol component. The major difference between these two systems is that the Lipid Concentrate replaces the phospholipid with cod liver oil which has a variable fatty acid composition[3], while the Chemically Defined Lipid Concentrate is made with a precisely known mixtures of eight specific fatty acids (see Table 2.1).

Of all the various quaternary systems available, we chose to use CDLC as the source of helical ribbons in our present investigation for four main reasons of experimental convenience. First, the CDLC system is commercially available from Gibco/BRL, a division of the Invitrogen Corporation. Designed to replace fetal bovine serum in cell culture media for a wide variety of applications, including growth and

[2]The following natural sterols were used to prepare the QSS2 systems: cholest-5-en-3b-ol (cholesterol), 5b-cholestan-3b-ol (coprostanol), 5b-cholestan-3a-ol (epicoprostanol), 5a-cholestan-3b-ol (cholestanol), cholesta-5,7-dien-3b-ol (7-dehydrocholesterol), ergosta-5,7,22-trien-3b-ol (ergosterol), and 5a-lanosta-8,24-dien-3b-ol (lanosterol).

[3]Typical fatty acids present in cod liver oil: myristic, palmitic, palmitoleic, oleic, stearic, α-linoleic, stearidonic, gadoleic, gondoic, 5,8,11,14,17-eicosapentaenoic, euricic, 7,10,13,16,19-docosapentaenoic, and 4,7,10,13,16,19-docosahexanenoic [46].

Table 2.1: The composition of the Chemically Defined Lipid Concentrate system manufactured by Gibco/BRL.

Component	Common Name	Concentration (mg/ml)	Molecular Weight (g)
Fatty Acids	Myristic Acid	10.0	228.4
	Palmitic Acid	10.0	256.4
	Stearic Acid	10.0	284.5
	Palmitoleic Acid	10.0	254.4
	Oleic Acid	10.0	282.5
	α-Linoleic Acid	10.0	280.4
	Linolenic Acid	10.0	278.4
	Arachidonic Acid	2.0	304.5
Sterol	Cholesterol	220.0	386.6
Surfactants	Tween^{TM} 80	2200	1310
	Pluronic® F-68	100000	8350
Antioxidant	Vitamin E	70.0	472.8

maintenance of Chinese hamster ovaries (CHO), a variety of hybridoma, and insect cells in culture [47, 48, 49, 50], CDLC happens to have a composition that falls into a region of ita phase diagram where helical ribbons routinely form with no additional modification necessary. Second, the yield of structures in CDLC is unusually high compared to many other quaternary systems, and is more than an order of magnitude greater than that of the model bile systems considered by Chung *et al.* In addition, the helical ribbons continue to form and remain in solution for a very long time after the sample is prepared (> 1-2 years). Finally, we have also found that the geometry of individual helices in CDLC will remain unchanged for several weeks when suspended in a highly dilute medium, and that they will remain unaffected for several days even when immersed in a rich growth medium. These properties greatly simplify the task of isolating and manipulating individual helices of various dimensions. Third, we have found that only helical ribbons from CDLC show any significant affinity for the epoxy

currently used as the tethering agent in our experiments (see section 2.4.2 below). In fact, of the more than 50 glues and adhesives studied, we have never successfully tethered a helix in any other quaternary system. Fourth, we found that, unlike most other quaternary systems, the helical ribbons formed in CDLC could be dehydrated for a short time ($\sim$20 minutes) without permanently destroying their structure. This feature will make it possible to carry out straightforward imaging experiments in air using an atomic force microscope (AFM), and will greatly simplify the development of a sample preparation protocol for performing AFM measurements in fluid.

In all of the systems studied, the kinetics was found to vary significantly depending upon the composition, but the temporal evolution of structures was found to follow the same basic pathway from micelles/vesicles to filaments to helical ribbons to tubules and finally to the thermodynamically stable cholesterol monohydrate crystals [28]. In their observations of this process, the most important finding of Zastavker *et al.* was that the formation of helical ribbons of at least two pitch angles ($11 \pm 2°$ and $54 \pm 2°$) was a general phenomenon in multicomponent systems containing a surfactant or nonionic detergent, a phosphatidylcholine or fatty acid(s), water, and a steroid analog of cholesterol. In addition, it was found that most of the quaternary systems also form low yields ($< 10\%$) of helical ribbons with an intermediate value of the pitch angles ranging from approximately 30° to 47° depending upon the precise chemical makeup of the system. Figure 2-1 shows examples of a representative low, intermediate, and high pitch helical ribbon formed in the CDLC system.

While the discovery of the, intermediate pitch structures is obviously of great interest, and needs to be explored more fully in future investigations, in the current work we will choose to focus only on explorations of the two dominate types of helical ribbons that are common to all quaternary systems.

The second extremely important finding of Zastavker *et al.* was the discovery that both left and right handed helical ribbons may self-assemble out of enantiomerically pure solutions of chiral molecules. Specifically, all chiral components used in the preparation of the QSS1 and QSS2 systems are known to have been *L*-enantiomers, and yet in seven of the sixteen systems studied, a small yield ($< 5\%$) of left handed

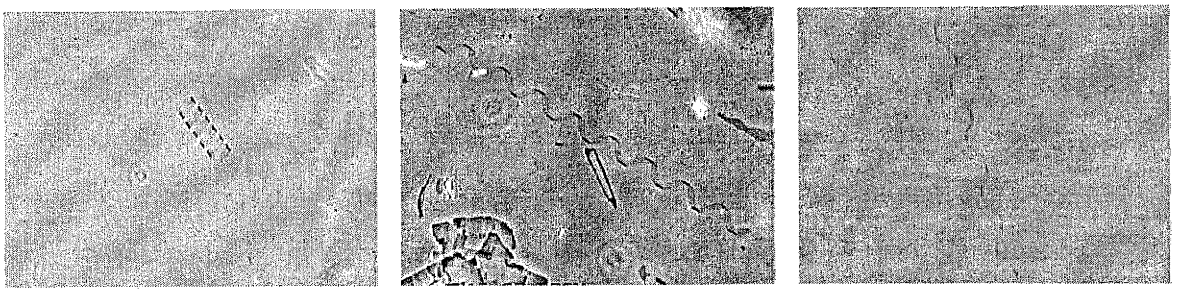

(a) (b) (c)

Figure 2-1: Typical examples of isolated helical ribbons in the CDLC system viewed with a phase contrast microscope (see section 2.3.1). (a) A low pitch helix with a pitch angle of $11 \pm 0.5°$ and radius 9 μm, (b) an intermediate pitch helix with a pitch angle of $40.8 \pm 0.5°$ and radius 15.5 μm, and (c) a high pitch helix with a pitch angle of $54 \pm 0.5°$ and radius 4.2 μm.

helices was observed. Interestingly, in the QFAS and LCS systems where the chiral phospholipids used in QSS1 and QSS2 were replaced by an achiral fatty acid or fatty acid mixture, only right handed helices were found to form. A similar phenomena had been observed previously by Thomas *et al.* working with helical ribbons formed from enantiomerically pure solutions of the common diacetylenic lipid 1,2-bis(tricosa-10,12-diynoyl)-*sn*-glycero-3-phosphocholine and a related phosphonate analogue [51, 52]. A possible explanation of the observations reported by Thomas *et al.* has been proposed in terms of a model based on collective chiral symmetry breaking (see sections 4.2.2 and 4.2.3), while the observations in the quaternary systems support the creation of a new achiral model (section 4.3).

This completes our overview of the important observations regarding the self-assembly of helical ribbons in the quaternary systems. We will now turn to a more formal discussion of the geometry of individual helices in general, and of those formed in CDLC in particular. In addition to extending the current knowledge of helix bulk geometry using standard light microscopy, we will also present the first direct measurements of the ribbon thickness using the atomic force microscope (AFM).

2.3 The Helix Geometric Properties

Throughout the remainder of this work, we will be interested in measuring the geometric and elastic properties of the helical ribbons described above. In order to do this, however, we must first define the notation we will adopt when describing the configuration of a particular structure. In general, any cylindrical helix can be described by a minimum of five independent variables related to the dimensions of the underlying ribbon and to how tightly the helix is wound. Figure 2-2 shows a schematic illustration of a typical helical ribbon which we will use to define the most common set of geometric parameters.

The ribbon making up our structures is taken to be a thin rectangular plate whose geometry is fully described by its width (w), thickness (t), and total contour length (s). The helix is then formed by wrapping this ribbon around a cylinder of radius R keeping a fixed angle ψ between the edge of the ribbon and the local vertical direction. This definition builds in the fact that we have only observed wound helical ribbons (i.e. those with zero Gaussian curvature) forming in the quaternary systems [27], as opposed to other types of structures such as twisted strips that have been reported in a variety of other systems composed of chiral amphiphiles or cationic surfactants and chiral counterions [32, 35, 53]. For the typical low pitch helices formed in CDLC we find that, despite all sharing a pitch angle of $11 \pm 2°$, the radius, total contour length, and width typically vary over roughly an order of magnitude from approximately 5 to 50 μm, 100 to 2000 μm, and 1 to 20 μm respectively while the typical ribbon thickness is found to lie between 30 and 140 nm.

Examining Figure 2-2, we note that in addition to the five parameters discussed so far (i.e. w, s, t, R, and ψ), there are two additional quantities of interest related to the helix geometry. These are the length the helix spans along its symmetry axis in one complete turn (i.e. the helix pitch P) as well as the total length spanned for a given total contour length (i.e. the axial length ℓ). Recalling that only five variables are need to completely determine the configuration of a helical ribbon, we know that we must be able to express ℓ and P in terms of the other parameters. In order to

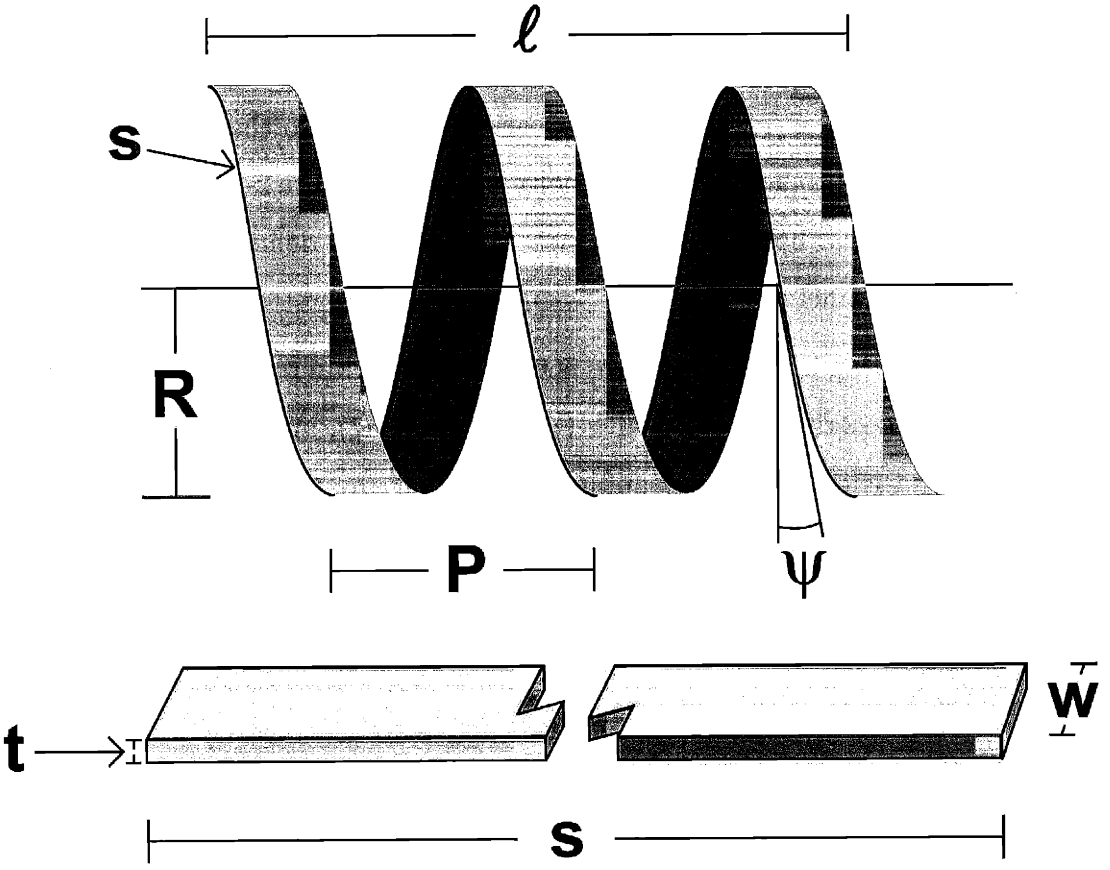

Figure 2-2: Definition of the notation we will adopt for the geometric variables that parameterize the conformation of a general helix of length ℓ formed by wrapping a thin ribbon with total contour length s, width w, and thickness t around a cylinder of radius R at a fixed pitch angle ψ (equal to 11° in this figure), or equivalently at a fixed pitch P.

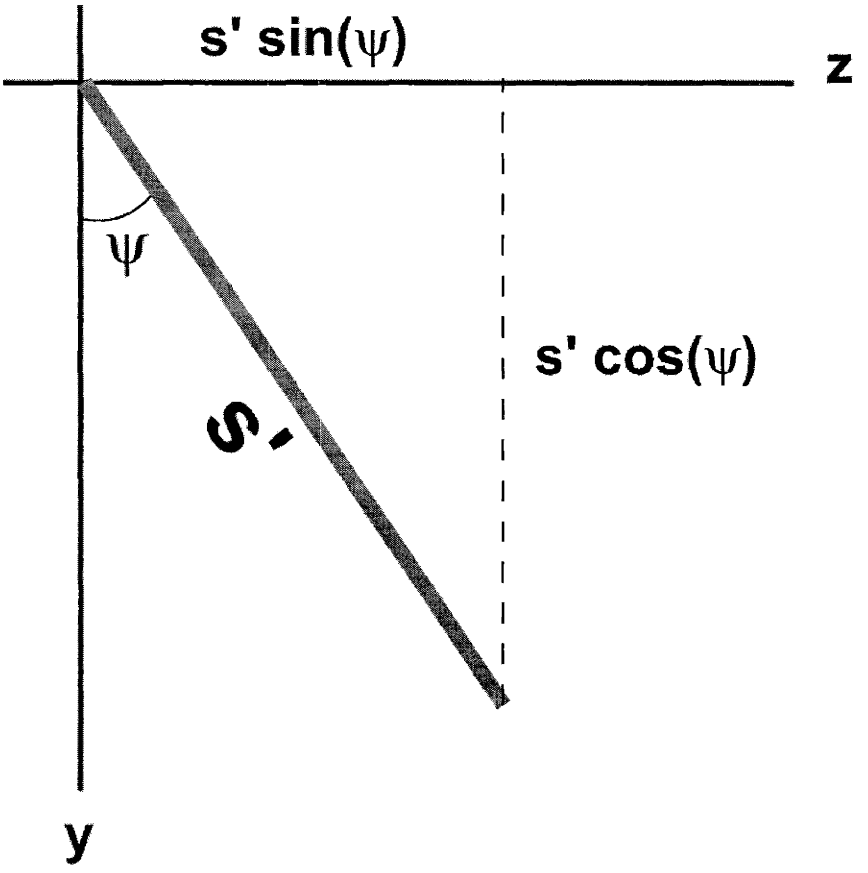

Figure 2-3: Two dimensional representation of a wound cylindrical helix used to relate the axial length and pitch to the other geometric parameters.

determine these relationships, we note that the process of winding a helix in three dimensions is conceptually equivalent to forming the triangle shown in Figure 2-3 in two dimensions.

The easier of the two cases to consider is the total axial length, and therefore we will begin with that. For this determination, we let s' in Figure 2-3 be set to the total contour length of the helix (s), and we find immediately that the axial length of the helix (i.e. its length along the z-axis) may be found from the following simple trigonometric relationship

$$\ell = s \sin(\psi) \tag{2.1}$$

The determination of the expression for the pitch is carried out in exactly this same way, only now we must first determine how much length s' is required to create a single turn of the helix. In the figure, the displacement along the y-axis is equivalent to the net length traveled around the circumference of the cylinder in three dimensions, and thus one complete revolution will have occurred when $s' \cos(\psi) = 2\pi R$. Using this length to determine the net displacement along the z-axis, we find that the helix pitch is equal to

$$P = 2\pi R \tan(\psi) \tag{2.2}$$

With these expressions for ℓ and P, we have thus completed our discussion of the parameters to be utilized throughout the remainder of this work. Before going on to give a description of our experimental measurements, however, we must introduce one additional piece of notation. Given that we wish to describe the response of a helical ribbon to external forces and torques, we need a simple way of distinguishing the values of the geometric parameters that will be changing as stress is applied (R, ℓ, ψ, etc.) from the value of these parameters when the helix is free in solution. In order to clearly draw this distinction, we will label the unstressed value of parameters with the subscript "$_o$". The only exception to this rule is the following. As discussed in the previous section, we find that the dimensions of the ribbon (w, s, and t) change extremely slowly when compared to the timescale of any manipulation experiments. In addition, we have also found experimentally that the ribbons are inextensible under stress and will break long before any resolvable change in their dimensions is observed. Therefore, we will omit the "$_o$" subscript from these parameters for clarity since they may be treated simply as constants in our description of the helical ribbons regardless of the external tension or torque applied. With this last piece of nomenclature, we are finally ready to begin our description of the experimental procedure and to discuss our results for the typical helix geometries observed in the quaternary systems.

2.3.1 Measurements Using Optical Microscopy

The helical ribbons that form in the quaternary systems typically grow to hundreds of microns in length, and are therefore well within the resolving power of optical microscopy in principle. However, much of the detail in their structure is undetectable using bright field microscopy because there is too little contrast between the thin, colorless ribbons and the surrounding aqueous material. In addition, even though the underlying ribbons themselves are quite thin, the bulk helices have radii on the order of tens of microns making dark field microscopy likely to give distorted images of their overall geometry. In order to overcome these limitations, we chose to use a technique known as phase contrast microscopy. This technique relies on the reduction in light observed at the objective lens caused by the phase shift and differential bending of light as it passes through medium of different refractive indices in the sample. Phase contrast microscopes provide a significant increase in contrast over other methods, particularly for thin or colorless objects (such as ours) or for those under high magnification. The only major draw back is that it requires an increase in the input light intensity over bright field viewing, which is easily provided by our apparatus.

The details of the experimental setup used are similar to those reported previously [28]. In brief, the helical ribbons and other structures were visualized using an inverted phase contrast light microscope (Diaphot-TMD, Nikon) which was placed on a vibration isolation tabletop (Newport Corporation, Irvine CA) mounted to a standard laboratory bench. The choice of using an inverted microscope instead of the more traditional upright model allows greater access to the sample, and makes possible the manipulation experiments to be described in the following sections. The images from the microscope were projected onto a CCD camera (Sony, DXC-970MD) and recorded using a four-head SVHS video recorder (Panasonic AG-1960). The images were further digitized with a built in frame grabber on a desktop computer (Power Macintosh 8500/120, Apple Computer Inc.) and analyzed using the public domain NIH-Image software package [54].

From the work of Chung *et al.* and Zastavker *et al.* we know that in all of the various quaternary systems, helical ribbons will form with pitch angles of either (11 $\pm$ 2)° or (54 $\pm$ 2)° regardless of their radius, width, or contour length [20, 27]. This observation implies that the underlying physical mechanism controling the equilibrium pitch angle must be highly robust, and must somehow be common to all of these chemically distinct systems. In our discussion of the possible models for the formation of helical ribbons presented in Chapter 4, it will be important to know how (or if) the various equilibrium geometric parameters are correlated with one another. Given that all of our tethering and manipulation experiments have been performed on helices from the CDLC system, we will adopt that as our typical model system, and use it for the measurements of the unstressed helix geometry.

In order to provide a basis for comparison, we will begin by briefly presenting the data for the radius versus pitch of helices in CDLC. From Equation 2.2, we know that the helix pitch (P) should vary linearly with the radius (R) having a y-intercept of zero and a slope on the order of approximately 1.22 for $\psi_o = 11°$. This expectation is related to general geometric arguments for a cylindrical helix, and has been demonstrated to be true for the structures formed in other quaternary systems [20]. Therefore, an examination of this data will provide an ideal means of calibrating our expectations for how well we expect to be able to identify these types of theoretical correlations from such simple experimental observations. The results for a series of measurements taken on an ensemble of typical low-pitch helices having a wide range of radii are shown in Figure 2-4.

It is important to point out that, like all the data sets to be presented in this section, this graph is meant to simply give a representative picture of the structures typically found in CDLC, and is not meant to indicate absolute boundaries in any way. In fact, structures of greater and smaller dimensions have certainly been observed, but they are simply much rarer. That being said, Figure 2-4 provides a good example of what we should expect to see for two clearly correlated geometric variables.

Now that we know it is possible to investigate the relationship between the geometric variables in this way, the first and most interesting potential correlation to

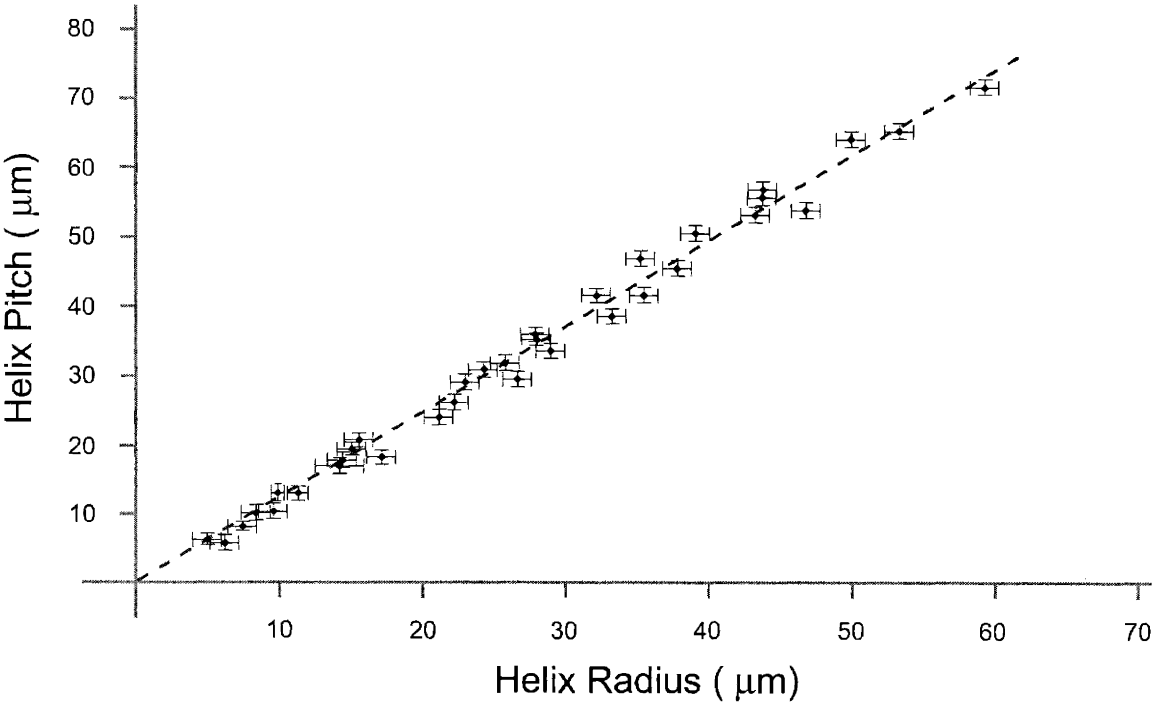

Figure 2-4: Measurements of the radius (R) versus pitch (P) for low-pitch helices in CDLC. The dashed line gives the linear least squares fit to this data which has a slope of 1.241 $\pm$ 0.015 and a y-intercept of -0.32 $\pm$ 0.41. These values corresponds to a pitch angle of (11.17 $\pm$ 0.14)° which is consistent with our expectations from previous work on this system.

look for is that between the helix radius and its width. This relationship has been discussed previously by Chung *et al.* for the helices formed in the model bile systems [20]. In their work, the authors predicted that the radius of a helix should increase monotonically with width, and asymptotically approach the radius of a cylindrically grown tubule for large w. They presented measurements of a variety of radii and widths for their helices that, appear at first glance to be widely and randomly scattered. However, there was some possible indication of clustering in their data points which they interpreted as indicating the superposition of a small number of distinct radius-width curves caused by the presence of ribbons with different thickness. This interpretation has been called into question by subsequent direct observations of the dissolution of helical ribbons by Dr. Zastavker which found that the predicted relationship between the radius and width did not hold for the individual structures. In addition, we will present additional arguments against the existence of this relationship in section 4.2.3. In order to further explore this relationship in our model system, we carried out a similar experiment to that of Chung *et al.* by measuring the radius and width of a large number of low-pitch helices in CDLC. Figure 2-5 shows our results for measurements on a typical ensemble of 66 low-pitch helical ribbons.

The apparent upward trend of the radius with increasing ribbon width seen in Figure 2-5 is merely an artifact caused by the fact that any structures which have radii that fall in the shaded region have already closed up into tubules, and would thus naturally not show up in our data set. Taking this fact into consideration, we see that from this data there is no obvious clustering or indication of any type of correlation between these two variables for the helices in CDLC.

The second potential correlation between geometric variables that will be important to explore is that between the helix radius and its axial length. One of the earliest models put forth to try and explain tubule formation was proposed by Lubensky and Prost (see section 4.2.1) and predicts that the radius of a structure will scale like the square root of the axial length times a material dependent constant [55]. In contrast, the majority of other models that have been proposed (including our own) predict that there will be no general correlation between R and ℓ. This square root dependence

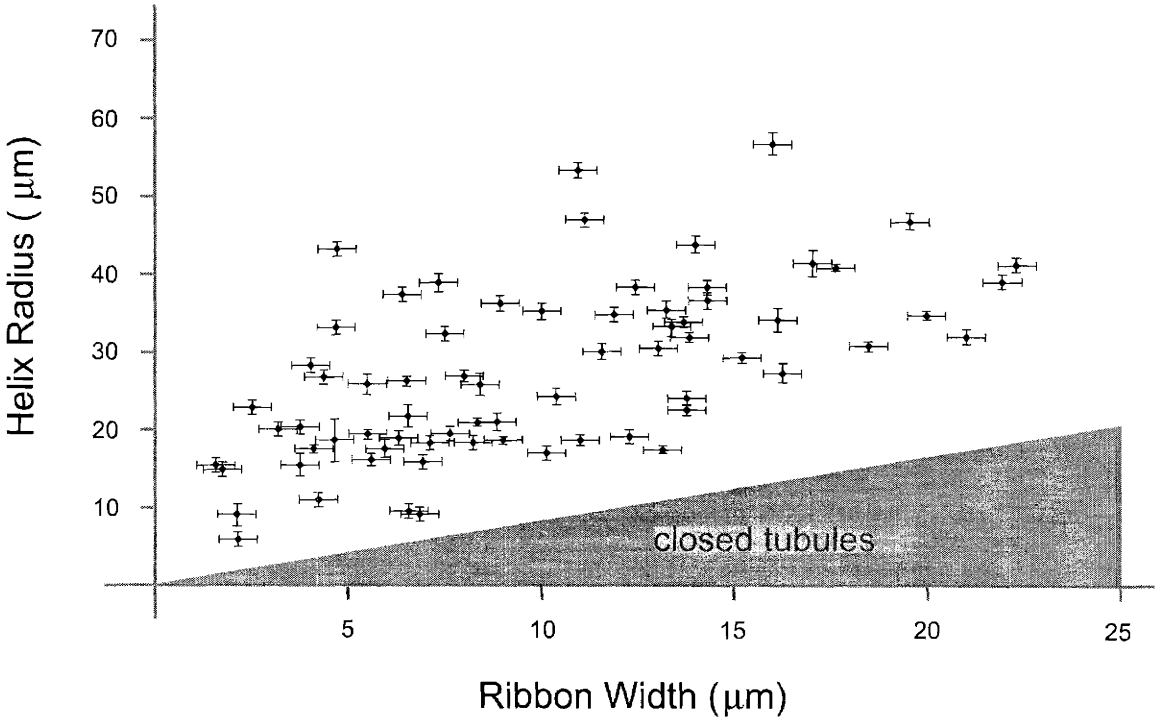

Figure 2-5: A representative set of measurements for the helix radius (R) versus the ribbon width (w) for the low-pitch helices in CDLC. The shaded area corresponds to a region of the parameter space in which a structure will have closed up into tubule guaranteeing that no helical ribbons could be found by definition.

has not been observed previously, however, no explicit verification or demonstration of its failure for the quaternary systems has yet been given. Figure 2-6 shows the results for a typical set of measurements on a variety of low-pitch helices.

The light gray area in the upper left hand side of Figure 2-6 corresponds to a region where helical ribbons would have less than one turn. No data points fall in this region because such structures would have naturally been ignored experimentally given the difficulties inherent in identifying them as helices and in measuring their radius. The darker gray area to the lower right, on the other hand, corresponds to helical ribbons which would have more than 11 turns. The longest helix measured had approximately this number of turns, and while undoubtedly helices with more turns do exist, they are rare and are likely to get broken due to jarring of the sample during manufacture, packaging, or transport. Taking these considerations in account, it is clear from the spread in R and ℓ that neither the square root dependence, nor any other obvious relationship, links the radius and axial length.

The final possible correlation of geometric parameters that could be investigated is that between the ribbon width and the total contour length. However, unlike the two previous cases where we had compelling theoretical reasons to examine the possibility of a relationship among the parameters, in this case it will only be of interest in our discussion of the likely spread in effective spring constants (see section 5.2). For this application, we have simply to note that performing the measurements show again that the length and width of a helix are unrelated in any meaningful way.

Until this point, we have been mostly been ignoring the fifth fundamental geometric parameter (i.e. the ribbon thickness) because we have found that it is not possible to accurately resolve this dimension using the light microscope. Previously, we have not had a means of overcoming this limitation of the apparatus, and have thus had to imply information about the thickness from indirect considerations such as the relative darkness of the helix image. In the following section, however, we will present the results of our first use of the atomic force microscope (AFM) as a means of directly measuring the ribbon thickness to a high degree of accuracy.

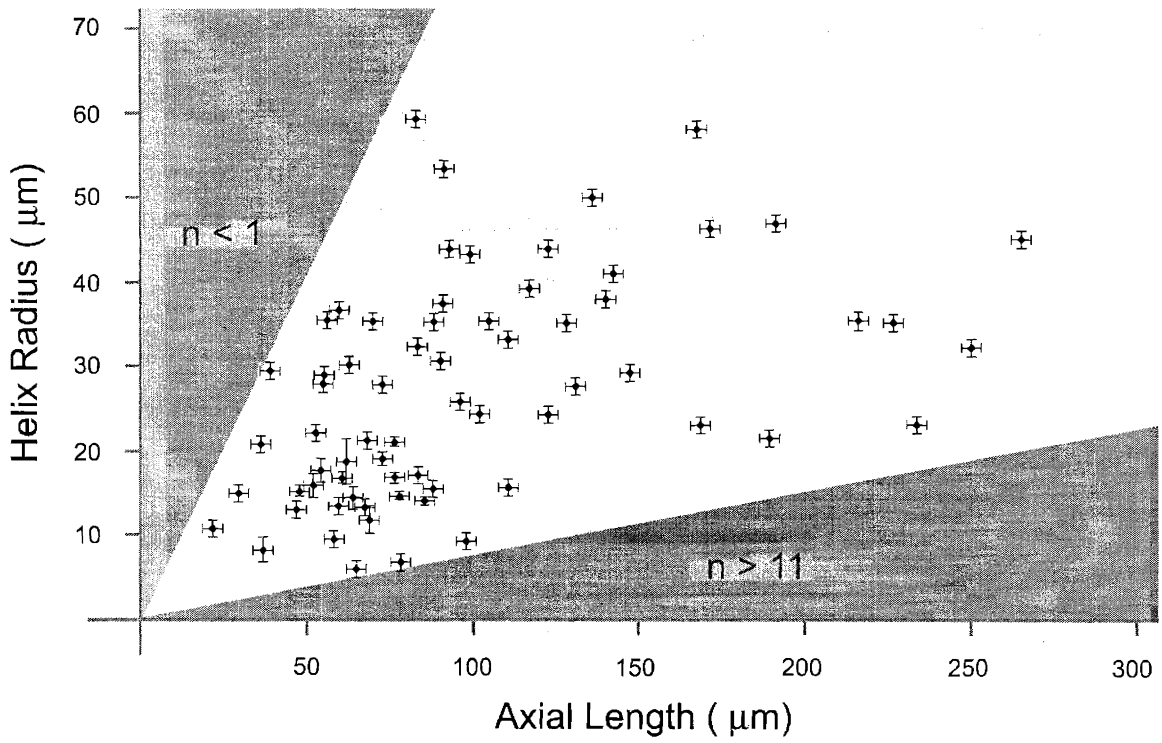

Figure 2-6: A representative set of measurements for the radius (R) versus the axial length (ℓ) for low-pitch helices in CDLC. The lightly shaded area in the upper left corresponds to a region where helices would have less than one turn ($n < 1$), while the darkly shaded area to the lower right would correspond to helices of greater than eleven turns ($n > 11$).

2.3.2 Measurements Using Atomic Force Microscopy

I would like to thank Winnie Yong for her invaluable help in developing the sample preparation protocol and in acquiring the AFM images of helical ribbons reported in this section. I would also like to thank Professor Christine Ortiz (Department of Materials Science and Engineering, Massachusetts Institute of Technology) for allowing us access to the Atomic Force Microscope and Laurel Ng for her patient help in training us in its use.

In this section we will present for the first time a direct measurement of the ribbon thickness using atomic force microscopy. In addition, we will be able to simultaneously measure the width of these ribbons, and thus show that it is typically from one to two orders of magnitude larger than the thickness. From these measurement, we will also be able to show that the width and thickness appear to be totally uncorrelated in the ensemble. Before we discuss the sample preparation, however, we need to give a brief overview of imaging with the atomic force microscope. AFM was invented in 1986 by Binnig, Quate, and Gerber [56]. Their apparatus made use of a tunneling junction to detect the deflection of a thin gold foil. This device was inconvenient for most applications, but within two years an optical detection mechanism had been developed by Alexander *et al.* and Meyer and Amer in which a visible laser is bounced off the cantilever tip into a position sensitive split photodiode detector [57, 58]. With this type of setup a vertical resolution of better than 1 $\AA$ can be achieved. Since this time, the AFM has matured into a robust commercially available tool for the investigation of a wide variety of materials.

All of our measurements presented in this section were taken with a MultiMode^{TM} Scanning Probe Microscope from Digital Instruments (a division of Veeco Instruments) which is capable of performing a wide range of atomic force microscopy (AFM) and scanning tunneling microscopy (STM) experiments. The quadrant photodiode and short mechanical path length between probe tip and sample in this model enables very fast scan rates to be used without loss of precision. The SPM was commanded by a Nanoscope^{TM} III Controller which allowed for scans from roughly 100 μm to

just a few nanometers with full 16-bit resolution. In addition the Nanoscope^{TM} software was used for analysis of the scans allowing quantitative measurements of the ribbon thickness and width. Finally, for the images taken in water, a fluid imaging cell was used which consisted of a glass cantilever holder and a silicon o-ring forming an enclosed environment.

We chose to use the softest possible silicon-nitride cantilevers to image the helical ribbons to try and minimize the mechanical damage done to the structures during the scan. For the tips available to us, this corresponded to a stiffness of approximately 0.05 N/m. These cantilevers were approximately 200 μm long with a typical thickness of 0.4 to 0.7 μm. These devices were partially coated in gold to improve their reflective properties, and thus to improve the determination of their deflection. The probe tip itself was pyramidal in shape with a nominal radius of curvature at the point of 20 to 60 nm.

There are three common modes of operation which may be used with the AFM when imaging a sample; they are Contact, Tapping, and Non-Contact mode. In Contact mode, the probe tip touches the surface and is scanned along without letting it come away from the material. This technique provides the highest achievable resolution and allows for the fastest scan rates, however, it is potentially destructive to soft biomaterials because of the high frictional forces the tip places on the material as it slides across. In Tapping mode, the tip is oscillated near its resonant frequency and makes intermittent contact with the sample. This technique is far lass destructive than Contact mode because of the much smaller lateral forces that are applied. Unfortunately, this reduction in destructiveness is accompanied by a significant loss in spatial resolution. The final mode of operation is Non-Contact AFM. In this mode, the cantilever is again oscillated near its resonant frequency, but it is now not allowed to make contact with the substrate. This technique is completely non-destructive because there is no contact between the material and the probe, however, this mode has even poorer spatial resolution than Tapping model and is difficult to implement properly. In the current investigations, we chose to use the AFM mainly in Contact mode, but some images in air were taken in Tapping mode for comparison. For com-

pleteness we verified that there was no appreciable damage to the ribbon caused by the use of Contact mode by performing a large number of repeated scans on the same area and looking for changes over time.

In order to image our helical ribbons in contact mode, it was necessary to force them to unwind and lay out flat on a freshly cleaved mica surface. We found that it in order accomplish this, it was necessary to filter the CDLC in order to remove the highly charged surfactant Pluronic® F-68. Pluronic free samples of helical ribbons were prepared by filtration in an ultrafree-MC centrifugal filter unit and then re-suspending the structures in water. We found that when the filtered CDLC suspension was deposited on mica and allowed to dry, the helical ribbons would naturally unwind and would remain stable in air for long enough to transfer the sample to the AFM equipment and perform a series of scans. A typical field of view for two of these experiments in air is shown in Figure 2-7.

From Figure 2-7, it is clear that, while being able to perform AFM on the structures in air is a significant advance, the ribbons appear highly damaged and it is unclear as to whether the thickness measured would correspond to the value when in water or not. Thus, it was necessary to extend our technique to allow for imaging the helices under fluid.

Unfortunately, however, it was found that in water the filtered helical ribbons no longer had an adequate affinity for the bare mica to allow them to lay down flat and certainly not enough binding strength to survive the shear forces associated with a Contact mode scan. Similar problems have long been known when attempting to image biomolecules in fluid, and a variety of techniques have therefore been developed to overcome this problem. In particular, it is known that a mica surface may be functionalized with active chemical groups such as amines which will serve as a hydrophilic adhesive for biomaterials. In the context of AFM, this approach was first tried by Lindsay *et al.* in order to stabilize DNA adsorption on a mica substrate [59, 60]. The authors treated the mica surface with 3-aminopropyltriethoxy silane (APS) followed by vacuum drying. After incubating the treated mica with a DNA solution, they were able to obtain images in air, water, and propanol, and found that

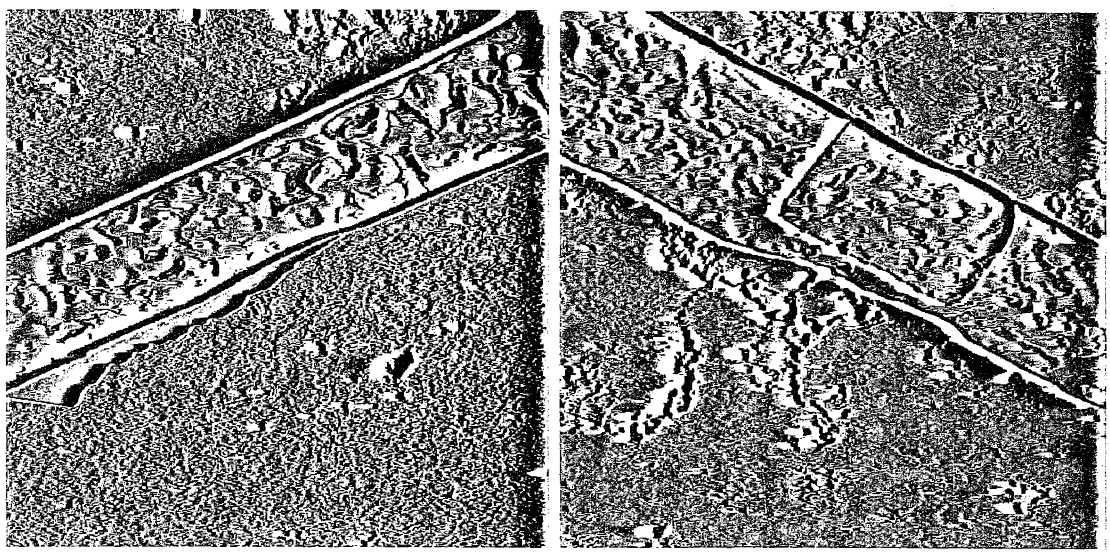

(a) (b)

Figure 2-7: Two representative Contact mode AFM scans in air of low-pitch helical ribbons laid out on freshly cleaved mica. The colors encode the height information in the scan with a progression from dark brown being zero height above the substrate through yellow to white/pink indicating 10 nm above the substrate for (a) and 5 nm for (b). The scan in (a) was taken over a 10 μm horizontal square while the scan in (b) was taken over a 15 μm square to show as much detail on the ribbon surface as possible.

the accuracy of the height measurement was, in fact, better in the fluids than in the air. In analogy to their work, we achieved the chemical deposition by drying a thin layer of APS on freshly cleaved mica, followed by continuous rinsing with water. Once dried, the chemically modified substrate was found to have a greatly improved affinity for the helical ribbons in filtered solutions, which would now lay down flat and remain fixed throughout the imaging process. Figure 2-8 shows two representative AFM scans taken in water using the chemically modified mica substrate.

Using the Nanoscope^{TM} software package, we measured the width and thickness of the various flattened helical ribbons in the two scans shown in Figure 2-8. As we did for the geometric parameters measured by optical means, we may plot the width versus ribbon thickness in Figure 2-9 in order to see if there is any obvious correlation present.

There are three important observations to point out from the data shown in Figure 2-9. First, we note that these are the first reported thickness measurements of helical ribbons formed in CDLC. We find that the thickness for these structures ranged from a minimum of 33.6 $\pm$ 1.6 nm to a maximum of 138.0 $\pm$ 0.7 nm. From the preliminary x-ray diffraction experiments carried out by Winnie Yong and Dr. David Moncton on samples of low-pitch helices from CDLC, it was found that the ribbons were lamellar with a constant layer spacing equal to 34.0 $\AA$. This data closely matches the value of 34.36 $\AA$ reported previously for cholesterol monohydrate crystals [61], which lends further weight to our claims in section 4.3.1 that the helical ribbons are likely to be crystalline in nature. Using this value for the fundamental step size, we estimate that the helical ribbons shown in Figure 2-8 are composed of from 10 to 40 layers which seems quite reasonable. It is worth pointing out again, however, that these are not to be considered as outer bounds on the thickness, but merely as representative values for the typical helical ribbons present in a given sample. In particular, we note that we have ignored ribbons with widths less than 3 μm in our measurements to avoid any possibility of confusing a thin helix with a filament or needle which are structurally distinct metastable intermediates that also form in the quaternary systems. In addition, we expect that very thick or very thin ribbons

(a) (b)

Figure 2-8: Two representative Contact mode AFM scans in water of low-pitch helical ribbons laid out on freshly cleaved mica that has been treated with APS to improve the binding of the structures. As before, the colors encode the height information in the scan with the progression from dark brown at zero through yellow to pink/white indicating 300 nm above the substrate for (a) and 500 nm for (b). In order to include as large a number of ribbons as possible, the scan in (a) was taken over a 95 μm horizontal square while the scan in (b) was taken over a 90 μm square.

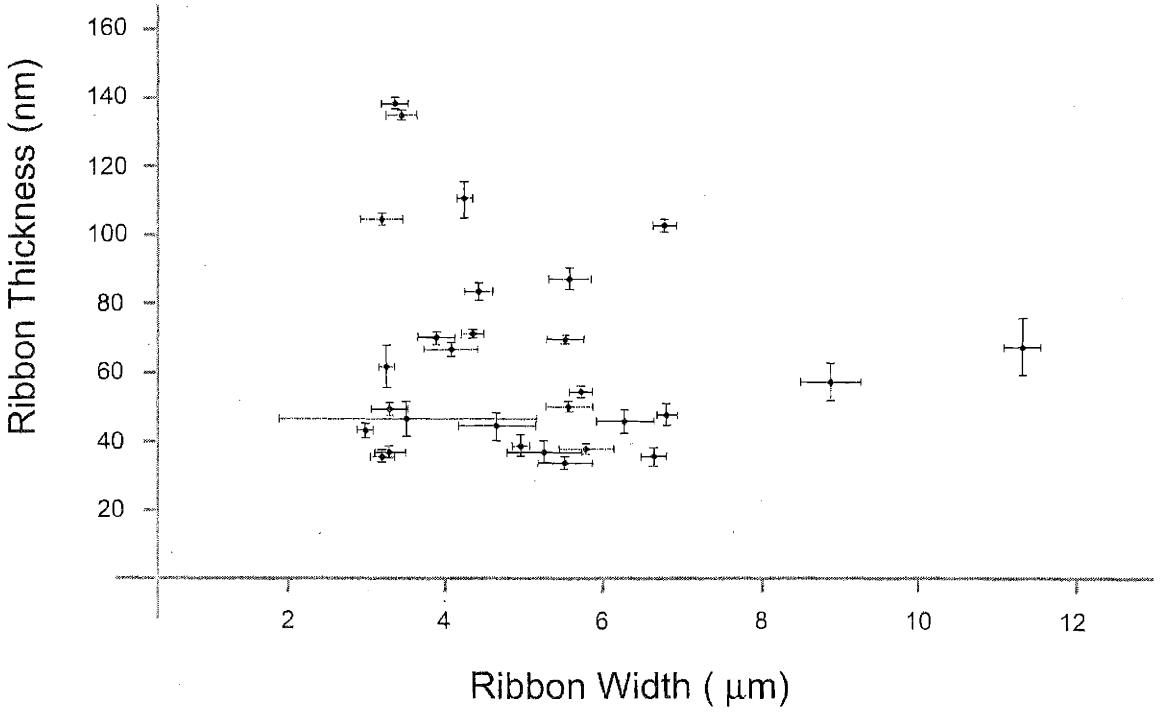

Figure 2-9: The measurements of ribbon width (w) versus thickness (t) for the two representative AFM scans of low-pitch helices shown in Figure 2-8.

would not survive the filtering and washing procedure used to prepare the sample for deposition on mica.

Second, we see from Figure 2-9 that the width and thickness do not appear to be correlated in any obvious way. It is possible to imagine several plausible kinetic pathways of helix growth that would lead to a width that increases with thickness, but no such relationship is found. This fact is important because, if a correlation between the width and thickness had been found, it would have had serious implications for our measurements of the radius versus width discussed in the previous section. This is because our theory, presented in section 4.3, predicts that their should be an explicit dependence of the radius on the ribbon thickness, while we found experimentally that R_o and w were uncorrelated.

Third, and finally, we note that even for these fairly wide ribbons, the ratio of the width to thickness varies from a little as 25 to as much as 200. Thus, we find that while the ribbons are always as least one order of magnitude thinner than they are wide, this ratio is not as large as might have been expected from the striking plate like appearance of the ribbons when free in solution. This result may have important consequences for the behavior of helical ribbons with the smaller values of w/t in light of the recent work of Kessler and Rabin [62]. In their model, the authors found that rod-like helices (i.e. structures with $t \sim w << s$) are predicted to have a markedly different response to axial tension than our predictions for plate-like helices (i.e. structures with $t << w$, s). In particular, Kessler and Rabin found that for a certain range of material parameters, a thin elastic rod will undergo a series of finite stepwise transitions in which it looses turns one at a time as the force is increased. In addition, after each transition the structure becomes progressively more distorted and less well approximated by a cylindrical helix of fixed radius and pitch. Investigations to search for this type of transition as distinct from the tension induced straightening transition to be discussed in section 2.5 have already begun.

With these results, we have thus completed our investigation of the geometric properties of the helical ribbons and are now ready to move beyond simple passive observations and will therefore seek to explore the response of a helix to externally

applied stress.

2.4 The Helix Elastic Properties

In the past twenty years, the field of biological physics has been revolutionized by the invention of techniques for probing the force and distance scales associated with biomolecules. This field of study, what one author has dubbed "mechanochemistry" [63], explores the relationship between structure, function, and force in a variety of biomaterials and has lead to dramatic new insights in areas as diverse as the binding of receptor-ligand pairs [64, 65], protein folding pathways [66], the functioning of molecular motors [67, 68, 69, 70], stress induced catalysis of enzymes [71], and DNA mechanics [72, 73, 74].

The scale of biologically interesting forces spans a remarkable range covering more than six orders of magnitude. At the smallest scale at a few to a few tens of femtonewtons (10^{-15} N) there are the entropic effects such as the Langevin forces responsible for the Brownian motion of small objects like bacteria in water. Three orders of magnitude above these, at the level of a few to a few hundreds of piconewtons (10^{-12} N), come the forces associated with weak non-covalent bonds such as hydrogen bonds, Van der Waals forces, and hydrophobic effects. This is the range of forces of greatest interest to most investigations on single bio-molecule functioning. At the lower end of this range (1 to 10 pN) are the forces associated with protein motor traction [75, 76, 70], while 10 to 15 pN will break the base-pair binding and "unzip" a double stranded DNA molecule. At the other end, it is found that unbinding of the biotin/streptavidin complex occurs at roughly 200 pN [77] while 150 to 300 pN will cause the unfolding of the Ig domains in titin [78]. At the largest scale, forces on the order of several nanonewtons (10^{-9} N) are sufficient to break individual covalent bonds and literally tear molecules apart. Even larger force can obviously be investigated by working on larger numbers of molecules in parallel or on supramolecular structure such as our helical ribbons.

Given the great interest in probing such small forces, there have been remarkable

advances in the development of a wide variety of equipment capable of achieving this level of resolution. In this section we will begin with a brief overview of the most commonly used techniques for measuring forces on the femto to nanonewton scale. They will include the atomic force microscope (AFM), laser/optical traps, magnetic traps, the biomembrane force probe (BFP), glass needles, and micofabricated silicon-nitride cantilevers. From this discussion, we will identify the technique most appropriate for use on the helical ribbons, and then proceed to discuss the details of our current experimental setup used to tether and manipulate individual structure. Using this setup, we have been able to measure the changes in helix geometry upon the application of an axial tension, as well measuring as the helix effective spring constant. In light of these results, we will present in Appendix A a comparison of the major advantages and disadvantages our helical ribbons would have as force probes when compared to the techniques reviewed in the beginning.

2.4.1 Techniques for Measuring Biological Forces

As mentioned, we will begin with a review of the current devices used for measuring forces on the scale of common biomaterials. The most important point of comparison for the techniques will be the range of forces and displacements they are capable of resolving. We will find that most of the devices to be discussed have a linear response over their operating range, and thus the force applied is simply proportional to the displacement. Therefore, in order to measure forces in the femto to nanonewton range, the device must have high positional resolution and a soft force transducer. It is important to note that the higher the resolution of the position detector, the proportionally stiffer the force probe may become without loss of dynamic range. This fact is important when considering the signal-to-noise ratio of a particular technique.

In general, the force resolution of a given device is limited by the effects of thermal vibrations on the probe. Using the equipartition theorem, we know that the root mean square displacement of a harmonic device with spring constant k_{probe} will scale like

$$\delta x_{\text{r.m.s.}} \propto \sqrt{\frac{K_B T}{k_{\text{probe}}}} \tag{2.3}$$

where K_B is Boltzman's constant. This corresponds to a thermally induced noise in the force measurement of

$$\delta J_{\text{r.m.s.}} = k_{\text{probe}}\, \delta x_{\text{r.m.s.}} \propto \sqrt{k_{\text{probe}} K_B T} \tag{2.4}$$

Thus, the signal to noise ratio of such a device at a given desired extension Δx will scale as

$$\frac{J}{\delta J_{\text{r.m.s.}}} = \sqrt{\frac{k_{\text{probe}}}{K_B T}}\ \Delta x \tag{2.5}$$

which increases as the square root of the probe stiffness. Interestingly, examining Equations 2.3 and 2.4 we note that stiffer probes will tend to have the advantage for applications where larger forces and greater resolution in the displacement is required, while softer probes will be advantageous for studies where smaller forces are involved and where having high positional accuracy is not necessary.

In addition to the resolution of these measuring devices with respect to force and distance, it will be of interest to consider their temporal resolution as well. In general, we note that the non-covalent interactions of biomolecules in solution are intrinsically dynamic by nature, and thus dynamic force detection capabilities are required to explore them. Many experiments have shown the power of real time force measurements to yield important information about the functioning of biological systems. For instance, Merkel *et al.* was able to determine a detailed map of the biotin-streptavidin binding potential by measuring forces at a wide variety of loading rates [79], while Ishijima *et al.* has been able to determine the on-off rates and forces generated by single myosin heads by examining the sub-millisecond force fluctuations in the interactions of small numbers of these protein motors with an actin filament [70]. The temporal resolution of modern techniques is, in fact, quite varied, and can range from essentially static ($>$ 1 second) to near real-time ($\sim$10 microseconds) depending on the type of force probe and the detection scheme used for sensing its position.

One of the most important devices in use today for measuring force on biomolecules is the atomic force microscope (AFM) [56, 80] which we have described previously in its imaging capacity (see section 2.3.2). The AFM measures force by

determining the vertical deflection of a silicon or silicon-nitride (Si_3N_4) cantilever with typical stiffness on the order of 0.001 to 100 N/m. Reflecting a visible laser off the cantilever tip into a position sensitive split photodiode detector, this setup can achieve a vertical resolution of better than 1 $\AA$. In addition, a piezoelectric drive provides nanometer control and positioning of the sample in the lateral plane. In practice, all this typically corresponds to an accessible force range of 10 pN to 100 nN with a maximum vertical displacement of 500 nm [81]. By using the latest, ultra-soft cantilevers as well as feedback positioning control, however, the force resolution of the AFM has been extended to nearly 0.1 pN allowing the strength of individual hydrogen bonds to be measured [82, 83]. In addition, of all the techniques currently employed, the AFM has the best overall temporal resolution with a lower typical lower limit on the order of just 10 microseconds [84].

The calibration of the system could in principle be determined theoretically from the known dimensions of the cantilever beam, however, the vapor deposition technique used to manufacture the silicon-nitride tips leads to a non-uniform Young's modulus across the device. Experimentally, the tips are usually calibrated either by measuring their deflection due to the addition of a known mass [85], or by measuring their vibration due to thermal fluctuations [86, 87].

The major advantages of the AFM are its ability to span a large range of forces in any type of environment (air, water, high or low temperatures, vacuum, etc.), its high spatial and temporal resolution and high signal-to-noise ratio due the relatively stiff cantilevers used, and the fact that it is highly standardized and commercially available as a complete system. Its main limitations are that the cantilevers must be switched manually in order to change the force range being investigated, and (more importantly for us) its vertical range is too short for pulling on anything beyond small numbers of biomolecules. For instance, the typical axial length of our helices is on the order of hundreds of microns, and thus even the maximum displacement of the AFM tip is about 1000 times too small to accommodate our structures.

The second technique widely used for probing forces on the molecular level is the laser/optical trap [88, 89]. Also referred to as laser tweezers, the optical traps

are capable of applying forces to a particle on the order of 0.1 to several hundred piconewtons. The optical traps makes use of the gradient force which draws an object with a higher index of refraction than the surrounding material towards the region of highest light intensity [90]. If a laser is passed through a high numerical aperture microscope objective, this force allows the focal point to be used as a three dimensional trap for objects like latex spheres in water. In addition to the gradient force, however, there is also a net force due to radiation scattering that will tend to push the object forward. It is to insure that the gradient force will overcome this scattering force and prevent the object from being ejected, that the laser light is given such tight focus in the axial direction [89, 91]. In its most common configuration, optical traps have an effective stiffness on the order of 10^{-10} to 10^{-3} N/m, subnanometer spatial resolution, a maximum displacement of approximately 500 nm, and a temporal resolution of $\sim$1 ms [63, 69]. However, utilizing the correlations between two optical traps connected to the ends of a single DNA molecule, Meiners and Quake were able to measure forces as low as 10 femtonewtons (10^{-15} N) with 20 μs temporal resolution [92, 93].

The force applied by the optical traps depends critically on the photon field gradient, the index of refraction mismatch, and the precise geometry of the setup so the trap must be calibrated before each use. This is most commonly done by inducing a laminar fluid flow in the cell and using Stokes Law to calculate the hydrodynamic force necessary to eject the bead from the trap. The requirement that the flow be non-turbulent limits these calibrations to relatively soft trap settings and the force law is simply extrapolated linearly to higher laser powers [94]. However, the trap is not isotropic in general, and therefore some care must be taken to ensure that the calibration is taken along the same path as the experiment will be, otherwise significant errors may arise.

The biggest advantage of an optical trap is its ability to apply extremely small forces with high force resolution due to the relative softness of the probe. In addition, it has highly localized force generation and can easily be combined with magnetic traps (see below) to allow the application of both tension and torque [95]. Finally, the probe stiffness can be changed dynamically without having to replace any components

as with most other techniques. Its major limitations are that it requires relative large beads ($\sim$1 to 3 μm), that it has less spatial resolution at low power due to thermal noise, and that its maximum force and distance are relatively small. In principle larger forces could be applied by increasing the laser power, however, laser heating and radiation damage of biomaterials place practical limits on the experimentally useful range of intensities [96, 97].

Another specialized force probe based on a similar idea to the optical trap is the magnetic trap. This technique makes use of the force felt by a paramagnetic bead in a static magnetic field [98, 99, 100]. The magnetic traps are typically calibrated using the viscous drag on the bead as described above [101]. With the use of very small magnets, this technique is currently capable of applying and measuring forces as low as 0.01 pN (i.e. 10 femtonewtons) which are the smallest ever applied in the investigation of biomolecule elasticity [102]. With larger magnetic fields this technique can typically achieve forces as large as 100 pN. Most importantly, however, is that this is the only technique capable of easily applying a known torque to a system. An elegant technique for calibrating the rotational stiffness of the trap has developed [95] that allows the absolute value of the torque applied to be measured directly. The technique, however, has the drawbacks that even beads from the same sample can have significantly different magnetic susceptibilities requiring individual calibration for every trial. In addition, the non-linearities in the induced dipole of the bead and in the rotational force law limit the accessible range of torques achievable with this technique to relatively modest values on the order of 10^{-18} Nm for typical experimental setups [95].

The above techniques have been widely applied to the investigation of a great variety of phenomena. However, their complex design and limitations when working with soft biological membranes or living cells lead Evans *et al.* to the development of the biomembrane force probe (BFP) [103]. Making use of a membrane capsule pressurized by micropippete aspiration as the force transducer, the BFP is capable of resolving forces from the sub-piconewton to nanonewton scale. In this device a spherical membrane, typically a swollen human red blood cell or phospholipid bilayer

vesicle, is held in place by micropipette aspiration. A latex bead is then glued to the opposite side of the membrane and serves as a means of attaching the force probe to various surfaces and biomolecules. In order to maintain a state of mechanical equilibrium, the surface tension of the capsule (and thus the stiffness of the probe) will increase with an increase in the external pressure exerted on it by the pipette. Thus by varying the suction with which the membrane is held over a range from approximately 10^{-6} to 10^{-1} atmospheres, the probe stiffness can be dynamically changed to scan a range greater than 10^{-6} to 10^{-3} N/m [103, 101, 104]. The location of the bead can be determined to an accuracy of 5nm with temporal resolution on the order of tens of milliseconds by monitoring the interference pattern it creates when illuminated by monochromatic light. However, for the softest setting of the apparatus thermal fluctuations limit the resolution to closer to 10nm. At the other extreme, maximum extensions of approximately 200 to 300 nm can be achieved before significant ($> 5\%$) deviations from a linear response are found in the force– displacement relationship of the pressurized capsule.

Assuming perfect axial symmetry and zero shear, it is possible to calibrate the force probe through a simple theoretical calculation taking into account the applied pressure, the inner radius of the pipette, the radius of the spherical vesicle, and the radius of the attached bead. This theoretical calibration was tested experimentally using a magnetic trap over a wide range of aspiration pressures and was found to be in excellent agreement throughout the linear operating range when red blood cells were used [101].

The use of the BFP has many important advantages. First, it has the ability to dynamically change the force region under investigation over nearly four orders of magnitude by simply changing the applied membrane pressure. Secondly, the use of the latex bead to couple to other systems allows great versatility in the types of systems that may be studied, and allows for the possibility of such novel experiments as the force mediated imaging of receptor sites to be performed [103]. Finally, its ability to closely match the elasticity of living cells allows it to measure their properties accurately while minimizing perturbations to the cell structure. Its major limitations,

however, are that it requires a somewhat simple but custom built apparatus to implement and that its dynamic range, while comparable to optical traps and the AFM, is quite limited for use with larger supramolecular structures.

So far, we have yet to discuss the simplest possible technique in general for applying forces to biomolecules, namely the use of thin, flexible glass needles. Glass microneedles with an effective stiffness as low as 10^{-6} N/m or as large as 1 N/m can easily be made by drawing glass pipettes [63]. This enormous range allows forces greater than 0.1 pN to be probed with ease. In addition, optical detection techniques with a resolution of 0.1 μm and video rate [105] as well split-photodiode detectors with nanometer precision and temporal resolution on the order of hundreds of microseconds [106, 70] have all been implemented for glass needles. At the other end of the distance scale, displacements on the order of microns to millimeters can readily be achieved using these needles. The major disadvantages to using the glass needles are that they again require the replacement of the probe to switch force scales and, more importantly, that they are custom made probes that require careful individual calibration before use. This characterization is usually achieved through cross calibration with cantilevers of known stiffness [67], or by measuring their deflection upon the addition of a known weight [106, 107].

The microfabricated silicon-nitride cantilevers were developed in order to try and achieve the wide range of forces, displacements, and temporal dynamics accessible to glass needles while eliminating their major drawback of requiring individual manufacture and characterization, [108, 109, 106]. The stiffness of a rectangular beam cantilever of known dimensions can be calculated from

$$k_{\text{probe}} = E\left(\frac{tw^3}{4L^3}\right) \tag{2.6}$$

where t is the cantilever thickness, w is the width, L is the length, and E is the Young's modulus of the material. Through the application of modern microfabrication techniques, cantilevers of highly reproducible dimensions ($< 5\%$ variability) can routinely be manufactured in large numbers on a single silicon wafer. This reduces the problem of calibration to the measurement of the Young's modulus for the material.

By examining the resonance condition of the cantilevers in air, Fauver *et al.* found a value of $E = 204 \pm 22$ Gpa for the thin (310 nm) layer of silicon-nitride and $E = 208 \pm 20$ Gpa for the thick (650 nm) layer [108]. With these values for E they determined that their fabrication process was capable of creating cantilevers with stiffness that ranged from 5×10^{-5} to 0.670 N/m. Using a simple split-diode detection scheme, the authors were able to integrate these cantilevers into a system with 5nm spatial resolution [106] and a temporal resolution from 10 μs for the stiffest tips (comparable to AFM) to 1 ms for the most flexible. In optical systems such as ours, these tips are found to remain linear out to displacements of over 100 μm giving them a remarkably large operating region. Given their range of stiffness, the scale of accessible displacements, and the ease with which they can be integrated with our existing apparatus, we decided to focus on using these cantilevers in our efforts to directly measure the elastic properties of the low-pitch helical ribbons (see section 2.4.3).

Finally, a variety of other common and novel techniques for manipulating objects and measuring forces have been developed based on ideas such as radial or linear fluid flow [110, 111, 112], using cantilevers made from chemically etched optical fibers [113], making use of the fact that a current carrying wire feels a small force when in the presence of a magnetic field [114], or creating "nano-tweezers" by attaching two carbon nanotubes to the end of a pipette which may then be drawn together or forced apart by the application a voltage difference between them [115, 116]. However, none of these is likely to have any potentially useful application in the context of our studies of helical ribbon elasticity.

2.4.2 Tethering and Manipulating Helical Ribbons in CDLC

Until recently, the investigations of helical ribbons formed in the quaternary systems were limited only to observations of their geometric properties when free in solution. In order to gain more information about their elastic properties and their microscopic structure, it was necessary to find means of apply stress to an individual structure. Obviously, this requires the development of a method for attaching a probe to a single helix. In our search for an adhesive capable of tethering the helices, we tried sticking

structures from multiple quaternary systems to over 50 different materials ranging from hydrophilic adhesives like 3-aminopropyltriethoxysaline (APS) to cyanoacrylate based superglues to binary epoxies [28].

In all of these trials, only two types of quick drying epoxy were found to both survive intact when placed in the aqueous environment with the helices, and to have any detectible affinity for sticking to the ribbons. These were the Toughen (fast-setting) epoxy from Loctite Corporation and the 5-Minute Epoxy® from Devcon Consumer Products. By mixing the hardeners from one brand with the resin from others we were able to determine that the epoxy hardener is the vital component for determining helix attachment. Unfortunately, the precise chemical makeup of the hardeners is unknown because the composition of most products is proprietary. Qualitatively, the sticking of low pitch helices was attributed by Dr. Zastavker to the presence of $-SH$ containing mercaptan in the hardener which simultaneously acts to stabilize the epoxy in the aqueous medium until curing may begin and to facilitate helix adhesion, presumably by creating hydroxyl groups as a byproduct of the resin-hardener reaction which may interact with the hydrophilic ribbon surface [28]. In the previous work, it was unclear as to whether these epoxies were capable of tethering to the high pitch helices as well, however, in the present work we will demonstrate the first conclusive cases of binding high-pitch helical ribbons in CDLC using Devcon 5-Minute Epoxy®.

In order to make use of this tethering agent, we added a piezoelectric micromanipulator (Burleigh, PCS-5000) with manual coarse adjustment to the experimental setup described above in section 2.3.1. With a limit of resolution of 60 nm in all three coordinate directions and an average drift of less than 17 nm per minute, we found this system to be more than adequate for our current experimental work which is typically limited to resolutions of approximately 0.5 microns. By attaching drawn glass micro-needles or the silicon-nitride cantilevers discussed in the previous section to this micromanipulator, and coating their tips with the Devcon 5-Minute Epoxy®, we were able to routinely isolate and manipulate individual low pitch helical ribbons with a variety of geometries and to, on rare occasions, tether to high pitch structures

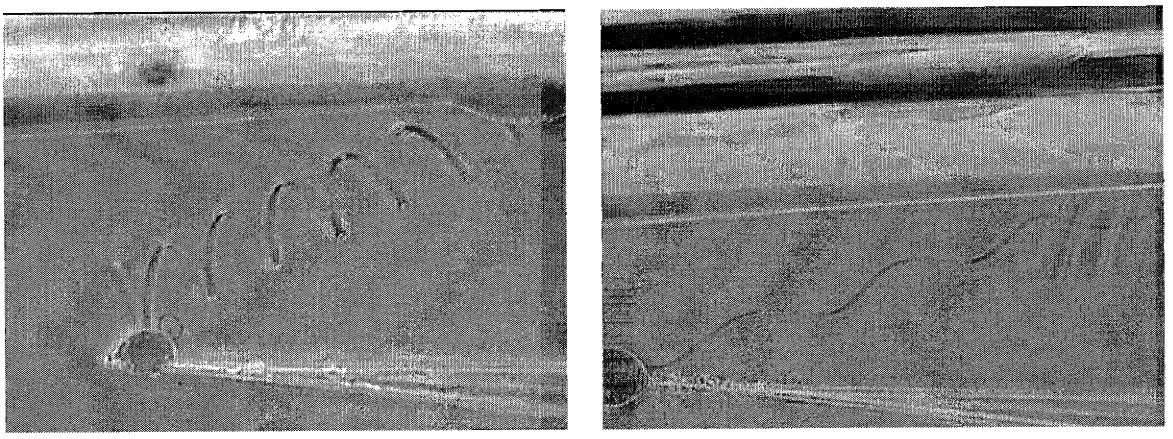

(a) (b)

Figure 2-10: Typical examples of a low pitch helical ribbon with raduis $\sim$ 24 μm (a) and a high pitch helical ribbon with radius $\sim$ 9 μm (b) in CDLC under tension. The thick glass rod at the top of the images is fixed to the bottom of the sample cell while the thin glass needle is attached to the micromanipulator. This combination allows us to have precise control over the deformation of the helices.

as well. Typical examples of manipulating a high and low pitch helical ribbon are shown in Figure 2-10

As pointed out before, the fact that the high and low pitch helices have different affinities for the epoxy provides powerful indirect evidence that they do, in fact, have measurably different surface properties. This is particularly interesting in light of the experiments carried out previously in which it was found that high and low pitch helical ribbons had qualitatively different fluorescence signatures when formed from a model bile system with a fluorescently labeled phospholipid [28]. While more work is needed to directly investigate the relative chemical structure and surface properties of the two types of ribbons, these experiments strongly suggest that the high and low pitch helices should be considered to have two distinct microscopic structures as in our current model (see section 5.3 and appendix E).

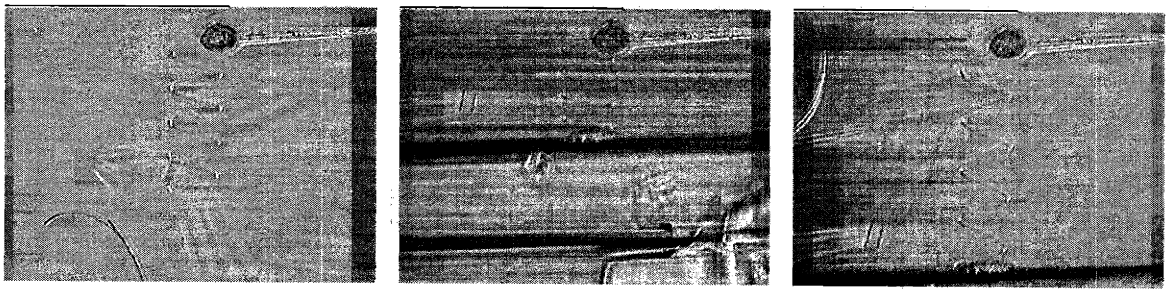

(a) (b) (c)

Figure 2-11: A typical low pitch helix with a radius of 22 μm in CDLC free from external stress while attached to the micromanipulator at one end (a), the same helix under compression (b), and under extension (c).

In addition, it is interesting to note that we have found that, over the full range of extensions and compressions investigated, the helical ribbons behave perfectly elastically with no evidence of plastic deformations. In other words, no matter what force had been applied or for what length of time (the longest forces applied to a single low pitch helix were held for over 30 hours before release), when the tension is removed the helix always relaxes back to the exact geometry that it had initially. In fact, we have even on two separate occasions applied a force large enough to tear a low and a high pitch ribbon respectively into two disconnected pieces and found that each section individually relaxed back to the same radius and pitch angle as the original continuous helix had.

Using this experimental setup, we may make a detailed investigation of the change in geometry for various low-pitch helices under the application of axial tension. In particular, it will be of great theoretical importance in Chapter 4 to know how the radius changes as a function of the pitch angle under tension. Figure 2-11 shows a representative set of pictures for a low-pitch helix free from stress as well as under both compression and extension.

Examining the helix Figure 2-11, it appears that the radius is changing very slowly, if at all, as the pitch angle is measurably increased or decreased. We took more than 50 measurements of the fractional change in helix radius as a function of the change in pitch angle across helices with dimensions ranging from $R_o = 8.458 \pm 0.096$, $w = 4.00 \pm 0.41$, and $\ell_o = 81.9 \pm 2.0$ to $R_o = 21.92 \pm 0.73$, $w = 5.37 \pm 0.49$, and $\ell_o = 132.2 \pm 2.4$. The data for the helix pictured in Figure 2-11 is representative of the entire data set and is plotted alone in Figure 2-12 to allow make its details more clearly visible.

In agreement with our estimates from a simple inspection of the helix pictures above, we find that the measurements of $(R - R_o)/R_o$ versus $\psi - \psi_o$ are uniformly scattered about zero. Fitting a straight line to the complete set of data, we find

$$\frac{\Delta R}{R_o} = (-0.002 \pm 0.029)\ \Delta\psi + (0.002 \pm 0.002) \tag{2.7}$$

where $\Delta R = R - R_o$ and $\Delta\psi = \psi - \psi_o$. The linear fit passes through zero within its uncertainty as required, and more importantly, we find that its slope is also statistically equal to zero.

The result that R does not change to first order for small extensions or compressions turns out to be a very significant piece of information that will actually allow us to uniquely distinguish between various plausible models for helix formation in Chapter 4. However, in order to make use of this data, we need to note one additional interesting property of the epoxy tether used. For larger deformations, we find that the ribbon is clearly sliding laterally along the surface of the epoxy allowing it to visibly rotate to relieve any torque that might otherwise build up during the deformation. The extent of this rotation is too small to accurately quantify given the difficulty in clearly imaging the entire ball of epoxy, however, the movements observed have all been consistent with a tether that is incapable of maintaining the application of a torque on a helical ribbon even at small extensions. In combination with theoretical arguments to be presented in section 5.3, we have high confidence in our interpretation of this torque free condition across the entire range of applied axial tensions.

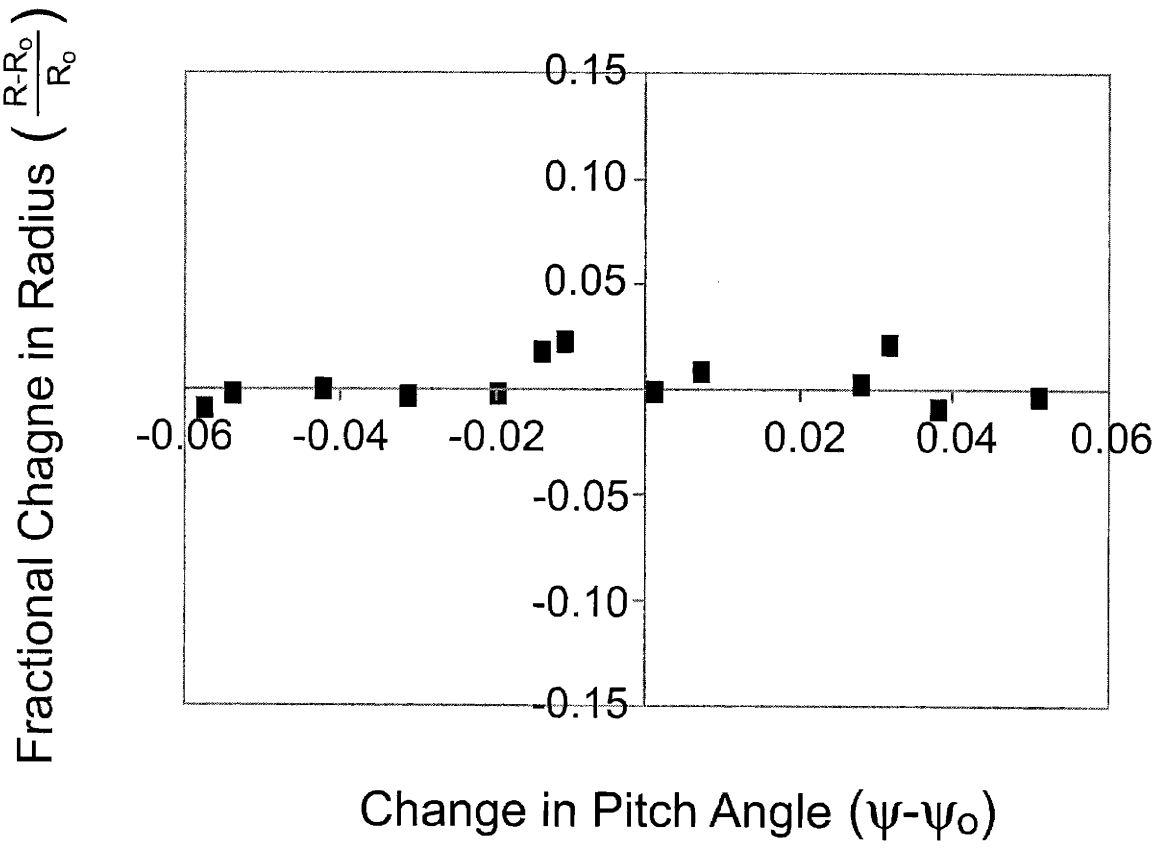

Figure 2-12: A plot of the experimental results for the fractional change in radius $((R - R_o)/R_o)$ versus the change in pitch angle $(\psi - \psi_o)$ in radians for the low-pitch helix shown in Figure 2-11. The uncertainty in the data in both parameters is represented by the size of the rectangle used at each point.

Now that we have developed a simple protocol for tethering and manipulating individual helical ribbons, and found that they behave in a fully reversible manner even under extremely large deformations, we next want to find a means of calibrating their elastic properties by directly measuring their effective axial spring constant.

2.4.3 Calibration of the Helical Ribbon Stiffness

I would like to thank Professor Gerald Pollack of the University of Washington for his generosity in providing us with a collection of the silicon-nitride cantilevers developed and fabricated in his laboratory.

In our discussion of the techniques used to measure single molecule forces, we found that there are a variety of techniques used to calibrate their force probes. Two of the most common calibration procedures involve the use of the equipartition theorem to analyze measurements of thermally induced fluctuations or the use of Stokes Equation to interpret data from fluid flow experiments. These were the first two methods we attempted as a means of measuring the elasticity of our helical ribbons [28].

For the thermal fluctuation experiments, we were limited to temperatures below approximately 80° C, because for temperatures above this the structures began to melt. However, even at such relatively high temperatures the helical ribbons showed no sign of any mechanical excitations. This is particularly interesting since we did not even observe transverse excitations corresponding to a buckling of the entire helix into an arc which are expected to be of significantly lower energy than the longitudinal modes that correspond to axial compression and extension for longer and more slender helices. From the equipartition theorem, we know that for the longitudinal modes

$$K_{\text{spring}}(\delta\ell)^2 = K_B T \tag{2.8}$$

where K_{spring} is the axial spring constant of the helix and $\delta\ell$ is the fluctuation in the axial length. Plugging $T = 353°$ K and a minimum resolvable $\delta\ell$ of 1 μm into this relationship, we find that we should be able to detect some degree of fluctuation for structures with a stiffness up to approximately 5×10^{-9} N/m. However, since we did not even observe the transverse excitations of the helices in solution we interpret

this as giving us the condition that $K_{\text{spring}} >> 5 \times 10^{-9}$ N/m. In section 5.2, we estimate that even the most compliant low pitch helical ribbons are predicted to still have spring constants on the order of 10^{-7} N/m which clearly satisfies this inequality.

The second method of calibration attempted was to extend a helix to a given axial length and measure the characteristic time associated with its relaxation when the tension is removed suddenly. The viscous drag force can be approximated from standard fluid dynamics, and thus this relaxation time can be related to K_{spring}. We know that in these experiments we are far from the top, bottom, and walls of the cell so we do not need to worry about the effects of the boundaries, and that the velocities are low enough so that there is no turbulence induced by the motion of the helix through the fluid. However, this technique suffers from two important sources of uncertainty in attempting to turn the time constant into a spring constant. First, while we are working in highly dilute samples, the helices are still in a complex mixture of CDLC and water which means that the viscosity is not known precisely and is only approximated by that of pure water. In addition, we did not control the temperature of the cell but allowed it to fluctuate from day to day with the room temperature. This further increases the uncertainty about the absolute value of the sample viscosity. Second, and more importantly, the precise form of the friction coefficient, including both its geometric dependence and the numerical constants for a helix moving through a viscous medium is not known. While a simple and elegant model can and has been proposed for this force [28], no exact solution has yet been found to the fully general problem. Given these uncertainties inherent in attempting to use this calibration technique, we will only report its results to the nearest order of magnitude. For the six helices we measured, K_{spring} was found to range from approximately 10^{-6} to 10^{-5} N/m in good agreement with our requirement from the thermal inequality.

Finally, with the failure of both thermal vibrations and fluid flow experiments to yield precise information about the stiffness of our helical ribbons, we chose instead to adopt a cross calibration technique using a cantilever of known stiffness. Given our estimates for the helix spring constant from the relaxation experiments, we know the

order of magnitude needed for the stiffness of the known cantilever is approximately 0.001 to 0.01 pN/nm and that it must be capable of undergoing displacements on the order of tens of microns. From the discussion in section 2.4.1, we note that this range is accessible to both glass needles and to the microfabricated silicon-nitride cantilevers. The silicon-nitride cantilevers are known to have many advantages over the glass needles, and thus we will choose to work with them as our given force probe. In particular, we chose to use the softest available cantilever which had a stiffness of roughly 0.05 pN/nm because it fell right in the middle of the desired force range.

The fabrication and calibration of these cantilevers has been described in detail by their inventors [108]. In our system, however, we cannot make use of the cantilevers while still attached to the silicon wafer because it is so large that it interferes with our ability to easily manipulate the helices. To overcome this limitation we have developed a means of integrating the cantilevers with our current micromanipulation techniques. This process is described in great detail in section 4.2.1 of [28] so we will only touch on the basic idea here. Figure 2-13 shows a schematic representation of a typical sequence in one of our experiments starting with the preparation of the cantilevers for use in our system through the final measurement of the force–extension relationship for a low-pitch helical ribbon.

Following the sequence shown in the figure, we begin by gluing one of the cantilevers from the softest differential pair to the end of a glass microneedle with an external diameter of approximately 5 μm using Devcon 5-Minute Epoxy®. After allowing the epoxy to cure for approximately one hour, we retract the glass needle holding the cantilever block fixed until the one glued to our needle separates from the wafer. In order to guarantee that its elastic properties were not effected by the transfer process, we then cross calibrate the silicon-nitride cantilever attached to the micromanipulator by bending it against one of the cantilevers remaining on the wafer. This needle/cantilever pair is quite delicate and prone to breaking along the epoxy joint, and so to protect it until it is needed we remove it from the micromanipulator and replace it with a standard rigid glass needle. We use this more durable needle to select a particular helix and tether one of its ends to a fixed rod in the cell. Once the

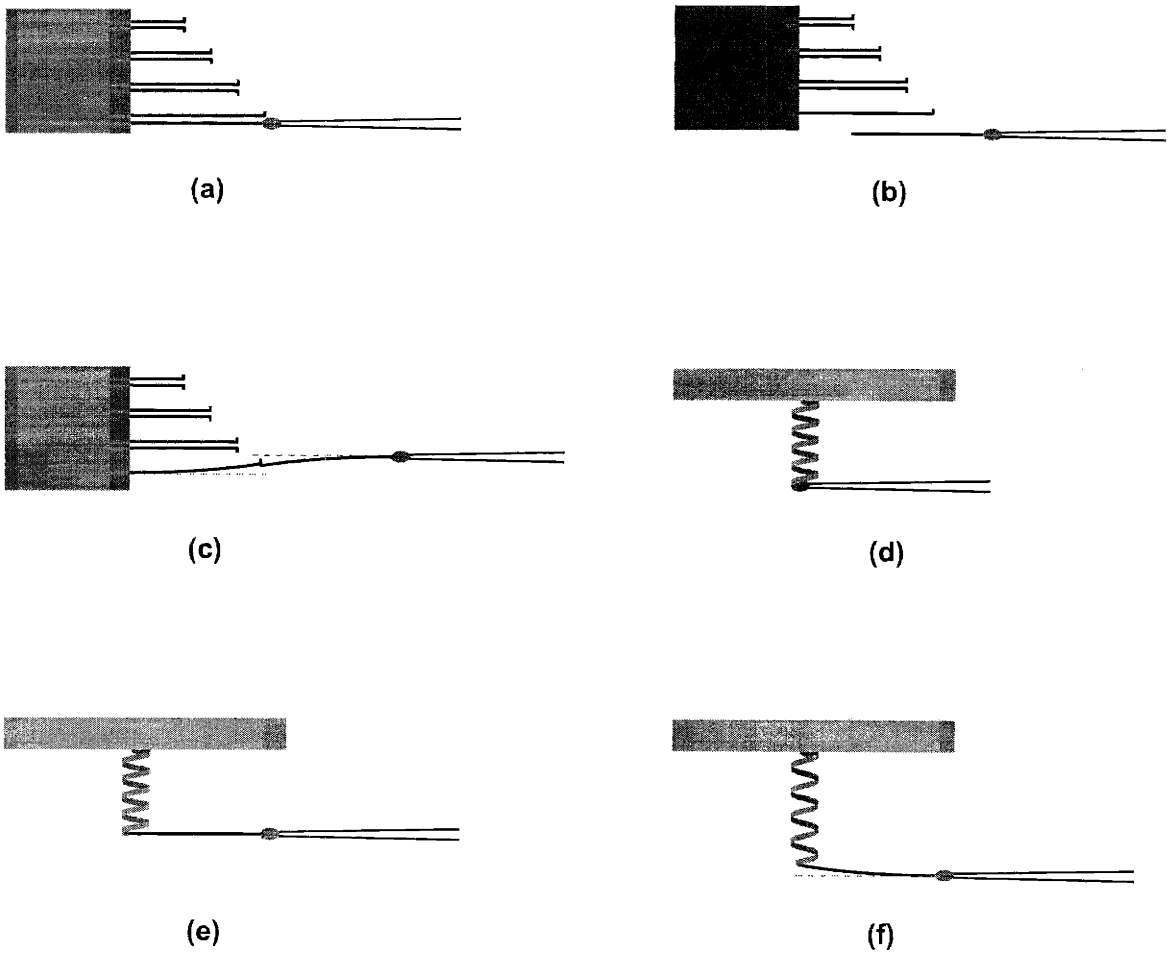

Figure 2-13: A cartoon schematic of the typical sequence in the experiments designed to calibrate the helix spring constant (not drawn to scale). (a) One of the softest cantilevers from a set on the silicon wafer is glued to an glass needle attached to the micromanipulator. (b) After allowing the epoxy to cure, the needle is retracted and the cantilever is separated from the block. (c) The cantilever attached to the needle is cross calibrated by bending against the remaining cantilever on the block to insure that its elastic properties have remained the same. (d) With the cantilever placed aside for safekeeping, a glass needle tethers one end of a low-pitch helix to a thick, rigid glass needle attached to the microscope slide. (e) The cantilever is returned to the micromanipulator and tethered to the free end of the helix, and (f) used to deform the helix allowing both the cantilever deflection and the helix extension to be measured simultaneously.

helix is attached to this fixed post it is ready to be measured, and thus we replace the stiff needle with the cantilever and tether it to the free end of the helix. Using the micromanipulator, we then extend the helix and simultaneously measure both the cantilever deflection and the extension of the helix.

In order to analyze the data collected from the manipulation experiments, we have simply to multiply the cantilever deflection by its stiffness (0.050 ± 0.008 pN/nm), and we can thus create the desired plot of the helix extension versus the force it exerts. Data collected in this manner for a typical low pitch helix with dimensions $s = 803 \pm 3$ μm, $w = 12.3 \pm 0.5$ μm, and $R_o = 19.2 \pm 1.0$ μm is shown in Figure 2-14.

From Figure 2-14, we see immediately that the helix exhibits linear behavior over this range of extensions making it a suitable candidate for use as a force probe. Fitting a straight line to the data, we find a slope of $(4.80 \pm 0.77) \times 10^{-6}$ N/m which defines the effective axial spring constant for this particular low pitch helical ribbon [28, 45]. Again this value is on the order we expected from our previous calibrations techniques, and this time there is no uncertainty in its interpretation as there was in the case of the relaxation experiments. While we know that the spring constant of the helical ribbons will depend in detail upon their geometry (see section 5.2), we have now determined directly the proper scale for the stiffness of the low pitch helices in CDLC and, just as importantly, we have developed a straightforward and unambiguous method for measuring the elastic properties of any given low-pitch helix in the CDLC system.

With these results, we can now look forward in Appendix A and speculate about the likely advantages and disadvantages the helical ribbons would have over the techniques discussed in section 2.4.1 if they were calibrated and used as probes for the measurement of forces in other biomaterials.

2.5 The Tension Induced Straightening Transition

We will conclude this chapter with a discussion of one of the most striking results to come out of our investigations into the response of helical ribbons to external stresses,

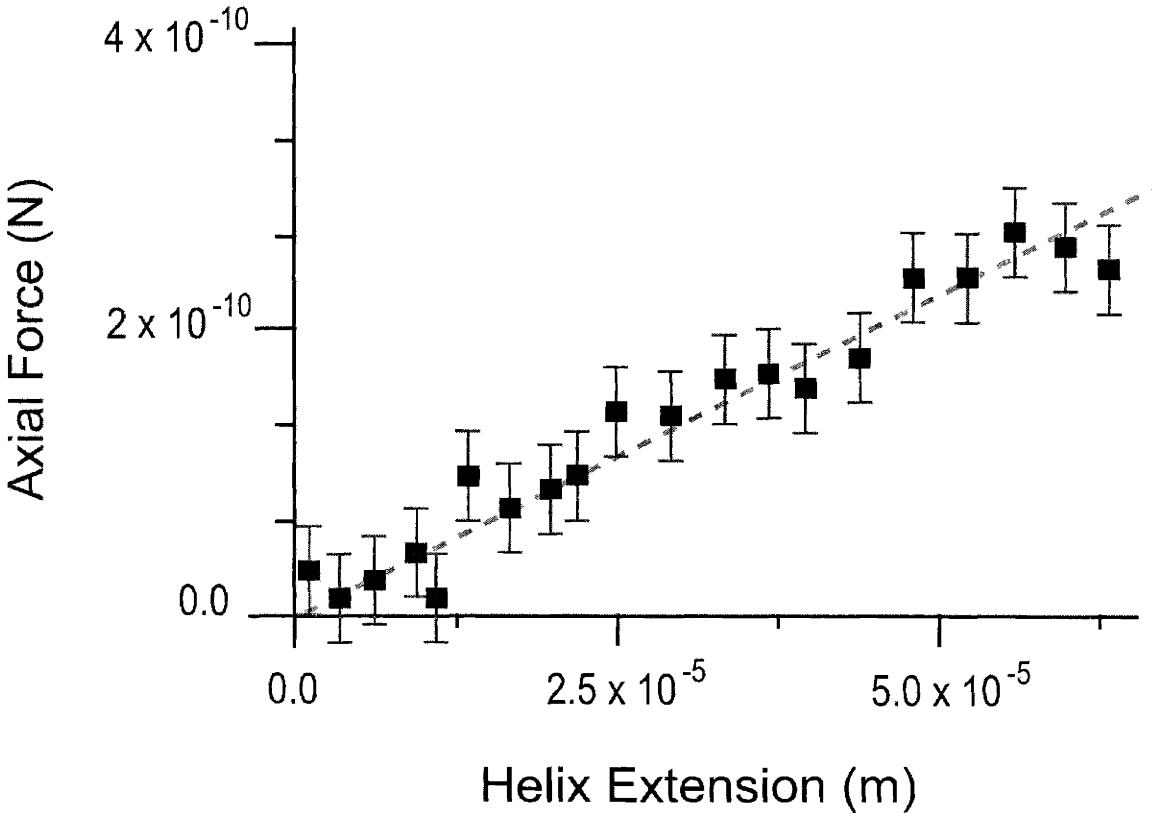

Figure 2-14: A typical graph of the restoring force versus helix extension measured using the silicon-nitride cantilevers. The slope of the linear curve fit (4.8×10^{-6}) is the spring constant of this helix in N/m.

namely our observation of a spontaneous, reversible separation of a helix into two domains with markedly different geometries. In particular, under the application of an axial tension we find that beyond a certain critical extension, all low-pitch helices investigated will routinely separate into a helical domain with pitch angle of 16.5 $\pm$ 1.3° connected to a straight domain with a pitch angle of 90°. Similarly, in a single set of experiments on a high-pitch helix, we have observed a separation into two domains with pitch angles of 59.6 $\pm$ 1.7° and 90° respectively (see below for caveats about this interpretation). We have reported on the tension induced straighten transition for the low-pitch helices previously [28, 45], however, this is the first time that the phenomena has been discussed for a high-pitch helix.

At first glance, this mechanical transition seems rather surprising. Such an instability will not occur for a classical springs such as a phone cord. However, this type of stress induced domain separation is not unique to our helical ribbons, and is in fact quite reminiscent of two other types of transitions. The first is the theoretical "coil-stretch" transition applicable in short polypeptides [117]. While the second is the "stem-flower" transition in globular polymers. Despite being based on completely different physics, the theoretical treatment of this transition phenomena in polymers has been formulated in a way directly analogous to our discussions in Chapters 3 and 5 [118, 119]. In addition, the "stem-flower" transition is interesting because it has actually been observed experimentally in DNA under strong flows and seems to agree qualitatively with the simple mean field theory [30, 31, 120].

In the coming sections, we will choose to discuss our experimental observations of the various features of the domain separation for the high and low pitch helices separately. We choose to divide it up in this way because, despite the many similarities, there are a number of important distinctions between the two sets of observations. We will begin with a discussion of the low-pitch case because, given the greater ease of tethering these structures, we have been able to perform more detailed investigations on this class of structure.

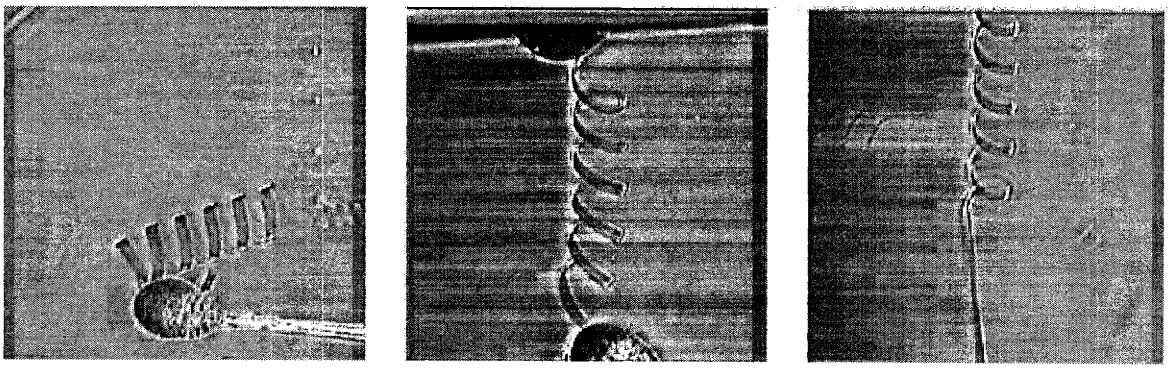

(a) (b) (c)

Figure 2-15: (a) A low pitch helix with radius 17 μm free from external force attached to a glass rod at one end and surrounded by other free low pitch helices in solution, (b) the same helix attached at both ends and slightly extended, and (c) the helix extended beyond 16.5° and allowed to come to equilibrium with respect to the straightening transition (the helix ends are off screen).

2.5.1 Observations of Domain Separation in Low-Pitch Helices Under Tension

As discussed above, low pitch helices have been observed to spontaneously undergo a reversible domain separation under the application of an axial tension. Figure 2-15 shows a typical experimental sequence in which a helix initially extends like an ordinary classical spring, but beyond some critical extension separates into two connected domains.

There are four important observations that we will note in regards to this phenomena within an individual helix. First, the domain separation is perfectly reversible. No matter how many times a helix undergoes the transition it always recovers its original unstressed geometry when the force is removed. In fact, we have actually torn a structure apart while in the domain separated state and observed both pieces as they relaxed back to the same radius and pitch angle as the original complete

helix had. Second, we found that the pitch angle of the helical domain was always the same ($16.5 \pm 1.3^{\circ}$) regardless of the rate at which we pulled, how long the tension was applied, whether we re-attached the helix to different parts of the epoxy, or whether we adjusted any of the other experimentally controlled parameters. Once it was in the separated state, increasing the total axial length merely changed the amount of material present in each domain without effecting the pitch angle of the helical domain. Third, while we found that the transition could be triggered anywhere between $16.5 \pm 1.3^{\circ}$ and $24.1 \pm 1.8^{\circ}$, there was absolutely no way to keep a helix in a single configuration for extensions corresponding to a pitch angle greater than $24.1 \pm 1.8^{\circ}$ [?]. Fourth, and finally, we found that while it was possible to form more than two domains (i.e. straight - helical - straight, etc.) these multilamellar configurations were much less stable than the two domain state. Given time they tended to spontaneously relax to the standard binary state in a relatively short time ($\sim$5 seconds). This observation is quite reasonable given the fact that each domain boundary necessarily has an associated crossover region (typically with a length on the order of R_o) that costs elastic energy to form. Given the rotational freedom of the helix when free from an external torque, it is possible for it to easily exchange material between the various regions, and to thus lower its total energy by eliminating all but a single domain wall.

When we now compare the results of our investigations of this phenomena amoung different helices, there are two additional pieces of information that are very important to note. First, the separation is found to occur for all low-pitch helices regardless of the age of the material, the dimensions of the helix (as long as it is long enough to tether and pull accurately), or the precise solution conditions such as temperature or pH. Second, the pitch angle of the helical domain is found to not only be constant for a given helix, but also to be fixed for all low-pitch helices in CDLC. This is a very interesting finding and, in fact, what one would expect given that the unstressed pitch angle is also a constant among these helices. Expanding upon this last point, we note that the pitch angle of the helical domain is the same even for helices with radii, widths, and lengths that vary significantly. It will turn out that the dependence of

this pitch angle on the width of the ribbon will be important in our discussions of the models in Chapter 4, and thus we point out explicitly that the width is completely uncorrelated with our measurements for this pitch angle.

These observations, taken together, imply that the domain separation cannot be merely an artifact of the particular angle of the glue joint, or how we applied the force, or any other such explanation, and must instead be an intrinsic property of the helical ribbons and as deeply robust as the unstressed pitch angle. As a means of presenting our average data is the clearest way possible, we show in Figure 2-16 a simple schematic diagram of an idealized experimental sequence labeling the values of the pitch angle at each point.

The consideration of the idealized case in Figure 2-16, completes our overview of the experimental findings concerning the domain separation in low-pitch helices. We will now turn to a consideration of the newly discovered transition phenomena observed in a particular high-pitch helix.

2.5.2 Observations of Possible Domain Separation in a High-Pitch Helix

While it has become routine to tether and manipulate the low-pitch helical ribbons that self-assemble in CDLC, working with the high-pitch structures remains a challenge. To date we have only successfully tethered two high-pitch helices in CDLC in such a way that we were able to apply a tension. One of the two was less than two full turns long, and thus could not display any interesting domain phenomena. The other helix, however, was longer and was found to undergo a type of spontaneous separation that appears in may respects to be quite similar to the tension induced straighten transition observed in the low-pitch helices.

The most important result of this section is simply the observation of this phenomena, and thus we will start off by showing a typical experimental sequence associated with extending this high-pitch helix. Figure 2-17 shows the helix free from stress, under a small extension in which it behaves linearly, and after it has come to equilibrium

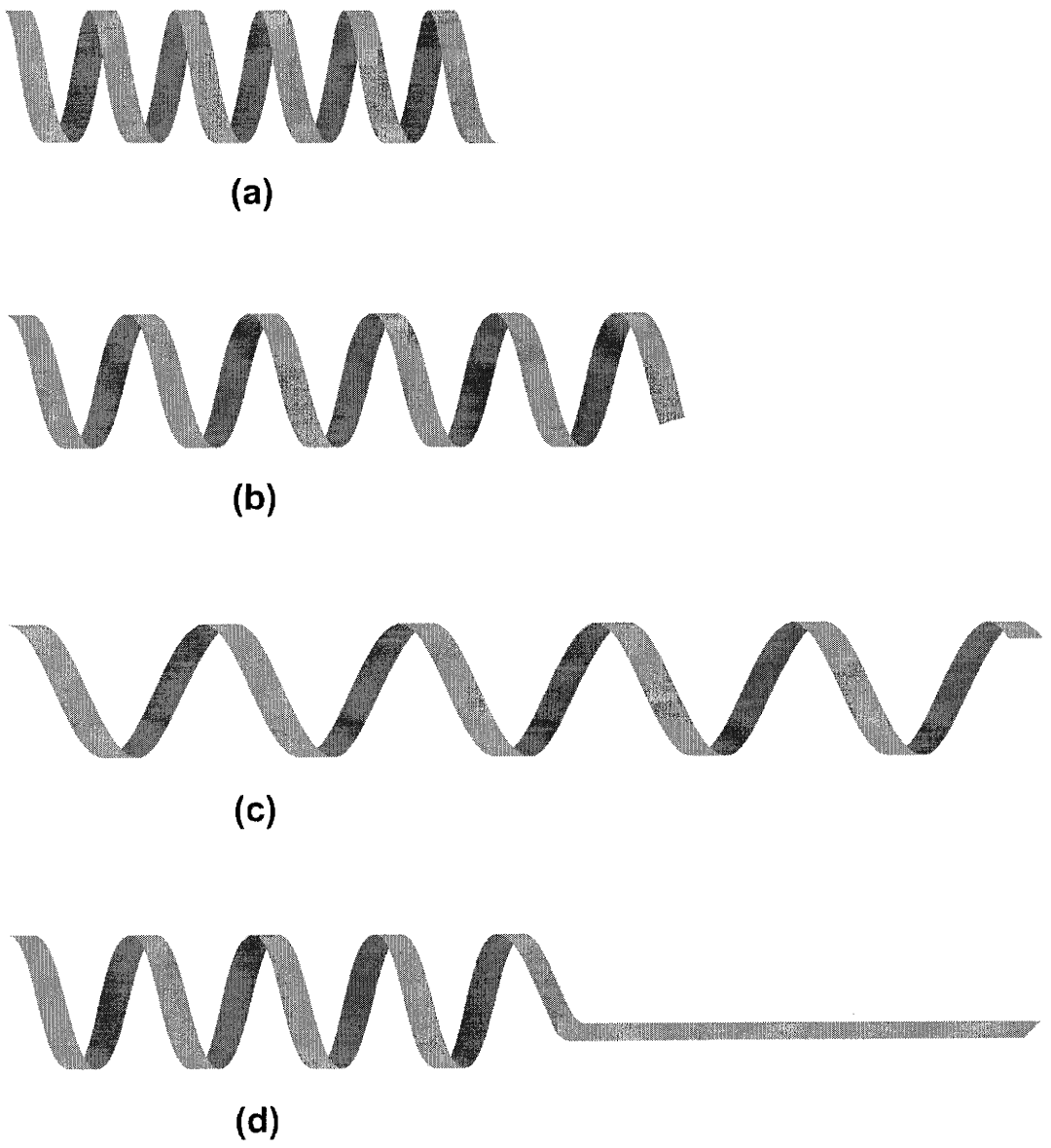

Figure 2-16: An schematic illustration of an idealized sequence in our pulling experiments. In (a) the helix is free from stress and has a pitch angle of 11°. Under the influence of a pure axial tension, (b) the helix is extended to a pitch angle of 16.5° at which point it is still stable as a single domain. As the tension is increased beyond this point (c) the helix expands metastably until it reaches a pitch angle of 24°. Here the helix will spontaneous separate (d) into two connected domains maintaining the same total axial length as it had before the transition. The two domains will consist of a helical domain with pitch angle 16.5° and a straight domain with pitch angle 90°. The two distinct conformations will be connected by a short crossover region with length on the order of R_o.

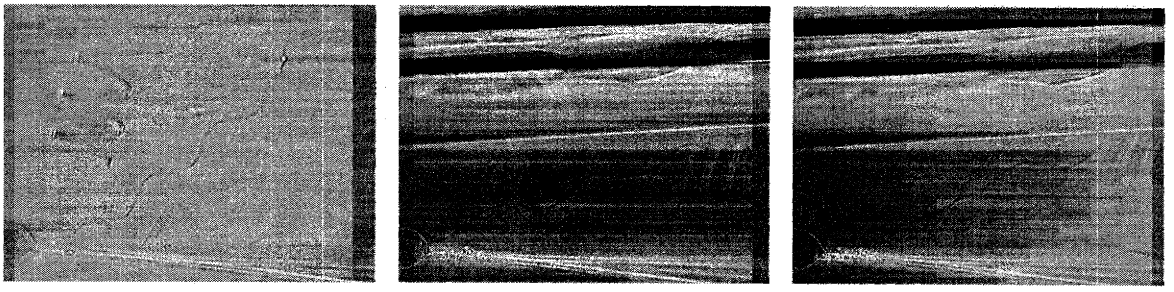

(a) (b) (c)

Figure 2-17: (a) The high pitch helix with radius 16.6 μm free from external force while attached to the glass rod at one end, (b) the same helix attached at both ends and slightly extended, and (c) the helix extended beyond 59.6° and allowed to come to equilibrium with respect to the observed domain separation phenomena.

in a domain separated state.

At first glance, Figure 2-17 would seem to clearly contain the same type of domain separation phenomena for the high-pitch helix as was discussed in the previous section for the low-pitch. The pitch angle of the helical domain is found to be 59.6 $\pm$ 1.7° while the maximum pitch angle we were able to achieve while keeping the helix in a single domain was 60.8 $\pm$ 1.6°. All of this so far is consistent with our previous discussion. However, there is one major difference that is obvious from an examination of Figure 2-17(c), namely the distinct "wobbles" that can be seen in what we are calling the straight domain. These type of local deviations from a straight filament were never observed in a domain separated low-pitch helix, but they formed reproducibly in this high pitch structure. Interestingly, as shown in Figure 2-18, the short high pitch helix also developed a "wobble" when pulled close to straight.

The fact that these defects always formed in the same type of location (i.e. where a helix turn used to be), it is unlikely that they are simply artifacts of a particularly flexible ribbon being disturbed by currents in the water or residual vibrations from

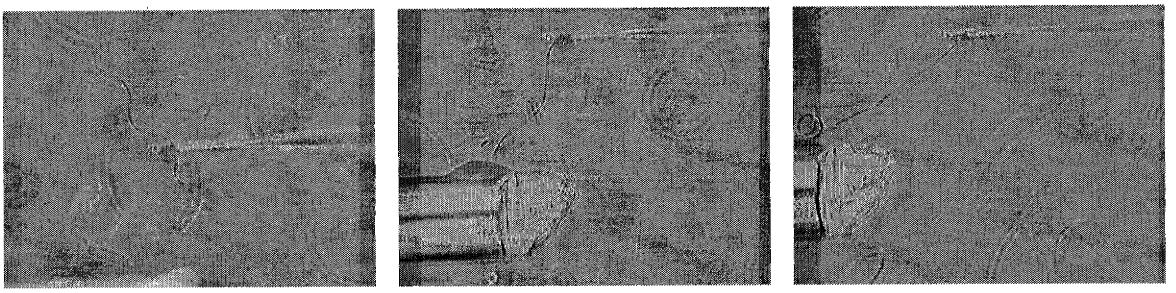

(a) (b) (c)

Figure 2-18: (a) The short high pitch helix with radius 20 μm free from external force while attached to the glass rod at one end, (b) the same helix attached at both ends and slightly extended, and (c) the helix under a large extension showing the same type of "wobble" defect observed for the longer helix in Figure 2-17.

the building.

One possible explanation for the formation of the "wobbles" is that the epoxy may not be forming the same type of zero torque bond with the high-pitch helix that it does with the low-pitch helices. We have already discussed the fact that the two types of helices have very different affinities for the epoxy. In addition we note that the epoxy seems to stick equally well to all locations on a low-pitch helix, whereas we had to try many different place along many different high-pitch helices before we could find any location that the epoxy would adhere to strongly enough to allow for their manipulation. It is therefore possible that the high-pitch helices form a tight, non-slipping bond with the epoxy allowing both tension and torque to be applied in these experiments. In that case, we will show in the following chapter that the helix would be required to maintain a fixed number of turns upon extension, and thus the "wobbles" may be residual, low radius turns. This possible explanation, however, suffers from two major drawbacks that make it highly unlikely. First, if these defects were actually the ribbon folding over on itself in order to preserve the total number

of turns, then they would be under great stress due to the high curvatures necessary and we know that the ribbons will tear apart under relatively modest forces. Second, we will find in Appendix E that this type of tight binding boundary condition for the tether is fundamentally incompatible with the observation of any type of stable and reversible domain separation.

Without a more plausible explanation available, we will choose to analyze the data from these observations based upon the assumption that this domain is effectively straight. Obviously, there is much work that must yet be done to look for this transition in other high-pitch helices, and to more fully characterize the "wobbles" under high tensions. It appears from these first experiments that the behavior of high-pitch helices under stress is equally as rich as that for the low-pitch structures, if not more so.

Chapter 3

The Generalized Mechanical Theory of Helical Ribbons

3.1 Introduction

Chapter 2 described our experimental observations of the helical ribbons formed in the quaternary cholesterol - surfactant - fatty acid / phospholipid - water systems. In order to describe these observed phenomena, we will formulate in this chapter a general theoretical framework capable of handling not only the case when the helices are free in solution, but also when various external stresses are applied to them. We will begin this formulation by considering the helix to be entirely elasto-mechanical in nature. This means that we will be able to completely describe it through an internal elastic potential energy (F). This function will reflect the energy costs and benefits incurred in deforming the ribbon away from a flat strip, which we will assume to be its zero elastic energy state. The various physical models for such a free energy will be described in the next chapter, while for now we will treat F in the most general way possible.

For consistency with previous work on our helical ribbons, we will adopt the standard nomenclature and henceforth refer to this function as the helix free energy [20, 44, 26]. It is important to point out, however, that this is a purely mechanical energy and not a true thermodynamic function. There is no temperature in our

problem and therefore there are no thermal fluctuations to be included. It will be useful at certain points in the coming analysis to draw analogies with various thermodynamic systems (particularly in regards to the straightening transition described in section 2.5), but care must be taken not to carry these analogies too far since we do not consider thermal effects such as collective excitations in our description of the helices.

We will begin the description of our formalism with a review of the basic geometry of a helical ribbon in section 3.2, and then discuss the important generic considerations that hold true for all physically reasonable model free energies. Once we have defined the proper variables for the problem, we will expand the formalism in section 3.3 to incorporate the most general possible application of external forces to a helix. In section 3.4 we will then examine some special cases in which an external constraint is imposed on how the helix is deformed such as the case of extension in the absence of torque which was discussed in section 2.4.2 for our pulling experiments on low pitch helices in CDLC using Devcon 5-Minute Epoxy. Finally, we will conclude the generalized theory in section 3.5 by describing the equilibrium conditions when a helix no longer remains in a single domain, but separates into two connected regions of different conformation.

3.2 Geometric Parameterization of the Helix Free Energy

As discussed above, the free energy in our theory is purely mechanical in nature and must therefore be determined entirely by the geometric conformation of the helix. We will thus begin our description of the general theory of helical ribbons with a review of their bulk geometry and the relationships that connect their important geometric state variables. Figure 3-1 (reproduced in part from section 2.3) shows a schematic illustration of a helix and labels the most useful physical parameters.

As discussed, the fundamental variables describing the geometry of the helix are

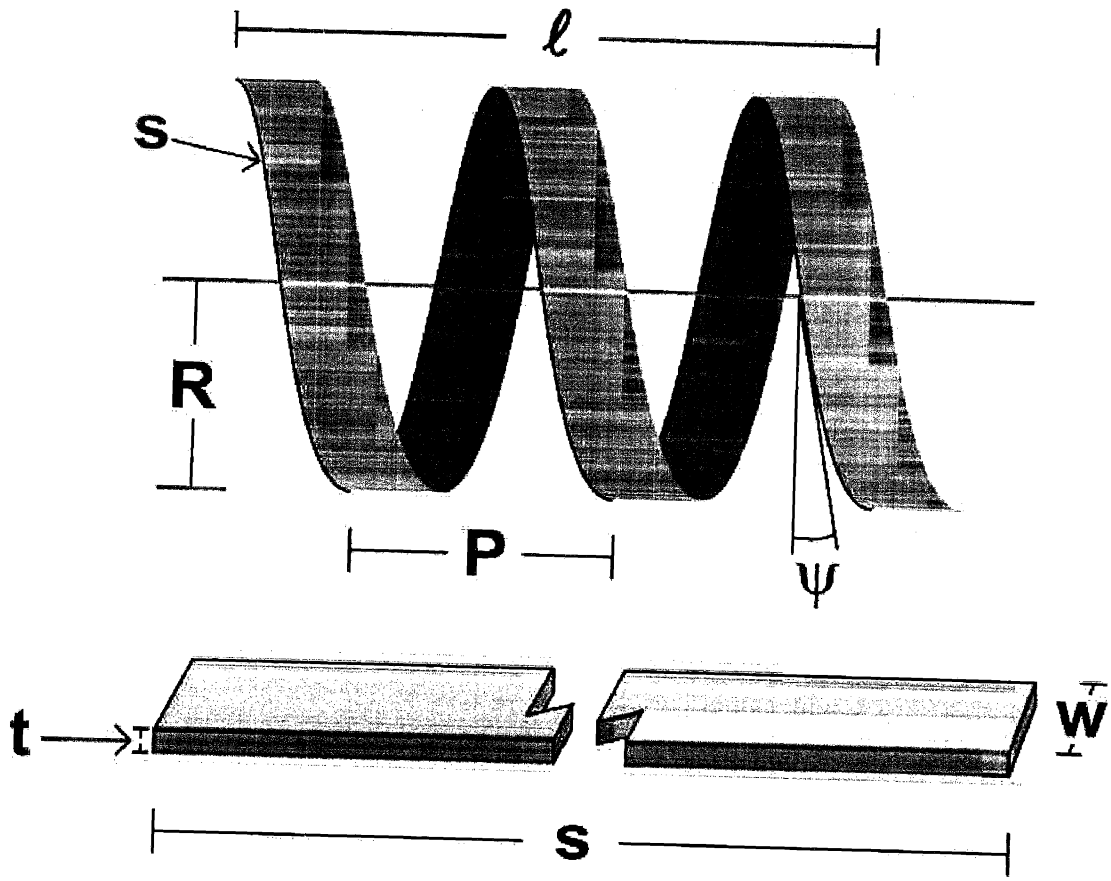

Figure 3-1: Definition of the geometric state variables that fully parameterize the conformation of a helix and of its underlying ribbon.

its radius (R), pitch angle (ψ), and axial length (ℓ). In addition, the geometry of the ribbon is described by its width (w), thickness (t), and total contour length (s). These six parameters are not totally independent, however, as is seen by examining Figure 3-1. In fact, the axial length, the contour length, and the pitch angle are linked by the simple trigonometric relationship

$$\ell = s\sin(\psi) \tag{3.1}$$

as derived in section 2.3. Any maximally independent set of the six variables listed above will fully describe the geometry of a helical ribbon, and therefore any geometric quantity of interest must be expressible in terms of that set. The most useful of these

parameter sets, which we will refer to as the independent primitive variables, will be R, s, w, t and either ψ or ℓ. With this general geometric description, we are now ready to consider what form the free energy will take in order to describe such a helix.

As already discussed, we know that the phenomenological free energies to be considered must be determined entirely by the bulk geometry of the helix. We also now know that any such function of the helix geometry may be expressed completely in terms of one of the two independent primitive variable sets. Thus in the most general sense we know that we will always be able to write $F = F(R, \psi, s, w, t)$ or $F = F(R, \ell, s, w, t)$. We can, however, go beyond this very general argument and further simplify our problem by considering some of the specific physical properties of the helices formed in the quaternary systems.

First, we noted in section 2.2 that despite being thermodynamically metastable, the helices in CDLC, will remain for several weeks without any observable change in their geometry when suspended in a highly dilute medium. Additionally, a helix may remain unaffected for several days even if it is suspended in a very rich growth medium. These observations imply that the ribbon parameters (w, t, and s) do not change due to material exchange over the time scale appropriate to any pulling experiment. This is a beneficial property for the helices to have if they are to some day be potentially useful as force transducers and measuring devices. In addition, if we add the observation that the ribbons are completely inextensible, we can make the simplifying assumption that the width, thickness, and total contour length may be treated as constants in our mechanical description of the helix free energy.

Second, we know that F must be extensive in the area of the ribbon. The ribbons are much thinner than they are wide or long (i.e. $t \ll w, s$), and thus they may be treated effectively as two-dimensional surfaces. The total free energy must therefore be given by an energy density determined entirely by the local deformations of the ribbon times the total area of the ribbon. In principle, given that we have already argued that the width, thickness, and total contour length are all constants, we could simply ignore them as parameters of interest and focus only on the remaining two variables (R and either ℓ or ψ). This simplification is not entirely desirable, however,

because in order to describe the straightening transition we must consider a situation in which portions of the contour length may be exchanged between regions of different conformations and therefore the dependence of the free energy on s will turn out to be quite important (see section 3.5).

Suppressing the dependence of F on the constants w and t for now, we thus expect that, in general, the free energy will be of the form

$$F = F(R, \ell, s) = s\hat{F}\left(R, \frac{\ell}{s}\right) \tag{3.2}$$

or alternatively

$$F = F(R, \psi, s) = s\hat{F}(R, \psi) \tag{3.3}$$

where $\hat{F}$ is the free energy per unit contour length (i.e. $\hat{F} \equiv F/s$). In other words, $\hat{F}$ divided by the width is equal to the local free energy density discussed above.

Up to this point, we have ignored the possibility that the microscopic structure of the ribbon may contribute additional degrees of freedom to F. However, in Chapter 4 we will show that a model capable of self consistently explaining our current experimental observations may be constructed without the need for additional microscopic parameters. Thus, without loss of any important physics, we will continue to focus only on the coarse grained free energy given by Equations 3.2 and 3.3.

By construction, these generalized free energy functions will contain all of the information necessary to determine the properties of an isolated helix free in solution. In order to examine how the application of external stresses will affect the helix and how the equilibrium restoring forces are related to the free energy, however, we must expand our formalism as described in the following sections.

3.3 Incorporation of Externally Applied Stress

Until recently, the only information available to guide the choice of the model free energy was limited to passive observations of the equilibrium pitch angle and radius [20, 27]. In order to go beyond an examination of the helix geometric properties while free in solution, it is necessary to deform it by applying an external stress.

The deformations we will consider in this work may be accomplished by applying a force along the helix symmetry axis (axial compression and expansion), by applying a torque to the helix ends (winding and unwinding), or by applying some combination of the two. The theoretical relationships between the applied forces and the helix free energy to be worked out in this section will provide the tools necessary to analyze our experimental results and to probe the form of the various terms in the free energy.

In order to incorporate the applied forces into our theory, we will first calculate the total energy of the system including the internal elastic potential energy of the helical ribbon (i.e. its free energy) and the amount of work supplied by the external forces. The condition of mechanical equilibrium will then be that this total energy is minimized with respect to the two free variables in the system, the axial length (ℓ) and the radius (R). By assuming that the contour length is constant, our means of incorporating the stress implicitly assumes that the helix remains in a single domain. Section 3.5 will examine the consequences of relaxing this constraint, but it is important to keep this fact in mind when examining the form of the tension and torque calculated in this manner.

3.3.1 The Internal Elastic Potential Energy

As noted, the internal energy of the helical ribbon is given by the model free energy $F(R, \ell, s)$ introduced in the previous section (Equation 3.2). At this point, it is not necessary to specify the details of how this function depends on R, ℓ, and s, and thus the analysis will be equally applicable to any of the phenomenological models to be described in Chapter 4. In the most general case, the radius and the contour length can be considered to be fully independent variables. Under many situations of interest, however, R and ℓ may be coupled by a constraint imposed on the manner in which the helix is deformed. These constraints may come from the way in which the stresses are applied (i.e. the nature of the tether may allow either a pure axial tension or a pure torque to be applied thus restricting the other stress to be zero) or they may come from fixing some aspect of the helix geometry upon deformation (i.e. holding the relative orientation of the ends constant upon extension). We will

begin by considering the general situation for arbitrary axial tension and torque, and then examine the effect of imposing these types of constraints and of the resulting coupling of R and ℓ in section 3.4.

3.3.2 The Work Done by External Stress

We will now calculate the contribution to the total energy from the work done by the external stresses applied to the helix. The geometric definition of the two types of external forces to be considered, namely the axial tension ($\vec{J}_{\parallel}^{ext}$) and the torque ($\vec{\tau}^{ext} = \vec{R} \times \vec{J}_{\perp}^{ext}$), is shown in Figure 3-2.

As discussed in section 2.2, the vast majority of the helices formed in the quaternary systems, including all of those observed in CDLC, are right-handed. We will thus use a right-handed helix to define the sign convention for the forces. At equilibrium, the restoring tension and the restoring torque exerted by the helix must be equal in magnitude and opposite in direction to the externally applied forces. For consistency we will choose the positive direction for the stresses to be defined relative to those applied to the helix. For the ribbon shown in Figure 3-2, therefore, the $\hat{z}$ axis is taken to be the positive direction for both the axial tension and the torque. Using this sign convention, the externally applied tension ($\vec{J}_{\parallel}^{ext} = J_{\parallel}^{ext}\ \hat{z}$) shown in the figure is positive and will result in an extension of the helix ($\ell > \ell_o$). In addition, the external torque from the figure ($\vec{\tau}^{ext} = J_{\perp}^{ext} R\ \hat{z}$), is also positive, and will result in the increased winding of a right-handed helix ($\Phi > \Phi_o$). Since the tension and the torque we will consider always lay along the plus or minus z-axis, for simplicity we will drop the vector notation and allow the sign of the force to carry its directional information throughout the rest of this work.

The amount of work done by the external axial tension in expanding or compressing the helix from its initial axial length ℓ_o to some final length ℓ is then given simply by

$$W_{axial} = +J_{\parallel}^{ext}[\ell - \ell_o] \tag{3.4}$$

In Equation 3.4, $J_{\parallel}^{ext}$ is taken to be constant throughout the extension or compression

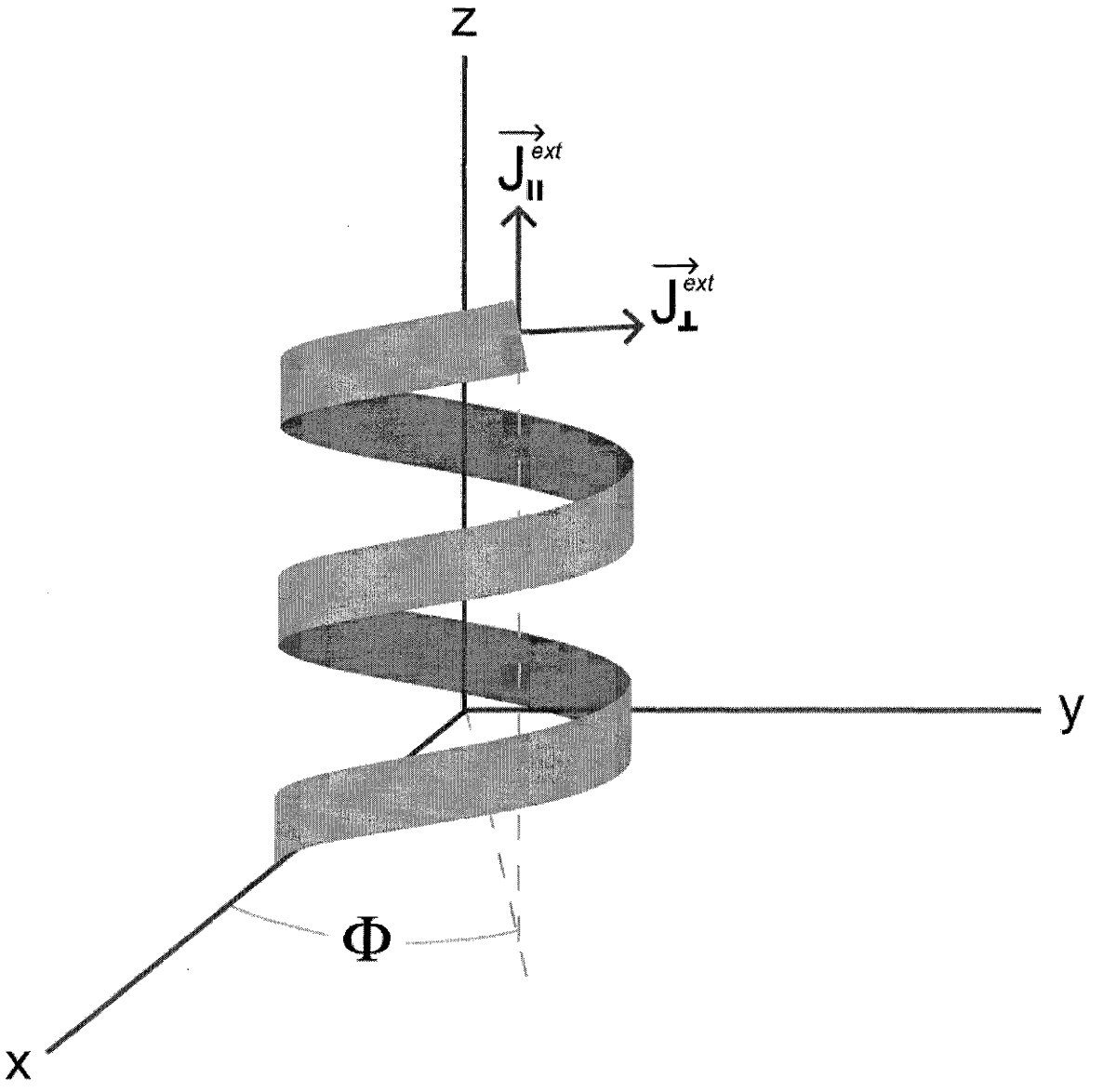

Figure 3-2: Schematic definition of the two types of external forces applied to a helical ribbon that we will consider. Throughout the following analysis, we will be interested not in the perpendicular force, but in the torque. The magnitude of the applied torque (not shown) may be calculated as $|\vec{\tau}^{ext}| = J_{\perp}^{ext} R$ and its direction will follow from the right-hand rule.

and, as we discussed, the final length ℓ is defined such that the resultant restoring force exerted by the helix is equal and opposite to the externally applied tension. Using this observation and the sign convention described above, we may redefine the axial work as

$$W_{axial} = -J_{\|}[\ell - \ell_{\mathrm{o}}] \tag{3.5}$$

where it is understood that the magnitude of the helix tension ($J_{\|}$) is correct only at the final length ℓ. We have chosen to incorporate the minus sign into our definition of W_{axial} in order to simplify the analysis and guarantee that $J_{\|}$ will be positive for extensions and negative for compressions. It must be noted that, in general, W_{axial} is greater than the work done by the helix during the deformation. This difference is due to the fact that both dissipative forces and the external agent that supplies the tension absorb part of the energy input while allowing the system to reach its new static equilibrium. An example demonstrating this energy balance as well as the general applicability of our formalism to a simple model system involving a classical spring that obeys Hooke's Law is discussed in Appendix B.

Turning to rotational deformations, we find that, in analogy to the discussion of an external axial tension, the work done by a constant external torque in winding or unwinding the helix is given by

$$W_{rot} = +\tau^{ext}[\Phi - \Phi_{\mathrm{o}}] \tag{3.6}$$

where Φ is the azimuthal angle in cylindrical coordinates between one end of the helix and the x-axis when the other end is aligned along that axis (see Figure 3-2). As we did for the axial tension, we will redefine the rotational work done in terms of the torque exerted by the helix. Incorporating a minus sign to take care of the difference in direction, we have that the work done by the torque may be written as

$$W_{rot} = -\tau[\Phi - \Phi_{\mathrm{o}}] \tag{3.7}$$

The parameterization of W_{rot} in terms of the angle Φ, however, is typically inconvenient to use because the phenomenological models to be described in Chapter 4 express the helix free energy most simply as a function of R, ℓ, and s. We will

thus re-express the rotational work done in terms of these more traditional geometric variables.

Examining the geometry of a helix, it is straightforward to see that the effective circumference swept out by the total contour length projected onto the x-y plane is $s\cos(\psi)$, and thus that the arc angle Φ must be given by

$$\Phi = \frac{s\cos(\psi)}{R} \tag{3.8}$$

More formally, we may directly calculate Φ by counting the number of helix turns (n). The number of turns in a helix is equal to its axial length divided by its pitch (P), and must also be equal to Φ over 2π. Equating these two expressions and substituting Equation 2.2 from section 2.3 for the pitch yields

$$n = \frac{\Phi}{2\pi} = \frac{\ell}{2\pi R\tan(\psi)} = \frac{1}{2\pi}\left(\frac{\ell}{\sin(\psi)}\frac{\cos(\psi)}{R}\right) \longrightarrow \Phi = \frac{s\cos(\psi)}{R} \tag{3.9}$$

where we have used Equation 3.1 to replace $\ell/\sin(\psi)$ by s. Finally, substituting the above definition for Φ into the formula for the rotational work (Equation 3.7) yields

$$W_{rot} = -\tau\left(\frac{\sqrt{s^2-\ell^2}}{R} - \Phi_o\right) \tag{3.10}$$

This set of variables is the more convenient parameterization of the rotational work, and will be carried throughout most of the coming analysis.

3.3.3 The Total Energy and Conditions of Mechanical Equilibrium

We may now define the total energy of the system which must be minimal at equilibrium. For the most general case, in which we keep R and ℓ as independent variables, we have

$$E^{tot}(R,\ell) = F(R,\ell,s) - F(R_o,\ell_o,s) - J_{\|}[\ell-\ell_o] - \tau\left(\frac{\sqrt{s^2-\ell^2}}{R} - \Phi_o\right) \tag{3.11}$$

where $J_{\|}$ and τ refer to the stresses exerted by the helix and $F(R_o,\ell_o,s)$ is included for completeness even though it is a constant, and thus will not effect the overall

minimization. In addition, it is important to again draw explicit attention to the fact that this analysis assumes the helix remains in a single domain, and thus that s is constant. It is important to be careful about such distinctions because of the experimentally observed straightening transition described in section 2.5. In light of this observation, we expect that the stress calculated in this manner must physically break down at some point indicating the failure of our continuous helix constraint and the onset of domain separation. This consideration is analogous to the way in which the pressure for the Van der Waals gas develops an unphysical region below a critical temperature signifying the breakdown of its assumption that the density is constant throughout the volume of the material (see Figure 3-3) [121].

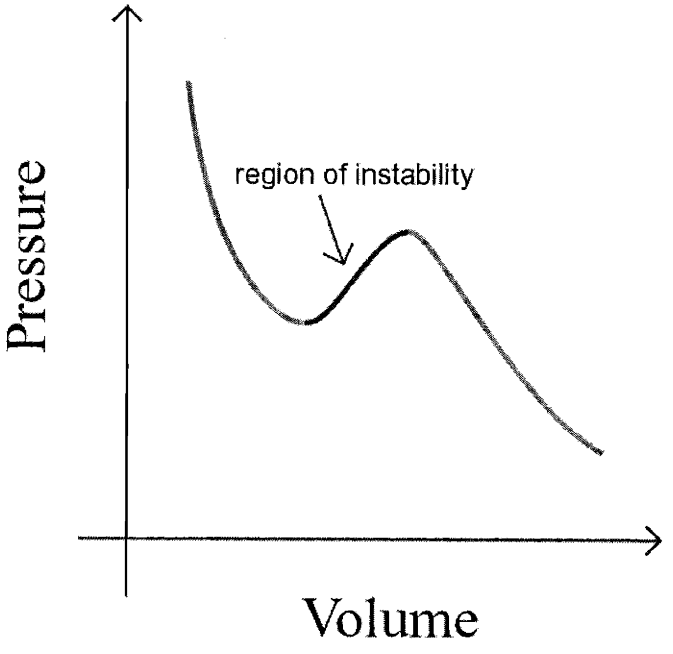

Figure 3-3: Schematic plot of a typical pressure-volume isotherm for a van der Waals gas below the critical temperature T_c. The region of instability (shown as the darkened portion of the curve) corresponds to a volume range where the gas is predicted to have a negative isothermal compressibility, which is not physically allowed.

Care must be taken not to carry this analogy too far, however, because for the gas, the failure of the imposed constraint is related to a thermodynamic instability triggered by the onset of collective excitations whereas for the helix the failure will

be related to a purely mechanical instability.

In order to determine the desired conditions of mechanical equilibrium for a helix under external stress, we must now find the minimum of the total energy given in Equation 3.11. Minimizing E^{tot} with respect to the two free parameters R and ℓ, and solving for the derivatives of the helix free energy gives us

$$\frac{\partial F}{\partial \ell} = J_{\parallel} - \frac{\ell}{\sqrt{s^2 - \ell^2}}\left(\frac{\tau}{R}\right) \tag{3.12}$$

and

$$\frac{\partial F}{\partial R} = -\Phi\left(\frac{\tau}{R}\right) \tag{3.13}$$

Equations 3.12 and 3.13 encapsulate everything that is needed in order to determine the equilibrium response of a helix to the application of an arbitrary external tension and/or torque. In principle, we are now in a position to apply this formalism to the various models for the helix free energy to be discussed in Chapter 4 and to compare the results with our experimental observations described in Chapter 2. In many important experiments, however, (including those that we carried out on the helices in CDLC) there are additional mechanical constraints imposed on the system by the manner in which the stress is applied. Therefore, before attempting to directly apply this formalism to any specific phenomenological models, it will be useful to explore the implications of the more common constraints, and to examine how they change and simplify the equations of mechanical equilibrium.

3.4 Implications of External Constraints on the Applied Stress

The previous section describes a general method for finding the state of mechanical equilibrium, and thus the response of a helical ribbon under stress, from considerations of the total energy. Equations 3.12 and 3.13 are valid for arbitrary axial tension and torque and may, in principle, be applied to any situation. However, there are four special cases worth examining in detail. These special cases are:

Case 1 no external stress is applied (i.e. the helix is free in solution)

Case 2 the helix is subjected to an axial force in the absence of torque (i.e. freely rotating ends)

Case 3 the helix is subjected to an axial tension and whatever external torque is required to hold Φ constant (i.e. clamped ends)

Case 4 a torque is applied to the helix in the absence of axial tension (i.e. pure winding and unwinding).

The four special cases described above are schematically illustrated in Figure 3-4.

3.4.1 Case 1 : Zero Tension and Zero Torque

The most important special case we will examine is when both $J_{\|}$ and τ are identically zero. This is the simplest possible situation and, because it describes the undeformed helices, it is also the case for which there is the most experimental information available. In this case the conditions of mechanical equilibrium given in Equations 3.12 and 3.13 take on the very simple form

$$\frac{\partial F}{\partial \ell} = 0 \tag{3.14}$$

and

$$\frac{\partial F}{\partial R} = 0 \tag{3.15}$$

respectively. As expected, in this limit the equations of mechanical equilibrium reduce to the condition that the internal energy of the helix must be at its minimum with respect to both its radius and its axial length. These two equations define the equilibrium radius (R_o) and axial length (ℓ_o), or alternatively R_o and the equilibrium pitch angle (ψ_o) given that the total contour length is assumed to remain fixed at its initial value. Thus, this simple special case provides another positive check on the validity of our general theoretical formalism by reproducing the correct equilibrium conditions in the zero stress limit.

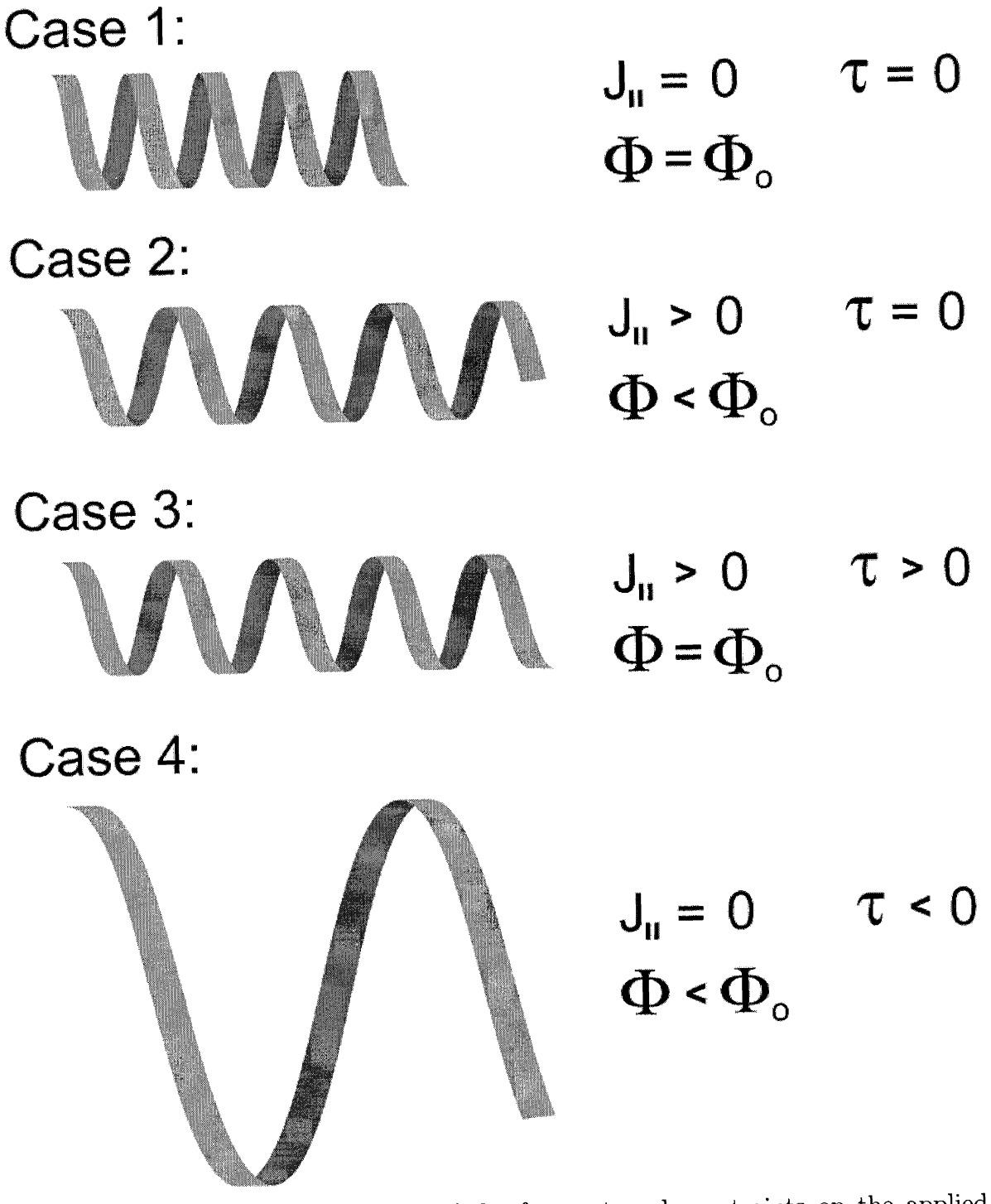

Figure 3-4: Schematic illustration of the four external constraints on the applied stress to be considered. Case 1 is a helix free from all forces. Case 2 corresponds to a helix extended by a positive axial tension in the absence of an applied torque. Case 3 is a helix that has been extended by a positive axial tension in addition to a positive torque that holds the azimuthal angle Φ fixed. Case 4 corresponds to a helix that has been unwound by a negative torque in the absence of an applied tension.

3.4.2 Case 2 : Externally Applied Axial Tension with Freely Rotating Helix Ends

The second most important special case is for a helix under the influence of an axial tension in the absence of an external torque. We will focus on this special case because it is the condition applicable to the pulling experiments we performed on the helices in CDLC using Devcon 5-Minute Epoxy as the tethering agent (see sections 2.4.2 and 5.3 for a description of the experiments and of the theoretical evidence that this constraint is the one appropriate to our system). Thus the formalism developed in the following discussion will provide the basis for properly analyzing the bulk of our experimental results.

For this case, we allow an arbitrary axial tension to be applied to the helix, but we require that the torque is identically zero for all configurations. This greatly simplifies the problem, and reduces the equilibrium conditions to

$$\frac{\partial F}{\partial \ell} = \tilde{J}_{\|} \tag{3.16}$$

and

$$\frac{\partial F}{\partial R} = 0 \tag{3.17}$$

where the tilde on the axial tension signifies that this is the value of the force appropriate only when τ is fixed at zero throughout the deformation.

There is far more, however, that can be drawn from this consideration then just the above simplification of the expression for the axial tension. As discussed, the zero torque condition, provides a constraint that couples the radius to the axial and contour lengths (i.e. we may define a function $\tilde{R}(\ell, s)$ for any given choice of F such that Equation 3.17 is automatically satisfied). This constraint then allows the problem to be reduced from one involving three variables (R, ℓ, and s) to one involving only two (ℓ and s). This reduction in degrees of freedom will be particularly useful in section 3.5 when we relax the constraint that s is constant because it will greatly simplify the considerations of how material may be exchanged between two connected domains with different geometric configurations.

Physically, the reduction in the number of independent parameters can be understood as follows. In the absence of torque, there is no resistance to rotation so Φ is allowed to change freely as the helix is deformed. From Equation 3.8, we see that for a given axial length, the freedom to adjust Φ corresponds to a freedom to adjust R as well. At each point along the extension, the radius may then adjust itself to find the minimum of the constrained helix free energy, which is exactly what is given by Equation 3.17.

Using the theoretical constraint on the radius derived from the equilibrium condition in Equation 3.17, we can now calculate how much the azimuthal angle Φ will change upon extension or compression. From Equation 3.8 and the definition of $\tilde{R}(\ell, s)$, we find that the angle changes according to

$$\tilde{\Phi}(\ell, s) = \Phi_o\left(\frac{R_o}{\tilde{R}(\ell, s)}\right)\sqrt{\frac{s^2 - \ell^2}{s^2 - \ell_o^2}} \tag{3.18}$$

Because of its explicit dependence on the radius, the details of how $\tilde{\Phi}$ depends on the axial and contour lengths will be determined by the choice of the specific model for the free energy.

Finally, we may use the relationship for the radius $\left(\tilde{R}(\ell, s)\right)$ to define a reduced free energy that is a function only of ℓ and s. We will denote this reduced free energy by $\tilde{F}$ because, like the tension in Equation 3.16 and the azimuthal angle in Equation 3.18, it is no longer general but is appropriate only for the special case of zero torque. Under this constraint, the reduced free energy is given by

$$\tilde{F}(\ell, s) \equiv F\left(\tilde{R}(\ell, s), \ell, s\right) \tag{3.19}$$

where, as before, $\tilde{R}(\ell, s)$ is the helix radius found from the minimization in Equation 3.17.

Using this definition, we must re-express the axial tension in terms of the reduced free energy. The partial derivative of $\tilde{F}$ with respect to the axial length is equal to

$$\frac{\partial \tilde{F}}{\partial \ell} = \frac{\partial F}{\partial \ell} + \frac{\partial F}{\partial \tilde{R}}\frac{\partial \tilde{R}}{\partial \ell} \tag{3.20}$$

Substituting Equation 3.16 for the first term in the above and using the fact that $\tilde{R}$ is defined so that the second term is identically zero, yields the simple result that

$$\frac{\partial}{\partial \ell}\tilde{F}(\ell, s) = \tilde{J}_{\parallel}(\ell, s) \tag{3.21}$$

Equation 3.21 thus completes our examination of the implications of constraining the external torque to be zero. With the definition of the reduced free energy ($\tilde{F}$), the discovery of the constraint relating the radius to the axial and contour lengths ($\tilde{R}$), and the re-definition of the axial tension ($\tilde{J}_{\parallel}$), we have found all of the quantities necessary to fully describe the equilibrium response of a helix under the influence of a pure axial tension. In addition, we have anticipated that the simplification of the problem from one involving three variables (R, ℓ, and s) to one involving only two (ℓ and s), will greatly simplify our consideration of the straightening transition in section 3.5.

3.4.3 Case 3 : Externally Applied Axial Tension With Clamped Helix Ends

We will now turn to an examination of the third special case, namely the clamped end boundary condition in which the helix is subjected to an axial tension in combination with whatever external torque is required in order to keep the azimuthal angle (Φ) fixed upon extension or compression. From Equation 3.9, it is clear that fixing Φ is also the same condition as fixing the total number of turns in the helix.

This special case is particularly important to examine for two reasons. First, as new tethers are developed it is likely that this condition will be the next one to be realized experimentally, and thus analyzing its implications will be useful in guiding what to look for in potential future experiments. In fact, for our potential tether ideas where a helix may be chemically bonded to the cantilever using free thiol groups or nickel chelaters, this constraint will most certainly be valid over some range. Second, our discussion in sections 4.2.3 and 4.3.2 of the possible forms of the helix free energy that are compatible with experimental observations, will be strongly dependent upon the type of boundary conditions assumed. As such, it will be necessary to show that

the clamped end boundary condition is not capable of simultaneously explaining all the observed phenomena. The failure of the predictions of this constraint will further validate the results of our analysis using the zero torque condition (i.e. our use of Case 2).

In order to incorporate the current geometric constraint (i.e. fixed Φ) into our formalism, more care must be taken then in the previous cases when we constrained the external forces directly. In the case of a pure axial tension for instance (Case 2), we found an expression relating the helix radius to the axial and contour lengths as a consequence of the imposed constraint on the derivatives of the free energy (Equation 3.17). In this case, however, the constraint directly couples the radius to ℓ and s, and we must then work out the impact this relationship has on the equations of mechanical equilibrium derived from minimizing the total energy.

From Equation 3.8, the relationship between the radius and the axial and contour lengths for $\Phi = \Phi_o$ is found to be

$$\bar{R}(\ell, s) = \frac{1}{\Phi_o}\sqrt{s^2 - \ell^2} \tag{3.22}$$

where the bar signifies that this is the radius appropriate only for the special case when the azimuthal angle remains fixed for all ℓ.

We must now examine how to incorporate this constraint into the conditions of mechanical equilibrium. Equations 3.12 and Equations 3.13 are valid in general and must therefore be adaptable to this constraint, but it will be more useful to begin by going back to the total energy and re-examining its minimization. From Equation 3.11 we see that even though τ will be non-zero, it still can do no work because the displacement (Φ - Φ_o) is fixed at zero. In addition, we can immediately substitute the expression for the radius given by Equation 3.22 into $F(R, \ell, s)$ and define a reduced free energy given by

$$\bar{F}(\ell, s) \equiv F\Big(\bar{R}(\ell, s), \ell, s\Big) \tag{3.23}$$

With these two simplifications, the total energy for this special case becomes

$$\bar{E}^{tot}(\ell) = \bar{F}(\ell, s) - \bar{F}(\ell_o, s) - \bar{J}_{\|}[\ell - \ell_o] \tag{3.24}$$

where again the constant $\bar{F}(\ell_o, s)$ has been included only for completeness. By construction, the total energy in the above expression is now just a function of the single variable ℓ. Minimizing Equation 3.24 with respect to this sole remaining variable and solving for the derivative of the free energy yields

$$\frac{\partial \bar{F}}{\partial \ell} = \bar{J}_{\|} \tag{3.25}$$

This result is identical in structure to Equation 3.21, but will lead to different results in general. This difference is because the radius found from Equation 3.17 ($\tilde{R}$) will not be equal to that found from Equation 3.22 ($\bar{R}$), and thus $\tilde{F}$ will typically be quite different from $\bar{F}$.

The above derivation of the equilibrium conditions from the total energy is useful in order to understand what is occurring physically, but we could have found this same result for $\bar{J}_{\|}$ directly from the general equilibrium conditions in Equations 3.12 and 3.13 as follows. The derivative of the reduced free energy is given by

$$\begin{aligned} \frac{\partial}{\partial \ell}\bar{F}\Big(\bar{R}(\ell, s), \ell, s\Big) &= \left(\frac{\partial F}{\partial \ell}\right) + \left(\frac{\partial F}{\partial R}\right)\frac{\partial \bar{R}}{\partial \ell} \\ &= \left(\bar{J}_{\|} - \frac{\bar{\tau}}{\bar{R}}\frac{\ell}{\sqrt{s^2 - \ell^2}}\right) + \left(-\Phi_o \frac{\bar{\tau}}{\bar{R}}\right)\frac{\partial \bar{R}}{\partial \ell} \end{aligned} \tag{3.26}$$

where we have substituted $\Phi = \Phi_o$ and Equations 3.12 and 3.13 in expanding the second result. From Equation 3.22, the derivative of the radius with respect to the axial length is found to be

$$\frac{\partial \bar{R}}{\partial \ell} = -\frac{1}{\Phi_o}\frac{\ell}{\sqrt{s^2 - \ell^2}} \tag{3.27}$$

Substituting this expression the derivative of $\bar{F}$ gives the final result that

$$\frac{\partial}{\partial \ell}\bar{F}(\ell, s) = \bar{J}_{\|}(\ell, s) \tag{3.28}$$

exactly as we found from our consideration of $\bar{E}^{tot}$.

Unlike the axial tension, the torque required to hold Φ constant cannot be extracted directly from the reduced free energy. This fact can easily be seen by noting that τ does not enter the expression in Equation 3.24 for the total energy ($\bar{E}^{tot}$). As discussed, the torque can do no work, and therefore the system is free to find its equilibrium under the applied tension and imposed constraint on the radius completely

independent of what value of τ is necessary to achieve this state. In other words, with s held constant the reduced free energy is a function of only one variable (ℓ) and, as we have just shown, its only derivative is equal to the axial tension.

In order to calculate the torque, therefore, we will have to consider a two step process that results in the same end state configuration for the helix as that which occurs for extension holding Φ fixed. The path we will consider is to first apply a pure axial tension to the helix until the desired length ℓ is reached, and then to increase the applied torque while holding the axial length fixed until Φ is returned to Φ_o. These two ways of extending the helix are physically quite distinct, but since the final radius, axial length, and contour length of the deformed helix will be the same, the resulting tension and torque in each case must be equal regardless of the path. Figure 3-5 illustrates the two ways of interest for arriving at the desired end state configuration.

The solid line in Figure 3-5 represents the desired path in which the angle Φ is held fixed at Φ_o as the axial length is increased from ℓ_o to ℓ_1. The dashed line represents the two-step extension we will use to calculate the torque. It is important to point out at this point that the area under the curves in Figure 3-5, is not equal to the work done because the tension is also doing work along some these paths, and more importantly because the axial length is not the appropriate conjugate variable to the torque. Appendix C contains a discussion of an analogous problem in which an external constraint is imposed upon a more familiar thermodynamic system (i.e. the monatomic ideal gas) that will help to both clarify and justify this approach for finding the torque.

The first portion of the dashed line in Figure 3-5 corresponds to an extension of the helix from ℓ_o to ℓ_1 under the condition of zero torque. This is exactly the problem of the free end boundary condition addressed in section 3.4.2, and thus we may immediately write down $\tilde{J}_{\|}(\ell_1, s)$ from Equation 3.21 and by definition τ is set to zero all along this leg. In addition, the intermediate value of the azimuthal angle is given by $\tilde{\Phi}(\ell_1, s)$ from Equation 3.18.

Along the second part of the dashed path, we apply a torque to the helix in order

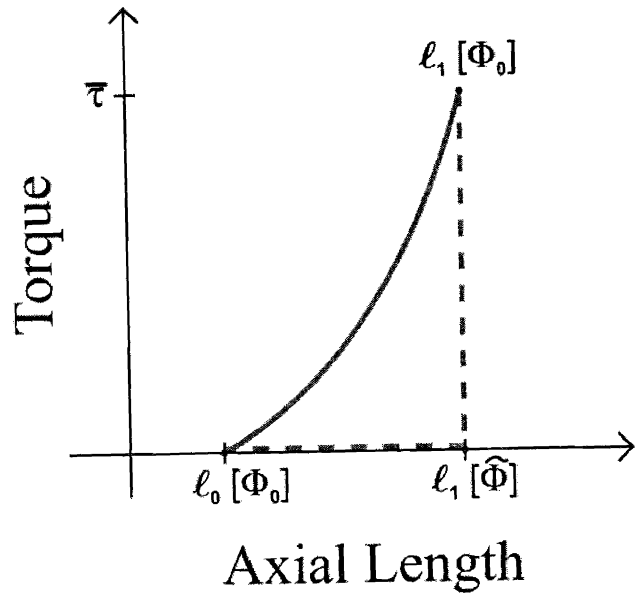

Figure 3-5: Schematic plot of the torque applied to a helix as function of the axial length for extension with clamped ends. The solid line represents the desired path along which Φ remains fixed as the helix is extended. The dashed line shows the proposed two-step path which begins with extending the helix at zero torque allowing the azimuthal angle to change from Φ_o to $\tilde{\Phi}$ followed by winding the helix at constant ℓ until Φ is returned to its initial value.

to take Φ from its intermediate value ($\tilde{\Phi}$) back to its initial value (Φ_o) while holding the axial length fixed at ℓ_1. This is not one of the cases examined thus far, and therefore, we must now determine the equilibrium conditions for this constraint.

We begin by noting that because the axial length remains constant, the tension can do no work along this leg. We can thus rewrite the total energy as

$$\ddot{E}^{tot}(R) = F(R,\ell_1,s) - F(R_o,\ell_o,s) - \ddot{\tau}\left(\frac{\sqrt{s^2-\ell_1^2}}{R} - \Phi_o\right) \tag{3.29}$$

where the double dot on the total energy and the torque indicate that these are the correct functions only when ℓ is constant. Minimizing the total energy given in Equation 3.29 yields the single equilibrium condition that

$$\frac{\partial F}{\partial R}\,|_{\ell=\ell_1} = -\Phi\frac{\ddot{\tau}}{R} \tag{3.30}$$

As expected, we simply reproduce Equation 3.13 with the explicit constraint that the

axial length is held fixed at some specified value (ℓ_1) throughout the deformation.

For this problem, we are interested only in the value of the torque that is required to hold Φ fixed (i.e. that which is required to constrain the radius to be equal to $\bar{R}$). Combining this additional consideration with Equation 3.30 gives us that the end state torque applied to the helix is equal to

$$\bar{\tau} = -\Big(\frac{\bar{R}}{\Phi_o}\Big)\frac{\partial F}{\partial R}|_{R=\bar{R}(\ell,s)} \tag{3.31}$$

With this result for $\bar{\tau}$ and Equation 3.25 for $\bar{J}_{\|}$, we have thus found the final expressions for both the torque and the tension for the case when the helix ends are not allowed to rotate.

It is important to note that along this second part of the dashed path, the axial tension increases from its initial value $\tilde{J}_{\|} = \frac{\partial \tilde{F}}{\partial \ell}$ after the zero torque extension to its final value $\bar{J}_{\|} = \frac{\partial \bar{F}}{\partial \ell}$ as the azimuthal angle is returned to its initial value (Φ_o) from its intermediate value ($\tilde{\Phi}$). Physically, the change in Φ typically results in an increase in the axial tension because we are going from a situation in which the free energy is minimized with respect to the radius ($\tilde{F}$) to one in which it is not ($\bar{F}$) as the radius is changed from $\tilde{R}$ to $\bar{R}$ (see Equation 3.22 and the discussion following Equation 3.17). Therefore, there will typically be a greater tension required after the change in Φ in order to keep the axial length from adjusting itself in order to offset this increase in internal energy.

The final quantity that must be calculated is the difference in work done by the helix along the two paths considered in Figure 3-5. Along the direct path, the work done by the expanding helix for fixed Φ is given by

$$W^a = \int_{\ell_o}^{\ell_1} \bar{J}_{\|} d\ell = \bar{F}(\ell_1, s) - \bar{F}(\ell_o, s) \tag{3.32}$$

where Equation 3.25 has been used in evaluating the integral. Along the two-step path, we must calculate the work done for each leg separately. Along the portion corresponding to zero torque extension, the work done is equal to

$$W_1^b = \int_{\ell_o}^{\ell_1} \tilde{J}_{\|} d\ell = \tilde{F}(\ell_1, s) - \tilde{F}(\ell_o, s) \tag{3.33}$$

where this time Equation 3.21 has been used to evaluate the integral. The work done along the second leg is equal to

$$W_2^b = \int_{\tilde{\Phi}}^{\Phi_o} \ddot{\tau} d\Phi \tag{3.34}$$

where $\ddot{\tau}$ is given by Equation 3.30. Substituting for $\ddot{\tau}$ and switching the integration variable to the radius for fixed ℓ and s (i.e. using $\frac{d\Phi}{\Phi} = -\frac{dR}{R}$) yields

$$W_2^b = \int_{\tilde{R}}^{\bar{R}} \frac{\partial F}{\partial R}|_\ell dR = \bar{F}(\ell, s) - \tilde{F}(\ell, s) \tag{3.35}$$

Finally, combining these expressions, we have that the total difference in work done by the helix along the two different paths ($\Delta W = W_1^b + W_2^b$ - W^a) is equal to

$$\begin{aligned} \Delta W &= \tilde{F}(\ell, s) - \tilde{F}(\ell_o, s) + \bar{F}(\ell, s) - \tilde{F}(\ell, s) - \bar{F}(\ell, s) + \bar{F}(\ell_o, s) \\ &= 0 \end{aligned} \tag{3.36}$$

since the zero stress equilibrium free energies $\left(\tilde{F}(\ell_o, s) \text{ and } \bar{F}(\ell_o, s)\right)$ must necessarily be equal regardless of the constraint imposed upon the subsequent helix deformation.

This result for ΔW can be understood as follows. First, we know from section 3.2 that the free energy, is entirely determined by the geometric conformation of the helix, and thus must be independent of the path taken. Second, the only way for a helix to change its internal energy is to do mechanical work. Combining these two considerations, we see that the work done along the two paths in Figure 3-5 must necessarily be equal. Physically, this balance is achieved because, as we argued above, $\bar{J}_\parallel$ is greater than $\tilde{J}_\parallel$ and thus the amount of work done by the axial tension along the direct path is greater than that done along the first leg of the indirect path. This difference is then exactly compensated for by the amount of work that the torque must do along the second leg in order to return Φ to Φ_o, thus making both complete paths equivalent.

The demonstration of the equivalence of the work done along the direct and indirect paths completes our examination of the consequences of fixing the angle Φ upon extension or compression of the helix. As in the case of the zero torque boundary

condition, we have identified a reduced free energy ($\bar{F}$) which is a function only of ℓ and s. We have then found all of the relationships between F, $\bar{F}$, $\bar{J}_{\|}$, and $\bar{\tau}$ necessary to fully describe deformations with fixed Φ. In addition, because the same type of reduction to a problem with only two variables and a related tension is possible, we anticipate that the formalism developed for this boundary condition will be as equally applicable as that for the zero torque constraint to the examination of the straightening transition to occur in section 3.5.

3.4.4 Case 4 : Externally Applied Torque in the Absence of an Axial Tension

Finally, for completeness we will conclude this section with a brief discussion of the case in which a pure torque is applied to the helix (i.e. $J_{\|}$ is identically zero throughout the deformation). This case is interesting to examine because, as in section 3.4.3, we anticipate that it will soon be achievable experimentally, and thus it will be interesting to determine if there are any instabilities or transitions possible under and applied torque. In fact, if we can find tethers that are successful at creating a non-slipping contact, it is simple to envision an experimentally feasible design capable of applying just such a pure torque. One possibility for such a setup may be adapted directly from an experiment commonly used to twist DNA [98, 99, 100]. This experiment would involve the use of a chemically modified feromagnetic bead bonded to one end of a helix and the application of an external, uniform magnetic field whose orientation may be rotated about the z-axis. If the field is rotated slowly enough to avoid the introduction of significant viscous forces, this setup would allow the helix to be twisted without in any way constraining its axial length by an applied tension.

As for the previous three cases, we will begin by examining how the equilibrium conditions derived from the total energy are affected by the external constraint. Examining the total energy in Equation 3.11 and its general minimization given in Equations 3.12 and 3.13, we see that when a torque is applied while fixing $J_{\|}$ to be

zero, the equilibrium conditions reduce to

$$\frac{\partial F}{\partial \ell} = -\frac{\ell}{\sqrt{s^2 - \ell^2}} \frac{\tau^\star}{R^\star} \tag{3.37}$$

and

$$\frac{\partial F}{\partial R} = -\Phi \frac{\tau^\star}{R^\star} \tag{3.38}$$

where the star on the torque and the radius signify that they are appropriate only for the special case when the tension is zero.

Combining the two equilibrium conditions in Equations 3.37 and 3.38 yields

$$\frac{\partial F}{\partial R} = \Phi \left(\frac{\sqrt{s^2 - \ell^2}}{\ell} \right) \frac{\partial F}{\partial \ell} \tag{3.39}$$

As for Cases 2 and 3, we find that we can obtain a relationship between the radius and the axial and contour lengths ($R^\star = R^\star(\ell,\, s)$) from the imposed constraint on the applied stress. The relationship for the radius derived from Equation 3.39 is more complicated then those derived from Equations 3.17 or 3.22 because of the fact that both the radius and the axial length couple to the torque in the absence of tension. In practice, however, given a particular form for the model free energy, we can now calculate the required derivatives of F in a straightforward manner and solve the expression in Equation 3.39 to find the desired equation for the radius.

With the definition of $R^\star$, we can once again define a reduced free energy as

$$F^\star(\ell, s) \equiv F\Big(R^\star(\ell, s), \ell, s \Big) \tag{3.40}$$

If we attempt to use the expressions in Equations 3.37 and 3.38 to directly determine the equilibrium condition appropriate for this reduced free energy, we find that

$$\frac{\partial F^\star}{\partial \ell} = -\left(\frac{\ell}{\sqrt{s^2 - \ell^2}} + \Phi \frac{\partial R^\star}{\partial \ell} \right) \frac{\tau^\star}{R^\star} \tag{3.41}$$

We can, in principle, eliminate the derivative of $R^\star$ in favor of derivatives of the free energy in the following way. Taking the derivative of both sides of Equation 3.39 with respect to R will result in three terms; one involving the second derivative of F with respect to R, one involving the mixed second derivative of F with respect to R and ℓ, and finally one that involves the first derivative of F with respect to R times the

derivative of ℓ with respect to R evaluated at $R = R^\star$. Solving that expression yields the following implicit equation for the desired derivative

$$\frac{\partial R^\star}{\partial \ell} = \frac{s^2}{s^2 - \ell^2}\frac{\partial F}{\partial R}\frac{1}{\left(\Phi\sqrt{s^2-\ell^2}\frac{\partial^2 F}{\partial R \partial \ell} - \ell\frac{\partial^2 F}{\partial R^2}\right)} \tag{3.42}$$

The solution to this expression may then be substituted into Equation 3.41, but it is obviously not a useful way to find the equilibrium condition.

We can greatly simplify this problem by recognizing that the appropriate variable conjugate to the torque is not the axial length, but the azimuthal angle Φ, and therefore for this case we should switch back to the original parameterization of the rotational work. Using Equations 3.8 and 3.39 we can define $\Phi^\star(\ell, s)$ as

$$\Phi^\star(\ell, s) = \frac{\sqrt{s^2 - \ell^2}}{R^\star(\ell, s)} \tag{3.43}$$

Formally, we may invert this relationship to find an expression for ℓ as a function of $\Phi^\star$ and s which we can use to re-express the reduced free energy as $F^\star(\Phi,\, s)$. With this new parameterization of the reduced free energy, we find that the equilibrium condition becomes

$$\begin{aligned}
\frac{\partial F^\star}{\partial \Phi} &= \frac{\partial F^\star}{\partial \ell}\frac{\partial \ell}{\partial \Phi} \\
&= -\left(\frac{\ell}{\sqrt{s^2-\ell^2}} + \Phi\frac{\partial R^\star}{\partial \ell}\right)\frac{\tau^\star}{R^\star} \times \frac{-R^\star}{\left(\frac{\ell}{\sqrt{s^2-\ell^2}} + \Phi\frac{\partial R^\star}{\partial \ell}\right)} \\
&= \tau^\star
\end{aligned} \tag{3.44}$$

where the derivative of ℓ with respect to Φ may be found by the inverse of $\partial\Phi/\partial\ell$ derived from Equation 3.43. This is exactly the expected result, and is obviously much simpler to work with than the expression in Equation 3.41 because it does not include the derivative of $R^\star(\ell, s)$. As in the case of extension with either free or clamped ends (Equations 3.21 and 3.25) we see that we can once again define a reduced free energy that is simply related to the integral of the applied stress.

With the derivation of the condition linking the radius to the axial and contour lengths, the definition of the reduced free energy as a function of both the common variables ℓ and s, and the more convenient force conjugate variables Φ and s, and the

re-expression of the equilibrium condition in Equation 3.44 we have found everything necessary to examine the consequences of applying a torque to a helix in the absence of an axial tension. In addition, a reduction to a problem with only two variables is possible, and yields a very similar expression linking the reduced free energy to the external stress as in cases 2 and 3. We thus expect that an examination of any potential mechanical instabilities will be directly analogous to our treatment of the tension induced straightening transition.

3.5 The Equilibrium Conditions For a Domain Separated Helix

As pointed out, the total contour length of the helical ribbons is constant over the time scale appropriate to the experiments discussed. However, the existence of the observed tension induced straightening transition described in section 2.5 indicates that, under certain situations, we must allow for portions of the contour length to be exchanged between regions of different conformations. This section will examine the consequences of relaxing the constraint that s is constant, and thus construct the equilibrium conditions for material exchange under stress. We will begin with general conservation considerations that must hold true for any transition, and then discuss the stability conditions for the observed tension induced straightening transition. We will conclude the section with a discussion of the stability conditions for a domain separated helix under the influence of a pure torque.

3.5.1 The Conditions of Material Conservation

We will begin our discussion by considering the constraints imposed due to conservation of the total contour length of the ribbon and due to the imposed constraint on the overall axial length. This part of the analysis is completely general for all possible types of two domain transitions and will provide a means of calculating how much of the material originally present in the helical ribbon will be in each domain for a given

experimental setup. Labeling the distinct domains as 1 and 2, these two conservation rules take on the simple form

$$s = s_1 + s_2 \tag{3.45}$$

and

$$\ell = \ell_1 + \ell_2 \tag{3.46}$$

where s is the total constant contour length of the ribbon, and ℓ is the total axial length of the helix set by the end to end distance between the tethers. The expressions given in Equations 3.45 and 3.46 are directly analogous to the conservation of total mass and total volume respectively in the treatment of the thermodynamic gas-liquid phase transition. Thus, these conservation rules will simply reproduce a version of the classic "Lever Rule" appropriate for our system [29]. Before combining these expressions, we will define the contour length fraction (χ) and the inverse axial density (ν) as follows

$$\chi_i = \frac{s_i}{s} \tag{3.47}$$

$$\nu_i = \frac{\ell_i}{s_i} \tag{3.48}$$

where the index i can be either 1 or 2. In addition, we will define the overall inverse axial density as

$$\bar{\nu} = \frac{\ell}{s} \tag{3.49}$$

which is equal to the value of ν that the helix would have if it remains in a single domain. Finally, solving Equations 3.45 and 3.46 for the fraction of the available material in each phase yields

$$\begin{aligned} \chi_1 &= \frac{\bar{\nu} - \nu_2}{\nu_1 - \nu_2} \\ \chi_2 &= 1 - \chi_1 = \frac{\nu_1 - \bar{\nu}}{\nu_1 - \nu_2} \end{aligned} \tag{3.50}$$

As expected, the point at which half of the available material is in each domain will be reached when $\bar{\nu}$ is equal to the average of ν_1 and ν_2. Comparing our result to the Lever Rule for the gas-liquid system, we see that for the straightening transition the helical domain is the analog of the liquid phase (i.e. the high density state), and the

straight domain is the analog of the gas phase (i.e. the low density state). Finally, we note that the expressions shown in Equation 3.50 provide two of the four relationships necessary to determine the four equilibrium values (s_1, ℓ_1, s_2, and ℓ_2).

The above analysis can be generalized in a straightforward manner to take into account any number of domains, thus allowing for a multilamellar configuration. From section 2.5, however, we know that for a typical straightening transition under tension, there are only two domains present at equilibrium. In addition, this generalization to more than two domains will not lead to any distinct physical effects of interest, and therefore we will consider only the two domain case.

3.5.2 The Conditions of Stability Under Axial Tension

Now that we have the conservation rules, we must work out the conditions for the stability of the interface between the domains. This portion of the analysis will have to make certain assumptions about the nature of the transition, and thus we will begin with an analysis of the observed straightening transition in which the separation into regions of different pitch angle and radius occurs under extension due to an axial tension.

First, the condition that the interface is mechanically stable requires that the axial tension must be equal in both domains. Therefore, the first of the two stability constraints may be written formally as

$$\tilde{J}_{\|}(\ell_1, s_1) = \tilde{J}_{\|}(\ell_2, s_2) \tag{3.51}$$

or

$$\bar{J}_{\|}(\ell_1, s_1) = \bar{J}_{\|}(\ell_2, s_2) \tag{3.52}$$

depending on the imposed constraint. This condition on the tensions must clearly be true because, if it were not, the interface would accelerate until it either reached one of the helix ends (thus eliminating one of the domains), or until the interface reached a stable point where the forces did in fact balance.

Second, the condition that the interface is stable with respect to a redistribution of the available material implies that the derivative of the free energy with respect to the

contour length in each domain must be equal. This condition may be demonstrated as follows. As shown in sections 3.4.2 and 3.4.3, for either the case of zero torque (Case 2) or for the case of clamped helix ends (Case 3), we can find a relationship between the radius and the axial and contour lengths which may be used to reduce the free energy to a function of only two variables. With this substitution, we may write the combined energy of both domains as

$$E^{combined} = E(\ell_1, s_1) + E(\ell_2, s_2) \tag{3.53}$$

where E is the total energy of each domain appropriate for the particular external constraint imposed (i.e. either for $\tau = 0$ or for $\Phi = \Phi_o$). Minimizing the combined energy with respect to the contour length yields

$$0 = \frac{\partial E}{\partial s_1}\Delta s_1 + \frac{\partial E}{\partial s_2}\Delta s_2 \tag{3.54}$$

We can simplify this relationship by noting that the only part of E that depends on the contour length is the reduced free energy $\left(\tilde{F}(\ell, s) \text{ or } \bar{F}(\ell, s)\right)$, and by substituting the fact that $\Delta s_2 = \Delta(s - s_1) = -\Delta s_1$. With this additional information, we may reduce Equation 3.54 to the condition that

$$\frac{\partial \tilde{F}}{\partial s}|_1 = \frac{\partial \tilde{F}}{\partial s}|_2 \tag{3.55}$$

or

$$\frac{\partial \bar{F}}{\partial s}|_1 = \frac{\partial \bar{F}}{\partial s}|_2 \tag{3.56}$$

depending on the imposed constraint. The derivative of the reduced free energy with respect to s is just equal to the energy change of the helix upon the addition of an infinitesimal amount of contour length, and thus we will define the effective contour length potential as

$$\begin{aligned} \tilde{\mu} &= \frac{\partial \tilde{F}}{\partial s} \\ \bar{\mu} &= \frac{\partial \bar{F}}{\partial s} \end{aligned} \tag{3.57}$$

in analogy with the chemical potential in thermodynamic systems [29]. With this definition, we have finished our derivation of the two stability conditions that will, when

combined with the conservation rules, uniquely determine the equilibrium between the two domains.

3.5.3 The Stability Constraints Under Tension as an Equal Area Construction

Before going on to an examination of the case when a torque is applied in the absence of tension, we will first re-express the stability conditions for the straightening transition as a simple integral equation. This form will be particularly useful in examining which models for F, and which external constraints are consistent with the observed phenomena.

We will begin by re-expressing the axial tension and the effective contour length potential in terms of a reduced free energy per unit contour length. From Equation 3.2 we know that the reduced free energy per unit contour length ($\hat{\tilde{F}} = \tilde{F}/s$ or $\hat{\bar{F}} = \bar{F}/s$) will be a function only of ℓ/s. This combination of ℓ and s is exactly what we have already defined to be ν in Equation 3.48. From Equations 3.21 and 3.25 we find that the axial tension can be re-expressed in terms of reduced free energy per unit contour length as

$$\begin{aligned} \tilde{J}_{\parallel}(\nu) &= \frac{\hat{\tilde{F}}(\nu)}{d\nu} \\ \bar{J}_{\parallel}(\nu) &= \frac{\hat{\bar{F}}(\nu)}{d\nu} \end{aligned} \tag{3.58}$$

In addition, from Equation 3.57 we have that the effective contour length potential may be rewritten as

$$\begin{aligned} \tilde{\mu} &= \hat{\tilde{F}} + s\frac{\partial \hat{\tilde{F}}}{\partial s} = \hat{\tilde{F}}(\nu) - \nu\frac{d\hat{\tilde{F}}(\nu)}{d\nu} \\ \bar{\mu} &= \hat{\bar{F}} + s\frac{\partial \hat{\bar{F}}}{\partial s} = \hat{\bar{F}}(\nu) - \nu\frac{d\hat{\bar{F}}(\nu)}{d\nu} \end{aligned} \tag{3.59}$$

Equating the effective contour length potentials in each domain and re-arranging the resulting expression to collect like terms, we have

$$\begin{aligned} \hat{\tilde{F}}(\nu_2) - \hat{\tilde{F}}(\nu_1) &= \tilde{J}_{\parallel}(\nu_1) \times [\nu_2 - \nu_1] \\ \hat{\bar{F}}(\nu_2) - \hat{\bar{F}}(\nu_1) &= \bar{J}_{\parallel}(\nu_1) \times [\nu_2 - \nu_1] \end{aligned} \tag{3.60}$$

where we have implicitly assumed the condition of equal tension in each domain by simplifying the right hand sides. Finally, we note that Equation 3.58 allows us to write the difference in the free energy per contour length in each domain as an integral over the tension. Thus, we find that the stability condition with respect to material exchange may be written as the following simple integral equation

$$\begin{aligned} \int_{\nu_1}^{\nu_2} \tilde{J}_{\|}(\nu')d\nu' &= \tilde{J}_{\|}(\nu_1) \times [\nu_2 - \nu_1] \\ \int_{\nu_1}^{\nu_2} \bar{J}_{\|}(\nu')d\nu' &= \bar{J}_{\|}(\nu_1) \times [\nu_2 - \nu_1] \end{aligned} \tag{3.61}$$

This integral equation is exactly equivalent to the equal area construction proposed by Maxwell for the thermodynamic gas-liquid transition [29]. Therefore, our comparison in section 3.3.3 of the expected mechanical instabilities in the tension when s is fixed to the instabilities that appear in the Van der Waals pressure when the density is fixed was, in fact, quite appropriate.

In addition to simplifying the stability conditions for the interface, the fact that the free energy can be written as the contour length times a function only of ℓ/s, effectively separates the two conservation conditions from the two stability conditions. The stability constraint in Equations 3.61 along with the equality of the axial tensions may be solved first to determine the inverse axial density of each domain. The conservation rules in Equation 3.50 may then be used to determine how the available material is divided between the two domains given the predicted values for ν_1 and ν_2.

Some care must be taken, however, when attempting to apply the conditions in Equation 3.61 because ν is bounded in our system to lay at most between zero and one. At $\nu = 1$ (i.e. when the helix axial length is equal to its contour length), the helix is completely straight, and therefore any additional force that is applied cannot cause the helix to extend further. This boundary condition means that the tension must become vertical at $\nu = 1$. Thus, any tension larger than that predicted by $\tilde{J}_{\|}(\nu = 1)$ for free ends or $\bar{J}_{\|}(\nu = 1)$ for clamped ends may be realized. This fact means that, if an instability exists, the condition of equal tensions between the domains is likely to be automatically satisfied for $\nu_2 = 1$, thereby reducing the expressions in Equation 3.61

to a single equation for the inverse axial density of the helical domain (ν_1). In addition to simplifying the stability constraint, we have also succeeded in explaining why one of the new domain will, in general, be straight.

In the previous discussion, however, we have ignored any potential reduction in the available parameter space due to the finite width of the helical ribbon. In general, ν may not be free to vary all the way from zero to one before the facing edges of each turn collide. At the point of collision, our theory would no longer be valid since it does not take into account the interactions as one helix turn contacts another. From Figure 3-6 it is clear that the ribbon edges will first touch when the projection of the width along the symmetry axis (δ) is equal to the helix pitch $\Big(P = 2\pi R \tan(\psi)\Big)$.

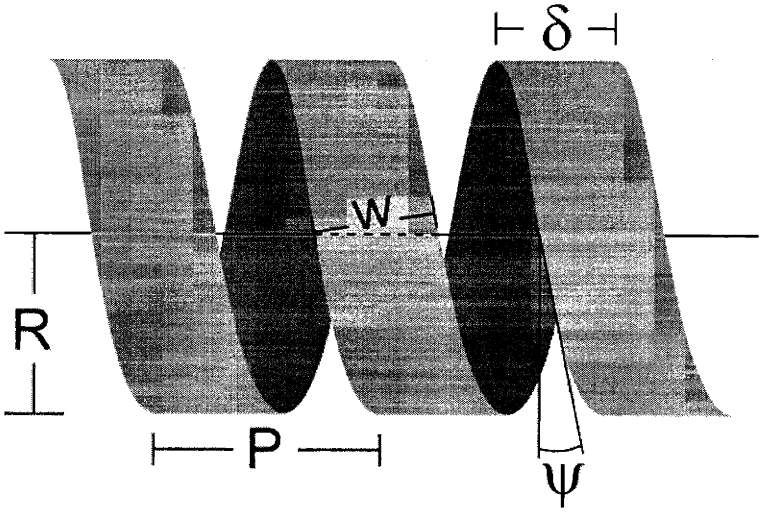

Figure 3-6: Illustration of the geometric variables for a helix which are constrained to lay in a restricted region by the finite width of the ribbons.

Examining the helix geometry (see Figure 3-6), we find that the projection of w along the axis may be written as $\delta = \frac{w}{\cos(\psi)}$. Equating δ and P, we have that the helix will initially close up into a tubule when the pitch angle satisfies

$$\frac{w}{R_o} = 2\pi \sin(\psi_b)\frac{R_b}{R_o} \tag{3.62}$$

where the subscript b on ψ and R signifies that this is their limiting boundary value. The unstressed radius in Equation 3.62 was included simply to define a physically

meaningful dimensionless parameter (w/R_o) that is easy to measure experimentally. Equation 3.62 will always define a lower bound greater than 0^o for the achievable pitch angle, and may define an upper bound less than 90^o as well depending on the details of how the radius changes upon extension.

For the case of freely rotating helix ends (Case 2), we found the radius upon extension or compression to be given by $\tilde{R}(\ell, s)$ which is defined through Equation 3.17. From Equation 3.2 we also know that the free energy may be written as s times a function of $\nu = \sin(\psi)$. Combining these considerations, we have that $\tilde{R}$ may be written as a function of ν, and thus that the boundary condition on the width may be written as

$$\frac{w}{R_o} = 2\pi\tilde{\nu}_b \frac{\tilde{R}(\tilde{\nu}_b)}{R_o} \tag{3.63}$$

This expression for $\tilde{\nu}_b$ defines the constraint on the inverse axial density for a given width, however, its solution will clearly be dependent upon the choice of the model free energy, and therefore its solution must wait until section 5.3.

For the case of clamped ends (Case 3), the constraint on the deformation imposes a universal relationship between R, ℓ, and s independent of F, and thus we will be able to derive the boundaries explicitly. From Equation 3.22 we have that

$$\frac{\bar{R}(\nu)}{R_o} = \sqrt{\frac{1-\nu^2}{1-\nu_o^2}} \tag{3.64}$$

Substituting this relationship into Equation 3.62 and squaring both sides yields

$$\frac{w^2}{R_o^2} = \frac{4\pi^2}{1-\nu_o^2}\bar{\nu}_b^2(1-\bar{\nu}_b^2) \tag{3.65}$$

Solving Equation 3.65 for $\bar{\nu}_b$ we find that there is an upper as well as a lower bound given by

$$\bar{\nu}_b^2 = \frac{1}{2} \pm \frac{1}{2}\sqrt{1 - \left(\frac{1-\nu_o^2}{\pi^2}\right)\frac{w^2}{R_o^2}} \tag{3.66}$$

where the plus sign is for the upper bound and the minus sign is for the lower bound if the square-root is always taken to be positive.

In order to determine what the minimum and maximum range ν may have, we need to evaluate Equation 3.66 for the minimum width, which we will take to be

effectively zero (i.e. $w \ll R_o$), and the maximum width, which is the value for which the edges just touch for the helix free from stress. This maximum helix width is given by

$$w_{max} = 2\pi\nu_o R_o \tag{3.67}$$

For the case of zero width, Equation 3.66 simply reduces to $0.5 \pm 0.5 = 1$ or 0. This is exactly what we would have expected since, if the width goes to zero, the only boundaries are those imposed by the inextensibility of the ribbon. For the case when $w = w_{max}$ we have for a low pitch helix

$$\begin{aligned} \bar{\nu}_{b,upper} &= \sqrt{1-\nu_o^2} \\ \bar{\nu}_{b,lower} &= \nu_o \end{aligned} \tag{3.68}$$

and vise versa for a high pitch helix. Plugging in the equilibrium value of the pitch angle, we find that for the low pitch helices, the lower bound for this constraint will lay between 0° and 11° and the upper bound will lay between 79° and 90°. For the high pitch helices, the ranges are 0° to 36° for the lower bound, and 54° and 90° for the upper bound.

With these results for $\bar{\nu}_b$, we see the first hint that the clamped ends boundary condition may not be compatible with the straightening transition. From Equation 3.66 it is easy to see that for any finite width, the helix can never become fully straight before the edges collide. This limitation is due to the fact that, as the helix straightens out, the constraint that the number of turns remain fixed forces the radius to shrink to zero. We cannot yet completely discount this case, unfortunately, because the maximum shift in the upper bound is so small that it may yield a long tightly wound domain that could simply appear straight in the experiment. As we will show in section 5.3 however, the same effect that creates the upper bound for ν will, in fact, make it impossible to simultaneously satisfy the stability and conservation conditions.

We have now completed our analysis of domain separation under axial tension for both the free and clamped end boundary conditions, and have found all of the conditions necessary to describe this phenomena. In addition to the general equilibrium conditions, our reformulation of the stability conditions into an integral equation will

allow us to more simply apply this theory to our experimental results. Before going on to apply this theoretical framework to a particular model for the free energy, however, we will conclude this section with an examination of the stability conditions for domain separation in the case when a torque is applied to the helix in the absence of an axial tension.

3.5.4 The Conditions of Stability Under a Pure Torque

While there may be other types of more complex topological changes possible for a helix under a torque such as supercoiling [122, 123], the following examination of a simple two domain separation is motivated by our predictions for the particular model free energy to be discussed in Chapter 5.4. To begin, we note that the conservation rules are valid for any two domain separation, and thus the results in Equation 3.50 may immediately be taken over and applied to this case. Therefore, we already have two of the four equilibrium conditions necessary to describe this problem. In order to determine the remaining two equilibrium conditions, we will construct the general stability conditions for the application of a pure torque exactly as we did for the case of the tension induced transition in the previous sections.

First, we know that the tension in each domain will automatically be equal since we have constrained it to be identically zero throughout the length of the helix. Thus the important condition for mechanical stability is that the torque is equal in each region. In other words, we require that

$$\tau^{\star}(\Phi_1, s_1) = \tau^{\star}(\Phi_2, s_2) \tag{3.69}$$

We know that if this condition was not met the interface would rotate under the influence of the net residual torque until either only a single domain remained, or until a stable configuration was found that would satisfy this condition.

Second, we must find the condition for stability with respect to material exchange. We have already shown in section 3.4.4 that a reduced free energy may be written which is a function only of Φ and s. With this substitution, we may write the

combined energy of both domains as

$$E^{combined} = E(\Phi_1, s_1) + E(\Phi_2, s_2) \tag{3.70}$$

where $E(\Phi, s)$ is now the total energy appropriate for $J_{\|} = 0$. As before, we must minimize the total combined energy with respect to the contour length in each domain. From Equation 3.69, we find that the stability constraint is given by

$$\frac{\partial F^{\star}}{\partial s}|_1 = \frac{\partial F^{\star}}{\partial s}|_2 \tag{3.71}$$

where we have already incorporated the material conservation rule that $s_2 = s$ - s_1. Therefore, exactly as in section 3.5.2, we may once again define an effective contour length potential as

$$\mu^{\star} = \frac{\partial F^{\star}}{\partial s} \tag{3.72}$$

which has the same physical interpretation as before of being the change in helix free energy upon the addition of an infinitesimal amount of contour length.

In principle, with the two general conservation equations given in Equation 3.50 and the two stability constraints given in Equations 3.69 and 3.71, we have found everything necessary in order to make predictions from the specific models for F to be considered in Chapter 4. In practice, however, it will turn out to once again be useful to first re-express the condition of equal effective contour length potentials as an integral equation in order to make the results easier to visualize graphically.

3.5.5 The Stability Constraints Under Torque as an Equal Area Construction

In order to reformulate the condition of stability with respect to material exchange as an integral equation, we will first define a reduced free energy per unit length for this case. As we argued in section 3.2, we know that the free energy must be extensive in the area of the ribbon and thus we have

$$\hat{F}^{\star}\left(\frac{\Phi}{s}\right) \equiv \frac{F^{\star}(\Phi, s)}{s} \tag{3.73}$$

In order to simplify the following analysis, we will first define the azimuthal angle density that parameterizes $\hat{F}^\star$ to be

$$\Omega \equiv \frac{\Phi}{s} = \frac{\cos(\psi)}{R} \tag{3.74}$$

(see Equation 3.8). From its definition, it is clear that the variable Ω can be visualized as a measure of how tightly the helix is wound.

Second, we will use the definition of the reduced free energy per unit contour length ($\hat{F}^\star$) and the definition of Ω to re-express the torque (Equation 3.44) and the effective contour length potential (Equation 3.57) as

$$\tau^\star = \frac{\partial F^\star}{\partial \Phi} = \frac{\partial}{\partial \Phi} s\hat{F}^\star = \frac{d\hat{F}^\star}{d\Omega} \tag{3.75}$$

and

$$\mu^\star = \frac{\partial F^\star}{\partial s} = \hat{F}^\star + s\frac{\partial \hat{F}^\star}{\partial s} = \hat{F}^\star - \Omega\frac{d\hat{F}^\star}{d\Omega} \tag{3.76}$$

respectively. Substituting these two expressions into Equation 3.71, and collecting all like terms, we find that the condition $\mu^\star(\Omega_2) = \mu^\star(\Omega_1)$ can be written as

$$\hat{F}^\star(\Omega_2) - \hat{F}^\star(\Omega_1) = \tau^\star(\Omega_1) \times [\Omega_2 - \Omega_1] \tag{3.77}$$

where we have already incorporated the additional constraint that the torque is equal in each domain by simplifying the right-hand-side. Finally, from Equation 3.75 we may write the difference in free energy per contour length as an integral of the torque. With this last substitution, we find that the equilibrium condition becomes

$$\int_{\Omega_1}^{\Omega_2} \tau^\star(\Omega')d\Omega' = \tau^\star(\Omega_1) \times [\Omega_2 - \Omega_1] \tag{3.78}$$

As in section 3.5.3, we find that the stability condition with respect to material exchange and the condition of mechanical stability of the interface may be combined to find an integral equation exactly analogous to the equal area construction proposed by Maxwell [29].

In the analysis of the straightening transition under tension, we noted that the force conjugate variable (ν) was bounded to lay within a range between zero and one

depending upon the width of the ribbon and the constraint on the deformation. We must now examine what the effective range of the variable Ω is for this case. Unlike the case of extension under axial tension, for unwinding due to a pure torque the pitch angle may in fact go beyond 90° signifying the reversal of the helix handedness for a positive radius. Over this range of pitch angles, the magnitude of the radius may go from zero to infinity and, thus from Equation 3.74 we see that Ω may range from negative infinity to positive infinity as ψ ranges from 0° to 180°. As before, however, this range will be significantly reduced when the finite width of the ribbon is taken into account.

In order to find the reduced range for Ω, we must find the value at which the edges of the ribbon collide and our theory breaks down. In order to do this, we must convert the edge boundary condition in Equation 3.62 into an expression involving only Ω. We know that Equation 3.39 may be taken to define a radius that is a function only of Ω (i.e. $R^\star = R^\star(\Omega)$). Using this fact, and the definition of Ω, we find that the boundary value for the azimuthal density is given by

$$\frac{w}{R_o} = 2\pi\sqrt{1-\Omega_b^2 R^{\star 2}(\Omega_b)}\left(\frac{R^\star(\Omega_b)}{R_o}\right) \tag{3.79}$$

As with the result derived for extension in the absence of torque (Equation 3.63), this equation cannot be solved in general and will depend in detail upon the form of the model free energy used. We can, however, note that as $R^\star$ becomes small it will reach a limit imposed by this constraint, and thus be cut of at some finite value. This will, in turn, cut off Ω at some finite magnitude on both the positive and negative branches.

With the above analysis, we have completed our analysis of the equilibrium conditions for domain separation upon pure winding and unwinding. As before, we found that the stability conditions and the conservation rules can be separated and solved consecutively. We also found that a Maxwell type equal area construction can be made for a transition under torque, and that it has the same physical interpretation as that for the transition under tension discussed in section 3.5.3.

3.6 Conclusion

In this chapter we have presented a very general theory for the equilibrium conditions of a helical ribbon under the influence of externally applied stress. We began by defining the geometry of a helix and used this to define a general free energy which fully describes the internal properties of the ribbon. We then generalized this description to include the influence of an externally applied axial tension and torque under the constraint that the total contour length remained fixed. We then applied this formalism to four important special cases; namely (Case 1) when the helix is free in solution, (Case 2) when a pure tension is applied along the symmetry axis, (Case 3) when the helix ends are clamped upon extension or compression, and finally (Case 4) the application of a pure torque. In each instance we found that the manner in which the stress is applied imposes a constraint on the radius which may be used to reduce the problem to one involving only two variables. From there, we made the final extension of our formalism and considered the equilibrium conditions necessary to describe the separation of a helix into two domains of different conformations. We discovered two universal conservation conditions that preserve the total amount of material and two further specific constraints that guarantee the overall stability of the interface. For all three special cases in which a stress was applied, we found that the condition for stability with respect to material exchange could be expressed as an integral equation in direct analogy with the Maxwell equal area rule for the gas-liquid phase transition. And finally, we considered the restriction of the available parameter space due to the fact that our theory ceases to be valid when the ribbon edges collide and the helix becomes a closed tubule.

With this general formalism and the results for the four special cases, we will now be able to fully analyze the experimental results described in Chapter 2 as well as to make predictions for what behavior to expect from future investigations. We will continue in the next two chapters to determine the proper model for the quaternary systems, and to apply this formalism to explain the geometric and mechanical properties of our helices. We will show that only our proposed crystalline model is capable

of explaining the current experimental observations, and finally we will conclude our analysis with a complete examination of the predictions of this formalism for the crystalline model.

Chapter 4

Choice of the Model Free Energy

4.1 Introduction

We began the examination of helices formed in quaternary systems in Chapter 2 with a description of our current experimental observations. These observations include both examinations of the structure and geometric properties of helices free in solution as well as examinations of how the helices are deformed by the application of small and large external stresses. We continued in Chapter 3 with the description of a generalized theoretical framework that treats a helix as a purely elasto-mechanical system. This formalism fully describes a helical ribbon through a free energy (F) that incorporates the energy costs and benefits incurred as the ribbon is bent from a flat strip into a helix. The free energy function contains all of the information necessary to fully describe a helix, as well as the information needed to relate the applied forces and torques to the associated deformations. In section 3.4, we worked out the conditions of mechanical equilibrium for four special cases of particular significance in which the applied forces are subject to an additional external constraint. Finally, in light of the observed tension induced straightening transition (see section 2.5 for a description of the phenomenon), the last chapter concluded with a description of the stability conditions necessary for two domains with different conformations to coexist.

We now wish to apply the general formalism from Chapter 3 to particular models for F and attempt to construct a phenomenological theory capable of self-consistently

explaining all of the observations described in Chapter 2. We must, however, first determine what type of model is appropriate to the helices formed in the quaternary systems. We will begin with a review of the previous theories proposed to explain the self-assembly of helices and tubules in a variety of different systems. These models consider a wide range of physical effects from the electrostatic interaction of polarization charges to the chiral elastic properties of bilayer membranes. Throughout the review we will point out major inconsistencies between the predictions of these models and experimental observations that have lead previous researchers to focus primarily on the chiral elastic models to explain the formation of helices and tubules. We will continue in section 4.2.3 with a discussion of the important differences between the microstructures formed in the quaternary systems and those formed in other systems, like the diacetylenic lipids, that have been successfully described by the various chiral models.

Taken as a whole, the inability of any of the previous models to self-consistently explain the available experimental evidence led us to formulate a completely new theory for our helical ribbons. In section 4.3, we will describe the new model we have proposed which is based on crystalline elasticity and includes an isotropic spontaneous curvature analogous to a difference in surface tension between the inner and outer ribbon faces. Interestingly, in contrast to the previous theories proposed for the helices formed in quaternary systems, we will find that to best fit the data our model must not explicitly include the elastic effects of molecular chirality. Finally, in the next chapter we will proceed to analyze our proposed free energy in terms of the general formalism and show that the crystalline model is consistent with all of our current experimental observations for helix formation and for the behavior of the helices in CDLC under stress. This will include examining the small stress region in which the helix may be approximated by a classical Hookean spring, and the large stress region in which a helix undergoes reversible domain separation.

4.2 Previous Models For Helix Formation

As discussed, the self assembly of helical ribbons and tubules occurs quite generally for a variety of systems composed of chiral amphiphilic molecules [21, 32, 24, 23, 33, 1, 34] or charged achiral surfactants with chiral counterions [35]. Similar helices have also been observed in systems of amphiphilic block copolymers containing a poly(styrene) tail and a charged poly(isocyanide) headgroup [36]. In Chapter 2, we showed that the formation of helical ribbons with characteristic low (11°) and high (54°) pitch angles was a general phenomenon in more than 22 distinct quaternary systems composed of a bile salt or non-ionic detergent, a phosphatidylcholine or fatty acid(s), a steroid analog of cholesterol, and water [27]. Despite the wide variation in the materials used and even in the number of constituent components in these systems, the geometric structure of the resulting helical ribbons and tubules share a remarkable degree of similarity. Motivated by this similarity across materials, a variety of theoretical models have been developed that focus on the course grained membrane degrees of freedom rather than on the details of the molecular interactions.

These models build on the geometric or effective surface Hamiltonian approach which models the membrane as a two dimensional surface and derives its elastic free energy in terms of its local and non-local curvatures [124, 125, 126, 127]. This technique was pioneered by Helfrich in an attempt to explain why under normal physiological conditions red blood cells (RBCs) take on a circular biconcave shape. Throughout the 1960s, a variety of theories were put forth to explain the RBC shape based on variations in the cell cholesterol content, membrane thickness, or surface charge, but they were all disproved by subsequent experimental measurements [128, 129, 130, 131, 132]. In 1973, Helfrich noted that in a fluid bilayer, the hydrophobic tails of the amphiphilic molecules have a certain degree of orientational order but no rigid positional order. He further argued that this type of order makes these structures exactly analogous to a homeotropic nematic liquid crystal [124]. Using the Frank free energy density derived for uniaxial liquid crystals [133], Helfrich was able to calculate the elastic energy of curvature per unit area for the red blood cell membrane.

Helfrich went on to generalize his result noting that the curved nature of any point on a surface must be describable in terms of its two principal curvatures (c_1 and c_2). He then argued that since the free energy must be invariant under the exchange of coordinate labels, the elastic bending energy must simply be a linear combination of (c_1+c_2), (c_1c_2), and $(c_1^2+c_2^2)$. This is the vital realization that forms the basis for all subsequent geometric models. From this simple model free energy, Helfrich and Ou-Yang derived the general shape equation for closed fluid bilayer membranes [134, 135, 136]. This equation, however, is a high order non-linear equation that is extremely difficult to analyze. Using numerical techniques, Ou-Yang showed that the equation predicted the existence of the Clifford torus in 1990 [137] which was subsequently discovered by Mutz and Bensimon in 1991 [138]. Naito, Okuda, and Ou-Yang finally solved the shape equation for the biconcave discoid in 1993 and received excellent agreement with the experimentally determined red blood cell geometry [139, 140].

Since Helfrich first proposed the curvature elasticity model, there have been a wide variety of theories that have attempted to expand upon it to explain the formation of helices and tubules. Following the arguments of Selinger *et al.* [25], we will divide these models into two classes based on the type of assumptions they incorporate. The first class consists of theories that consider effects not based on a chiral contribution to the membrane elasticity. This class will include models that incorporate electrostatic interactions of edge charges, topological defect energies of membranes with orientational order, and tilt induced spontaneous curvature. The second class consists of theories which explicitly include the effects on the ribbon elastic properties due to molecular chirality or due to a collective spontaneous chiral symmetry breaking within the membrane. This class will include the attempts to explain the formation of helices based on analogies to tilted chiral smectic-C* or cholesteric liquid crystals, and will include the three previous models for helices formed in the quaternary systems.

Although it is not the intent of this work to provide an exhaustive description of the previous theories and their derivations, we will present their general features, important conclusions, as well as their strengths and limitations at explaining the bulk geometric properties of self-assembled structures. Throughout we will show that

despite the apparent topological similarity of the resulting helices and tubules, and the wide applicability of some models to a broad subset of systems, that there appears to be no truly general theory based solely on long-wavelength elastic behavior. In fact, we will show that none of these previous theories is capable of completely and self-consistently explaining our experimental observations on the helices formed in quaternary systems.

4.2.1 Class One: The Non-Chiral Theories

In aqueous solutions, amphiphilic molecules self-assemble into bilayers in order to expose their hydrophilic headgroups to the water while shielding their hydrophobic hydrocarbon tails [123]. A priori it would be reasonable to assume that, given the energy cost of deforming the bilayer away from its normally flat configuration, the equilibrium geometry of such a self-assembled structure would correspond to a large closed spherical vesicle. As we have noted, however, under certain conditions a very wide variety of systems instead form helices and tubules. The specific physical effect that drives the formation of such high curvature structures distinguishes the various theories in this class. The three models to be discussed in this section will include those that incorporate the interactions of polarization induced edge charges, those that consider the energy cost of topological defects required by different geometries, and those that allow for the introduction of a spontaneous membrane curvature due to molecular tilt order. While all of these effects are quite reasonable assumptions in the absence of experimental observations, we will show that none of these theories is consistent with the formation of helices and tubules in most systems (including the quaternary systems).

The earliest approach to explain the spontaneous formation of tubules was proposed by de Gennes [141, 142]. He formulated a theory for the elastic properties of chiral and achiral smectic-C liquid crystals and showed that the lack of mirror symmetry in the tilted chiral L_{β^*} phase leads to local ferroelectric properties. The spontaneous polarization, which develops perpendicular to the tilt direction, causes the buildup of line charges of opposite sign along the two opposing ribbon edges. It

is the electrostatic interaction of these line charges that can induce buckling in the membrane and thus form the microstructure. Although the induction of polarization charges is clearly due to the chirality of the lipid molecules, this theory ignores the chiral contribution to the membrane elastic properties and thus will be included as part of the first class of models. Originally, de Gennes only considered the direct formation of tubules from flat ribbons, but his theory was subsequently expanded by several authors to explain the more complicated helical geometry [143, 144].

These models were able to demonstrate that electrostatic interactions were capable of mechanically stabilizing a helical ribbon. In addition, the decrease in energy associated with increasing the ribbon width due to drawing the opposite charges closer together offered a plausible mechanism for the often observed growth of a helix into tubule. Finally, and most importantly, they also predicted that this interaction would be mediated through the solution not the ribbon, and therefore that it should be strongly attenuated by the presence of even dilute electrolytes in the solution. Chappell and Yager tested this prediction for tubules made from the common diacetylenic lipid 1,2-bis(tricosa-10,12-diynoyl)-*sn*-glycero-3-phosphocholine, henceforth referred to as $DC_{8,9}PC$ because it has eight methylenes between the ester and the diacetylene group and nine methylenes between the diacetylene and the terminal methyl group [144]. They found that the presence of molar levels of many different inorganic salts had no effect on the formation or radius of the tubules, and thus concluded that electrostatic interactions must not be responsible for inducing the tubule curvature. It is only in the special case of tubules formed from amphiphiles with charged headgroups that such electrostatic interactions appear to play an important role in stabilizing the structures [145].

In 1991, Lubensky and Prost approached the problem from a different direction and developed a theoretical phase diagram for bilayers with in-plane orientational order in an attempt to explain the vesicle to tubule transition [55]. Tilted bilayers in the $L_{\beta'}$ phase tend to have both tilt and hexatic order, and Lubensky and Prost showed that such orientational order would couple to membrane shape due to the energy cost of topological defects required by some geometries. For example, a sphere with

hexatic order would require the formation of disclinations while a cylinder would not require any defects. The authors showed that when in-plane positional correlations were sufficiently strong this defect energy would cause the vesicle to rupture and form a cylindrical tubule.

The predictions of the Lubensky-Prost phase diagram, however, have two main inconsistencies when compared to experimental observations. The first is that they only predict the formation of tubules and not of helical ribbons. This drawback may be resolvable by a straightforward expansion of their theory which currently makes two major simplifying approximations. First, they did not consider a general aggregate shape, but restricted themselves to determining the energy of a sphere with or without pores, a cylinder, a flat sheet, and a torus. Second, they ignored any contributions of molecular chirality to the membrane elasticity which, as we will show in section 4.2.2, can be quite significant. By expanding the geometries considered it may, in fact, be possible to use this formalism to explain the vesicle to helix transition as well. The second, and more important, inconsistency between this theory and experiments is the prediction of a universal scaling law between the tubule radius and its axial length given by

$$R_{\mathrm{LP}} \propto \sqrt{\ell} \tag{4.1}$$

Many experimental investigations, however, have shown no correlation at all between R and ℓ [22, 146, 147, 20]. In most systems, the radius is quite monodisperse whereas the axial length varies over a wide range. For example, the tubules formed from the diacetylenic lipid $DC_{8,9}PC$ have a typical diameter of 0.5 μm while their lengths may range from 50 to 200 μm [147]. In contrast, the tubule radius as well as its axial length in the quaternary systems are very polydisperse, but they still show no correlation whatsoever as shown in section 2.3.1. Thus, the Lubensky-Prost theory is not a good description of any of these self-assembled structures.

The last non-chiral attempt to explain the formation of tubules came in 1999 when Chen considered the effects of cooling a spherical vesicle from the high temperature L_α phase to the low temperature $P_{\beta'}$ ripple state [148]. In this model, minimizing the membrane edge energy leads to the development of a spontaneous curvature, or

equivalently to the development of a preferred area difference between the inner and outer bilayer faces. In the untilted phase, a bilayer has isotropic bending rigidity, and for a dilute solution of lipids this spontaneous curvature leads to spherical vesicles. Upon cooling through the transition temperature, the molecules within the bilayer take on a collective tilt. After this tilt transition, it becomes harder to bend the bilayer along the direction of the tilt relative to bending perpendicular the tilt, thus introducing anisotropy into the membrane elasticity. For systems with large tilt anisotropy and large gaussian rigidity, the membrane can reduce its free energy by distorting from a sphere into a tubule. Chen predicted that the sphere to tubule transition would be first order and, in analogy to the arguments of Lubensky and Prost, that an additional energy cost due to topological defects in a vesicle with orientational order would further destabilize the sphere relative to the cylinder.

The theory proposed by Chen predicts that the tubules will form with a monodisperse radius distribution proportional to the membrane bending rigidity divided by its line tension. In addition, Chen also eliminated the correlation between the tubule radius and axial length by allowing for an arbitrary number of vesicles to fuse in the formation of a single tubule. Using this assumption (the applicability of which has been questioned recently by Selinger *et al.* [25]), Chen calculated a value for the line tension of diacetylenic lipid membranes of roughly 10^{-7} dyn using the reported values of R and ℓ. This value is consistent with the result from standard liquid crystalline theory that states that the bilayer line tension should be approximately equal to its splay elastic constant [141].

Despite the successes of this theory, it has two important problems when compared to experiments. First, this model considers only a single kinetic pathway for tubule formation. While some tubules do form from spherical vesicles upon cooling through the tilt transition temperature, others form directly from lipids dissolved in solution or from the lateral growth of helical ribbons [52, 146]. Second, Chen predicts that the tubule radius should always be equal to half the radius of the vesicle from which it formed. However, even for tubules which do follow this pathway, the tubule radius is typically found experimentally to be significantly less than half the vesicle radius

[52, 147]. Thus as with the two previous non-chiral models, this theory is not capable of self-consistently explaining the features of the helical ribbons and tubules formed in most systems, including our own.

These previous non-chiral models all describe plausible physical effects that are capable of driving the formation of tubules and helical ribbons in general. However, they all lead to predictions that are fundamentally inconsistent with observations across the vast majority of self-assembling systems. With these various effects ruled out from playing an important role, we will now turn to a consideration of models that include the effects molecular or collective chirality can have on the bilayer elastic properties and thus on the formation of non-spherical geometries.

4.2.2 Class Two: The Chiral Theories

In contrast to the models described in the previous section, all of the models in the second class explain the formation of high curvature helices and tubules by the same underlying physical effect, namely that chiral molecules lack mirror symmetry and thus preferentially pack at a slight angle relative to their neighbors. This non-parallel packing is known to give rise to the three dimensional cholesteric and chiral smectic-C* phases in liquid crystals [141] as well as more complex modulated phases in thin smectic films [149]. In the context of self-assembled structures, the molecules are assumed to form a tilted bilayer phase, and thus a microscopic twist in the molecular packing will result in a macroscopic twist of the entire membrane. In the models to be discussed, it is this intrinsic preference for bilayer twist that will overcome the elastic energy disadvantage of bending and thus drive the formation of helices and tubules.

The earliest model of helix formation based on chiral elastic properties of ribbons was proposed by Helfrich in 1986 [150]. He argued that the edges of a bilayer in a tilted chiral phase would develop a spontaneous torsion (τ_o) due to the distorted states along their lengths. Combining this effect with an isotropic elastic bending stiffness, Helfrich predicted the formation of helices with a universal pitch angle of 45°. Two years later, Helfrich and Prost generalized this theory by including the

effects of anisotropic membrane elasticity and by explicitly including a spontaneous bending force allowed in bilayers of tilted chiral molecules [151]. The free energy term linear in membrane curvature that leads to spontaneous bending was first introduced by de Gennes in his study of chiral smectic-C* phases for liquid crystals [141], but received little attention prior to the work of Helfrich and Prost. The local coordinate system for a symmetric tilted bilayer used in this model is shown in Figure 4-1, where we have translated the notation of Helfrich and Prost into that used later by Chung *et al.* [20] for consistency.

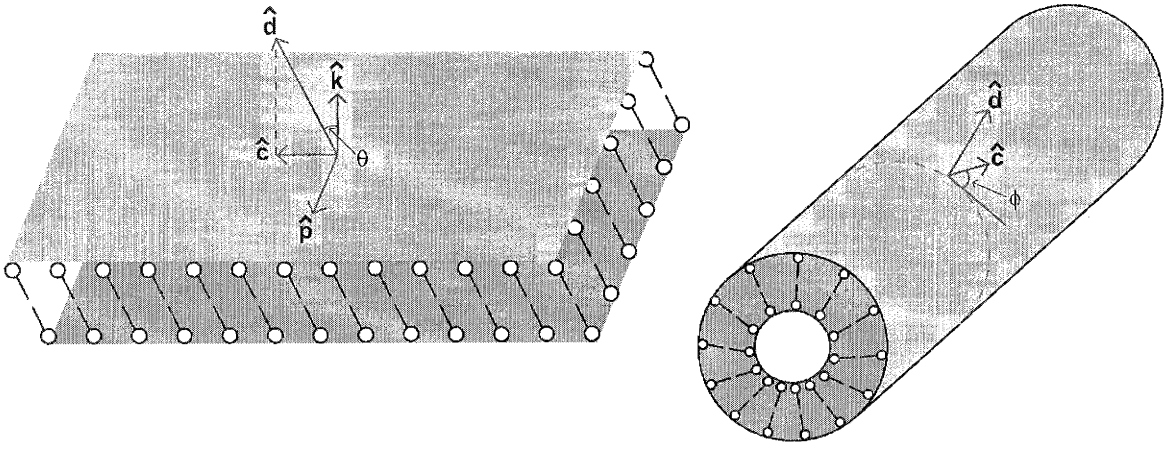

Figure 4-1: The local coordinate system for a tilted symmetric bilayer determined by the orthonormal set $\hat{k}$, $\hat{c}$, and $\hat{p}$. In this notation, $\hat{c}$ represents the normalized projection of the molecular tilt ($\hat{d}$) onto the ribbon plane, $\hat{k}$ represents the unit normal to the ribbon, and $\hat{p} = \hat{k} \times \hat{c}$ coincides with the expected axis of ferroelectric polarization. In addition, the molecular tilt angle (ϕ) is defined as the angle in the tangent plane between the projection of the tilt direction ($\hat{c}$) and the equator.

In order to simplify their analysis, Helfrich and Prost assumed that the ribbons had crystalline order in that the direction of the molecular tilt ($\hat{c}$) was taken to be fixed throughout the ribbon. In addition, the tilt direction (ϕ) was assumed to be aligned with the edge of the ribbon, and thus with the pitch angle (ψ). The free energy for this

system was derived by finding the complete set of independent invariants of quadratic and linear order in the curvature tensor ($\nabla\hat{k}$) which are allowed by symmetry. For a cylindrical deformation, this expansion of the free energy may be written as

$$F^{\mathrm{HP}}(R,\psi,s) = sw \left(\frac{K_{cc}\cos^4(\psi) + 2K_{cp}\cos^2(\psi)\sin^2(\psi) + K_{pp}\sin^4(\psi)}{2R^2} - \frac{K^*\cos(\psi)\sin(\psi)}{R} + \frac{\lambda}{w}(\tau^2 - 2\tau\tau_{\mathrm{o}}) \right) \tag{4.2}$$

where we have used our existing notation for the helix radius (R), contour length (s), and pitch angle (ψ) for clarity. The K_{cc} and K_{pp} terms correspond to elastic bending along the $\hat{c}$ and $\hat{p}$ directions respectively. The K_{cp} term represents the twist of the coordinate system in the $\hat{c}$ - $\hat{p}$ plane. The K^* term is the linear bending energy allowed because the chirality of the constituent molecules break reflection symmetry in the $\hat{p}$ direction. Finally, the λ term represents the energy cost associated with deviations of the edge torsion $\left(\tau = \frac{1}{R}\cos(\psi)\sin(\psi)\right)$ from its spontaneous value.

To simplify the analysis further, Helfrich and Prost restricted their analysis to the isotropic case in which $K_{cc} = K_{cp} = K_{pp} \equiv K$, and combined the chiral and torsion terms by defining a new parameter

$$\tilde{\tau}_{\mathrm{o}} \equiv \tau_{\mathrm{o}} + \frac{w}{2\lambda}K^* \tag{4.3}$$

With these substitutions, the free energy in Equation 4.2 becomes

$$F^{\mathrm{HP}}_{\mathrm{iso}}(R,\psi,s) = sw\left(\frac{K}{2R^2} + \frac{\lambda}{w}(\tau^2 - 2\tau\tilde{\tau}_{\mathrm{o}})\right) \tag{4.4}$$

Minimizing this free energy with respect to the radius and the pitch angle (equivalent to the zero tension and zero torque conditions in Equations 3.14 and 3.15), Helfrich and Prost found an equilibrium pitch angle and radius given by

$$\psi_{\mathrm{o}} = \pm 45^{\circ} \tag{4.5}$$

and

$$R_{\mathrm{o}} = \left(\frac{wK}{\lambda} + \frac{1}{2}\right)\frac{1}{|\tilde{\tau}_{\mathrm{o}}|} \tag{4.6}$$

respectively, where the sign of ψ_{o} is determined by the sign of $\tilde{\tau}_{\mathrm{o}}$.

As pointed out in their paper, the universal 45° equilibrium pitch angle is a consequence of the simplification to an isotropic bending rigidity. For an isotropic ribbon, there is no preferred bending direction so the chiral contributions to F are free to select the maximally asymmetric state. More significantly, these results explicitly showed that elastic properties due to chirality could be the driving force for helix formation. In other words, if the molecules were achiral then $\tilde{\tau}_0$ would go to zero resulting in R_0 going to infinity (i.e. a flat bilayer).

The Helfrich-Prost theory was soon extended in two papers by Ou-Yang and Liu that reformulated the helix free energy in terms of an analogy to cholesteric liquid crystals [152, 153]. This analogy allowed the two dimensional membrane elastic constants in Equation 4.2 to be expressed in terms of the three dimensional Frank constants of a liquid crystal, yielding an explicit form for their thickness dependence. This extension of the formalism also allowed Ou-Yang and Liu to treat the more difficult cases of twisted strips and spherical vesicles and compare their stabilities to that of helical ribbons (see Figure 4-2).

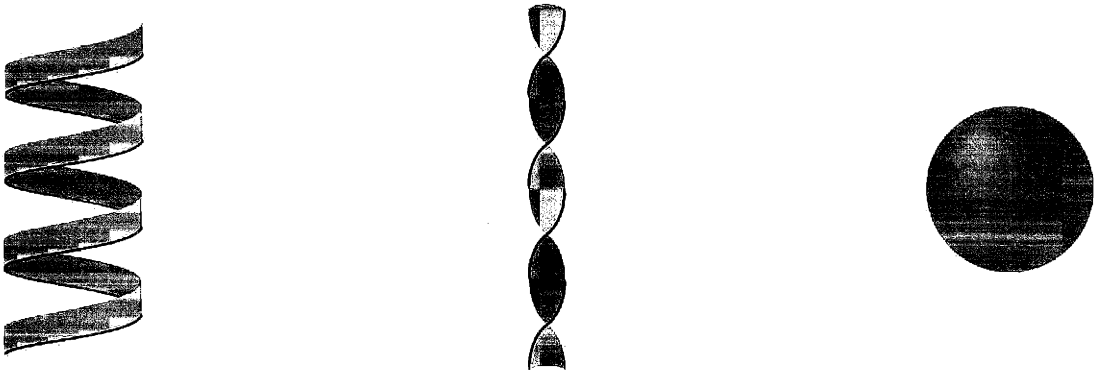

Figure 4-2: Schematic illustrations of the bilayer geometries considered in the work of Ou-Yang and Liu: (a) a helical ribbon with cylindrical curvature, (b) a twisted strip with non-zero Gaussian curvature, and (c) a spherical vesicle.

For simplicity, the tilt angle was assumed to be fixed and only the anisotropic effects of the chiral term was considered in their calculations, yielding an equilibrium pitch angle of

$$\psi_o = \pm 45^\circ \tag{4.7}$$

in agreement with the Helfrich-Prost theory. Ou-Yang and Liu then carried out numerical analysis of the free energies for the three morphologies shown in Figure 4-2 in order to investigate their relative stabilities upon cooling from the un-tilted L_α phase to the tilted L_{β^*} phase. The authors found that in the tilted phase, the spherical vesicle has the highest energy, the energy of the twisted strip is in the middle, and the helical ribbon has the lowest energy. This sequence of energetic advantage agrees quite well with the spontaneous transition from vesicular dispersion to twisted strips to helical ribbons observed by Nakashima *et al.* in systems of chiral ammonium amphiphiles [32].

Finally, this extension of the chiral theory demonstrated explicitly the need for both molecular tilt and molecular chirality in helix formation. Ou-Yang and Liu found the equilibrium radius of a helical ribbon to be given by

$$R_o = \frac{|p_{ch}|}{2\pi} \frac{1 + \sin^2(\theta)}{\sin^2(\theta)} \tag{4.8}$$

where p_{ch} is the pitch of the cholesteric liquid crystal and θ is the molecular tilt angle defined in Figure 4-1 [153]. In this case, if one takes the limit of either $p_{ch} \to \infty$ (i.e. achiral molecules) or $\theta \to 0^\circ$ (i.e. an untilted phase) then the equilibrium radius diverges, and thus the helix would open up into a flat ribbon. In addition, these results also predict a direct relationship between the microscopic molecular handedness and the macroscopic helix handedness. Swapping the constituent molecules for their enantiomers will transform the entire ribbon into its mirror image, and therefore p_{ch} must change sign. From Equations 4.7 and 4.8, we note that under this transformation the equilibrium radius does not change, but the sign of the pitch angle is reversed thus yielding a helix of the opposite handedness.

The predictions of the Helfrich-Prost theory and its extension by Ou-Yang and Liu are in good agreement with equilibrium observations on a wide variety of self-

assembling systems (see section 4.2.3). Motivated by the apparent success of the chiral elasticity approach, these models were further extended by several authors in an attempt to explain the appearance of non-45° helices in systems including the diacetylenic lipids ($\psi_o = 60°$) and the quaternary systems ($\psi_o = 11°$ or $54°$).

In 1993, Chung *et al.* developed a more complete chiral model for helical ribbons and tubules based on an analogy to tilted chiral smectic bilayers [20]. In their paper, the authors noted that in a membrane with tilt order a bend along the tilt direction would typically cost a different amount of energy than a bend along the perpendicular direction. Following this assumption, Chung *et al.* chose to adopt the fully anisotropic elastic energy for such membranes derived by de Gennes instead of directly expanding the work of Helfrich and Prost.

The free energy developed by de Gennes for tilted bilayers parameterizes the membrane deformation in terms of small rotations of the local frame around the spatial axes [141]. This choice of variables is inconvenient for analysis, and thus Chung *et al.* adopted the reformulation of this energy expression in terms of the orthonormal vector basis $\hat{k}$, $\hat{c}$, and $\hat{p}$ (see Figure 4-1) derived by Dahl and Langerwall [154]. As with the previous models, however, Chung *et al.* only analyzed the case of fixed molecular tilt which was assumed to lie parallel to the ribbon edge (i.e. $\phi = \psi$). Finally, the authors argued that a helix was equivalent to a tubule from which a parallel strip had been cut along a constant pitch angle, thus exposing two edges. Including an additional energy cost due to the spontaneous torsion of these ribbon edges, Chung *et al.* derived the following total free energy

$$F^{C}(R,\psi,s) = sw \left(\frac{K_{cc}\cos^4(\psi) + 2K_{cp}\cos^2(\psi)\sin^2(\psi) + K_{pp}\sin^4(\psi)}{2R^2} - \frac{K^*\cos(\psi)\sin(\psi)}{R} + \frac{\lambda}{w}(\tau^2 - 2\tau\tau_o) \right) \tag{4.9}$$

where, for clarity, we have dropped an overall additive constant considered by the authors. As expected, this expression is in precise agreement with the earlier results of Helfrich and Prost [151]. The various terms in Equation 4.9 have the same interpretation those in Equation 4.2, only now the phenomenological constants (K_{cc}, K_{cp}, K_{pp}, K^*, λ, and τ_o) are all taken to be explicit functions of the ribbon thickness.

Minimizing the anisotropic free energy in Equation 4.9, and solving for the equilibrium radius and pitch angle yields

$$\tan^4(\psi_o) = \frac{K_{cc}}{K_{pp}} \tag{4.10}$$

and

$$R_o = \left(\frac{w\bar{K}}{\lambda} + \frac{1}{2}\right)\frac{\sin(2\psi)}{|\tilde{\tau}_o|} \tag{4.11}$$

where $\tilde{\tau}_o$ has the same definition as in Equation 4.3 and $\bar{K}$ is given by

$$\bar{K} \equiv \frac{K_{cp} + \sqrt{K_{cc}\,K_{pp}}}{2} \tag{4.12}$$

The major improvement of these results over those of the previous chiral theories is that they do not require the pitch angle to be fixed at 45°, but allow it to take on any value by tuning the elastic anisotropy of the ribbon (K_{cc}/K_{pp}). As required, if we let $K_{cc} = K_{cp} = K_{pp} \equiv K$, then the results given in Equations 4.10 and 4.11 reduce immediately to those for the isotropic Helfrich-Prost model.

Plugging the observed equilibrium pitch angles for helices formed in the quaternary systems into Equation 4.10, yields a value for the elastic anisotropy of 3.6 for the high pitch ($\psi_o = 54°$) and 0.0014 for the low pitch ($\psi_o = 11°$) respectively. As pointed out by Selinger *et al.* , the ratio $K_{cc}/K_{pp} = 3.6$ for the high pitch helices seems quite reasonable given that the same physical mechanism must determine both modulii. However, it is very unlikely that for the low pitch helices a bend perpendicular to the tilt direction would cost nearly 700 times more energy than a bend parallel to it would [44]. This difference is on the same order of magnitude as the difference in Young's modulus between a piece of stiff rubber such as the sole of a shoe and a piece of oak. In an attempt to eliminate this unphysical requirement on the elastic anisotropy, Selinger *et al.* expanded upon the theory of Chung *et al.* by allowing the direction of the molecular tilt to vary across the width of the ribbon [155, 44].

The earliest model to relax the assumption of fixed molecular tilt was actually developed by Nelson and Powers in 1992 [156]. They generalized the isotropic Helfrich-Prost free energy (Equation 4.4) to include terms giving the energy cost of variations in the tilt direction. Nelson and Powers considered a uniform zero temperature tilt

state, and then performed a renormalization group calculation to determine the softening of the effective chiral coupling due to thermal fluctuations. They found that, due to thermal effects, the chiral elastic constant K^* would fall off with distance as a power law with an exponent that scales linearly with temperature and inversely with the renormalized effective bending rigidity of the membrane.

While the Nelson-Powers theory improved upon the previous models by allowing thermal fluctuations in the tilt direction, it retained the assumption that the lowest energy configuration of the membrane has a uniform tilt direction. In contrast to this approach, Selinger *et al.* considered the effects of allowing systematic modulations in the tilt direction in the absence of thermal effects. This approach was motivated by the known connection between tilt modulation and pattern formation in a variety of liquid crystals and multi-lamellar lipid membranes. For example, in bulk liquid crystalline systems, chiral molecules can form the cholesteric phase in which the tilt direction forms a helical pattern or they can form the smectic-C* phase in which the tilt rotates from layer to layer [141]. In addition, thin chiral smectic liquid crystal films can form various types of modulated one and two dimensional striped patterns as well as spiral star defects [149]. Finally, for a number of lipids with saturated actyl chains, such as dimyristoyl phosphatidylcholine (DMPC), a ripple $P_{\beta'}$ phase characterized by one-dimensional height and tilt modulation is found to form in hydrated multi-lamellar membranes between the L_α and $L_{\beta'}$ phases [157, 158, 159].

These modulated one and two dimensional phases arise as a consequence of the coupling between the membrane curvature and variations in the direction of the molecular tilt. Figure 4-3 illustrates a simplified picture for the microscopic origin of this connection.

In their study of the ripple $P_{\beta'}$ phase, Lubensky and MacKintosh showed that incorporating the coupling between systematic tilt modulation and curvature elasticity in a mean field calculation would lead to a simple rescaling of the elastic constants within their model [160]. In particular, they found that the longitudinal tilt elastic constant was reduced by the coupling, while the perpendicular constant was left unchanged. This result thus provided a possible mechanism which could be extended to

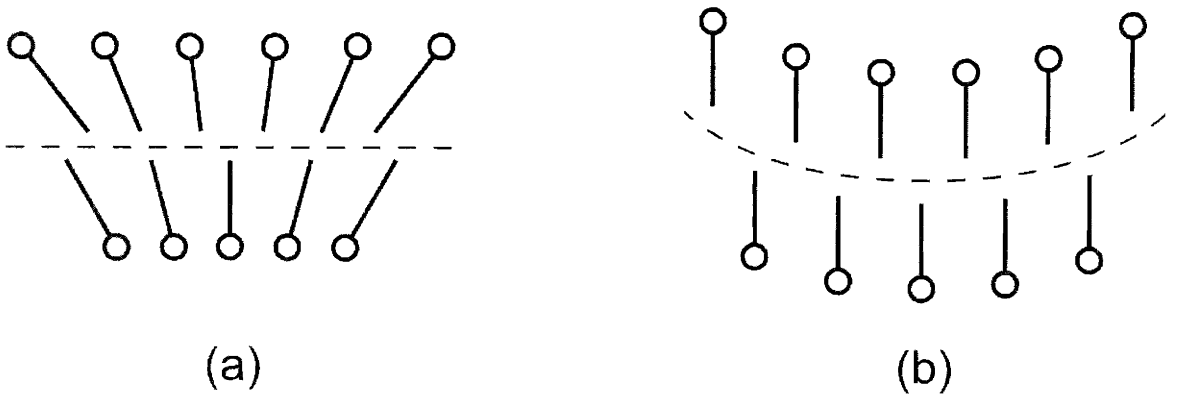

Figure 4-3: Schematic illustration of the physical mechanism responsible for linking tilt modulation to membrane curvature. (a) A splay in the tilt direction ($\nabla \cdot \hat{c} \neq 0$) induces a spontaneous curvature in the membrane (b) in order to keep the molecules more nearly parallel to one another as favored by steric interactions.

explain the apparently unphysical ratio of elastic bending constants required by the theory of Chung *et al.* to describe the low pitch helical ribbons.

Initially, Selinger and Schnur used a simplified free energy model appropriate to an isotropic three dimensional liquid crystal in order to demonstrate that in addition to causing the membrane to curve into a cylinder, chiral effects would also favor a variation in the molecular tilt along the surface of the tubule [155]. This model predicted a periodic striped pattern that would wind around the tubule separated by domain boundaries across which the tilt changed direction sharply. These orientational domain walls provide sites at which impurities preferentially accumulate, and thus the authors argued that these stripes could corresponded to the helical structure often observed on self-assembled tubules.

In 1996, Selinger *et al.* extended their theoretical approach in an attempt to provide a more systematic and general model of anisotropic tubules and helical ribbons [44]. Instead of beginning with the full three dimensional elastic free energy as they had previously done, Selinger *et al.* chose to use a two dimensional geometric curvature model in order to simplify the analysis. They began with the assumption that the

membrane is in a fluid phase which may have hexatic orientational order, but no long range positional order. This assumption was based upon the theoretical arguments of Nelson and Peliti who showed that thermal fluctuations would induce dislocations in a flexible membrane and thus destroy long rage positional order at finite temperatures [161]. In addition, Treanor and Pace found a distinct fluid-like character in nuclear magnetic resonance and electron spin resonance experiments on diacetylenic lipid tubules [162], and Brandow *et al.* found that a tubule membrane could flow to seal a cut made in its wall [163]. However, x-ray and electron diffraction experiments performed by Caffrey *et al.* and others have yielded conflicting evidence of possible crystalline order in these tubules over at least some length scales [164, 165, 166]. Incorporating the fluid bilayer assumption, the free energy considered by Selinger *et al.* was given by

$$F^{\mathrm{S}}(R,\psi,s) = \int dA \quad \Big(\quad \frac{1}{2}\kappa\frac{1}{R^2} + \frac{1}{2}\kappa'\frac{1}{R^2}\cos^2(\phi) - K^*\frac{1}{R}\sin(\phi)\cos(\phi) - K^*_{\mathrm{LS}}\hat{k}\cdot\nabla\times\hat{c} + \gamma\frac{1}{R}\nabla\cdot\hat{c} + \frac{1}{2}K_{\mathrm{F}}[(\hat{k}\cdot\nabla\times\hat{c})^2 + (\nabla\cdot\hat{c})^2]\Big) \tag{4.13}$$

where ϕ is the tilt angle which may, in general, be different from the helix pitch angle ψ. The κ term in Equation 4.13 gives the isotropic bending energy while κ' gives an anisotropic contribution to the membrane rigidity. A further anisotropy $\left(\frac{1}{2}\kappa''\frac{1}{R^2}\cos^4(\phi)\right)$ considered by Chung *et al.* was omitted in order to simplify the algebra. The K^* term is the chiral contribution considered previously that favors a finite membrane curvature while K^*_{LS} is an additional chiral energy that favors a modulation in the tilt direction ($\hat{c}$). The γ term represents the coupling between curvature and splay as discussed above (see Figure 4-3). The final set of terms in Equation 4.13 is the isotropic two dimensional Frank energy for variations in the molecular tilt of a fluid bilayer. If, however, the ribbon had not been taken to be in a fluid phase, the tilt direction would be locked to the crystalline axes and thus varying it would cost more energy than simply the square of the deformation. As noted, this model free energy does not include all of the possible terms allowed by symmetry, but rather keeps only those terms that lead to distinct physical effects in order to simplify the mathematics.

As a specific ansatz, the authors assumed that there were discrete domains that wound around the tubules in a helical pattern, and that within each domain the tilt direction (ϕ) varied linearly from one side to the other about some average value ϕ_o. This model had five variational parameters given by the tubule radius (R), the average tilt direction (ϕ_o), the magnitude of the tilt variation ($\Delta\phi$), the stripe direction / pitch angle (ψ), and the number of domains (n). Minimizing the free energy with respect to these variables, Selinger *et al.* found that the behavior of F^S depended strongly upon a phenomenological parameter given by

$$\nu_S = \frac{1}{6}\sqrt{\left(\frac{\kappa'}{2R^2}\right)^2 + \left(\frac{K^*}{R}\right)^2} \tag{4.14}$$

In their expansion of the model free energy, $\frac{1}{2}\nu_S(\Delta\phi)^2$ gives the elastic energy cost associated with variations of the tilt away from its average value. Selinger *et al.* found that for large values of ν_S, the free energy had a single minimum corresponding to $\Delta\phi = 0$ (i.e. $\phi = \phi_o = \psi$). This result is quite reasonable given that large values of ν_S would suppress any variations in the tilt due the elastic energy penalty. As ν_S decreases, a second minimum develops in the free energy for non-zero tilt modulation. At a critical value of ν_S, the authors predict a first-order phase transition to a state with finite $\Delta\phi$. In this tilt modulated state, Selinger *et al.* demonstrated that the tubule free energy per unit area could be expressed as

$$\frac{F^S_{tilt}}{sw} = \frac{1}{2}\frac{\kappa_r}{R^2} + \frac{1}{2}\frac{\kappa'}{R^2}\cos^2(\phi_o) - \frac{K^*}{R}\sin(\phi_o)\cos(\phi_o) \tag{4.15}$$

where κ_r is a negatively renormalized bending rigidity. Physically, this renormalization of κ can be understood as due to the effective isotropic elastic energy cost being reduced by the energy gained by the introduction of systematic tilt modulation.

Minimizing the effective free energy density in the modulated state (Equation 4.15) over the two remaining variational parameters yields the following equations for the average tilt direction and equilibrium radius respectively

$$\tan^4(\phi_o) = \frac{\kappa_r + \kappa'}{\kappa_r} \tag{4.16}$$

and

$$R_o = \frac{\kappa_r^{1/4}(\kappa_r + \kappa')^{1/4}\left(\kappa_r^{1/2} + (\kappa_r + \kappa')^{1/2}\right)}{K^*} \tag{4.17}$$

In addition to these results for ϕ_o and R_o, Selinger *et al.* also demonstrated that the variation in molecular tilt would induce higher order ripples in the tubule curvature. This result is analogous to the result of Lubensky and MacKintosh for planar lyotropic liquid crystalline films [160]. The ripples predicted by Selinger *et al.* may, in fact, be the helical modulations in curvature seen by Yager *et al.* in electron micrographs of tubules composed of the lecithin 1,2-bis(10,12-tricosadiynoyl)-*sn*-glycero-3-phosphocholine ($DC_{23}PC$) [34], although many other experiments have not shown any evidence of such ripples in related systems [22, 167, 168, 147, 169]. Finally, Selinger *et al.* generalized their analysis to the case of an open helix by drawing an explicit analogy between a single domain stripe of a modulated tubule and a single helical ribbon.

From these results, the authors drew the following two major conclusions. First, the same mechanisms that stabilize the striped pattern on a tubule can stabilize a free standing helical ribbon. Thus, for a certain range of the phenomenological parameters in F^S, a helical ribbon may be a true equilibrium form instead of just a metastable intermediary on the path to tubule formation. Second, they showed that the quantity measured in experiments (i.e. the pitch angle) may not in general be equal to the average tilt direction. In particular, the difference between these two angles was found to scale as the arctangent of γ/κ which may be large or small. This conclusion is important because it is the tilt angle not the pitch angle that is governed by the renormalized elastic anisotropy $\left(\frac{\kappa_r+\kappa'}{\kappa_r}\right)$, and thus the observation of an 11° pitch angle does not necessitate an anomalously high ratio as in the model of Chung *et al.* [20].

The results of Selinger *et al.* demonstrated that the appearance of low pitch helices in quaternary systems may be explained by systematic modulations in the tilt direction across the ribbon width. However, the particular ansatz they imposed on the tilt variation was not motivated by any experimental observations, and therefore in 1999 Shigeyuki and Ou-Yang further extended this work in an attempt to directly solve the Euler-Lagrange equations for the tilt field ($\hat{c}$) derived from the free energy [26]. Shigeyuki and Ou-Yang generalized their previous theory of helix formation to

include the complete free energy of chiral cholesteric liquid crystals including both anisotropic elastic rigidity and systematic tilt modulation. Noting the x-ray diffraction studies of Caffrey *et al.* on tubules of $DC_{8,9}PC$ and its saturated analogue [166], they argued that at the sides, the tilt direction must be aligned along the ribbon edge. This boundary condition leads to two possible types of helices, one with the tilt pointing in the same direction at the two edges (designated P-helix for parallel packing) and one with the tilt pointing in opposite directions (designated A-helix for anti-parallel packing). The P-helix was found to require a uniform tilt angle for stability, while the A-helix obviously necessitates a modulation in tilt direction across the ribbon. Numerical and graphical analysis of the resulting free energies showed that the parallel packing configuration was only allowed for helices with a pitch angle greater than 45°, while the equilibrium pitch angle of the A-helix was typically less than 30°. Thus, in agreement with the results of Selinger *et al.* [44], Shigeyuki and Ou-Yang [26] found that the high pitch helices formed in quaternary systems could be explained by a ribbon with uniform tilt, and that the low pitch helices could be explained by a configuration with systematic tilt modulation without the need for an unphysically large elastic anisotropy.

Finally, we will discuss the models built not on the elastic properties of molecular chirality, but rather on the analogous effects of a spontaneously broken chiral symmetry within a membrane. This extension of the theories is motivated by a number of experimental observations on simple systems that can not be resolved with the previous molecular chirality models. In fact, the phenomena of collective chiral symmetry breaking of achiral molecules has long been known, and has been investigated in a wide variety of systems from bulk three dimensional domains [170] and two dimensional films [171, 172] of smectic-C liquid crystals, to hexatic liquid crystalline films [149, 173, 174], and to Langmuir monolayers with tilt order [175, 176, 177, 178]. Similarly, tubules and equal mixtures of left and right handed helical microstructures have been found to self-assemble in two different systems of achiral amphiphilic molecules [179, 180]. In addition, Katsaras *et al.* found that, despite ideal mixing between the d and l enantiomers in racemic mixtures, hydrated bilayers of dimyristoyl phosphatidyl-

choline (DMPC) as well of dipalmitoyl phosphatidylcholine (DPPC) displayed chiral ground states in the $P_{\beta'}$ ripple phase [181, 182, 183]. Finally, two experiments carried out by Thomas *et al.* have found that helical ribbons with either handedness can self-assemble out of systems containing molecules of only one handedness [51, 52, 184]. By achieving a very low cooling rate, Thomas *et al.* was able to observe the direct formation of helical ribbons from vesicles in a solution of $DC_{8,9}PC$. However, despite the presence of only one enantiomer, helices of either handedness were initially observed to form with nearly equal probability $\left(\frac{N_{\text{right}}}{N_{\text{right}}+N_{\text{left}}} \approx 0.60\right)$ [146]. These helices then grew in width and thickness to form multilamellar tubules which had uniformly right handed helical markings in agreement with previous equilibrium observations. In addition, Thomas *et al.* investigated a new tubule forming material they created by replacing the oxygen linkage to the phosphate group in $DC_{8,9}PC$ with a methylene group ($-CH_2-$) [52, 184]. The microstructures formed from this new molecule had roughly equivalent pitch angles and twice the radius of those formed from unmodified $DC_{8,9}PC$. Unlike other systems, however, both left and right handed tubules were found to form from an enantiomerically pure solution of the new material. Finally, the authors determined that the relative yield of each handedness in this new solution was not fixed, but depended strongly on the rate of tubule formation.

In their development of a mean field phase diagram for Langmuir monolayers and freely suspended smectic films, Selinger, Wang, Bruinsma, and Knobler (SWBK) proposed three particular mechanisms for spontaneous parity breaking [185]. First, they noted that if the monolayer is in a tilted hexatic phase, then the tilt direction can be locked at a fixed angle between 0° and 30° relative to the local bond direction. This coupling between tilt and bond orientational order breaks chiral symmetry. The chiral order parameter (ζ) for such a system had been worked out previously, and is given by $\zeta = \sin(6[\theta(\vec{r}) - \beta(\vec{r})])$, where θ is the tilt angle and β is the bond angle. Second, they argued that even without hexatic orientational order, the molecules in the monolayer might pack in two distinct configurations that are mirror images of each other. For example, the achiral molecule 10,12-tricosadiynoic anhydride which forms both left and right handed helical ribbons, has two inequivalent ways of packing

its headgroups which are simple reflections of one another [179]. The order parameter for such a case would be given by the difference in densities of each configuration. Third, they argued that in a monolayer made up of a racemic mixture, the two different enantiomers can phase separate into domains of opposing local chirality. For this final mechanism, the chiral order parameter would simply be the difference in densities of the two enantiomers.

A concrete example of collective symmetry breaking in bilayer membranes that combines features of the first two ideas in the SWBK theory was proposed by Seifert *et al.* in 1996 [186]. In their model, the authors relaxed the requirement that the molecular tilt ($\hat{c}$) be the same in the top ($+$) and bottom ($-$) monolayers of a bilayer. To lowest order, they found that the effect of asymmetric tilt is to induce an anisotropic spontaneous curvature in the membrane. If the tilt directions in the two monolayers are fixed at a relative angle α, then the bilayer spontaneously breaks reflection symmetry. In this case, the two states with relative tilt angle $\pm\alpha$ are inequivalent mirror images of one another even if the molecules are themselves achiral. Seifert *et al.* then showed that the chiral order parameter for this mechanism is given by $\zeta = (\hat{c}_+ \times \hat{c}_-) \cdot \hat{k} = \sin(\alpha)$, where $\hat{c}_+$ and $\hat{c}_-$ are the tilt directors for the top and bottom monolayers receptively. Finally, the authors demonstrated that for a fixed relative angle, the induced anisotropic spontaneous curvature leads to an energy contribution exactly equivalent to the K^* chiral term considered in the previous molecular chirality models.

Generalizing upon these concepts, in 2001 Selinger *et al.* proposed the following generic free energy appropriate for membranes with spontaneous chiral symmetry breaking [25]

$$\begin{aligned} F^{\mathrm{S}}_{\mathrm{spon}}(R,\psi,s) = \int dA \quad \Big(& \frac{1}{2}\kappa\frac{1}{R^2} + \frac{1}{2}\kappa'\frac{1}{R^2}\cos^2(\phi) - (\Pi^*\zeta)\frac{1}{R}\sin(\phi)\cos(\phi) \\ - & (\Pi^*_{\mathrm{LS}}\zeta)\hat{k}\cdot\nabla\times\hat{c} + \gamma\frac{1}{R}\nabla\cdot\hat{c} + \frac{1}{2}K_{\mathrm{F}}[(\hat{k}\cdot\nabla\times\hat{c})^2 + (\nabla\cdot\hat{c})^2] \\ + & \frac{1}{2}K(\nabla\zeta)^2 + \frac{1}{2}t\zeta^2 + \frac{1}{4}u\zeta^4 \Big) \end{aligned} \tag{4.18}$$

where the final three terms are a standard Landau-Ginzburg expansion in the chiral order parameter (ζ) described above, while Π^* and Π^*_{LS} give the effective chiral en-

ergy cost for a given value of ζ. When the experimentally controllable parameter t is reduced (analogous to lowering the temperature in a standard thermodynamic system), we expect that this free energy will lead to a phase transition from a non-chiral state ($\zeta = 0$) to a chiral state ($\zeta \neq 0$). In order to analytically examine the behavior of this function, we will use the results derived by Selinger *et al.* in the analysis of Equation 4.13 [44] to rewrite this generic free energy as

$$\begin{aligned} \frac{F^{\mathrm{S}}_{\mathrm{spon}}}{sw} &= \frac{1}{2}\tilde{\kappa}\frac{1}{R^2} + \frac{1}{2}\kappa^{'}\frac{1}{R^2}\cos^2(\phi_{\mathrm{o}}) - \Pi^{*}\zeta\frac{1}{R}\sin(\phi_{\mathrm{o}})\cos(\phi_{\mathrm{o}}) \\ &+ \frac{1}{2}K(\nabla\zeta)^2 + \frac{1}{2}t\zeta^2 + \frac{1}{4}u\zeta^4 \end{aligned} \tag{4.19}$$

where the bending rigidity $\tilde{\kappa}$ is either the bare value (κ) for the uniform tilt state or the negatively renormalized value (κ_{r}) for the tilt modulated state. Minimizing Equation 4.19 with respect to the radius and tilt angle we find

$$\tan^4(\phi_{\mathrm{o}}) = \frac{\tilde{\kappa} + \kappa^{'}}{\tilde{\kappa}} \tag{4.20}$$

and

$$R_{\mathrm{o}} = \frac{\tilde{\kappa}^{1/4}(\tilde{\kappa} + \kappa^{'})^{1/4}\left(\tilde{\kappa}^{1/2} + (\tilde{\kappa} + \kappa^{'})^{1/2}\right)}{\Pi^{*}\zeta} \tag{4.21}$$

as expected. Substituting Equations 4.20 and 4.21 into Equation 4.19, we can further reduce the free energy to

$$\frac{F^{\mathrm{S}}_{\mathrm{spon}}}{sw} = \frac{1}{2}K(\nabla\zeta)^2 + \frac{1}{2}\bar{t}\zeta^2 + \frac{1}{4}u\zeta^4 \tag{4.22}$$

where the new effective control parameter $\bar{t}$ is given by

$$\bar{t} = t - \left(\frac{\Pi^{*}}{\tilde{\kappa}^{1/2} + (\tilde{\kappa} + \kappa^{'})^{1/2}}\right)^2 \tag{4.23}$$

We can now recognize Equation 4.22 as the standard Landau-Ginzburg free energy that in a mean-field treatment describes a second-order phase transition as $\bar{t}$ is decreased through zero from a state with $\zeta = 0$ to a state with finite ζ (i.e. the onset of spontaneous chiral symmetry breaking). In such a model, one would expect an equal number of left and right helical ribbons to form since the solutions for $\pm\zeta$ will

necessarily be degenerate. This prediction is in good agreement with the observations of Lindsell *et al.* on helices formed from the achiral diacetylenic amphiphile 10,12-tricosadiynoic anhydride [179].

As noted, the free energy in Equation 4.18 is appropriate only for achiral molecules, and therefore Selinger *et al.* speculated that the effects of molecular chirality could be incorporated by including a bias term to the Landau-Ginzburg free energy given by $-h\zeta$ [25]. This free energy would still generate two minima, however, due to the chiral field (h) one minimum would be stable while the other would be only metastable (see Figure 4-4(b)).

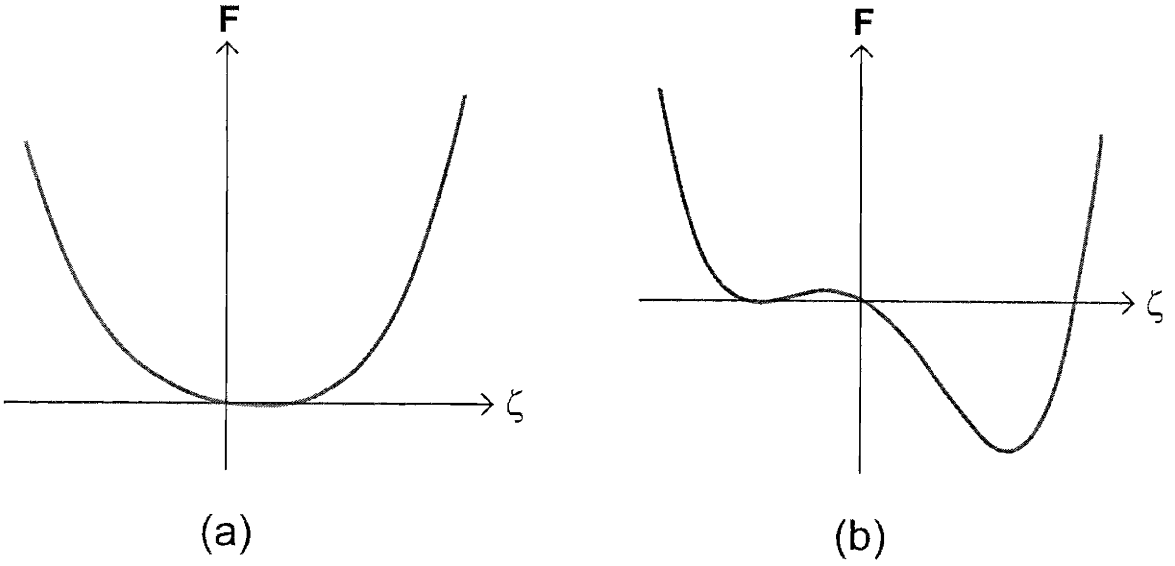

Figure 4-4: A schematic plot of the biased free energy density considered by Selinger *et al.* as a function of the chiral order parameter ζ [25]. (a) The free energy (in arbitrary units) for a positive value of the control parameter $\bar{t}$ corresponding to a single packing state with small effective chiral order. (b) The same function with a negative value of $\bar{t}$, yielding to two inequivalent packing configurations. The bias field favors one state relative to the other based upon the sign of h thus resulting in a membrane with large effective chirality.

This dual well free energy could offer an explanation for the observations of

Thomas *et al.* [51, 52, 184], in that helices in the fast growing early stages of formation might adopt either handedness, but over time the tubules would slowly shift towards the more energetically favored sense. In addition, this bias term offers a possible means of understanding why diacetylenic lipids form tubules while other chiral lipids do not. As suggested by Spector *et al.*, the key feature of the diacetylenic lipids is that the diacetylene group introduces a kink in the acyl chain of the molecules [169]. This kink forces two neighboring lipids to pack at a significant angle relative to one another in either of the two possible configurations. Due to the chirality of the molecules, one of these packing arrangements is energetically favored over the other. Other chiral lipids that lack such a kink would only pack at a slight angle, and thus would only induce a slight membrane curvature. In terms of the free energy model, this effect would lead to a larger value of Π^* for the diacetylenic lipids relative to the non-kinked lipids. Examining Figure 4-4, we see that even if the chiral bias field (h) is the same for both materials, the diacetylenic lipids with a negative $\bar{t}$ would have a much larger effective chiral order parameter (ζ), and thus be more likely to form stable tubules, than lipids with a positive value for $\bar{t}$.

We have now completed our discussion of the previous models proposed to explain the formation of helices and tubules. Motivated by the clear inconsistencies between the results of the existing non-chiral theories and experiments across a variety of systems, the chiral elastic models (both molecular and spontaneous) have received the majority of the recent theoretical and experimental effort. We will now turn to a discussion of further experimental evidence that both supports and calls into question these chiral models. In particular, we will focus primarily on the differences between the systems where these theories work well (such as the diacetylenic lipids), and the quaternary systems where they lead to important inconsistencies.

4.2.3 Successes and Failures of The Chiral Theories

I would like to thank Dr. Jonathan Selinger for his helpful discussions about the important similarities and differences between the structures that self-assemble in the quaternary and diacetylenic lipid systems, and the implications of these distinctions for the type of free energy model appropriate.

In the previous section we presented a detailed overview of the various models for helix/tubule formation which explicitly incorporate the elastic effects of chirality on a membrane. This effect may be due to the intrinsic chirality of the constituent molecules, or it may be a due to a collective breaking of chiral symmetry within the material. In this section we will further show that the predictions of these theories are generally found to be in good agreement with equilibrium observations on a wide variety of self-assembling systems. However, we will also argue that there are several important problems when comparing these theoretical results to our experiments on helical ribbons formed in the quaternary systems. The contradictions discussed in this section will provide the motivation for our formulation of the new non-chiral crystalline theory to be discussed in section 4.3.

The first major success of the chiral elastic models is their demonstration that tilt order appears to be essential in stabilizing a tubule or helix. This effect is most clearly illustrated by the prediction of Ou-Yang and Liu for the equilibrium radius of a helix (Equation 4.8) [153]. Their result correctly predicts the observation that lowering the temperature through the L_α to $L_{\beta'}$ phase boundary reversibly shifts the equilibrium from favoring spherical vesicles to favoring helical ribbons and tubules with cylindrical geometry in many simple chiral amphiphilic systems [21, 51, 52]. In order to further explore the role of molecular tilt, Thomas *et al.* conducted a detailed study of the tubule formation process for the diacetylenic lipid $DC_{8,9}PC$ using high resolution x-ray scattering [146]. Measurements of the intralamellar positional correlation of the lipids in both the spherical vesicle and tubule configurations lead them to conclude that tubule formation is, in fact, driven primarily by a first-order chain freezing transition upon passage through the Krafft temperature.

Second, these models presuppose that the molecular packing within the membrane of the helix or tubule is chiral. Schnur and others have carried out extensive studies of the tubules formed from $DC_{8,9}PC$ using circular dichroism spectroscopy as a probe of their microscopic packing structure [147, 187, 169]. These experiments have shown that the lipid in the tubules has a much higher chiral order than the lipid dissolved in solution or in the high temperature spherical vesicles. When the lipid is replaced by its enantiomer, the signal simply switches sign indicating that the molecular handedness controls the packing chirality in fully formed tubules. These results are consistent with the observations of the macroscopic chirality as indicated by the helical markings visible on the tubule surface. Finally, upon heating the solution, the circular dichroism signal of the tubules either vanishes smoothly as the structures dissolve, or it drops to zero sharply at the L_α to L_{β^*} phase boundary when the tubules transform back into vesicles.

Third, the chiral models provide a reasonable physical mechanism for selecting a particular radius. Chirality sets a single length scale given by $\frac{2\pi}{q}$, where q is the preferred packing angle between neighboring molecules divided by the distance between their centers of mass [155]. This length scale may be determined by the intrinsic chirality of the constituent molecules or it may be a feature of the two possible packing configurations in a membrane with spontaneous symmetry breaking, but it must be the same for all structures of a given material. It is this fixed length scale that translates into a fixed radius for the helices and tubules. For example, in the work of Ou-Yang and Liu the chiral length sets the pitch of the cholesteric (p_{ch}) and thus the equilibrium helix radius (see Equation 4.8) [152, 153]. In the models of Selinger *et al.* this length determines the ratio of elastic rigidity to the chiral modulus, once again leading to a monodisperse radius distribution (see Equation 4.17) [155]. Typical cholesterics have a pitch on the order of 0.1 to 100 μm, and thus we would expect that helices would form with a diameter on this same order of magnitude. This prediction agrees well with experimental results in a variety of systems. For example, Nakashima *et al.* found the diameter of helices from the chiral ammonium amphiphile $2C_{12-L}$-Glu-$C_{11}N^+$ were all roughly 0.15 μm while their lengths typically varied from

10 to 100 μm [21, 32]. In addition, many authors have reported a typical diameter of 0.5 μm for tubules formed from the diacetylenic lipid $DC_{8,9}PC$ while their lengths generally varied from 50 to 200 μm [22, 147].

A further consequence of the linkage between the chiral length $\frac{2\pi}{q}$ and the radius is that for nearly racemic mixtures of left and right handed molecules, the radius is expected to scale inversely with enantiomeric excess, diverging for precisely equal mixtures of the two enantiomers. This scaling is consistent with observations on twisted strips formed from cationic gemini surfactants and chiral counterions such as *L*-tartrate [35]. In addition, solutions of $2C_{12-L}$-Glu-$C_{11}N^+$ and $2C_{12-D}$-Glu-$C_{11}N^+$ form helices with a right and left handed sense respectively, while racemic mixtures form only long elastic fibers [21]. Racemic mixtures of diacetylenic lipids, however, form tubules of the same diameter as those formed in enantiomerically pure solutions [167, 169]. Schnur and others have used circular dichrosim (CD) spectroscopy and electron microscopy to investigate this apparent inconsistency and showed that it was, in fact, due to the near complete phase separation of the two enantiomers which allowed formation of purely left and right handed structures in agreement with the chiral models [167, 169, 25].

Unlike these other systems, however, all of the quaternary systems have a very polydisperse radius distribution. For instance, in CDLC the radius of low pitch helices typically varies over an order of magnitude from approximately 5 to 50 μm, while larger ($R > 100$ μm) and smaller ($R < 2$ μm) structures have been observed less frequently. In addition, as noted, the radius of the helical ribbons is totally uncorrelated to their axial lengths which typically range from 30 to 300 μm. One possible way to resolve the observation of multiple length scales with the results of the chiral models is to include a spontaneous torsion term as was done by Helfrich and Prost and by Chung *et al.* Including such a term adds an additional parameter (λ in Equations 4.2 and 4.9) to the expression for the radius that would allow for a range of radii to be possible. This mechanism, however, can be ruled out by two sets of experimental results. First, the spontaneous edge torsion introduces an explicit width dependence into the expression for the equilibrium helix radius. In

section 2.3.1 we showed that there is no apparent relationship between the width and radius in a typical ensemble of low-pitch helices in CDLC. In addition, the growth and dissolution of many individual high and low pitch helices was followed over time in several different quaternary systems, and no evidence was found to support the predicted relationship for the change in radius as a function of the width [28]. We have also, on occasion, observed helices with a single radius, but regions of significantly different width (see Figure 4-5).

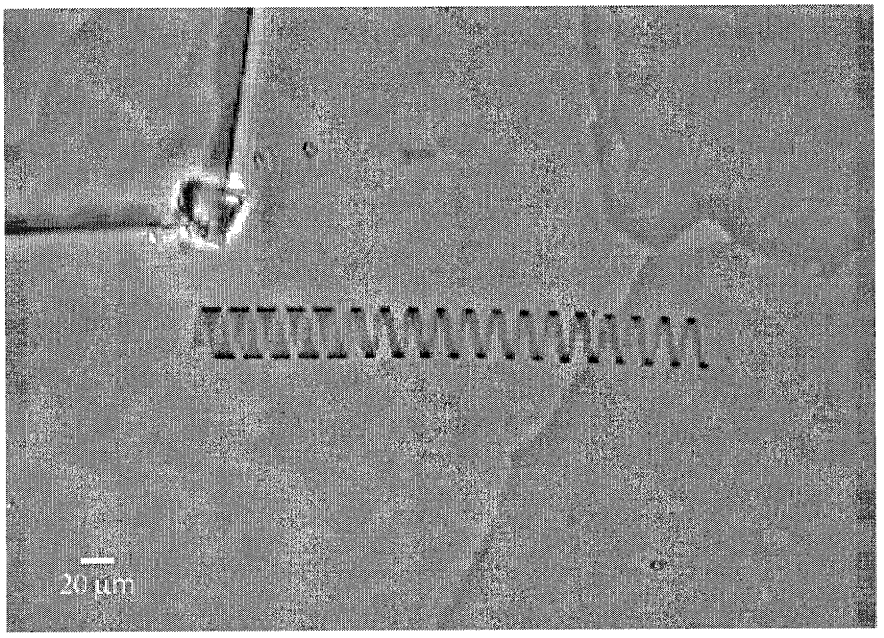

Figure 4-5: An illustrative example of a low-pitch helix formed in a model bile system that exhibits two regions of different width (w = 6 or 12 μm) while maintaining a single radius (R = 16 μm).

The existence of such helices are again inconsistent with the predictions of Chung *et al.* for a monotonically increasing radius as a function of the ribbon width. Second, it can be shown that the inclusion of a spontaneous edge torsion term would also impart a width dependence to the equilibrium pitch angle in the domain separated state (ψ_h). As discussed in section 2.5.1, the value of the pitch angle for the helical domain is independent of the helix bulk geometry in contradiction with the edge torsion models. We can therefore state that, in these quaternary systems, the effect

of a spontaneous torsion of the ribbon edges is negligible and that it cannot account for the observed wide variation in helix radii. Thus, we conclude that it is an important inconsistency between the chiral models and our helices that they lack a possible mechanism for selecting the wide range of length scales observed in the quaternary systems.

The fourth major success of the chiral models in many systems is that they can account for the often observed correlation between the sense of the molecular chirality and the sense of the helix handedness. A number of experiments have demonstrated that for enantiomerically pure solutions, the helices formed had a single handedness and that upon substitution of one enantiomer for its mirror the resulting helices reversed handedness as expected [21, 147, 188, 35]. We have already noted that Thomas *et al.* found both left and right handed helical ribbons in studies of enantiomerically pure systems of $DC_{8,9}PC$ and of a related phosphonate analogue [51, 52, 184], however, an explanation of these observations has been proposed by Selinger *et al.* in terms of the spontaneous chiral symmetry breaking models described at the end of the previous section [25].

This correlation between the chirality at different length scales was further investigated theoretically by Nandi and Bagehi using a simplified effective pair potential model [189]. In their approach the chiral interactions of the molecules are explicitly retained while the non-chiral effects are coursed grained as in the elastic curvature models. In order to demonstrate their formalism, the authors predicted that a helix formed from either a right-handed 12-hydorxystearic acid or a right-handed glutamic ammonium amphiphile would be left-handed, and that the helix would switch sense if the molecules were switched for their left-handed forms. The predictions of Nandi and Bagehi agreed well with the existing experimental observations on systems of these types of molecules [32, 188].

On the other hand, in seven of the enantiomerically pure quaternary systems studied by Zastavker *et al.*, both right and left handed helical ribbons of either 11° or 54° formed [27]. These systems were composed of the $L-$ forms of the bile salt sodium taurocholate, a phospholipid, and cholesterol or one of its steroid analogs. In each

of the systems where left handed helices routinely formed, they typically represented less than 5% of the total yield.

It is more difficult to offer a consistent explanation for the observations of Zastavker *et al.* in terms of collective symmetry breaking because of the more complex nature of the quaternary systems compared to the single amphiphile systems. The robust 11° and 54° equilibrium pitch angles, the fact that the sterol dominates the chemical composition of the ribbon, and the observation that no helices or tubules were found to form for one particular analog of cholesterol (epicprostanol) all suggest that it is the sterol packing that dominates the elastic behavior of the ribbons [27, 28]. In addition, Konikoff *et al.* found that the removal of the phosphotidylcholine from pre-formed helices in one of the model bile systems did not affect their structure [190, 191] and Dr. Zastavker observed that, in preliminary tests, swapping the detergent or phospholipid for its enantiomer had no observable effect on the resulting helices. Interestingly, systems where the chiral phospholipid was replaced by an achiral fatty acid or fatty acid mixture (i.e. the Lipid Concentrate and Quaternary Fatty Acid Systems described in section 2.2) yielded only right handed helical ribbons. In particular, no left handed helices have ever been observed in the CDLC system in which cholesterol is the only chiral component. These observations are not consistent with the expectations from the chiral symmetry breaking models. Reasonably, one would expect that these models would predict that an enantiomerically pure chiral lipid would be more likely to further bias the distribution towards the preferred macroscopic handedness while the achiral fatty acids would be expected to more easily form the metastable left handed helices. As noted, however, this is the exact opposite of what was found experimentally.

Fifth and finally, we have found that the chiral models predict that the radius should change dramatically upon extension or compression in direct contradiction to our experimental findings. Experimentally, we found that to first order the radius does not change as the pitch angle is increased or decreased. We have also argued that the nature of the epoxy tether allows a uniaxial force to be applied to the helix without the application of a torque (i.e. Case Two from section 3.4.2). As we discussed, the

condition of zero torque (Equation 3.17) holds for all values of the applied tension, and thus may be used to determine an expression for the radius as a function of the axial and contour lengths (i.e. $R \equiv \tilde{R}(\ell, s)$). In order to evaluate $\tilde{R}$ we must choose a specific form for the model free energy we wish to analyze. For simplicity we will adopt the free energy of Chung *et al.* with the λ modulus set to zero as discussed above. In fact, our conclusions will be valid for all constant tilt models and afterwards we will turn to a discussion of the models with systematic tilt modulation.

Applying Equation 3.17 to the free energy given in Equation 4.9 yields

$$-\frac{K_{cc}\cos^4(\psi) + 2\,K_{cp}\cos^2(\psi)\sin^2(\psi) + K_{pp}\sin^4(\psi)}{\tilde{R}^3} + \frac{K^*\cos(\psi)\sin(\psi)}{\tilde{R}^2} = 0 \quad (4.24)$$

Solving this expression for the radius gives us

$$\tilde{R}(\psi) = \frac{1}{K^*}\frac{K_{cc}\cos^4(\psi) + 2\,K_{cp}\cos^2(\psi)\sin^2(\psi) + K_{pp}\sin^4(\psi)}{\cos(\psi)\sin(\psi)} \quad (4.25)$$

Next, we must examine how $\tilde{R}$ changes for distortions about the unstressed equilibrium pitch angle. To first order this expansion is given by

$$\frac{\tilde{R}(\psi) - R_o}{R_o} = \left(\frac{1}{R_o}\frac{d\tilde{R}}{d\psi}|_{\psi=\psi_o}\right)[\psi - \psi_o] \quad (4.26)$$

Substituting Equation 4.25 into Equation 4.26, and using the expressions for R_o and ψ_o derived in section 4.2.2, we find that the fractional change in radius is given by

$$\frac{\Delta\tilde{R}}{R_o} = \left(\frac{1 - \tan^2(\psi_o)}{\tan(\psi_o)}\right)\Delta\psi \quad (4.27)$$

where $\Delta\tilde{R}$ is defined to be $\tilde{R}(\psi) - R_o$ and $\Delta\psi$ is given by $\psi - \psi_o$. Finally, plugging in the equilibrium value of 11° for the low pitch helices gives a value of 4.95 for the slope of the fractional change in radius versus the change in pitch angle. This result is in sharp contrast to our experimental finding of zero slope. Figure 4-6 shows our data for a typical low pitch helix with the prediction of Equation 4.27 superimposed for comparison.

As is clear from Equation 4.27, since the chiral elastic modulus (K_s) factors out of the result for the fractional change in the radius, this expression is quite general for the constant tilt models. In fact, since the inclusion of a spontaneous edge torsion

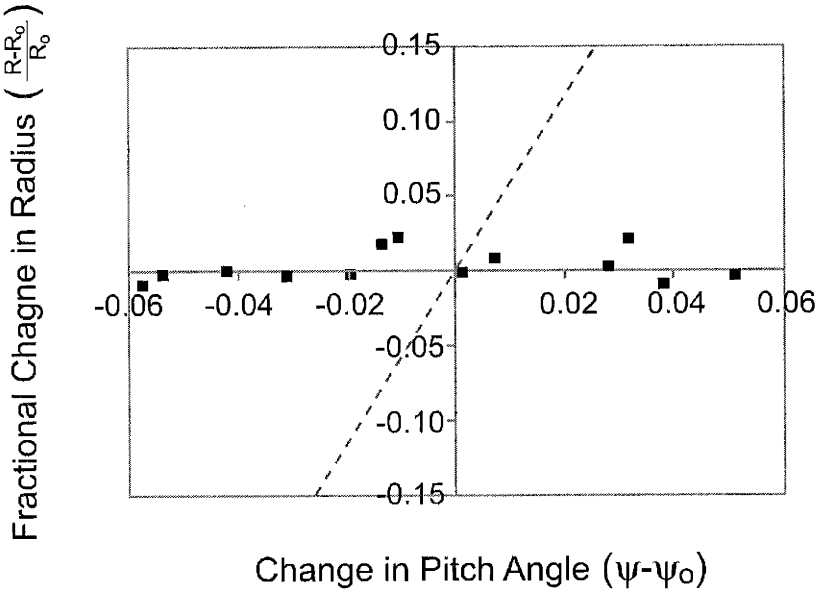

Figure 4-6: Plot of a typical set of experimental results for the fractional change in radius versus the change in pitch angle in radians for a low pitch helix in CDLC (squares). The theoretical results using a chiral model with uniform tilt (dashed line) are clearly inconsistent with the data.

leads to an energy with the same functional form as chiral elasticity, even if we had kept λ in the free energy it would not have effected the results. In section 4.3.2, we will show that for the crystalline models (i.e. those with fixed tilt direction) only an isotropic spontaneous curvature is consistent with the observed vanishing of the linear term in the expansion of $\tilde{R}$ about ψ_o.

There are, however, two possible ways in which our experimental finding can be fitted into the framework of the chiral models. First, if we take the model of Selinger *et al.* with tilt modulation [44] (arguably the more correct form of the chiral models for the low pitch helices), we would have found the same result as that in Equation 4.27 only with the tilt angle (ϕ) replacing the pitch angle (ψ). This decoupling between the tilt and pitch angles means that we cannot simply substitute 11° into the expression for the slope. In fact, the entire motivation for the analysis by Selinger *et al.* was to show that while the pitch angle is quite small, the tilt angle (which is controlled by the renormalized elastic anisotropy of the ribbon) may be closer to 45°. Taking into

account the experimental uncertainty in our measured slope ($\frac{\Delta\bar{R}}{R_o}$ = -0.002 $\pm$ 0.029 from Equation 2.7), we could make the theory consistent with our observations if the tilt angle was anywhere between 44.6° and 45.5°. This argument, however, suffers from several drawbacks. Primary among these is that it would now require that the renormalized bending rigidity, the elastic anisotropy, as well as the ratio of the γ and K^*_{LS} moduli in the free energy (Equation 4.13) always be just right in all of the many different quaternary systems to yield helices of exactly 11°. In light of this and the other inconsistencies between the chiral models and the quaternary systems, as well as the arguments that the ribbons are most likely crystalline in nature which we will present in section 4.3.1, it is highly unlikely that this tilt modulated model is correct.

The second possible means of reconciling our measurements with the chiral theories is to reconsider the applicability of the zero torque condition for these pulling experiments. If, instead of assuming we have a freely rotating helix, we assume that we have a clamped end (i.e. Case Three from section 3.4.3), Equation 3.22 would give us that

$$\bar{R}(\psi) = \frac{s}{\Phi_o}\cos(\psi) \tag{4.28}$$

Expanding this expression around the unstressed pitch angle ψ_o yields

$$\frac{\Delta\bar{R}}{R_o} = -\tan(\psi_o)\Delta\psi \tag{4.29}$$

Here there is no ambiguity as to the tilt versus pitch angle since Equation 4.28 was derived from a purely geometric relationship. Plugging 11° into this expression, we find a slope of -0.19 for $(\Delta\bar{R}/R_o)$ vs $\Delta\psi$. This value is nearly 6.5 standard deviations away from the measured value, but it is far closer than the predicted slope shown in Figure 4-6. Thus, while highly unlikely to be true, this possibility cannot be so easily dismissed as inconsistent, especially given the size of the error bars on the individual data points. However, other evidence helps to argue strongly against the clamped end boundary condition. First as discussed in section 2.4.2 we have observed the helix freely rotating on the epoxy in agreement with the assumption of zero torque. Second, we will show in section 5.3 that the clamped end boundary condition is not capable of explaining the tension induced straightening transition, while the zero-

torque description is fully self-consistent. Thus, we can conclude that the chiral models are indeed fundamentally inconsistent with measurements of the fractional change in radius upon extension and compression.

This completes our discussion of the successes and failures of the chiral models. Our findings strongly indicate that despite their ability to explain phenomena in a number of self-assembling systems, the chiral models are not appropriate to the structures formed in the quaternary systems. Taken as a whole, the inconsistencies and contradictions outlined in this section imply the need for a totally new theory not built on chiral elastic properties. In the next section, therefore, we will present our proposed crystalline model which incorporates a fixed tilt direction and an isotropic spontaneous bending energy analogous to a surface tension imbalance between the inner and outer ribbon faces.

4.3 The Crystalline Model

In the last section, we reviewed the previous models that have been proposed in order to try and explain the self-assembly of tubules and helical ribbons. We broke these theories down into two categories, one for those that considered effects other than the chiral elastic properties of the membrane (Class One) and one for those that considered only chiral effects (Class Two). The non-chiral models were shown to be inconsistent with observations across most systems, including our own. The chiral models, on the other hand, have been quite successful at describing the structures formed in many different systems. However, we concluded the previous section by arguing that several serious questions arise when attempting to apply these chiral models to helices formed in the quaternary systems. These inconsistencies are fundamental to the choice of chirality as the driving force of helix formation, and thus the new model to be presented in this section will be a non-chiral (i.e. Class One) theory. We will begin with the assumption that the ribbon has anisotropic crystalline elastic properties and add to that an isotropic spontaneous curvature which will stabilize the resulting helix. We will then show that this model offers a more self-consistent

explanation of the observed microstructures the form in the quaternary systems, and finally we will conclude with a discussion of the questions left unresolved by our new approach.

4.3.1 Arguments for Positional Order in Helical Ribbons

In their development of the tilt modulated model (see section 4.2.2), Selinger *et al.* argued that the ribbons must be in a fluid phase [44]. The experimental evidence for tubules made from diacetylenic lipids was somewhat contradictory about the presence of long range positional order, and so the authors also pointed to theoretical results that argued against the stability of thin two dimensional crystals. These arguments begin by noting that a flexible membrane can relieve the strain field surrounding a topological defect by buckling out of the plane. This bending costs elastic energy while relieving the much larger defect energy associated with membrane stretching. In 1987, Nelson and Peliti argued that this trade off would allow the energy of a dislocation in a buckled membrane to remain finite as the system size tends to infinity [161]. This screening of defect energies leads to the prediction that dislocations will form at any nonzero temperature in the thermodynamic limit, and thus that they will cause a crystal to melt. A more complicated numerical analysis carried out by Seung and Nelson in 1988 demonstrated that the energy cost of buckled dislocations, while perhaps not finite, at least increase slower than any logarithmic divergence, and therefore that unbound defects will form in large systems due to the entropy gained by their creation [192].

There are two possible ways to avoid the result of Nelson and Peliti, and to maintain crystalline order throughout a tubule or helical ribbon. First, it is possible that the melting transition occurs on a much longer length scale than that of the helices and tubules formed in our systems. In this case the proliferation of defects would simply not yet be sufficient to destroy the positional order in this amount of material, and thus they could be maintained as solid crystals. Second, a possible mechanism for the stabilization of long range crystalline order in flexible two dimensional membranes was proposed by Chappell and Yager in 1991 [193]. In their model they assumed the

helix was made up of quasi-one-dimensional chains that would line up side by side to give the ribbon width. These chains were taken to have strong internal interactions holding them together with weaker interactions connecting the chains. The authors justified their model by noting that the highly anisotropic growth of a crystalline phase is often a reflection of highly anisotropic cohesive interactions between the molecules, and the ribbons obviously grow much greater in contour length than they do in width. In addition, we also note that this anisotropy would in general lead to different bending rigidities along the two directions, and thus to a non-45° pitch angle in agreement with our observations of $\psi_o = 11°$ or 54°. In the Chappell-Yager model, the introduction of a topological defect in one chain costs additional energy through its interactions with the neighboring chains. This effect can greatly enhance the defect energy and cause its cost to dominate over the entropy advantage of introducing it. Therefore, below a certain critical temperature, the crystal may be made thermodynamically stable with respect to this type of melting transition.

In addition, the connection between crystalline vs. liquid crystalline order and the preferred geometry of the resulting microstructure has been investigated both experimentally and theoretically by several authors. In 1999, Oda *et al.* chose to study systems of cationic gemini surfactants consisting of twin surfactants joined by a hydrocarbon spacer of variable length and chiral counterions such as $L-$tartrate which were known to form gels by creating extended networks of self-assembled microstructures [35]. The authors found that surfactants with short hydrocarbon chains (14 to 16 carbons) formed twisted strips while those with longer chains (18 carbons) formed helical ribbons with cylindrical curvature instead (see Figure 4-2). They argued that this difference is likely due to the fact that the longer lengths lead to an elevated chain melting transition temperature, and thus to a more ordered phase than for the surfactants with shorter hydrocarbon chains. In order to more quantitatively explain these observations, Oda *et al.* extended the Helfrich-Prost model for nematic liquid crystals [124] to include the possibility of the membrane having non-zero Gaussian curvature. Analysis of their model led to the conclusion that the optimal shape for a fluid bilayer would be the twisted strip because it allows each layer to have the same curvature

and thus the same surface contact area. Oda *et al.* further argued that the only way to stabilize the cylindrical curvature present in wound helical ribbons was to allow the membranes to have long range crystalline order which would strongly oppose the creation of saddle-like curvature because it would require stretching the membrane. This result is in good agreement with the work of Ou-Yang and Liu already discussed [152, 153]. For cholesterics, Ou-Yang and Liu found that the twisted strip was of higher energy than the helical ribbon for membranes with fixed tilt direction. These conclusions were further supported by the work of Spector *et al.* with equimolar solutions of $DC_{8,9}PC$ and 1,2-bis(dinonanoyl)$-sn-$glycero-3-phosphocholine (DNPC) [53]. The authors found that at low temperatures ($\sim 4^{\circ}$ C) the solutions formed stable nanotubules while at higher temperatures ($\sim 26^{\circ}$ C) the structures transform into twisted strips. The authors interpreted this transition as due to the fact that at the higher temperatures, the DNPC chains became disordered and act to fluidize the entire membrane which favors Gaussian (i.e. saddle-like) curvature over cylindrical curvature.

In addition to these general arguments for the existence of crystalline order in the helical ribbons at finite temperature, we have two pieces of experimental evidence that also suggest the structures formed in the quaternary systems do indeed have long range positional correlation. First, Zastavker *et al.* found that the formation of helical ribbons with one of two distinct pitch angles was a general phenomenon in a diverse set of systems with wide variation in the number of components as well as their chemical structures and physical properties such as chirality [27]. They argued that it is very unlikely that the same two packings could occur for each of these distinct systems unless they shared a robust and ordered microscopic structure. Second, Konikoff *et al.* showed that in the model biles, one class of quaternary systems, the filament precursors of helical ribbons were a polymorph of cholesterol monohydrate crystals and anhydrous cholesterol covered by a monolayer of phosphotidylcholine [190, 191]. In addition, the helical ribbons are themselves known to be precursors to stable plate-like cholesterol monohydrate crystals. These observations suggest that the helices may, in fact, maintain some type of positional ordering during their transition from

filament to bulk crystal. This conclusion is further supported by the preliminary x-ray diffraction experiments noted in section 2.3.2 in which it is found that the helical ribbons have a layer spacing equivalent to that of cholesterol monohydrate crystals.

Taken as a whole, these theoretical arguments and experimental observations led us to adopt the thin anisotropic elastic crystal as our starting point for developing a model for helices and tubules. We will now discuss the derivation of the free energy which will include the elastic bending energy for such a crystal as well as our choice of the mechanism by which the curvature of a helix is stabilized.

4.3.2 Derivation of the Crystalline Model Free Energy

I would like to thank Dr. Aleksey Lomakin for his help in developing the original concept for the elastic free energy to be presented in this section, as well as his help in determining its initial parameterization. In addition, I would like to thank Dr. Yevgenyia Zastavker for placing the formal derivation of this free energy on solid mathematical footing through her detailed treatment of the helix differential geometry.

As noted above, the derivation of the model free energy in this section will consist of two parts. First, we will derive the elastic energy cost of deforming the ribbon away from its flat state, which we will take to be its zero energy configuration. This derivation will be quite general and will follow the theory for the bending of thin plates as set forth by Landau and Lifshitz in their *Theory of Elasticity* [194]. Second, we will derive an empirical form for the spontaneous bending energy that stabilizes the helix curvature. As noted in section 4.2.3, the key piece of information that will allow us to distinguish between choices for this stabilizing term is the fractional change in radius as a function of the change in pitch angle.

The general form of the elastic free energy per unit volume of a crystal that has undergone a small deformation may be expressed as [194].

$$\frac{F}{V} = \frac{1}{2}\lambda_{ijkl}U_{ij}U_{kl} \tag{4.30}$$

where λ_{ijkl} is the elastic modulus tensor of the crystal and U_{ij} is the strain tensor

associated with the deformation. In general, the strain tensor is defined through

$$U_{ij} = \frac{1}{2}\left(\frac{\partial u_i}{\partial x_j} + \frac{\partial u_j}{\partial x_i}\right) \tag{4.31}$$

where the displacement u_i is given by $x_i' - x_i$ (i.e. the difference between the location of a point within the membrane before and after the deformation). As is clear from its definition, the strain must be symmetric with respect to the exchange of its two indices (i.e. $U_{ij} = U_{ji}$ and the product $U_{ij}U_{kl}$ must be equal to $U_{kl}U_{ij}$). Together, these properties of the strain tensor constrain the elastic modulus tensor to have the same general symmetries reducing its number of independent components from 81 to 21. In addition, if the underlying crystal has further degrees of symmetry, such as a mirror plane or axis of rotation, then the lambda tensor must also have the same symmetry properties with respect to its indices. For thin plates of thickness t and area A, the free energy per unit area can thus be found from

$$\frac{F}{A} = \int_{-t/2}^{+t/2} \frac{1}{2}\lambda_{ijkl}U_{ij}(t')U_{kl}(t')dt' \tag{4.32}$$

where the integral is symmetric about the neutral surface within the ribbon.

We begin the calculation of F by noting that, from our experimental observations, the ribbons are best modeled as thin elastic plates. In particular, we note from the measurements discussed in section 2.3 that the typical thickness of the ribbons is on the order of tens to hundreds of nanometers, while the typical contour lengths are on the order of hundreds to thousands of microns. Some care, however, must be taken when comparing the ribbon width (w) to its thickness (t) . From Figure 2-9, we find that even for fairly wide helices ($w \geq 3$ μm), the ratio of the width to the thickness can vary from as much as nearly 200 to as little as just 25. As discussed in section 2.3.2, from these measured values for w/t, it would be somewhat hard a priori to definitively conclude that the structures would best be modeled as thin plates ($t \ll w$, s) rather than as elastic rods ($t \sim w \ll s$). However, we also note that we have never been able to induce any observable twisting of these ribbons, even under external tensions large enough to tear the structure apart. Therefore we conclude that the structures we have been working with must have a large internal torsional

rigidity making them behave like elastic plates. This assumption thus restricts us to considering only cylindrical deformations with zero Gaussian curvature in our model for the helices. A detailed derivation of the components of the strain tensor (U_{ij}) for this type of deformation is given in the thesis of Dr. Yevgeniya Zastavker and will not be repeated here [28]. The final result for the elastic bending energy we derived was found to be

$$F_{elastic} = sw \int_{-t/2}^{+t/2} \frac{t'^2}{R^2} \Big(K_1 \cos^4(\psi) + K_2 \cos^3(\psi)\sin(\psi) + K_3 \cos^2(\psi)\sin^2(\psi) + K_4 \cos(\psi)\sin^3(\psi) + K_5 \sin^4(\psi) \Big) dt' \tag{4.33}$$

where the coefficients K_n (n = 1,2,3,4,5) are combinations of the components of the elastic modulus tensor (λ_{ijkl}) that we will treat collectively as phenomenological parameters. Performing the integral in Equation 4.33 assuming the underlying elastic moduli are independent of the ribbon thickness yields

$$F_{elastic} = sw \Big(\frac{K_1' \cos^4(\psi) + K_2' \cos^3(\psi)\sin(\psi) + K_3' \cos^2(\psi)\sin^2(\psi)}{R^2} + \frac{K_4' \cos(\psi)\sin^3(\psi) + K_5' \sin^4(\psi)}{R^2} \Big) \tag{4.34}$$

where the primed coefficients are related to their unprimed values by

$$K_n' \equiv K_n \frac{t^3}{24} \tag{4.35}$$

The factor $\frac{1}{24}$ is of no importance since we were already treating the unprimed constants as unknown parameters to be fit by experimental data, however, the explicit dependence on ribbon thickness will turn out to be important in our discussion of possible mechanisms to explain the observed polydispersity of the radius distribution in quaternary systems.

The free energy in Equation 4.34 represents the simplest and most general form for describing helical ribbons with crystalline order in the long wavelength limit. In order to simplify our analysis, however, we will impose a further physically reasonable symmetry upon the ribbon. Experimentally we note that the ribbons grow very anisotropically in contour length versus width. As pointed out in the previous section,

this type of directed growth often implies highly anisotropic interactions between the molecules, and therefore if the ribbons possess a mirror plane it must be aligned along either the direction of the contour length or width. This symmetry is consistent with the model of Chappell and Yager in which the ribbon is composed of long tightly bound one-dimensional chains stacked side-by-side in a highly ordered array [193]. If present, such a crystal symmetry must be reflected in the symmetry of the elastic modulus tensor, and thus certain components of λ_{ijkl} will be constrained to be identically zero. Imposing this symmetry upon the ribbon, we find that the both the K_2' and the K_4' terms are eliminated from Equation 4.34. With the two cubic terms set to zero, the elastic free energy simplifies to

$$F_{elastic} = sw\left(\frac{K_\alpha \cos^4(\psi) + 2K_\beta \cos^2(\psi)\sin^2(\psi) + K_\gamma \sin^4(\psi)}{R^2}\right) \tag{4.36}$$

where we have defined $K_\alpha \equiv K_1'$, $K_\beta \equiv \frac{1}{2}\, K_3'$, and $K_\gamma \equiv K_5'$ in order to simplify the subsequent analysis. This is the final form of the elastic free energy that we will carry throughout the remainder of this work.

Despite the complicated algebra involved in its derivation, the form of the elastic free energy in Equation 4.36 has a very simple physical interpretation. First, as noted in our general treatment of the free energy in section 3.2, we are effectively modeling the ribbon as a two dimensional surface where each point locally is equivalent to every other point. This translation invariance over the membrane means that the bending energy cannot depend upon where it is calculated, and thus F must simply be extensive in the total surface area (sw). Second, we are considering only an elastic bending energy, and therefore, according to the generalized Hookes Law, the local energy cost must scale like the square of the deformation (see Equation 4.30). For a helical ribbon the membrane deformation may be characterized by a single radius of curvature (R) and a pitch angle (ψ) [28]. For the special case of a purely cylindrical deformation, the anisotropic ribbon may be bent in two inequivalent ways ($\psi = 0°$ or $90°$) as shown in Figure 4-7.

Examining the geometry of a helix (see Figure 3-1) we note that the ribbon will, for a general pitch angle, be bent along both its contour length and its width. In

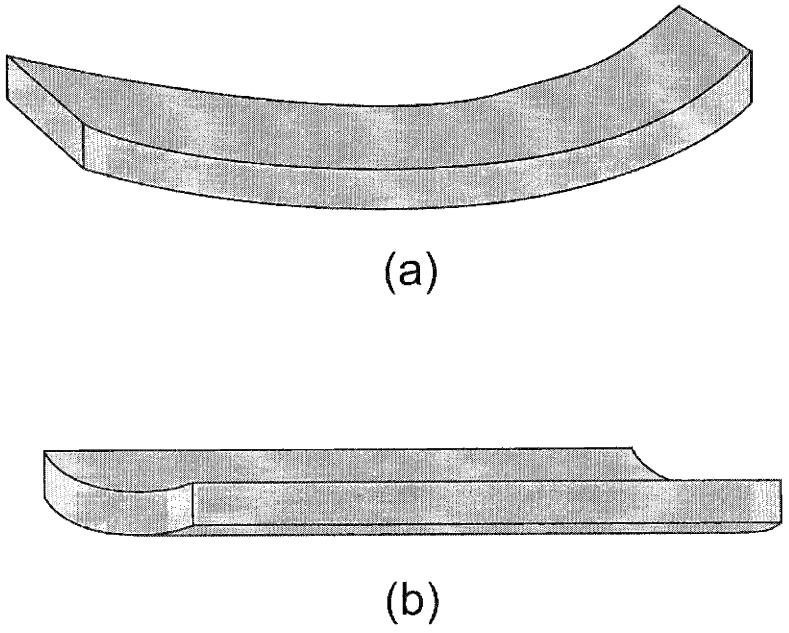

Figure 4-7: Schematic representation of the two principle modes of bending for cylindrical deformations of a thin rectangular plate. (a) A deformation which bends all lines parallel to the contour length of the ribbon creating a cylinder equivalent to a helix with zero pitch angle. (b) The complimentary deformation bending lines parallel to the ribbon width which creates a cylinder equivalent to a helix with a 90° pitch angle. [NOTE: the thickness of the ribbon has been greatly exaggerated for clarity.]

order to determine the amount of curvature along these two perpendicular directions as a function of the pitch angle, we will examine the generalized equation for a helix in three dimensions and proceed to determine the rate of change of the tangent vector as a function of the arc length. Using cylindrical coordinates, a line that runs along the contour length of the ribbon can be parameterized as

$$\vec{r}(\phi) = R\cos(\phi)\hat{x} + R\sin(\phi)\hat{y} + R\phi\tan(\psi)\hat{z} \tag{4.37}$$

where ϕ is the standard azimuthal angle. The curvature of this line (κ) may then be found from its mathematical definition

$$\kappa = \frac{|\vec{r}' \times \vec{r}''|}{|\vec{r}'|^3} \tag{4.38}$$

where $\vec{r}' = d\vec{r}/d\phi$ and $\vec{r}'' = d^2\vec{r}/d\phi^2$. Substituting Equation 4.37 into Equation 4.38, we find that the curvature of the ribbon along its contour length is given by

$$\kappa_s = \frac{\cos^2(\psi)}{R} \tag{4.39}$$

In order to find the curvature along the ribbon width, we can simply rotate the entire coordinate system by 90° and use Equation 4.39 to immediately write down

$$\kappa_w = \frac{\sin^2(\psi)}{R} \tag{4.40}$$

With these two expressions for the ribbon curvature (Equations 4.39 and 4.40) we can now easily interpret the various terms in the free energy. First, the K_α term in Equation 4.36 is proportional to κ_s^2 and will thus give the energy cost of bending the ribbon along its contour length. Second, the K_γ term, proportional to κ_w^2, will give the energy cost of bending the ribbon along its width. Third, the cross term (K_β) represents an additional energy due to the twist in the coordinate system induced when both modes of bending are present. These interpretations of the terms in F, based on purely geometric considerations, are in exact agreement with the interpretation of Zastavker based upon an examination of the components of λ_{ijkl} that they contain [28].

Finally, we should note that it is not surprising that our elastic free energy (Equation 4.36) is exactly equivalent to that derived by Helfrich and Prost (Equation 4.2) or Chung *et al.* (Equation 4.9) despite the very different physical models we began with for the ribbon structure. This equivalence arises because regardless of whether it is derived from soft deformations of a liquid crystal with fixed molecular tilt or from small deflections of an anisotropic crystalline plate, the energy of elastic bending must simply be related to the square of the membrane curvature. This realization is, in fact, the fundamental assumption of the effective surface Hamiltonian approach upon which all of the models described in this chapter are built.

With Equation 4.36, we now have a general form for the elastic energy cost associated with a helical deformation of the ribbon. If this was the only contribution to the free energy, however, then the sole equilibrium state would obviously be a

completely flat plate. Therefore, we know that we must add to our model some force that will tend to favor finite curvature and thus stabilize the helix. As we have noted before, none of the previous physical models for this force are consistent with our observations on the quaternary systems. In order to determine the correct form of this stabilizing force, we recall that it was the fractional change in radius under extension and compression that helped to rule out the chiral and spontaneous torsion models as possibilities for this effect. We will now show that this piece of information is, in fact, enough to uniquely determine the leading order behavior of the spontaneous bending force.

We will begin our derivation of the stabilizing force by assuming that the non-elastic contribution to the free energy can be expanded as a Taylor series in the helix curvature ($\frac{1}{R}$). This assumption is reasonable because the additional energy must favor a finite curvature and it must vanish in the limit of infinite radius. In addition, we will keep only the lowest order term since the quadratic term could be absorbed into the elastic bending energy and terms of cubic order and higher have already been ignored by our restriction to the small deformation limit in the derivation of Equation 4.36. With these assumptions, we can write the full free energy for a helical ribbon as

$$F(R,\psi,s) = sw\left(\frac{f(\psi)}{R^2} - \frac{K_s(\psi)}{R}\right) \tag{4.41}$$

where $f(\psi)$ is given by

$$f(\psi) \equiv K_\alpha \cos^4(\psi) + 2K_\beta \cos^2(\psi)\sin^2(\psi) + K_\gamma \sin^4(\psi) \tag{4.42}$$

and $K_s(\psi)$ is an arbitrary function of the pitch angle and has the units of force. In order to determine the precise form of the this stabilizing term, we will now use the equilibrium conditions worked out in Chapter 3 to determine how the fractional change in radius as a function of the change in pitch angle under torque-free extension is related to $K_s(\psi)$. By comparing our experimental findings to this theoretical relationship, we will be able to infer how the spontaneous bending force depends on the pitch angle.

In order to determine $\Delta\tilde{R}/R_o$ vs $\Delta\psi$ as we did for the chiral models in Equa-

tion 4.27, we must first work out the zero stress equilibrium conditions for our model. Applying the zero torque condition in Equation 3.17 to the free energy in Equation 4.41 and solving for the radius yields

$$\tilde{R}(\psi) = 2\frac{f(\psi)}{K_s(\psi)} \tag{4.43}$$

Next, applying the zero tension condition (Equation 3.14) to the free energy yields the following implicit expression for the free equilibrium pitch angle

$$\frac{df}{d\psi}|_{\psi=\psi_o} - 2\frac{f(\psi_o)}{K_s(\psi_o)}\frac{dK_s}{d\psi}|_{\psi=\psi_o} = 0 \tag{4.44}$$

where we have already substituted for $R_o = R(\psi_o)$ as given by Equation 4.43.

We will now expand $\tilde{R}(\psi)$ (Equation 4.43) about ψ_o (Equation 4.44) to lowest order and divide through by the unstressed radius. After a little algebra, the fractional change in helix radius as a function of the pitch angle is found to be

$$\frac{\tilde{R}(\psi) - R_o}{R_o} = \left(\frac{1}{K_s(\psi_o)}\frac{dK_s}{d\psi}|_{\psi=\psi_o}\right)[\psi - \psi_o] \tag{4.45}$$

Experimentally, our measured value for the slope of this line ($\Delta\tilde{R}/R_o$ vs $\Delta\psi$) is zero to within experimental uncertainty. Thus, we must find a model that will give $\left(1/K_s(\psi_o)\ (dK_s/d\psi)|_{\psi=\psi_o}\right) = 0$. We know that $1/K_s(\psi_o)$ cannot be zero since, from Equation 4.43, that would imply the equilibrium radius would be zero. That realization leaves us with the requirement that the derivative be zero at ψ_o. The simplest and only physically reasonable model that has this property is for K_s to be independent of the pitch angle (i.e. for the ribbon to possess an isotropic spontaneous curvature). As we have noted before, this model is analogous to imposing a difference in surface tension between the inner (compressed) and outer (stretched) faces of the ribbon (see Appendix D for details). Finally, Figure 4-8 shows the good comparison of our results for $\Delta\tilde{R}/R_o$ vs $\Delta\psi$ using the isotropic model to the same experimental data set shown in Figure 4-6.

Combining all of the above arguments, the final model for the total free energy in the crystalline model we propose is thus given simply by [28, 45]

$$F(R, \psi, s) = sw\left(\frac{f(\psi)}{R^2} - \frac{K_s}{R}\right) \tag{4.46}$$

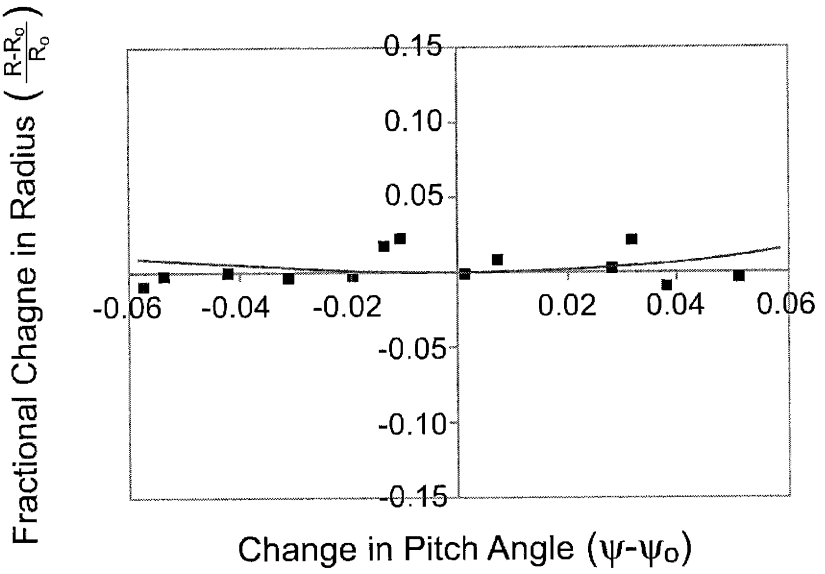

Figure 4-8: Plot of a typical set of experimental results for the fractional change in radius versus the change in pitch angle in radians for a low pitch helix in CDLC (squares). The theoretical result using the crystalline model with an isotropic spontaneous bending energy (solid line) is in good agreement with the data shown.

where $f(\psi)$ is defined through Equation 4.42. With this expression for the free energy, we have completed our derivation of the crystalline model. In the next section, we will examine some of the implications of this model for the helices free in solution in order to compare the results against those for the chiral models.

4.3.3 Implications of the Crystalline Model Free Energy

Before going on to apply the general formalism of Chapter 3 concerning the application of forces to the proposed crystalline model, we will first examine the special case of zero tension and zero torque for which we have data spanning all of the various quaternary systems. This discussion will allow us to demonstrate that our model does, in fact, offer an improvement over the chiral models when applied to these systems. Applying the conditions of zero stress to our free energy (Case One in section 3.4.1),

we find the following expressions for the equilibrium pitch angle and radius

$$\tan^2(\psi_o) = \frac{K_\alpha - K_\beta}{K_\gamma - K_\beta} \tag{4.47}$$

and

$$R_o = \frac{2}{K_s} f(\psi_o) = \left(\frac{2}{K_s}\right) \frac{K_\alpha K_\gamma - K_\beta^2}{K_\alpha - 2K_\beta + K_\gamma} \tag{4.48}$$

respectively. We can immediately draw three important conclusions from these results.

First, we find that the free energy for the unstressed radius and pitch angle is given by

$$F(R_o, \psi_o, s) = -sw\frac{K_s^2}{4}\left(\frac{K_\alpha - 2K_\beta + K_\gamma}{K_\alpha K_\gamma - K_\beta^2}\right) \tag{4.49}$$

This part of the equilibrium free energy is negative and extensive in the area, and thus the helix will grow more energetically favorable as its width increases. This effect could offer a simple explanation of the observed lateral growth of helices towards tubules if the energy advantage gained by adding material to the ribbon outweighs the entropic disadvantage of removing it from the solution and localizing it at a single crystal site.

Second, plugging the observed values of 11° and 54° for the equilibrium pitch angle into Equation 4.47, we find ratios for the elastic energy constants $\Big((K_\alpha - K_\beta)/(K_\gamma - K_\beta)\Big)$ of 0.038 and 1.89 respectively. These ratios are far more physically reasonable than those derived by Chung *et al.* [20]. The ratio for the low pitch helices in this model is only about $\frac{1}{25}$ instead of nearly $\frac{1}{700}$ as it was in the constant tilt chiral models. This result also means that our model requires less of a difference between the mechanical properties of the high and low pitch ribbons than previously implied. Our results for the elastic anisotropy differ by less than a factor of 50 between the two types of helices, while the theory of Chung *et al.* requires a factor of nearly 2300 between the high and low pitch ratios.

Third, our model provides a physically reasonable means of selecting the multiple length scales required to explain the polydispersity of the radius distribution in quaternary systems. As noted in Equation 4.35, the elastic energy constants (K_α, K_β,

and K_γ) will all scale with the cube of the ribbon thickness. However, in our model there is no reason to require the spontaneous curvature (K_s) to scale with thickness in the same way as these constants. Therefore, the ratio that determines the equilibrium radius ($f(\psi)/K_s$ from Equation 4.48) will likely have some residual thickness dependence, and thus the polydisperse radius distribution may simply be a simple consequence of a polydisperse thickness distribution. In particular, in Appendix D we demonstrated that for the case of a surface tension imbalance between the two ribbon surfaces, the K_s modulus would scale linearly with the ribbon thickness. This scaling of K_s would make R_o proportional to the ribbon thickness squared. Out of two representative sets of AFM data collected on low pitch helices from CDLC which had been laid out on mica and imaged under water (see section 2.3.2), we found the thickness (t) varied from roughly 40 to 138 nm. While it is likely that very thin or very thick ribbons would not survive the deposition and rinsing process intact, this range represents a good estimate for the typical variation amongst the helices. For this set of thickness bounds, the ratio $t_{\text{thick}}/t_{\text{thin}}$ is found to be 4.11 which, upon squaring, gives a factor of approximately 17. This result is consistent with the observed spread in typical radii for similar ribbons, which spans roughly one order of magnitude for low pitch helices in CDLC (see section 2.3.1).

From the above discussion, we can conclude that our proposed crystalline model does, in fact, eliminate three of the major inconsistencies between the chiral models and our experimental observations. First, our model predicts a reasonable value for the elastic anisotropy of the ribbons without the need for complex tilt modulation. In so doing, it also imposes a rigid microscopic structure that makes the appearance of the same two robust pitch angles across all the various quaternary systems more reasonable. Second, our model builds in the result that the radius does not change to first order upon extension or compression of a low pitch helix in the absence of an applied torque. Third, our model allows for the selection of multiple length scales to explain the polydisperse radius distribution observed across the quaternary systems. There are, however, two important (and related) questions that have yet to be resolved in relation to this model. First, direct evidence for long range positional

order must be obtained in order to rule out the previous tilt modulated models based on fluid membranes. As mentioned in section 2.3.2, along with Winnie Yong and Dr. David Moncton we have begun an investigation of the packing order within the ribbons using x-ray diffraction. To date, the preliminary work has explicitly shown the existence of stacked layers with rigid one dimensional order in the ribbon normal direction, however, the question of intra-layer positional order has yet to be definitively resolved. Second, and more importantly, our current model is achiral and thus predicts that an equal number of left and right handed helices should form in solution. As already mentioned, however, even in the seven quaternary systems that do form left handed helices, these structures usually represent only about 5% of the total yield. The mechanism that biases the distribution towards right handed structures is likely a kinetic effect and therefore cannot be explained entirely in terms of these simple equilibrium energy considerations. However, further experimental and theoretical studies need to be undertaken before any substantial insight may be gained into this question. Whatever the resolution of the handedness question, it is likely to be an important point of connection between the concepts that govern the chiral and non-chiral models.

With this discussion we have completed both our review of the previous theories for the helical ribbons, as well as the presentation of a new model which was constructed to be more consistent with experimental observations. We are now ready to apply the general formalism of Chapter 3 to the model free energy given in Equation 4.46 and explore the helix behavior under non-zero stress. In the next chapter we will show that using this theoretical framework, we can explain the results of each pulling experiment we have performed on low and high pitch helical ribbons in CDLC. In addition, we will actually over specify the model for the low pitch structures, and show that our predictions are internally self-consistent. We will conclude the discussion with predictions for future types of pulling experiments that will become possible as new types of tethering techniques are developed.

Chapter 5

Analysis of Experimental Results Using the Crystalline Model

5.1 Introduction

In the three previous chapters, we have discussed our experimental observations of helical ribbons formed in the quaternary systems as well as a theoretical framework in which to interpret these results. This formalism revolves around a geometric model free energy $F(R, \ell, s)$ parameterized by four phenomenological constants (K_α, K_β, K_γ, and K_s). The first three are the elastic energy constants associated with the costs of deforming the ribbon away from a flat state, while the fourth is the isotropic spontaneous curvature that provides the intrinsic bending force. In order to fully characterize our model, therefore, we have only to determine these four constants from experimental measurements. In section 4.3.3, we have already analyzed the special case of zero stress (Case 1) using the crystalline model, and found that our new free energy improved upon many of the important inconsistencies inherent in previous theories. In addition, the analysis of the unstressed helix lead to two expressions (Equations 4.47 and 4.48) relating the equilibrium pitch angle and radius to the phenomenological constants in the model. Before the current work, and that of Dr. Zastavker [28], these two geometric properties were the only pieces of information available to be fit to the model free energies [20, 44, 27]. In this chapter we will

proceed to apply the general formalism developed in Chapter 3 for non-zero tension and/or torque to the crystalline model. In so doing, we will be able to completely specify the free energy for the low pitch helices in CDLC.

We will begin this process in section 5.2 by analyzing the response of a helix to the application of a small axial tension. We define "small" to mean that the response of the system due to the introduction of the axial force can be treated in a perturbative manner. To lowest order, this expansion of the force around the unstressed state will yield the linearized response function for the structures. The slope of the force–extension curve will define the effective axial spring constant for our helices in terms of their geometric properties and the phenomenological elastic energy constants in our model free energy. Our measurement of this slope (see Figure 2-14 in section 2.4.3) will provide a third expression for the constants in our model. This relationship will turn out to be the only one analyzed that relates an experimental measurement directly to the value of the elastic energy constants instead of to a ratio of the free energy parameters. Thus, the spring constant will allow us to set the absolute scale of the model free energy.

We will continue in section 5.3 with an analysis of the tension induced straightening transition observed in the low pitch helices in CDLC. We will begin by demonstrating explicitly our previous claims that the predictions of the clamped end boundary condition (Case 3 from section 3.4.3) are incapable of satisfying the two stability conditions for domain separation. We will proceed to show that using the zero torque boundary condition (Case 2 from section 3.4.2), it is possible to fit the equal area construction in Equation 3.61 to our measured value for the pitch angle of the helical domain. This equation will provide a fourth expression for the phenomenological constants allowing them, and thus the free energy, to be fully determined for the low-pitch helices. In addition, we will show that our model predicts a theoretical value for the limit of metastability (i.e. the maximum pitch angle achievable for a helix to remain in a single domain). By careful control of the experimental environment, we have been able to measure the value of this limit which provides a fifth piece of information relatable to the free energy. This last condition obviously over specifies

our model, and we will show that all of our predictions are internally self-consistent with our experimental results. In Appendix E, we will present the preliminary experimental evidence for the same type of straightening transition in high-pitch helices, and examine the consequences of our current observations for this class of structure.

Finally, in section 5.4 we will examine the case of rotating a helix by the application of a pure torque (Case 4 from section 3.4.4). We will demonstrate that our model predicts no special instability for this case, and that upon the application of a negative torque the helix will simply unwind continuously, expanding to a straight state and then proceed to rewind into a left-handed helix with the sense of the torque reversed. Using the results for the free energy parameters of the low pitch helices worked out in section 5.3 of this chapter, we will make predictions for the forces required to achieve these deformations as well as for the form of the stressed radius and azimuthal angle as a function of the pitch angle. These predictions may be tested experimentally as new tethers are developed, and will thus provide the first fully independent test of our mechanical model for the helical ribbons. We will conclude this chapter with a brief comparison of our predictions for the response of a helix under torque to what would be expected if the chiral models had been correct. This comparison will highlight three distinct and unmistakable experimental observations that would help to further rule out the chiral models as describing the helices in CDLC as well as definitively verify our isotropic form for the spontaneous curvature.

5.2 The Helix Spring Constant

In sections 3.4.2 and 3.4.3, we described two distinct ways of constraining an axial tension applied to a helix. The first (Case 2) described a helix under extension free from torque which allows the ends to rotate freely, while the second (Case 3) described a helix extended with clamped ends which is equivalent to conserving the number of helix turns. The formalism developed in these sections was fully general for the case of constant s, and made no assumptions about the magnitude of the applied tension. In this section, we will apply our general formalism to the crystalline model free energy

with the additional constraint that the tension is small enough that we need only keep the lowest order term in its Taylor expansion about ℓ_o.

From Equations 3.21 and 3.28, we know that the axial tension for each constraint is found from the derivative of a reduced free energy with respect to the axial length. Our first step must therefore be to find $\tilde{F}(\ell, s) \equiv F(\tilde{R}(\ell, s), \ell, s)$ (Equation 3.19) and $\bar{F}(\ell, s) \equiv F(\bar{R}(\ell, s), \ell, s)$ (Equation 3.23) for the crystalline model. In order to find these reduced free energies, obviously the first step must be to find the relationship between the radius and the axial and contour lengths governed by the external constraint on the deformation (i.e. $\tilde{R}(\ell, s)$ for the case of free ends and $\bar{R}(\ell, s)$ for clamped ends) so that they may be substituted into the full free energy (Equation 4.46). Beginning with the free end constraint, we find that plugging our model free energy into the zero torque condition (Equation 3.17) yields

$$\tilde{R}(\psi) = \frac{2}{K_s} f(\psi) \tag{5.1}$$

where again $f(\psi) \equiv K_\alpha \cos^4(\psi) + 2K_\beta \cos^2(\psi)\sin^2(\psi) + K_\gamma \sin^4(\psi)$ (see Equation 4.42). Substituting this expression for the radius back into the free energy gives us

$$\tilde{F}(\psi) = -sw\frac{K_s^2}{4}\frac{1}{f(\psi)} \tag{5.2}$$

Going back to the case of the clamped end boundary condition, the constraint in Equation 3.22 immediately gives us that

$$\bar{R}(\psi) = \frac{s}{\Phi_o}\cos(\psi) \tag{5.3}$$

independent of the specific choice for $F(R, \ell, s)$. Substituting this equation for $\bar{R}$ into the crystalline model gives us that the reduced free energy for this constraint is equal to

$$\bar{F}(\psi) = sw\frac{\Phi_o}{s}\left(\frac{\Phi_o}{s}\frac{f(\psi)}{\cos^2(\psi)} - \frac{K_s}{\cos(\psi)}\right) \tag{5.4}$$

Using Equations 4.48 and 3.22 for the unstressed radius, we may re-express the above equation for $\bar{F}$ in order to allow easier comparison with the result of the free end boundary condition. Making a substitution for Φ_o/s in favor of K_s, we find that the reduced free energy for the clamped end constraint may also be written as

$$\bar{F}(\psi) = -sw\frac{K_s^2}{4}\frac{1}{f(\psi)}\left[\left(\frac{\cos(\psi_o)f(\psi)}{\cos(\psi)f(\psi_o)}\right)\left(2 - \frac{\cos(\psi_o)}{\cos(\psi)}\frac{f(\psi)}{f(\psi_o)}\right)\right] \tag{5.5}$$

Before proceeding to determine the helix spring constant from the above, it is worth noting that, as we claimed in sections 3.2 and 3.5.3, the reduced free energy for both constraints can be written as s times a function only of ψ (or equivalently of ν). This fact guarantees that our general formalism for domain separation (which we will examine in detail in the following section) will, in fact, be applicable to the crystalline model.

Now that we have found the form of the reduced free energy for the two constraints, we must find an expression for the expansion of the tension about the unstressed axial length. In general, the expansion of a function $J_{\|}(\ell, s)$ about $\ell = \ell_o$ with s held constant is given by

$$J_{\|}(\ell, s) \approx J_{\|}(\ell_o, s) + \frac{\partial J_{\|}}{\partial \ell}|_{\ell=\ell_o} [\ell - \ell_o] \tag{5.6}$$

to first order. In this case, however, we know that $J_{\|}(\ell_o, s)$ must be zero, and so it may be dropped from Equation 5.6. Comparing the resulting expression to Hooke's Law, it is clear that, in general, the tension may be written as

$$J_{\|}(\ell, s) \approx K_{\text{spring}} [\ell - \ell_o] \tag{5.7}$$

where the effective spring constant for our helical ribbons is defined as

$$K_{\text{spring}} \equiv \frac{\partial J_{\|}}{\partial \ell}|_{\ell=\ell_o} \tag{5.8}$$

However, in this analysis it will be most convenient to re-express the effective spring constant in terms of the reduced free energies. From Equations 3.21 and 3.28, we find that the effective spring constant for the free end (i.e. zero torque) and the clamped end (i.e. $\Phi = \Phi_o$) boundary conditions may also be expressed as

$$\begin{aligned} \tilde{K}_{\text{spring}} &\equiv \frac{\partial^2 \tilde{F}}{\partial \ell^2}|_{\ell=\ell_o} \\ \bar{K}_{\text{spring}} &\equiv \frac{\partial^2 \bar{F}}{\partial \ell^2}|_{\ell=\ell_o} \end{aligned} \tag{5.9}$$

respectively. From Equations 5.2 and 5.4, however, we note that the reduced free energies are most easily expressed as functions of ψ and not of ℓ. Since all of the

derivatives are taken with s held constant, we may easily convert from one choice of variables to the other through

$$\frac{\partial}{\partial \ell} = \frac{1}{s\cos(\psi)}\frac{\partial}{\partial \psi} \tag{5.10}$$

and

$$\frac{\partial^2}{\partial \ell^2} = \frac{1}{s^2\cos^2(\psi)}\left(\frac{\partial^2}{\partial \psi^2} + \tan(\psi)\frac{\partial}{\partial \psi}\right) \tag{5.11}$$

Plugging the above expression for $\tilde{F}(\psi)$ into Equation 5.9, and using the change of variables just described, we find that the effective spring constant for the zero torque case is given by

$$\tilde{K}_{\text{spring}} = 8\frac{w}{R_o^2 s}\left(K_\alpha - K_\beta\right) \tag{5.12}$$

This expression for $\tilde{K}_{\text{spring}}$ is equivalent to that which was worked out previously in the work of Zastavker using a thermodynamic analogy to guide the treatment of a helix under tension [28].

Examining Equation 5.12, we note that the effective axial spring constant of a helix is predicted to depend strongly upon its bulk geometry. In addition to the explicit geometric pre-factor $w/(R_o^2 s)$ which is of the same form as that which is predicted for an ordinary classical spring [195], there is also an implicit thickness dependence in $\tilde{K}_{\text{spring}}$ that comes both from the elastic energy constants (K_α and K_β) as well as from the equilibrium radius (R_o). This fact therefore gives us a means of probing the intrinsic thickness dependence of the free energy parameters from measurements of the helix elastic properties on the bulk scale. Substituting Equation 4.48 for R_o into the expression for $\tilde{K}_{\text{spring}}$ we have

$$\tilde{K}_{\text{spring}} = 2\frac{w}{s}\left[\frac{K_\gamma(K_\alpha - K_\beta)(K_\alpha - 2K_\beta + K_\gamma)^2}{(K_\alpha K_\gamma - K_\beta^2)^2}\right]\left(\frac{K_s^2}{K_\gamma}\right) \tag{5.13}$$

where we have chosen to divide by K_γ for consistency with the ratios reported in section 5.3 (see Equation 5.42). The factor inside the brackets depends only on the ratio of the elastic energy constants and must therefore be independent of the ribbon thickness. In addition, from recent experiments we find that the width and contour length also appear to be completely uncorrelated with the ribbon thickness

(see section 2.3.1). Thus, measurements of the effective axial spring constant for helices of different geometries would provide a direct measurement of the ratio of the thickness dependence of the K_s modulus to that of the elastic energy constants. For the crystalline model, we argued in section 4.3.2 that K_α, K_β, and K_γ will all scale with the thickness cubed, while in Appendix D we showed that a surface tension model would lead to a K_s modulus that is equal to the surface tension imbalance ($\delta\sigma = \sigma_{\text{in}} - \sigma_{\text{out}}$) times the ribbon thickness (see Equation D.10). If we assume that this difference in the surface tension between the inner and outer ribbon faces is the same for all helices, then we predict that the overall geometric dependence of the effective spring constant will scale like

$$\tilde{K}_{\text{spring}} \propto \frac{w}{st} \tag{5.14}$$

where t is again the ribbon thickness.

An alternative, and more experimentally convenient, way to formulate this consideration of the geometric dependence of $\tilde{K}_{\text{spring}}$ is found by replacing only one power of the radius in Equation 5.12 with its dependence on K_s and the elastic energy constants. Making this substitution, we find that the effective axial spring constant may also be written as

$$\tilde{K}_{\text{spring}} = 4\frac{w}{R_o s}\left[\frac{(K_\alpha - K_\beta)(K_\alpha - 2K_\beta + K_\gamma)}{K_\alpha K_\gamma - K_\beta^2}\right] K_s \tag{5.15}$$

In this form, the quantity within the brackets is again found to be independent of the thickness, but the geometric pre-factor now retains a residual dependence on t due to the inclusion of the equilibrium radius. However, R_o is an easy parameter to measure experimentally, and therefore we can simply treat it as a given constant for any particular helix. Thus, using Equation 5.15 instead of Equation 5.13 to analyze data from measurements on helices of different sizes, we would be able to directly probe variations in the spontaneous bending modulus (K_s) between helices in addition to probing the variations of the ratio K_s^2/K_γ. In particular, for the values of the elastic energy constants derived in the next section (Equation 5.42), we predict that the axial spring constant for the case of extensions in the absence of torque may be expressed

simply as

$$\tilde{K}_{\text{spring}} = (4.1 \pm 1.9)\,\frac{w}{R_o s}\,K_s \tag{5.16}$$

Finally, we note that in section 4.3.3 we found that the surface tension model of K_s predicts that $R_o \propto t^2$ for fixed $\delta\sigma$, and therefore we recover the result that the net geometric dependence of $\tilde{K}_{\text{spring}}$ will scale like w/st as required.

In order to determine what range of available spring constants this geometric ratio (Equation 5.14) works out to, we first note that in section 2.3.1 we showed that the width and contour length of the low pitch helices typically vary by a little more than one order of magnitude each across the structures in CDLC. Second, from the AFM data described in section 2.3.2, we found that the thickness spanned roughly a factor of four across the ribbons measured so far. As discussed, it is likely that very thin or very thick ribbons would not survive the deposition and rinsing process intact and therefore, combining these observations, we predict that the effective spring constants for the low pitch helices in CDLC will vary over approximately three orders of magnitude due just to these geometric effects. Using the measurement of $\tilde{K}_{\text{spring}}$ shown in Figure 2-14 for a particular low-pitch helix, we estimate from the observed variation in typical helix dimensions that the available spring constants in CDLC will range from roughly 0.13 to 130 pN/μm. This wide range of possible values for the helix stiffness is a very advantageous property to have if these structures are to be used as force probes for the investigation of other biological or mechanical systems (see Appendix A). Being able to select a particular axial spring constant simply by selecting a particular helix geometry will allow for a wide variety of force and distance scales to be probed in a straightforward manner using helices from just this one quaternary system.

Turning back to the case of the clamped end constraint, we find that the effective axial spring constant for the clamped end constraint derived from $\bar{F}$ (Equation 5.4) is given by

$$\bar{K}_{\text{spring}} = 8\frac{w}{R_o^2 s}\left(K_\alpha - K_\beta\right) + 2\frac{w}{R_o^2 s}\tan^2(\psi_o)\left(K_\alpha + \tan^2(\psi_o)K_\beta\right) \tag{5.17}$$

As expected, the spring constant for the clamped end boundary condition is greater

than that for the free end constraint signifying the greater energy increase required to hold the number of helix turns fixed upon extension. For easier comparison, the effective spring constant for the clamped end constraint may also be re-expressed as

$$\bar{K}_{\text{spring}} = \tilde{K}_{\text{spring}} \left[1 + \left(\frac{\tan^2(\psi_o)}{4} \right) \left(\frac{K_\alpha + \tan^2(\psi_o) K_\beta}{K_\alpha - K_\beta} \right) \right] \tag{5.18}$$

The factor inside the brackets depends only on the unstressed pitch angle and the ratio of the elastic energy constants. As discussed in section 4.3, both ψ_o and K_β/K_α should be independent of the ribbon thickness, and thus should be the same for all helices in a given system. Therefore, the spring constant for the clamped end condition will have the same geometric scaling as that for the free end case discussed above. In addition, the following section will show that K_β is approximately equal to zero for the low pitch helices in CDLC (see Equation 5.42), and thus the spring constant for the clamped end boundary condition becomes $\bar{K}^{CDLC}_{\text{spring}} \approx (1.01 \pm 0.04)\tilde{K}^{CDLC}_{\text{spring}}$. Thus, we find that the expected increase in the spring constant when switching to the clamped end condition is at most only about 5% of the free end result and nominally closer to 1%. This increase is far to small to be measured accurately with our current technique, and would thus require a much more sensitive experimental apparatus to observe.

In addition to comparing the effective axial spring constants for the two boundary conditions, we may also compare the scale of the axial force to that of the transverse force ($\bar{J}_\perp$) required to maintain the clamped end constraint (see Figure 3-2). Knowing this relative force scale will be important in guiding the search for new tethers that could potentially satisfy the clamped end condition experimentally. Using the expression derived for the torque given in Equation 3.31, we have that the transverse force may be found from

$$\bar{J}_\perp = -\left(\frac{1}{\Phi_o} \right) \frac{\partial F}{\partial R}|_{R=\bar{R}} \tag{5.19}$$

Unlike in our treatment of the axial spring constant above, however, this force is related to a derivative of the full free energy which is a function of both ℓ and R. Therefore, we will need to determine the full form of $\bar{J}_\perp$ before attempting to expand it about the unstressed axial length.

Plugging the crystalline free energy into Equation 5.19, we find that the transverse force as a function of the inverse axial density is equal to

$$\bar{J}_{\perp}(\nu) = \frac{\bar{\tau}}{\bar{R}} = \frac{wK_s^2}{2g_o^2}\left(\frac{1}{1-\nu^2}\right)\left(\frac{f(\nu)}{1-\nu^2} - g_o\right) \tag{5.20}$$

where $\bar{\tau}$ is the torque exerted by the helix and the parameter g_o is defined as

$$g_o \equiv \frac{f(\psi_o)}{\cos(\psi_o)} = \frac{K_\alpha K_\gamma - K_\beta^2}{\sqrt{(K_\gamma - K_\beta)(K_\alpha - 2K_\beta + K_\gamma)}} \tag{5.21}$$

Despite the fact that the axial length is not the proper conjugate variable to the transverse force, we may still expand $\bar{J}_{\perp}$ about $\ell = \ell_o$ in order to compare it with the magnitude of the axial tension for small extensions. In other words, we may define an effective transverse spring constant such that $\bar{J}_{\perp}(\ell) \approx \bar{K}^{\perp}_{\text{spring}}[\ell - \ell_o]$ exactly as we did for the axial force ($\bar{J}_{\parallel}$) above. Thus, in analogy to Equation 5.8, we may define a transverse spring constant as

$$\bar{K}^{\perp}_{\text{spring}} \equiv \frac{\partial J_{\perp}}{\partial \ell}|_{\ell=\ell_o} \tag{5.22}$$

Substituting our expression for $\bar{J}_{\perp}$ into the definition of the transverse spring constant we find

$$\bar{K}^{\perp}_{\text{spring}} = 2\frac{w}{R_o^2 s}\tan(\psi_o)\Big(K_\alpha + \tan^2(\psi_o)K_\beta\Big) \tag{5.23}$$

Comparing this expression to that for the axial spring constant with free ends (which is what we have actually measured experimentally), we find that the transverse spring constant for this case can be expressed as

$$\bar{K}^{\perp}_{\text{spring}} = \tilde{K}_{\text{spring}}\left[\left(\frac{\tan(\psi_o)}{4}\right)\left(\frac{K_\alpha + \tan^2(\psi_o)K_\beta}{K_\alpha - K_\beta}\right)\right] \tag{5.24}$$

As in our comparison of $\bar{K}_{\text{spring}}$ to $\tilde{K}_{\text{spring}}$, we find that the ratio in Equation 5.24 is independent of the ribbon thickness. For the above expression, we find that the constant inside the brackets is equal to 0.049 ± 0.015 using the ratio of elastic constants given below in Equation 5.42. With this result we see that the transverse force required to maintain the clamped end boundary condition is only about 5% of the measured free end axial tension for small deformations. Thus we predict that new tethers which may be developed to implement this clamped end constraint are not

required to be significantly stronger than the epoxy currently used in our experiments on freely rotating helices.

With the above predictions, we are finally ready to begin analyzing our experimental measurements for the slope of the force curve within the given theoretical framework. In order to determine the typical scale for the stiffness of our helical ribbons we explicitly measured the force–extension relationship for low pitch helices in CDLC using micro-fabricated silicon-nitride cantilevers (see section 2.4 for details). As discussed throughout this work, the free end boundary condition is the one applicable to these experiments, and therefore we will use the expression for $\tilde{K}_{\text{spring}}$ to interpret our data. For the measurements shown in Figure 2-14, the axial spring constant was found to be equal to $(4.80 \pm 0.77) \times 10^{-6}$ N/m. Using the dimensions of the helix for which this data was taken ($s = 803 \pm 3$ μm, $w = 12.3 \pm 0.5$ μm, and $R_o = 19.2 \pm 1.0$ μm) we find from Equation 5.12 that $K_\alpha - K_\beta = (1.5 \pm 0.6) \times 10^{-14}$ Nm. It is important to again note that this value for $K_\alpha - K_\beta$ depends strongly upon the thickness of the ribbon studied, and will therefore be different for different helices within the same system. In particular, the crystalline model predicts a cubic thickness dependence which would translate in to a two (typical) or three (outer bound) order of magnitude range for our current measurements of the ribbon thickness. However, our result does provide a good indication of the typical scale to expect for the elastic constants of low-pitch helices formed in CDLC.

With these results, we have thus completed our analysis of the small tension limit, and will now proceed to examine the case when the axial tension is no longer small enough to approximate by the first term in its Taylor expansion. As we know from our experimental observations (see section 2.5), under larger forces the helices become unstable with respect to a separation into domains of different pitch angle, and so the following section will focus primarily on the explanation of this unique phenomenon.

5.3 Domain Separation in Low-Pitch Helices Under Axial Tension

Section 2.5.1 detailed our experimental observations of the tension induced straightening transition in low-pitch CDLC helices. Figure 2-15 shows a typical sequence in one of these experiments including the domain separated state clearly exhibiting a helical region and a straight region. In section 3.5.1, we have already derived the material conservation rules for a generic two domain separation, which obviously includes this particular mechanical transition. In addition, our predictions for the fraction of the original contour length that will be present in each domain after the transition (Equation 3.50) were found independent of the particular model chosen for the free energy, and may thus be applied directly to this problem. The stability conditions discussed in sections 3.5.2 and 3.5.3, however, depend in detail on the form chosen for $F(R, \ell, s)$. In this section, therefore, we will work out the consequences of applying the two stability conditions to the crystalline model free energy and attempt to fit the predictions to our experimental results. We will first show that the clamped end boundary condition is incapable of satisfying either of the stability constraints, and thus finally eliminate it from consideration in analyzing our data. We will then show that for the free end boundary condition, the stability constraints provide two further relationships between the phenomenological constants in F and experimentally measured quantities. With these additional relationships our model is over specified, and we will show that our predictions are capable of self-consistently explaining the observed mechanical response of low-pitch helices in CDLC. Finally, the question of such a transition in a high-pitch helix will be discussed separately in Appendix E.

For the domain separation under consideration, we note that the two stability conditions (Equations 3.51 and 3.61) have been expressed completely in terms of the axial tension. Thus, in order to analyze this mechanical transition we have only to work out the form of $\tilde{J}_{\|}(\nu)$ and $\bar{J}_{\|}(\nu)$ for the crystalline model. From Equation 3.58, we note that the tension is found by taking the total derivative of the reduced free energy per unit contour length with respect to the variable ν. Switching from the

pitch angle (ψ) to the inverse axial density ($\nu = \ell/s = \sin(\psi)$) in Equations 5.2 and 5.5, the reduced free energy per unit contour length for the free and clamped end boundary conditions are found respectively to be

$$\tilde{\hat{F}}(\nu) = \frac{\tilde{F}(\nu)}{s} = -\frac{wK_s^2}{4}\frac{1}{f(\nu)} \tag{5.25}$$

and

$$\begin{aligned}\hat{\bar{F}}(\nu) &= \frac{\bar{F}(\nu)}{s} \\ &= -\frac{wK_s^2}{4}\frac{1}{f(\nu)}\left[\left(\frac{f(\nu)}{f(\nu_o)}\sqrt{\frac{1-\nu_o^2}{1-\nu^2}}\right)\left(2-\sqrt{\frac{1-\nu_o^2}{1-\nu^2}}\frac{f(\nu)}{f(\nu_o)}\right)\right]\end{aligned} \tag{5.26}$$

where the function $f(\nu)$ is given by

$$f(\nu) \equiv (K_\alpha - 2K_\beta + K_\gamma)\nu^4 - 2(K_\alpha - K_\beta)\nu^2 + K_\alpha \tag{5.27}$$

In this notation, the zero stress inverse axial density $\left(\nu_o = \sin(\psi_o)\right)$ is found from Equation 4.47 to be

$$\nu_o^2 = \frac{K_\alpha - K_\beta}{K_\alpha - 2K_\beta + K_\gamma} \tag{5.28}$$

as expected. Taking the derivatives of $\tilde{\hat{F}}(\nu)$ and $\hat{\bar{F}}(\nu)$, we find that the axial tension for the free and clamped end constraints are given by

$$\tilde{J}_\parallel(\nu) = wK_s^2\nu\left(\frac{(K_\alpha - 2K_\beta + K_\gamma)\nu^2 - (K_\alpha - K_\beta)}{f(\nu)^2}\right) \tag{5.29}$$

and

$$\bar{J}_\parallel(\nu) = \frac{wK_s^2}{2g_o^2}\frac{\nu}{(1-\nu^2)^2}\left(K_\gamma - g_o\sqrt{1-\nu^2} + (K_\alpha - 2K_\beta + K_\gamma)(1-\nu^2)^2\right) \tag{5.30}$$

respectively, where the constant g_o is again given by $f(\psi_o)/\cos(\psi_o)$ (Equation 5.21). Typical plots of these two tensions over the full range $\nu \in [0,1]$ are shown in Figures 5-1(a) and (b). For now, we will delay a discussion of the possible restrictions in the allowed range for ν due to the finite width of realistic ribbons until later in the analysis.

Examining the general shape of the axial tension functions shown in Figure 5-1, we immediately see that the clamped end boundary condition cannot possibly satisfy

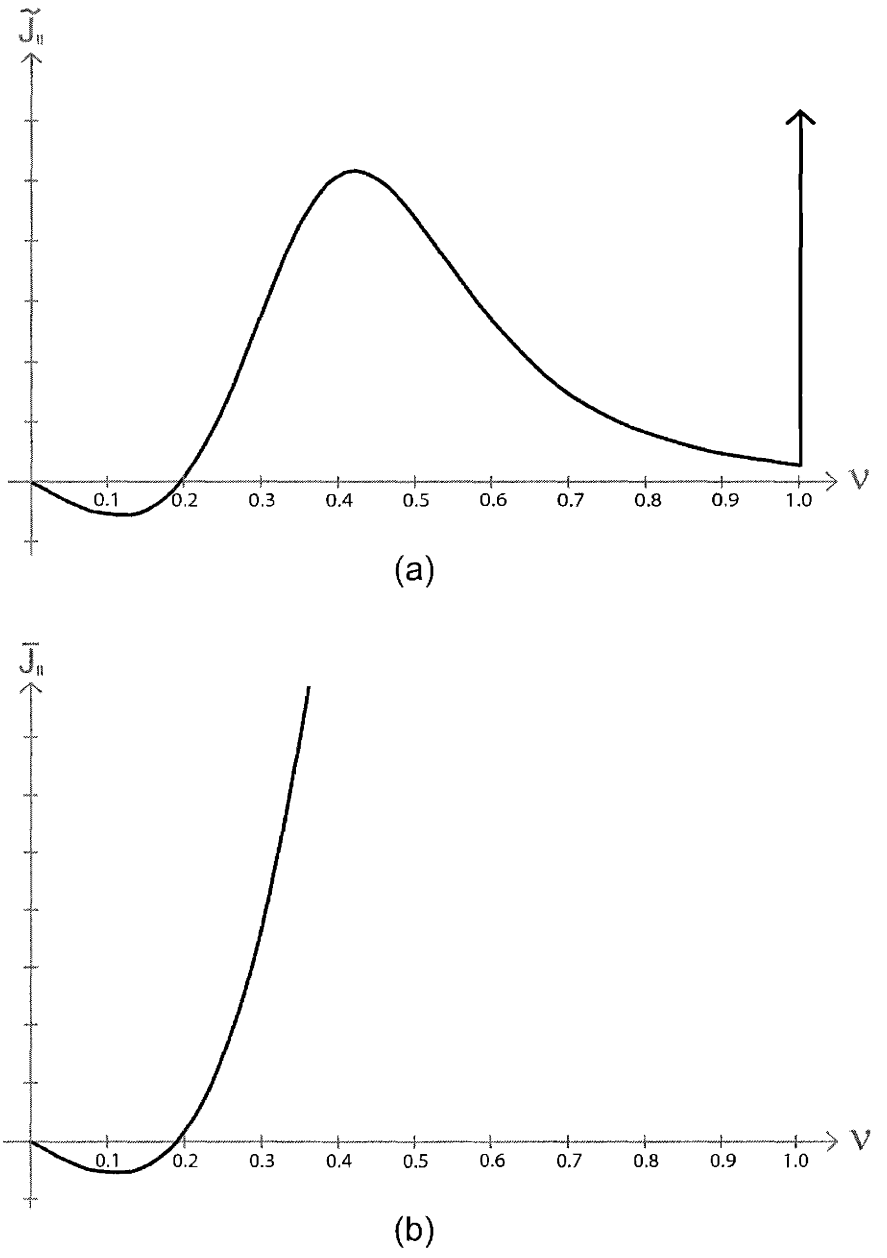

Figure 5-1: A schematic plot of the theoretical tension vs. inverse axial density curves for the case of extension with zero external torque (a) and for the case of extensions with clamped helix ends (b). For consistency, the elastic energy constants used to generate these plots have been set to the ratios calculated later in this section (Equation 5.42) while their overall magnitudes have been left arbitrary. The vertical scale in plots (a) and (b) has been set the same in order to allow for more easy comparison of the shape and relative magnitudes of the two tensions.

either of the equilibrium stability conditions given in Equations 3.61 and 3.52. In order to satisfy the integral equation and/or the condition of equal axial force, the tension must obviously become multi-valued over some range of ν. This condition is equivalent to the requirement that the slope of the tension become negative over some range, which would correspond to a mechanically unstable region. Physically, it is this region of mechanical instability that will drive the experimentally observed domain separation of the helix. Clearly, the tension for the free end boundary condition $\left(\text{Figure 5-1(a)}\right)$ has such an unstable region, however, the tension for the clamped end condition $\left(\text{Figure 5-1(b)}\right)$ is monotonic upon extension, diverging analytically as the pitch angle approaches 90°. This rapid rise in force at higher extensions comes from the fact that as the ribbon approaches a straight configuration (i.e. as ψ approaches 90°), the radius must shrink to zero in order to conserve the original number of helix turns (see Equation 3.9). As the radius shrinks, the local curvature of the helix (and thus the deformation of the ribbon) increases rapidly which makes it more energetically costly to continue the extension. In order to more fully explore this failure of the clamped end condition to allow for domain separation, we varied the ratio of K_β to K_γ used to plot $\bar{J}_\parallel(\nu)$ keeping the ratio K_α/K_γ such that the unstressed pitch angle was fixed at 11°. We found that, as expected, there was no possible value of K_β for which the tension was not single-valued over the complete range of extensions. Thus, as we have claimed throughout the previous three chapters, the theory of extension with clamped helix ends can not explain the type of domain separation we have observed. When combined with our direct observations of the helix rotating about the epoxy tether, this theoretical result strongly justifies our use of the zero torque condition to determine the form of the spontaneous bending force included in the crystalline model (see section 4.3.2).

Turning back to the case of the free end boundary condition, we are now in a position to plug our equation for $\tilde{J}_\parallel(\nu)$ into the equal area stability condition (Equation 3.61). Our goal will be to then fit the predictions of this relationship to our measured value of the pitch angle for the helical domain. From section 3.5.3, we

know that a stable two domain configuration must satisfy

$$\begin{aligned} \int_{\nu_1}^{\nu_2} \tilde{J}_{\|}(\nu')d\nu' &= \tilde{J}_{\|}(\nu_1) \times [\nu_2 - \nu_1] \\ \hat{\tilde{F}}(\nu_2) - \hat{\tilde{F}}(\nu_1) &= \tilde{J}_{\|}(\nu_1) \times [\nu_2 - \nu_1] \end{aligned} \tag{5.31}$$

where $\nu_2 > \nu_1$. For the low-pitch helices in CDLC, we found experimentally that one domain was straight (i.e. $\nu_2^{\text{expt}} = 1$) and that the other domain was helical with a pitch angle of $\psi_1^{\text{expt}} = 16.5 \pm 1.3^{\circ}$ (i.e. $\nu_1^{\text{expt}} = 0.284 \pm 0.022$).

As pointed out previously, $\nu = 1$ is a special point at which the tension curve becomes vertical due to the fact that any additional tension may be applied to a fully straightened helix without further increasing its pitch angle. From Figure 5-1(a), we see immediately that the only value for the inverse axial density of the second domain which will allow the stability conditions to be met is $\nu_2 = 1$, exactly as we found experimentally. It is important to point out here, however, that while the second domain is predicted to be straight (i.e. it will have a pitch angle of 90°), it is not predicted to be flat (i.e. it will not have an infinite radius of curvature). From Equation 5.1, we find that the radius of the straight domain will scale like

$$\frac{\tilde{R}(\psi = 90^{\circ})}{R_{\text{o}}} = \frac{K_\gamma}{f(\psi_{\text{o}})} = \frac{K_\gamma(K_\alpha - 2K_\beta + K_\gamma)}{K_\alpha K_\gamma - K_\beta^2} \tag{5.32}$$

Using the elastic energy constants derived for the low-pitch helices (Equation 5.42), we find that this ratio of radii is equal to 27 ± 12. Thus, the straight domain is predicted to have a radius of curvature which is more than an order of magnitude greater than that of the original helix, but still quite finite (see Figure 4-7(b) for the geometric definition of curvature for a fully extended ribbon).

Until now, we have delayed discussion for the free end constraint of any possible reduction in the allowed range of ν due to the finite width of real ribbons. We must now take up this question in order to guarantee that the condition $\nu_2 = 1$ is, in fact, physically achievable. For the crystalline model, Equation 5.1 for $\tilde{R}$ may be substituted into the edge boundary condition (Equation 3.63) to give

$$\frac{w}{R_{\text{o}}} = 2\pi\tilde{\nu}_{\text{b}}\frac{f(\tilde{\nu}_{\text{b}})}{f(\nu_{\text{o}})} \tag{5.33}$$

where the solutions for $\tilde{\nu}_b$ will be the points at which the edges of adjacent pairs of turns collide and our formalism first breaks down. In the limit of zero width (i.e. $w << R_o$), there is obviously no additional constraint placed upon ν, and it may thus vary over its full range from zero to one as before. On the other hand, substituting the maximum ribbon width ($w_{max} = 2\pi\nu_o R_o$) allowed for the helix into the above expression we have the condition that

$$\nu_o f(\nu_0) = \tilde{\nu}_b f(\tilde{\nu}_b) \tag{5.34}$$

This equation clearly has a lower-bound solution at $\tilde{\nu}_{b,lower} = \nu_o$ guaranteed by the definition of w_{max}. Unfortunately, this relationship cannot be solved analytically to determine if it predicts an upper-bound for the inverse density. It may, however, be examined graphically in a very straightforward manner as follows. Figure 5-2 shows a typical plot of the two sides of Equation 5.34, and the boundaries for ν may simply be read off from wherever the two lines intersect.

From Figure 5-2 it is easy to see that there is no upper-bound on ν, and therefore we are correct in allowing the second domain to be considered fully straight. As in our discussion of $\bar{J}_{\|}(\nu)$, we varied the ratio of elastic energy constants used in the graphical solution to Equation 5.34 to check this result, and found that, indeed, there was never an upper limit to ν for any allowed value of K_β/K_γ. This lack of an upper-bound is in sharp contrast to the case of the clamped end boundary condition worked out in section 3.5.3, which found an upper-bound given by $\bar{\nu}_{b,upper} = \sqrt{1-\nu_o^2}$ independent of the model chosen for the free energy. This difference is due to the fact that in the clamped end case, the constraint that the number of turns remain fixed forces the radius to shrink to zero as ψ goes to 90°, whereas in the free end case we have shown above that the radius remains finite and non-zero when straight allowing the helix to fully open up as it is extended. This "opening up" eliminates the possibility of two turns colliding because as ψ goes to 90° there are no simply turns left in the helix.

Substituting $\nu_2 = 1$ into Equation 5.31 reduces the equilibrium condition to an equation for the single quantity ν_1. However, examining this stability constraint, we

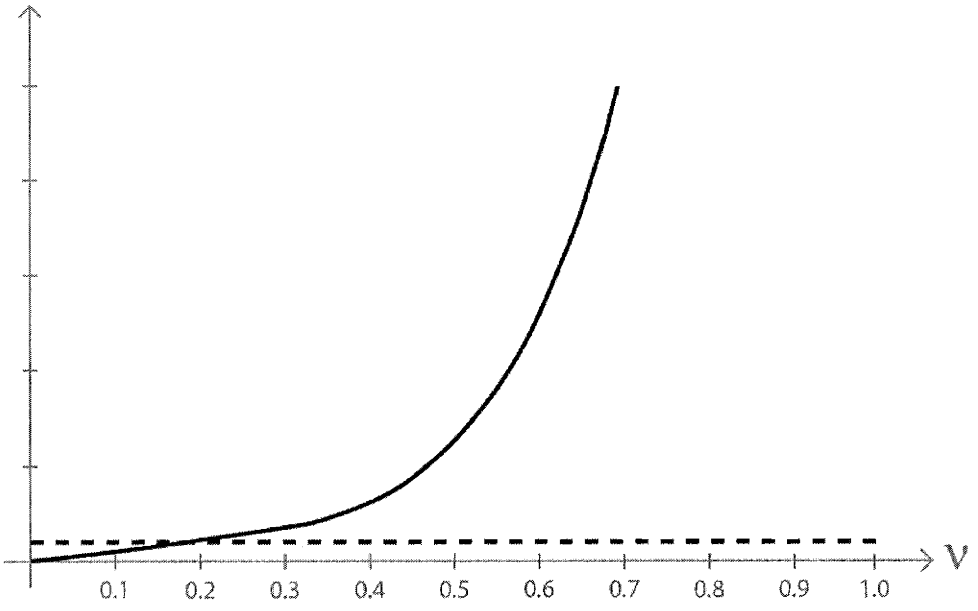

Figure 5-2: A plot of $\nu_o f(\nu_0)$ (dashed line) and of $\nu f(\nu)$ (solid line) over the maximum range $\nu \in [0,1]$. The crossings of these two lines define the realistic boundaries for the inverse axial density given the maximum possible width of a low-pitch helical ribbon. As in Figure 5-1, the elastic energy constants used to generate these plots have been set to the ratios given in Equation 5.42 while leaving their overall magnitudes arbitrary.

find that it is not solvable analytically when viewed as an equation for ν_1 given the free energy parameters. If we instead treat ν_1 as a known constant (which we will define to be $\nu_h = 0.284 \pm 0.022$), we may then re-express the stability constraint as an equation for K_s and the three elastic energy constants. With these substitutions, the equal area construction becomes

$$-\frac{wK_s^2}{4}\left(\frac{1}{K_\gamma} - \frac{1}{f(\nu_h)}\right) = wK_s^2\nu_h\left(\frac{(K_\alpha - 2K_\beta + K_\gamma)\nu_h^2 - (K_\alpha - K_\beta)}{f(\nu_h)^2}\right)[1-\nu_h] \quad (5.35)$$

where we have used Equations 5.25 and 5.29 for $\hat{\tilde{F}}(\nu)$ and $\tilde{J}_{\|}(\nu)$. The first thing that we can note from this expression is that wK_s^2 cancels from both sides leaving an equation involving only the elastic energy constants. Therefore, the implicit thickness

dependence of these constants must necessarily cancel out providing an explanation for the experimental observation that the value of ν_h is independent of the helix radius, width, thickness, or total contour length. From this consideration, it is clear that Equation 5.35 can be written as a function for K_α/K_γ and K_β/K_γ given the measured pitch angle of the helical domain. In addition, we recall that by using the expression for the inverse axial density of an unstressed helix (ν_o in Equation 5.28), the ratio K_α/K_γ may be replaced by

$$\frac{K_\alpha}{K_\gamma} = \frac{\nu_o^2}{1-\nu_o^2} + \left(1 - \frac{\nu_o^2}{1-\nu_o^2}\right)\frac{K_\beta}{K_\gamma} \tag{5.36}$$

With this relationship, we can further reduce the stability condition in Equation 5.35 to the following equation for K_β/K_γ given the measured values of both ν_o and ν_h

$$a_{oh}^2\left(\frac{K_\beta}{K_\gamma}\right)^2 - [a_{oh}(2a_{oh}+1) - b_{oh}]\left(\frac{K_\beta}{K_\gamma}\right) + a_{oh}(a_{oh}+1) - b_{oh} = 0 \tag{5.37}$$

where the experimentally determined parameters a_{oh} and b_{oh} are given by

$$\begin{aligned} a_{oh} &\equiv (2\nu_o^2 - \nu_h^2 - 1)\frac{1-\nu_h^2}{1-\nu_o^2} = -(0.9610 \pm 0.0016) \\ b_{oh} &\equiv 4\nu_h(1-\nu_h)\frac{\nu_o^2 - \nu_h^2}{1-\nu_o^2} = -(0.038 \pm 0.013) \end{aligned} \tag{5.38}$$

respectively. This quadratic equation for K_β/K_γ may be factored analytically to yield the following two solutions

$$\frac{K_\beta}{K_\gamma} = \begin{cases} 1 \\ 1 - \left((b_{oh} - a_{oh})/a_{oh}^2\right) \end{cases} \tag{5.39}$$

The first solution for this ratio can immediately be discounted because, from Equation 5.28, we note that $K_\beta = K_\gamma$ would fix the unstressed pitch angle to 90° for $K_\alpha \neq K_\beta$ or leave it undefined for a fully isotropic ribbon with $K_\alpha = K_\beta$. Thus, we have shown that the stability condition for material exchange may be combined with the expression for the unstressed pitch angle to predict a simple relationship between the measured values of ν_o and ν_h and the single ratio K_β/K_γ.

Since we now have the solution to Equation 5.37 for K_β/K_γ, we may substitute it and the measured value of ν_o into Equation 5.36 to determine the value of the

ratio K_α/K_γ. In addition, we note that the expression for the unstressed helix radius derived in section 4.3.3 (Equation 4.48) can be recast as

$$\frac{K_s}{K_\gamma} = \left(\frac{2}{R_o}\right)\left(\frac{(K_\alpha/K_\gamma) - (K_\beta/K_\gamma)^2}{(K_\alpha/K_\gamma) - 2(K_\beta/K_\gamma) + 1}\right) \tag{5.40}$$

allowing a third ratio of the free energy parameters to be calculated from the known ratios of elastic energy constants and the measured value of the unstressed radius. With these three equations, we can now determine all three ratios of the phenomenological constants in our model free energy from simple measurements of the geometric properties ν_o, ν_h, and R_o. We chose to focus primarily on the ratios because they can be presented in such a way as to cancel out the implicit thickness dependence of the moduli making them common to all low pitch helices in a given quaternary system, whereas the absolute values will vary from helix to helix. The three thickness independent ratios for low-pitch helices in CDLC are thus found to be

$$\begin{aligned} \frac{K_\beta}{K_\gamma} &= 0.000 \pm 0.015 \\ \frac{K_\alpha}{K_\gamma} &= 0.038 \pm 0.012 \\ \frac{K_s R_o}{K_\gamma} &= 0.073 \pm 0.022 \end{aligned} \tag{5.41}$$

These are the ratios of the free energy parameters which we have used throughout the analysis presented in the earlier parts of this chapter. It is interesting to note from these results that the coupling between the two bending modes due to the twisting of the local coordinates (K_β) is very small, and is, in fact, equal to zero within our experimental uncertainty. This interesting prediction may be tested directly in future experiments using an atomic force microscope (see section 2.4.1) which can measure force vs. deflection curves sensitively enough to directly determine K_β/K_γ using a simple experimental setup in analogy to previous works on both organic and inorganic materials [196, 197, 198]. This type of experiment would provide a powerful and fully independent check on the results of our free energy formalism. In addition, we note that in section 4.3.3 we compared our predictions for $\Big((K_\alpha - K_\beta)/(K_\gamma - K_\beta)\Big)$ to the predictions of Chung *et al.* for K_{cc}/K_{pp} [20]. We now see that we were, in

fact, quite correct in making this comparison since for the helices under investigation $\left((K_\alpha - K_\beta)/(K_\gamma - K_\beta)\right) \approx \left(K_\alpha/K_\gamma\right)$ which is the elastic anisotropy in the crystalline model directly analogous to the quantity reported by Chung *et al.*

We have thus shown that by fitting our model free energy to three pieces of experimental data (ν_o, ν_h, and R_o), we may determine all three of the thickness independent ratios of the parameters K_α, K_β, K_γ, and K_s. In addition, the spring constant may be used as a fourth equation to allow the determination of the overall magnitude of the constants for any particular helix, and thus fully characterize its free energy. Using our calculated ratios, and the spring constant for the measurement shown in Figure 2-14, we may finally plot a realistically scaled theoretical prediction for the axial tension curve of a typical low-pitch helix in CDLC, and examine the various features of the equal area construction.

Examining Figure 5-3, we see that under extensions corresponding to ν between points A and B (i.e. for ψ between ψ_o and ψ_h), the helix is stable and will remain in a single configuration no matter what the magnitude of any mechanical fluctuations are. Between points B and C (i.e. between ψ_h and $\psi_{J_{max}}$), however, the helix is metastable with respect to domain separation. The transition may therefore be triggered anywhere along this portion of the extension by the introduction of a macroscopic mechanical perturbation such as shaking the needle attached to the helix (see Figure 2-10). Beyond point C, the helix is mechanically unstable, and will thus separate spontaneously due to the microscopic fluctuations occurring constantly along the ribbon. Given this fact, we will refer to the point C as the limit of metastability. If the experiment is conducted very slowly and smoothly so that no external vibrations cause the transition to occur in the metastable region, the peak value ($\nu_{J_{max}}$) may be determined experimentally. In our experiments on low-pitch helices in CDLC (see section 2.5), we were able to approach the limit of metastability, and found that it was given by $\nu_{J_{max}} = 0.409 \pm 0.029$ which corresponds to a pitch angle of $\psi_{J_{max}} = (24.1 \pm 1.8)°$. Theoretically, this peak value may be found from our model by setting the derivative of $J_\parallel(\nu)$ equal to zero. This condition gives the following cubic

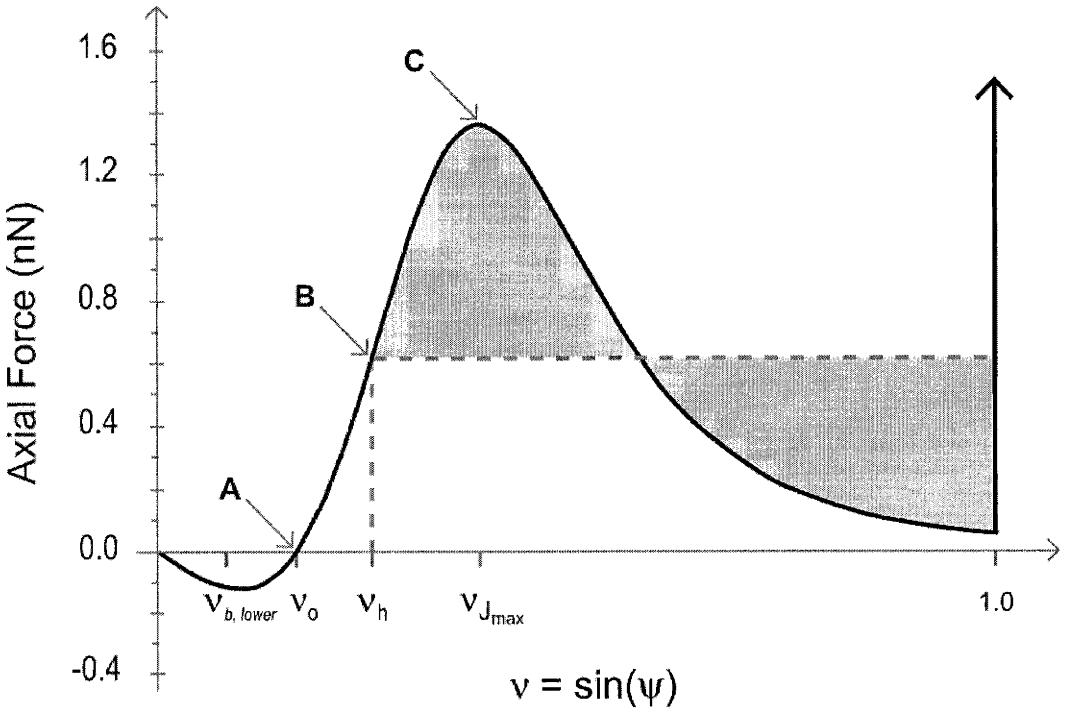

Figure 5-3: A plot of the theoretical tension in nN vs. ν for a particular low pitch helix in CDLC showing the appropriate equal area stability condition. The figure also labels the free equilibrium value of ν (Point A: $\nu_o = 0.19$), the value of the order parameter in the helical phase (Point B: $\nu_h = 0.28$), and the limit of metastability with respect to the straightening transition (Point C: $\nu_{J_{max}} = 0.42$). The lower bound for ν given the finite width of the helical ribbon used to determine $\tilde{K}_{spring}$ ($\nu_{b,lower} = 0.10$) is shown for completeness.

equation for $\nu_{J_{\max}}$

$$5(K_\alpha - 2K_\beta + K_\gamma)^2\left(\nu_{J_{\max}}^2\right)^3 - 9(K_\alpha - K_\beta)(K_\alpha - 2K_\beta + K_\gamma)\left(\nu_{J_{\max}}^2\right)^2$$
$$-3[K_\alpha(K_\alpha - 2K_\beta + K_\gamma) - 2(K_\alpha - K_\beta)^2]\left(\nu_{J_{\max}}^2\right) + K_\alpha(K_\alpha - K_\beta) = 0 \qquad (5.42)$$

Using the ratios given in Equation 5.42, we predict that the limit of metastability is equal to $\nu_{J_{\max}} = 0.418 \pm 0.037$ for our model. This theoretical value is obviously well within the uncertainty of our experimentally determined value, and it is worth noting that our average experimental result is actually slightly lower than the theoretical prediction exactly as one would expect given that we are approaching the metastability limit from below. Thus, we have successfully shown that our model is capable of making self-consistent predictions about the mechanical response of helical ribbons under axial tension.

Until now, we have mainly restricted ourselves to a discussion of what happens upon the extension of a helix under positive axial tension. However, our theoretical formalism is equally valid for compression, and therefore we will conclude this section with a brief discussion of our predictions for the range $\nu < \nu_o$. In particular, from Figure 5-1 we note that the tension for both the free and clamped end constraints reach a minimum upon compression below which the helix would again be in an unstable configuration. For the free end boundary condition, the minimum of the tension occurs at $\tilde{\nu}_{J_{\min}} = 0.112 \pm 0.021$ corresponding to a pitch angle of $\tilde{\psi}_{J_{\min}} = (6.5 \pm 1.2)^\circ$, while for the clamped end constraint, the minimum occurs at $\bar{\nu}_{J_{\min}} = 0.112 \pm 0.020$ $\left(\bar{\psi}_{J_{\min}} = (6.4 \pm 1.1)^\circ\right)$. For both constraints these values are quite close to each other and both are comfortably far from ψ_o to allow for easy experimental measurements in principle. Physically, therefore, this situation is directly analogous to our description of the tension induced straightening transition, and thus raises the possibility of domain separation upon compression. Interestingly, we note that in sharp contrast to the above case in which only the zero torque condition could satisfy the stability conditions, we will find in this case that a transition is predicted to occur upon compression for either the clamped or the free end constraint. Finally, while the following analysis will show that our model predicts that a spontaneous separation

should occur, we will also find several important features of our actual experiments that will tend to inhibit its observation in real helical ribbons.

The first and most important thing to note in our treatment of this case is that the material conservation and domain stability conditions worked out in Chapter 3 are equally applicable to a helix under compression as they were to one under extension. Thus, we may immediately carry over all of the results from our treatment of a general two domain separation, including the Lever Rule (Equation 3.50) and the Maxwell equal-area construction (Equation 3.61), by merely changing our interpretation of the two regions. The first domain, which we will again label as domain 1, will have an inverse axial density that lies on the mechanically stable portion of the tension curve between ν_o and $\tilde{\nu}_{J_{\min}}$ or $\bar{\nu}_{J_{\min}}$ depending upon the desired constraint (see Figure 5-4). This portion of the ribbon, therefore, will be the analog of the helical domain in our treatment of the tension induced straightening transition described above.

Some care, however, must be taken when considering the proper inverse axial density for the second, fully compressed domain (i.e. ν_2 in Figure 5-4). As in our treatment of helix extension where we found that $\nu = 1$ was a special boundary point at which the tension curve becomes vertical (see section 3.5.3), we must now consider what happens when the lower boundary of ν (i.e. $\tilde{\nu}_{\text{b,lower}}$ or $\bar{\nu}_{\text{b,lower}}$) is reached. At this minimum allowed value of ν, the neighboring turns of the helix just touch and begin to subtend one another. Therefore, below this point the magnitude of the applied tension must increase rapidly in order to overcome the added friction of the ribbon rubbing against itself. While we have not measured this rise in frictional force precisely, we have been able to observe that it is significantly larger that the elastic energy normally associated with deforming the helix. Thus, to a good approximation, we may let the tension curve become vertical at this boundary as well. With this realization, we note that we can immediately replace ν_2 in the stability conditions with either $\tilde{\nu}_{\text{b,lower}}$ or $\bar{\nu}_{\text{b,lower}}$ depending upon the constraint imposed on the deformation. Again, this replacement is exactly analogous to our replacement of ν_2 with the value 1 for the case of domain separation under extension. However, with this substitution in the case of compression, we note the second major difference between the two

types of mechanical transitions. On one hand, the transition under positive tension in the absence of torque always yields a straight domain with a pitch angle of 90° and a helical domain with a pitch angle of (16.5 ± 1.3)° regardless of the radius, width, thickness, or length of the original helix. On the other hand, we have now found that the transition predicted upon compression will yield one domain that is a closed tubule and a second domain which is helical with a pitch angle that depends explicitly upon the width and radius of the particular structure chosen through $\tilde{\nu}_{\mathrm{b,lower}}$ or $\bar{\nu}_{\mathrm{b,lower}}$.

From Equation 3.61, we know that the conditions of mechanical stability for this domain separation may be written as

$$\begin{aligned}\hat{\tilde{F}}(\tilde{\nu}_{\mathrm{b,lower}}) - \hat{\tilde{F}}(\tilde{\nu}_1) &= \tilde{J}_{\|}(\tilde{\nu}_1) \times [\tilde{\nu}_{\mathrm{b,lower}} - \tilde{\nu}_1] \\ \hat{\bar{F}}(\bar{\nu}_{\mathrm{b,lower}}) - \hat{\bar{F}}(\bar{\nu}_1) &= \bar{J}_{\|}(\bar{\nu}_1) \times [\bar{\nu}_{\mathrm{b,lower}} - \bar{\nu}_1]\end{aligned} \tag{5.43}$$

where $\hat{\tilde{F}}(\nu)$ and $\tilde{J}_{\|}(\nu)$ are given by Equations 5.25 and 5.29 and $\hat{\bar{F}}(\nu)$ and $\bar{J}_{\|}(\nu)$ are given by Equations 5.26 and 5.30 respectively. Neither of these two equations can be solved analytically for ν_1, but they may easily be solved numerically. In order to do this calculation, however, we must input a specific value for w/R_{o} into the equations for the lower boundary of ν thus making our results valid only for those helices that have that exact width ratio. In order to explore the typical behavior of the helices in CDLC and to give some representative bounds for our predictions, we note that from the data presented in section 2.3.1 (see Figure 2-5) the ratio of the width to the radius for the low pitch helices we are interested in typically lay between 0.15 and 0.65. Plugging these values into Equation 5.33, we find that $\tilde{\nu}_{\mathrm{b,lower}} = 0.0230 \pm 0.0005$ and $\tilde{\nu}_{\mathrm{b,lower}} = 0.1015 \pm 0.0014$ for the free end condition. Repeating this calculation for the clamped end constraint using

$$\bar{\nu}^2_{\mathrm{b,lower}} = \frac{1}{2} - \frac{1}{2}\sqrt{1 - \left(\frac{1-\nu_{\mathrm{o}}^2}{\pi^2}\right)\frac{w^2}{R_{\mathrm{o}}^2}} \tag{5.44}$$

(see Equation 3.66), we find that $\bar{\nu}_{\mathrm{b,lower}} = 0.0234 \pm 0.0002$ for $w/R_{\mathrm{o}} = 0.15$ and $\bar{\nu}_{\mathrm{b,lower}} = 0.1021 \pm 0.0006$ for $w/R_{\mathrm{o}} = 0.65$. Substituting the numerical values of ν_2

for $w/R_o = 0.15$ into the stability condition in Equation 5.43, we find

$$\begin{aligned} \tilde{\nu}_1 &= 0.150 \pm 0.030 \qquad & \tilde{\nu}_2 &= 0.0230 \pm 0.0005 \\ \bar{\nu}_1 &= 0.150 \pm 0.029 \qquad & \bar{\nu}_2 &= 0.0234 \pm 0.0002 \end{aligned} \tag{5.45}$$

for the two constraints. These values for the inverse axial density of the two domains correspond to pitch angles of

$$\begin{aligned} \tilde{\psi}_1 &= (8.6 \pm 1.7)^\circ \qquad & \tilde{\psi}_2 &= (1.318 \pm 0.029)^\circ \\ \bar{\psi}_1 &= (8.6 \pm 1.7)^\circ \qquad & \bar{\psi}_2 &= (1.341 \pm 0.011)^\circ \end{aligned} \tag{5.46}$$

The value of the pitch angle for the helical domain is significantly larger than that of the tubule domain, that it should in principle be possible to resolve the two distinct regions experimentally. Figure 5-4 shows a realistically scaled plot of our theoretical predictions for the axial tension upon compression including the equal-area constructions for a typical low-pitch helix with this small width ratio.

First, examining Figures 5-4(a) and (b), we see that under compressions corresponding to ν between points A and B, the helix is stable for either constraint, and will thus remain in a single configuration no matter what mechanical fluctuations might be introduced. Second, just as in the case of the tension induced straightening transition, we find that between points B and C the helix is, in fact, metastable with respect to domain separation, which may therefore be triggered by a suitably large macroscopic perturbation. However, unlike the previous case, we expect that there will not typically be fluctuations present in real experiments strong enough to trigger domain separation under compression. Thus, we expect that one would routinely be able to compress a helix all the way to point C without having any significant probably of observing a transition. Beyond point C, the helix again becomes mechanically unstable, and must therefore separate spontaneously due to the microscopic fluctuations occurring constantly along the ribbon. Given this fact, we will again refer to the point C as the limit of metastability. Finally, as described above, once the helix reaches equilibrium after the transition occurs, it will consist of a helical domain corresponding to point B and a tubule domain corresponding to point D.

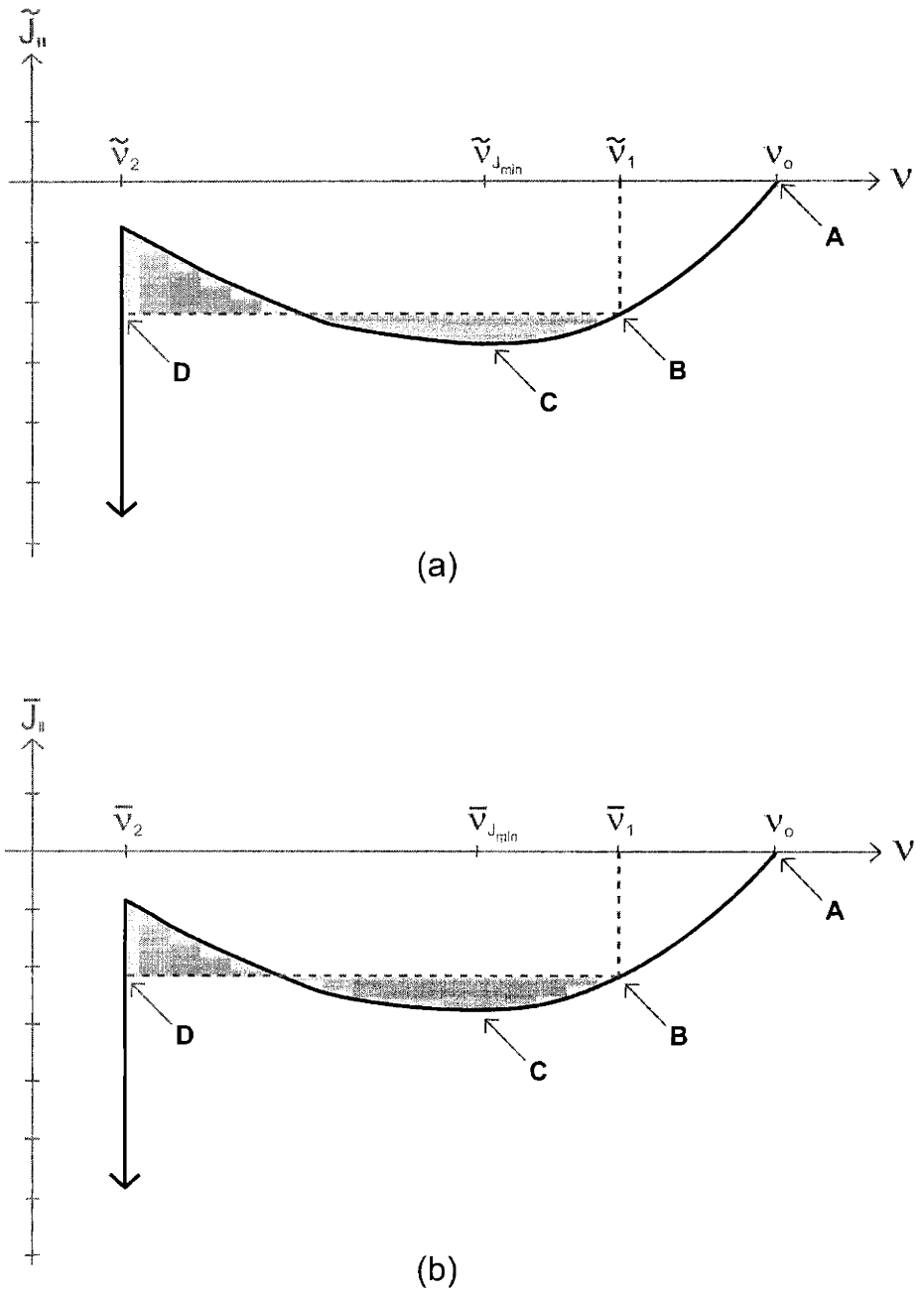

Figure 5-4: A plot of the theoretical tension in nN vs. ν for a typical low pitch helix in CDLC with $w/R_o = 0.15$ showing the appropriate equal area stability condition upon compression for the free (a) and clamped (b) end constraints. The figure also labels the unstressed equilibrium value of ν (Point A: $\nu_o = 0.191$), the value of the order parameter in the helical phase (Point B: $\tilde{\nu}_1 = 0.150$ / $\bar{\nu}_1 = 0.150$), the limit of metastability (Point C: $\tilde{\nu}_{J_{min}} = 0.112$ / $\bar{\nu}_{J_{min}} = 0.112$), and the lower boundary of ν at which point the helix closes up into a tubule (Point D: $\tilde{\nu}_2 = 0.0230$ / $\bar{\nu}_2 = 0.0234$).

Returning to the analysis for the larger width ratio ($w/R_o = 0.65$), however, we note right away that the value calculated for the lower bound of ν at which point the helix forms a closed tubule lies within the uncertainty of our determination for the minimum of the tension. Physically, if $\tilde{\nu}_{J_{min}}$ (or $\bar{\nu}_{J_{min}}$) is less than $\tilde{\nu}_{b,lower}$ (or $\bar{\nu}_{b,lower}$) then the helix will be able to fully close up into a tubule while still in a stable configuration, and thus preempt the onset of any type of spontaneous domain separation. With this realization, we must take into account that beyond $\tilde{\nu}_1 = \tilde{\nu}_2 = \tilde{\nu}_{J_{min}} = 0.1025$ (or $\bar{\nu}_1 = \bar{\nu}_2 = \bar{\nu}_{J_{min}} = 0.1024$), the transition will simply cease to occur. Finally, incorporating these considerations we find from the solutions to the stability conditions in Equation 5.43 that

$$\begin{aligned} \tilde{\nu}_1 &= 0.118 + 0.030 - 0.016 & \tilde{\nu}_2 &= 0.1015 + 0.0010 - 0.0014 \\ \bar{\nu}_1 &= 0.116 + 0.030 - 0.014 & \bar{\nu}_2 &= 0.1021 + 0.0003 - 0.0007 \end{aligned} \tag{5.47}$$

for $w/R_o = 0.65$. This discussion brings up the first of the two major practical limitations that will tend to inhibit the observation of domain separation in real helices. As the ratio of the ribbon width to the helix radius increases, the separation between the pitch angles of the two domains shrinks rapidly, disappearing entirely at a value of $w/R_o = 0.72 \pm 0.14$ for the free end constraint and $w/R_o = 0.71 \pm 0.13$ for the clamped end case. For widths above these values, domain separation can no longer occur since the unstable region of ν ceases to be physically accessible. In addition, for widths close to but below these cutoff values, the pitch angles of the helical and tubule domains are predicted to lay so close together that the inherent experimental uncertainty in determining ψ will completely washout our ability to distinguish whether one or two domains are actually present. While this limitation does severely restrict the allowed geometry of helices that can be used to look for this transition, we note from Figure 2-5 that this is not a fatal concern given that we typically have many helices with sufficiently narrow widths and large radii to allow for a clear separation of the two domains.

The larger practical concern, however, that will tend to further inhibit our ability to observe this type of transition is the fact that a helix will naturally start to buckle

under compression. This type of bending mode is not possible under extension, and thus we were correct in considering only deformations along the symmetry axis for positive tensions. For the case of negative tensions, however, the lowest energy deformation of long slender helices will, in general, consist of both an axial compression and a bowing of the entire helix beyond some critical loading force. This buckling of helical springs is directly analogous to the buckling of cylindrical elastic rods [194], and thus depends in detail upon the boundary conditions imposed on the attachment of the ends as well as on the precise cross section of the ribbon. In general, however, it is found that for springs with 2 or more turns, the critical buckling force (or equivalently the critical buckling compression) decreases rapidly as the slenderness ratio of the helix (ℓ_o/R_o) increases [199, 200, 201]. Because our mechanical treatment of the helix has thus far ignored any potential effects due to the finite size of real structures, we have implicitly been working in what could be called the "infinite helix" limit. This limit, where we let ℓ and s become large keeping ψ_o fixed, is directly analogous to the thermodynamic limit in the treatment of traditional phase transitions [202]. In practice, this requirement means that we must select a helix with a large enough number of turns that we can safely ignore the edges and focus only on the bulk of the ribbon. Unfortunately, this requirement also guarantees that we will be working with helices that are more prone to buckling. In order to try and quantify this consideration, we note that the slenderness ratio of our structures may be expressed simply as a function of the number of helix turns (n) and the pitch angle (ψ). From Equation 3.9 we find that

$$\frac{\ell_o}{R_o} = 2\pi n \tan(\psi_o) \tag{5.48}$$

For typical low-pitch helices with seven or eight turns, this ratio works out to 8.6 ± 1.6 and 9.8 ± 1.8 respectively. While we do not have a precise theoretical treatment of buckling appropriate for our particular springs, comparing this number to those used in calculations for rod-like helices with fixed ends [200] as well as to our experimental observations in CDLC, we expect that for such long helices buckling will begin to seriously effect the helix deformation long before it can close up into a tubule, and quite likely before the limit of metastability ($\nu_{J_{\min}}$) is reached. For example, the

figure below shows a long ($n = 11$) low-pitch helix in CDLC under extension and compression. It is clear from the pitcure that the onset of buckling has already occured even at these small levels of compression.

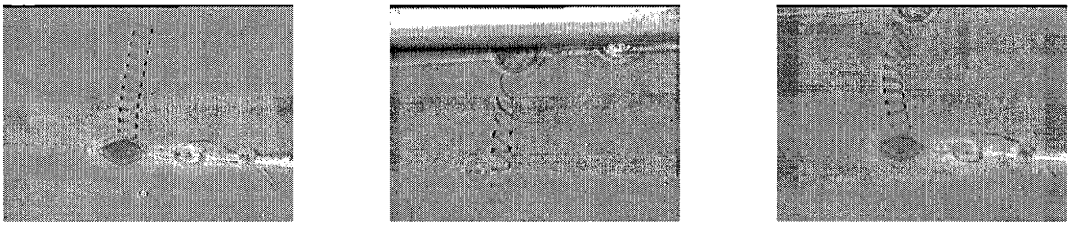

(a) (b) (c)

Figure 5-5: (a) A particularly long ($\ell = 243.8 \pm 3$ μm) and narrow ($R_o = 21.21 \pm 0.37$) low pitch helix free from stress and (b) extended by a positive axial tension. (c) The same helix under a very small compressive force clearly showing the onset of buckling.

With these results, we have completed our analysis of the response of low-pitch helical ribbons to large axial stresses. We have demonstrated that the clamped end boundary condition is incapable of supporting a stable two domain separation upon extension while the free end constraint can provide a self-consistent interpretation of the observed tension induced straightening transition. In doing so, we have determined the three thickness independent ratios of the free energy parameters common to all low-pitch helices in CDLC as well as their absolute scale for a particular helix. This determination allowed us to fully characterize our model free energy, and thus to plot a properly scaled tension curve over the full range of the inverse axial density. In addition, our characterization of the free energy has allowed us to make predictions about the possible onset of a new type of domain separation upon compression for either the clamped or free end constraints, as well as to make predictions about the likely experimental limitations to observing such as transition.

In the following section, we will turn to a consideration of winding and unwinding in the absence of an axial tension (Case 4 from section 3.4.4) and, using the results from this analysis, we will again be able to make specific and quantitative predictions

about the expected response of a low-pitch CDLC helix under this type of stress.

5.4 Predictions for Low-Pitch Helices Under Torque

The true test of any theory is its predictive capabilities. In the last section, we showed that our crystalline model is capable of accurately predicting the limit of metastability given the measured values of the pitch angle of the unstressed helix and of the helical domain after the straightening transition occurs. As discussed in section 3.4.4, we expect that as new non-slipping tethers are developed, it will become experimentally possible to apply an external torque to a helix in the absence of axial tension. In this section, we will therefore examine the three main predictions of our model for a low-pitch helix in CDLC subject to this type of force. First, we will examine the theoretical dependence of the radius on the pitch angle upon such a winding or unwinding. Second, we will work out the form of the torque (τ) and the transverse force ($J_\perp = \tau/R$) both as functions of the proper conjugate variable Φ, as well as of the more convenient variable ψ. By comparing these forces to the tension applied in our measurement of the effective axial spring constant (see section 5.2), we will be able to predict what level of force would be required to wind or unwind a typical low-pitch helix. Third, we will show that the torque is such that a helix cannot sustain a stable domain separated state at non-zero stress, and thus that it will remain in a continuous configuration throughout the full range of allowed deformations. We will conclude this section with a brief comparison of the results predicted by the crystalline model with those that would be expected from the constant tilt chiral model of Chung *et al.* As with our results for the fractional change in radius versus pitch angle under tension (see section 4.3.2), the predictions of these two models will be quite distinct, and therefore, performing such experiments would provide important positive checks on our formalism and on our choice for the form of the model free energy.

From section 3.4.4, we know that the constraint of zero axial tension upon winding and unwinding allows us to determine a relationship between the radius and the axial and contour lengths $\Big(\text{i.e. } R = R^\star(\ell,\, s)\Big)$ through the partial derivatives of $F(R, \ell, s)$.

Plugging the crystalline model free energy into the definition of $R^\star$ (Equation 3.39) we find that the helix radius for this case is given by

$$\begin{aligned} R^\star(\psi) &= \frac{1}{K_s}\left(2f(\psi) + \frac{1}{\tan(\psi)}\frac{df}{d\psi}\right) \\ &= \frac{2}{K_s}\left(K_\gamma - (K_\alpha - 2K_\beta + K_\gamma)\cos^4(\psi)\right) \end{aligned} \tag{5.49}$$

Despite the complexity of the constraint in general, the resulting functional form of the relationship for $R^\star$ in the crystalline model turns out to be quite simple. A plot of $R^\star(\psi)/R_o$ (where $R_o = (2/K_s)f(\psi_o)$ from Equation 4.48) is shown in Figure 5-6.

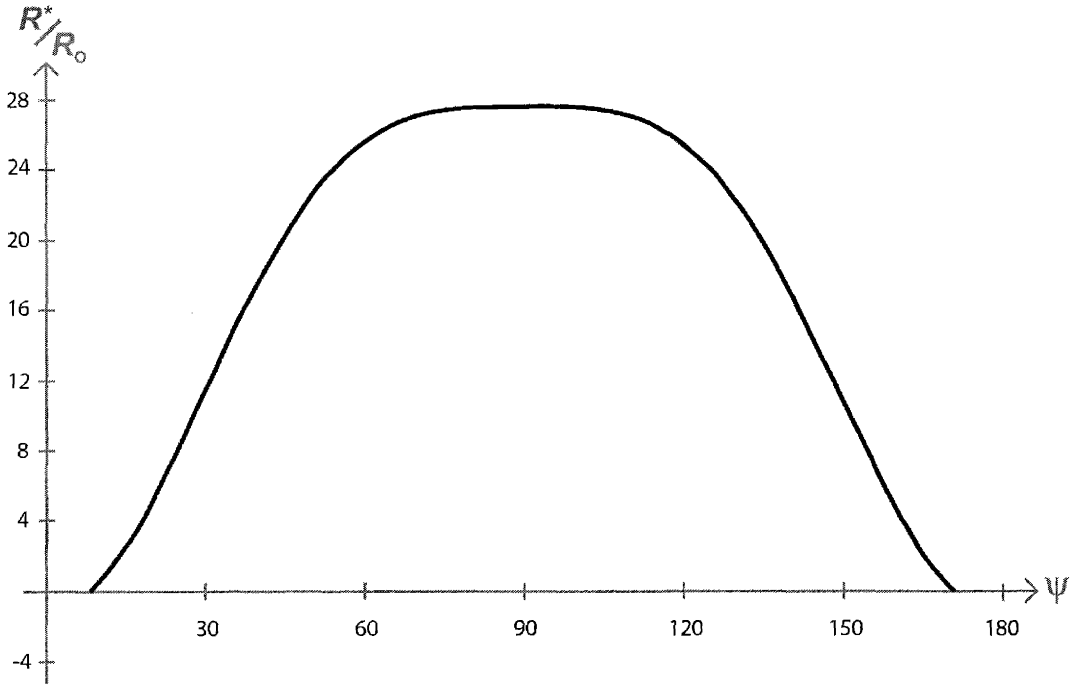

Figure 5-6: A plot of the theoretical ratio of the helix radius ($R^\star$) upon the application of a pure torque to the unstressed equilibrium radius (R_o) using the ratios of the elastic energy constants given in Equation 5.42. As already discussed, the pitch angle of the helix may go beyond 90° for this type of deformation, and therefore we must examine the function over the full range of ψ from 0° to 180°.

There are four important features of the radii ratio plotted in Figure 5-6 that require discussion. First, and most importantly, we note that the radius is symmetric about 90°. This fact implies that, barring domain separation, we predict a smooth

transition from a right-handed helix ($\psi \in [0^\circ, 90^\circ]$, $R > 0$) to an equivalent left-handed helix ($\psi \in [90^\circ, 180^\circ]$, $R > 0$) upon unwinding. This is exactly the behavior we would expect because (as discussed in section 4.3.3) the crystalline model with an isotropic spontaneous curvature does not distinguish energetically between left and right-handed helices.

Second, we note from Figure 5-6 that the radius shrinks to zero at two points (one upon winding a right-handed helix and the other upon winding a left-handed helix). At these two points, the helix collapses to an infinite curvature state, and thus they represent symmetric lower and upper cutoffs for the physically achievable range of the pitch angle. Neglecting the ribbon width for now, we find from Equation 5.49 that the intrinsic cutoff values of ψ (i.e. the values for the pitch angle where $R^\star = 0$) are given by

$$\cos^4(\psi_c) = \frac{K_\gamma}{K_\alpha - 2K_\beta + K_\gamma} \tag{5.50}$$

Substituting our values for the ratios of the elastic energy constants into this expression, we predict that the helix radius will shrink to zero at $\psi_{c,lower} = (7.8 \pm 2.4)^\circ$ and $\psi_{c,upper} = 180 - \psi_{c,lower} = (172.2 \pm 2.4)^\circ$. Turning back to the more realistic case of non-zero width, we know from Equation 3.62 that the actual physical boundaries of ψ are given by

$$\frac{w}{R_o} = 2\pi \sin(\psi_b)\Big(K_\gamma - (K_\alpha - 2K_\beta + K_\gamma)\cos^4(\psi_b)\Big)\frac{K_\alpha - 2K_\beta + K_\gamma}{K_\alpha K_\gamma - K_\beta^2} \tag{5.51}$$

As for the case of extension with free helix ends, this expression can only be solved graphically. Increasing w from zero to the maximum allowed width ($w_{max} = 2\pi\nu_o R_o$), we find that the lower-bound on the pitch angle ($\psi_{b,lower}$) is restricted to lay between $\psi_{c,lower} = (7.8 \pm 2.4)^\circ$ and $\psi_o = (11 \pm 2)^\circ$ while the upper-bound ($\psi_{b,upper}$) falls within the symmetric region between $(169 \pm 2)^\circ$ and $(172.2 \pm 2.4)^\circ$.

Third, we note from the figure that the helix radius remains finite upon achieving a straight configuration (see Figure 4-7). At $\psi = 90^\circ$, Equation 5.49 gives us that

$$\frac{R^\star(\psi = 90^\circ)}{R_o} = \frac{K_\gamma}{f(\psi_o)} = \frac{K_\gamma(K_\alpha - 2K_\beta + K_\gamma)}{K_\alpha K_\gamma - K_\beta^2} \tag{5.52}$$

Interestingly, this result is exactly the same expression as we derived for $\Big(\tilde{R}(\psi =$

$90°)/R_o\Big)$ in the case of extension under a pure axial tension (Equation 5.32). We thus predict the ratio of the straight to unstressed radii to again be 27 ± 12 for the pure torque case. This ratio, while finite, is still large enough that quantifying the non-zero nature of the ribbon curvature would be difficult in the types of experiments currently envisioned.

Fourth, and finally, we can predict the slope of the fractional change in helix radius versus pitch angle for small deformations. Expanding $R^\star(\psi)$ around the unstressed equilibrium pitch angle ψ_o to first order we have

$$R^\star(\psi) = R_o + \frac{dR^\star}{d\psi}|_{\psi=\psi_o}\, \Delta\psi \tag{5.53}$$

where $\Delta\psi \equiv \psi - \psi_o$. Taking the desired derivative, and solving for the fractional change in radius we find

$$\frac{R^\star(\psi) - R_o}{R_o} = \left(\frac{4(K_\gamma - K_\beta)^2}{K_\alpha K_\gamma - K_\beta^2} \sqrt{\frac{K_\alpha - K_\beta}{K_\gamma - K_\beta}} \right) \Delta\psi \tag{5.54}$$

Plugging our values for the elastic energy constants into this expression, we predict a slope for the fractional change in radius versus the change in ψ of 20.5 ± 5.2 for the low-pitch CDLC helices. Our model therefore predicts a very rapid, and thus easily observable, change in the helix radius for very small changes in the pitch angle. This strong dependence is not surprising in light of the fact that we have already shown above that the radius must shrink to zero as the pitch angle changes over the relatively small amount from 11° (0.192 radians) to 7.8° (0.136 radians).

Now that we have explored in detail the expected form of the radius ($R^\star$) under this constraint, we will turn to a consideration of the torque required to wind and unwind the helix. Until this point, we have expressed our various predictions only in terms of the pitch angle ψ, however, throughout the coming analysis we will also be interested in expressing our predictions in terms of the azimuthal angle Φ. This second variable is important both because it is the theoretically correct conjugate to the torque, and because experimentally it is the variable most easy to control. From the definition of Φ given in Equation 3.8, we have that

$$\Phi^\star(\psi) = \frac{sK_s}{2}\left(\frac{\cos(\psi)}{K_\gamma - (K_\alpha - 2K_\beta + K_\gamma)\cos^4(\psi)}\right) \tag{5.55}$$

Unfortunately, the azimuthal angle (unlike the pitch angle) is extensive in the ribbon contour length, and therefore we will typically choose to focus instead on the intensive ratio $\Phi^\star/\Phi_o$. Figure 5-7 shows a plot of our prediction for the form of the azimuthal angle as a function of ψ.

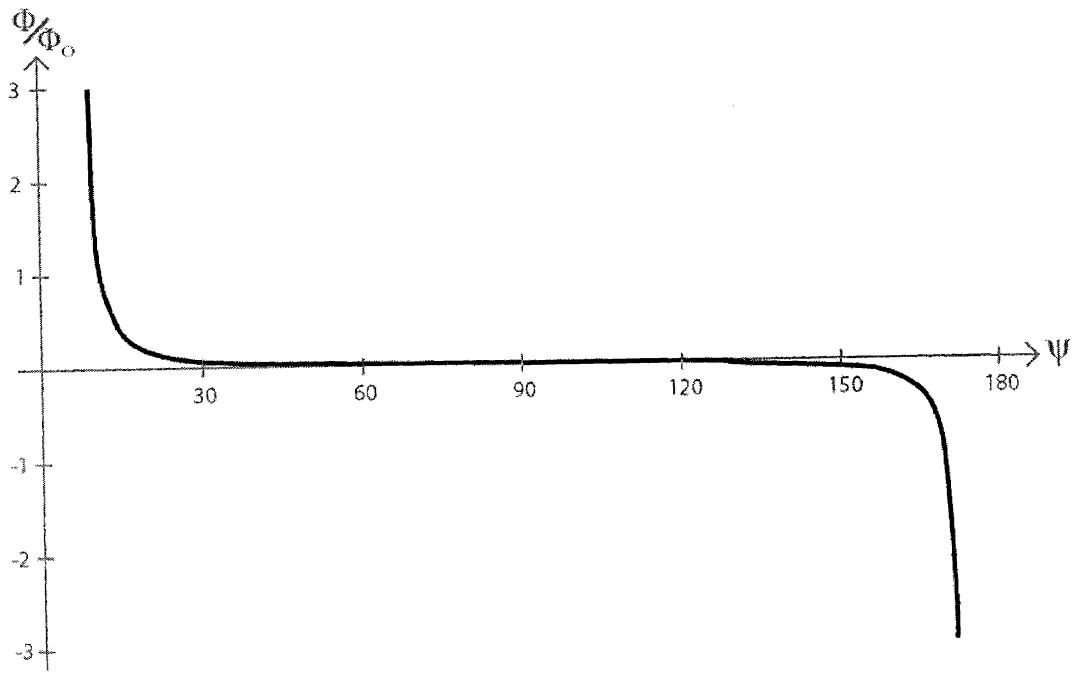

Figure 5-7: A plot of the predicted ratio of the azimuthal angle under a pure torque ($\Phi^\star$) to its unstressed value (Φ_o) for low-pitch helices in CDLC. For generality, the curve is shown over the full range of the pitch angle running from $\psi_{c,lower} = (7.8 \pm 2.4)^\circ$ to $\psi_{c,upper}) = (172.2 \pm 2.4)^\circ$.

As expected from its definition, Φ diverges at the upper and lower cutoff values of ψ where the radius vanishes, and varies smoothly in between passing through zero at 90°. In addition, because the radius is symmetric and the cosine is anti-symmetric about 90°, the azimuthal angle must also be anti-symmetric, as is clear from the figure. While this relationship for $\Phi^\star$ in terms of ψ cannot be inverted analytically, it can be inverted numerically. With this expression, therefore, any result we find in terms of the pitch angle may immediately be transformed via Equation 5.55 into one in terms of the azimuthal angle instead.

From Equation 3.13, we find that the equilibrium torque exerted by the helix can be found from

$$sw\left(-2\frac{f(\psi)}{(R^\star)^3}+\frac{K_s}{(R^\star)^2}\right)=-\Phi^\star\frac{\tau^\star}{R^\star} \tag{5.56}$$

Substituting our expression for the radius (Equation 5.49) into the above equation, we find that the torque is given by

$$\tau^\star(\psi)=2wK_s\cos(\psi)\,\frac{(K_\alpha-2K_\beta+K_\gamma)\cos(\psi)^2-(K_\gamma-K_\beta)}{K_\gamma-(K_\alpha-2K_\beta+K_\gamma)\cos^4(\psi)} \tag{5.57}$$

In order to more easily compare this result with the tension measured under axial extension, we will also convert the torque into the associated transverse force as follows (see Figure 3-2)

$$J_\perp^\star(\psi)=\frac{\tau^\star}{R^\star}=wK_s^2\cos(\psi)\,\frac{(K_\alpha-2K_\beta+K_\gamma)\cos(\psi)^2-(K_\gamma-K_\beta)}{(K_\gamma-(K_\alpha-2K_\beta+K_\gamma)\cos^4(\psi))^2} \tag{5.58}$$

As with all of the forces considered in this work, the magnitude of these functions depend in detail upon the geometry of the helix under investigation, while their shape and general topological features depend only on the thickness independent ratios of the elastic energy constants. Figure 5-8 shows the predicted graphs of $\tau^\star$ and $J_\perp^\star$ versus the azimuthal angle Φ for winding and unwinding. The ratios of the free energy parameters used in these plots have been set to those given in Equation 5.42, and we have used our measurement of the effective axial spring constant to give the proper order of magnitude we would expect to see for typical low-pitch helices.

Now that we have a graph of the torque versus azimuthal angle, we may examine whether or not it predicts that a stable domain separated state is possible. In section 3.5.5, we were able to formulate the stability conditions for this constraint as an integral equation for the torque over the azimuthal angle density (see Equation 3.78). Since we would be holding the total contour length fixed in these experiments, we note that the azimuthal angle density ($\Omega=\Phi/s$) differs from the ratio $\Phi^\star/\Phi_o$ only by a constant multiplicative factor ($s/\Phi_o=R_o/\cos(\psi_o)$) which will not affect any of our following conclusions. Thus, despite the fact that we do not have an analytic expression for the torque or for the reduced free energy in terms of Ω, we may perform the required stability analysis graphically from Figure 5-8(b). Examining the plot,

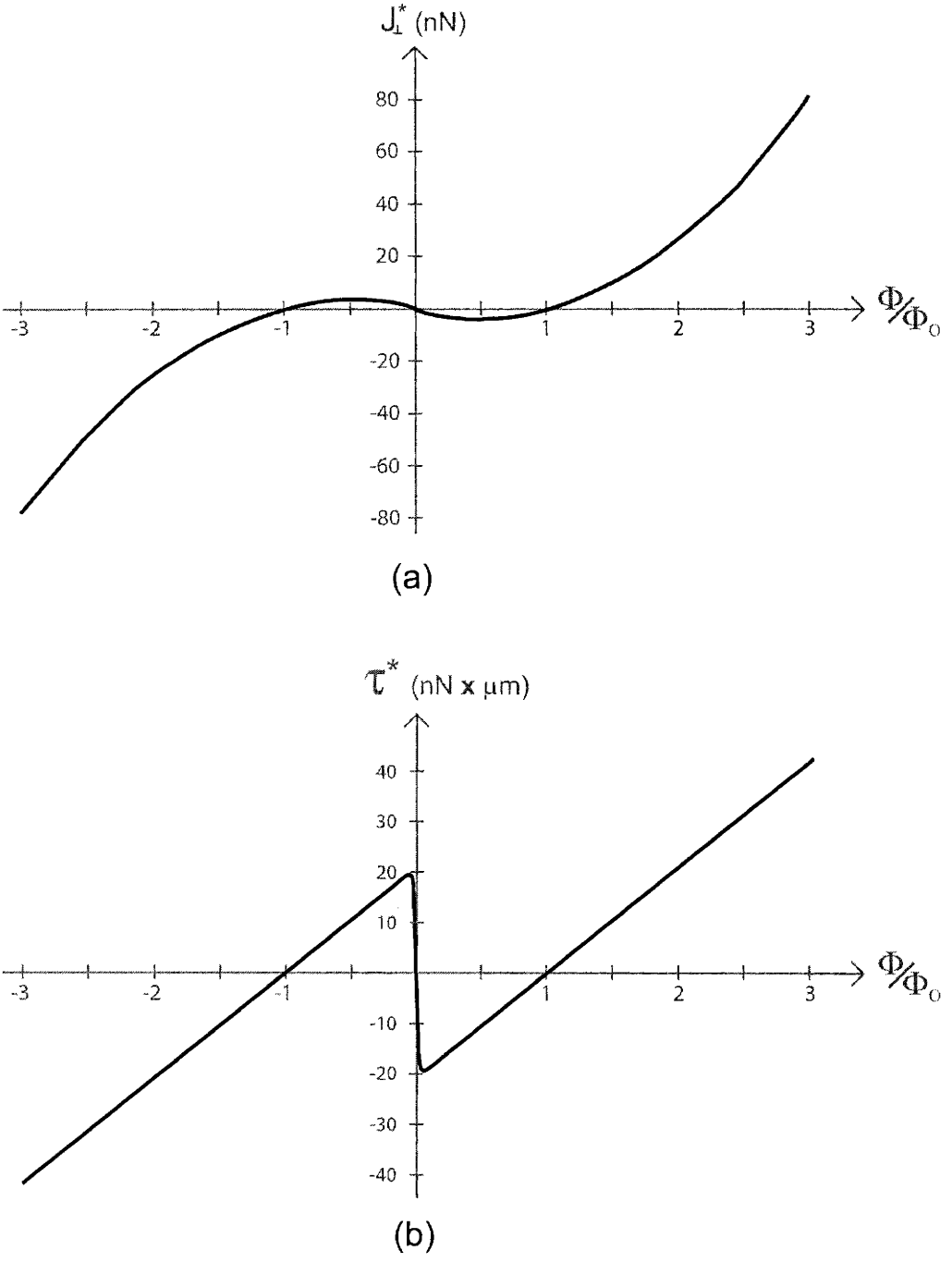

Figure 5-8: A plot of the properly scaled theoretical predictions for the transverse force in nN (a) and the helix torque in nN $\times$ μm (b) vs. the azimuthal angle for the typical low-pitch helix used to measure $\tilde{K}_{\text{spring}}$. As noted above, the range of Φ is unbounded, and thus we have chosen to cut it off at a reasonable value in order to allow the more interesting features of the curves around the straight configuration to be seen more clearly.

we see immediately that because the torque is anti-symmetric about $\Phi = 0$, the equal area condition can only be met at zero torque. This result represents something very different than our solution to the equal area construction for the case of finite axial tension (as described in section 5.3). In this case, the zero torque solution indicates nothing more than the fact that in our achiral model, the left and right-handed equilibrium states are equivalent minima in the free energy. In practice, however, there is no way to create a bistable or perverted helix (i.e. a helix with both a right and left-handed domain at zero external torque) [203, 204] with the type of experiment currently envisioned, because the helix is required to remain in a single continuous configuration for all non-zero torque. Thus, the crystalline model predicts that upon the application of a pure torque, a low-pitch helix in CDLC will unwind uniformly and transform smoothly from right to left-handed without experiencing any type of instability or spontaneous domain separation.

Finally, as we have noted above, many of our predictions for the behavior of a helix under a pure torque depend strongly upon the fact that our model free energy is left-right symmetric. It will be interesting therefore to compare our results with those that would be expected from the chiral models discussed in Chapter 4 that explicitly break this symmetry. For simplicity in performing the calculations and interpreting the results, we will choose to analyze the constant tilt model of Chung *et al.*, and merely note that the effective elastic constants may be renormalized by a spatial modulation in the director field [20, 44]. From Equations 4.10 and 4.11, we already have two relationships for the free energy parameters in this model. Without going into the details of the analysis, a treatment of the tension induced straightening transition similar to that in section 5.3 is possible for this model and leads to a third equation for the elastic constants. Solving the three equations given the experimentally determined geometric parameters ν_o, ν_h, and R_o, we find that the thickness independent ratios of the elastic constants for the model of Chung *et al.* are given by

$$\begin{aligned} \frac{K_{cp}}{K_{pp}} &= 0.140 \pm 0.028 \\ \frac{K_{cc}}{K_{pp}} &= 0.00147 \pm 0.00013 \end{aligned} \tag{5.59}$$

$$\frac{K^* R_o}{K_{pp}} = 0.070 \pm 0.012$$

As with the results of the crystalline model, these ratios predict a limit of metastability that is consistent with our experimental measurement of $\nu_{J_{max}} = 0.41 \pm 0.04$, and thus both models may be made formally consistent with the geometry of an unstressed helix as well as with the observed domain separation phenomenon (although there are still many important inconsistencies in chiral model as discussed in section 4.2.3).

Turning back to the case of a helix under a pure torque, if we use the free energy of Chung *et al.* (Equation 4.9) to determine the radius and associated azimuthal angle as a function of ψ we find

$$R^\star_{\mathrm{Ch}}(\psi) = \frac{1}{K^*}\frac{\tan(\psi)}{\cos^2(\psi)}\Big(K_{pp} - (K_{cc} - 2K_{cp} + K_{pp})\cos^4(\psi)\Big) \tag{5.60}$$

and

$$\Phi^\star_{\mathrm{Ch}}(\psi) = sK^*\frac{\cos^4(\psi)}{\sin(\psi)}\left(\frac{1}{K_{pp} - (K_{cc} - 2K_{cp} + K_{pp})\cos^4(\psi)}\right) \tag{5.61}$$

respectively. Figure 5-9 shows a plot of both $R^\star_{\mathrm{Ch}}/R_o$ and $\Phi^\star_{\mathrm{Ch}}/\Phi_o$ over the full range of $\psi \in [0°, 180°]$ using the values for the elastic constants given in Equation 5.60.

These graphs of the predictions for the chiral model show unmistakably different behavior than do those in Figures 5-6 and 5-7 for the crystalline model. First, we see that $\Phi^\star$ is now symmetric about $\psi = 90°$ while the radius is anti-symmetric as required by the linear form of the chiral bending term in the free energy. A negative radius, while seemingly unphysical at first glance, actually translates simply into a left-handed helix for $\psi \in [0°,90°]$ and a right-handed helix for $\psi \in [90°,180°]$. In fact, this property of the radius was built into the chiral model originally to guarantee that no left-handed solutions were allowed in the absence of stress (see section 4.2.2), and thus it is not too surprising that there are none allowed under the application of a pure torque. This prediction thus provides a completely unambiguous test to distinguish between the physics of the chiral and achiral models. In other words, if the helix reverses handedness upon unwinding, then the chiral models (either molecular or collective) can be conclusively excluded from consideration. Second, from Figure 5-9(a) we see that there are no intrinsic cutoff values for the pitch angle (neglecting

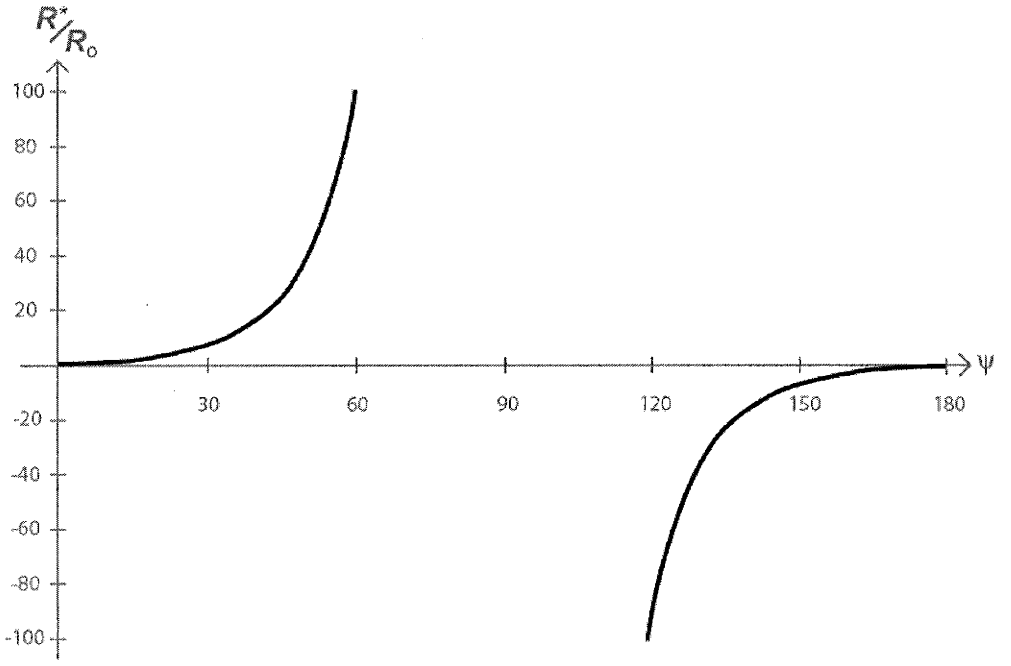

(a)

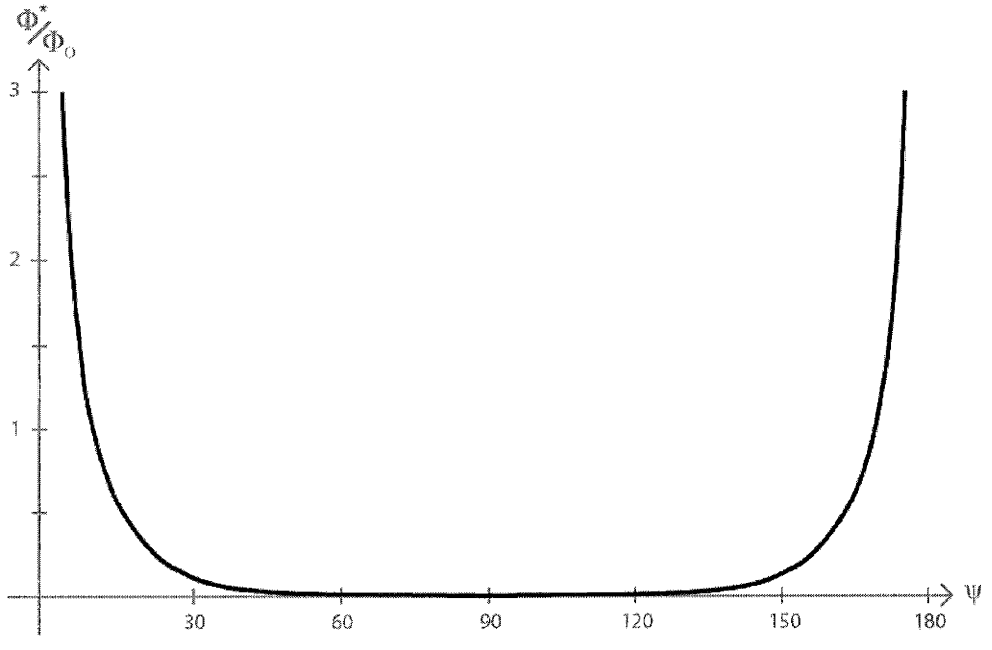

(b)

Figure 5-9: A plot of the theoretically predicted ratios of the stressed to unstressed radii ($R^{\star}/R_{o}$) (a) and of the azimuthal angle under a pure torque ($\Phi^{\star}$) to its unstressed value (Φ_{o}) (b) using the free energy model of Chung *et al.* In this case we find that there are no lower or upper cutoff values for the allowed range of ψ so the full range from 0° to 180° is shown.

finite width effects), and that the radius is predicted to go to zero only at $\psi = 0°$ and 180°. Again, this behavior is quite distinct from that of the crystalline model where the radius is predict to vanish at both $\psi = 7.8°$ and $\psi = 172.2°$. Third, and finally, the radius is predicted to diverge as the helix is unwound, increasing far more rapidly than in crystalline model even at relatively low values of ψ. This result is again distinct from that of the crystalline model where $R^\star$ remains finite and reaches a simple maximum when the ribbon is straightened out. However, experimentally it is difficult to determine quantitatively if the radius of curvature for the straight ribbon is truly infinite, or simply very large (i.e. $27R_o$ as predicted by Equation 5.52), and therefore this feature does not provide as useful an additional means of distinguishing between the two model free energies as the two previous differences do.

Finally, turning to the torque and transverse force predicted using the model of Chung *et al.*, we find

$$\tau^\star_{\mathrm{Ch}}(\psi) = wK^* \frac{\sin(\psi)\cos^2(\psi)}{K_{pp} - (K_{cc} - 2K_{cp} + K_{pp})\cos^4(\psi)} \times \left(K_{cc}\frac{1-\sin^2(\psi)}{\sin^2(\psi)} - K_{pp}\frac{1-\cos^2(\psi)}{\cos^2(\psi)} \right) \tag{5.62}$$

and

$$J^\star_{\perp,\mathrm{Ch}}(\psi) = wK^{*2} \frac{\cos^5(\psi)}{\left(K_{pp} - (K_{cc} - 2K_{cp} + K_{pp})\cos^4(\psi)\right)^2} \times \left(K_{cc}\frac{1-\sin^2(\psi)}{\sin^2(\psi)} - K_{pp}\frac{1-\cos^2(\psi)}{\cos^2(\psi)} \right) \tag{5.63}$$

respectively. Before plotting these functions, we must come up with a means to determine what their overall scale should be. As we did for the case of the crystalline model in section 5.2, this determination may be done accomplished by examining the effective axial spring constant the free end boundary condition. Performing the Taylor expansion of the axial tension in the absence of torque, the spring constant for the model of Chung *et al.* is found to be

$$\tilde{K}_{\mathrm{spring,Ch}} = \frac{4}{\sin^2(\psi_o)}\frac{w}{R_o^2 s}K_{cc} = 8\frac{w}{R_o^2 s}\left(\frac{K_{cc} + \sqrt{K_{cc}K_{pp}}}{2}\right) \tag{5.64}$$

which is again consistent with the previous work of Dr. Zastavker [28]. The second form of this result has been included simply to allow for an easier comparison of this expression to the predictions of the crystalline model (Equation 5.12). Substituting our values for the spring constant and the helix geometric parameters into this equation, we find $K_{cc} = (1.1 \pm 0.4) \times 10^{-15}$ Nm for the measurement shown in Figure2-14. Again, this value for the phenomenological elastic energy constant is predicted to be dependent upon the ribbon thickness, however it will still provide the proper order of magnitude for typical low-pitch helices in CDLC. Finally, with this value for K_{cc} setting the absolute energy scale, and the parameter ratios from Equation 5.60, we may now plot the torque and transverse force for this model in Figure 5-10.

As expected, we see from Figure 5-10 that the chiral model predicts very different behavior than the crystalline model for the transverse force and the torque. We note first that are no values of $\tau^{\star}_{\mathrm{Ch}}$ or $J^{\star}_{\perp,Ch}$ for negative Φ. This restriction of the parameter space is due to the fact that, in this model, a helix with a pitch angle ψ is not just energetically equivalent to a helix with a pitch angle of $180 - \psi$, but is in fact exactly the same geometry. Second, we see that there is no way to satisfy the equal area stability condition for domain separation (Equation 3.78) even at zero torque. This fact means that the helix is predicted to unwind smoothly to a straight configuration, and to then rewind continuously back into a right-handed helix. Third, we note that the torque is on the same scale as that found from the crystalline model for small deformations. However, unlike our earlier predictions, the chiral torque is monotonically decreasing upon unwinding, diverging for $\Phi = 0$ as the radius goes to infinity. For the potential experimental setup described in section 3.4.4, we imagine a magnetic bead tethered rigidly to the end of a helix in the presence of a an externally controlled field. In this type of apparatus, the force applied can be related directly to the magnitude and direction of the applied magnetic field [100]. Thus, in principle, the transverse force should be a completely straightforward quantity to measure as the helix is deformed. Comparing the form of the transverse force for the two models (Figures 5-8(a) and 5-10(a)), we note that the despite the same basic inverted "U" shape upon winding, these two curves are also easily distinguishable. This portion

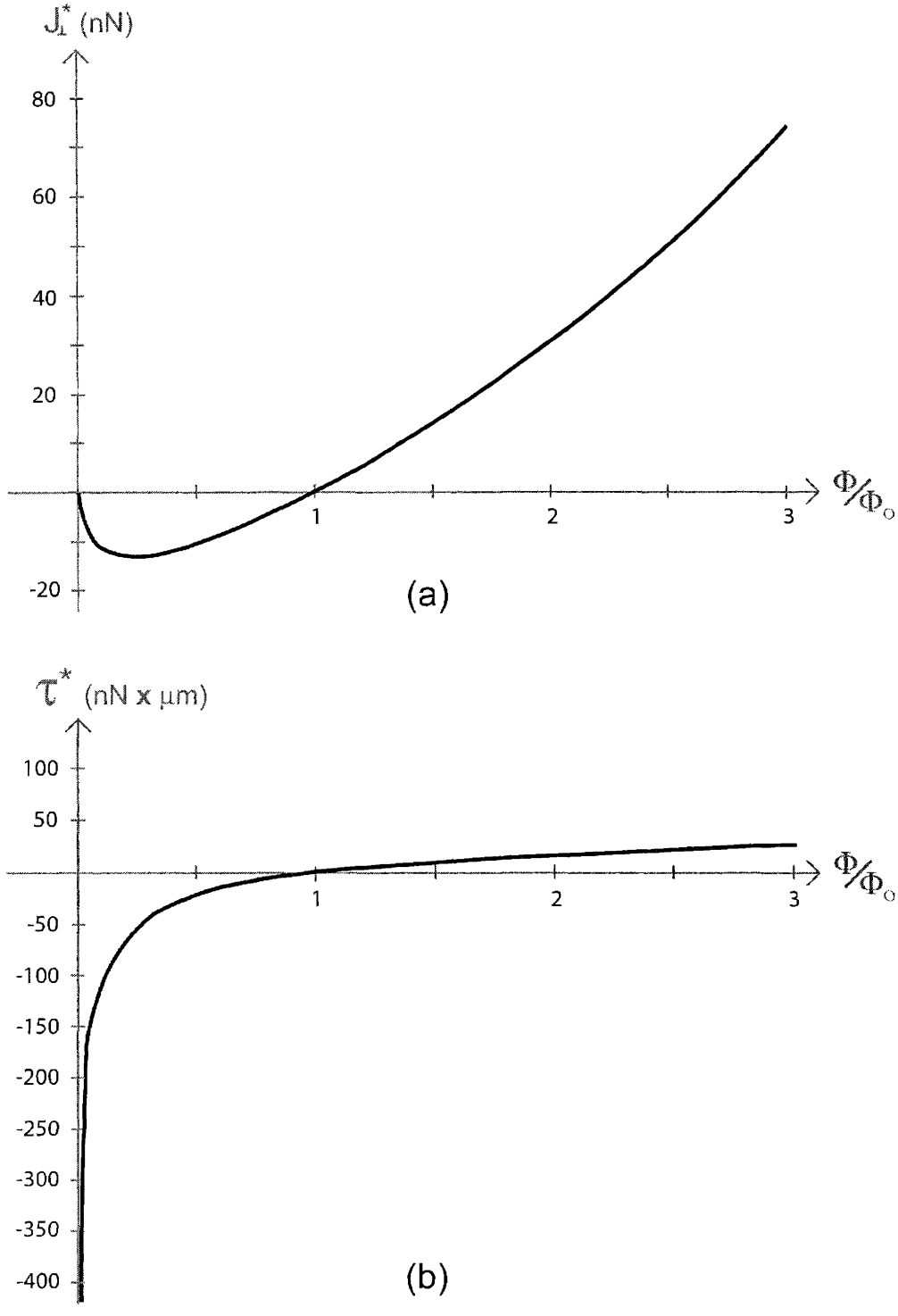

Figure 5-10: A plot of the predictions from the model of Chung *et al.* for the transverse force in nN (a) and the torque in nN $\times$ μm (b) vs. the azimuthal angle for the typical low pitch helix used to measure $\tilde{K}_{\text{spring}}$. Again, the range has been cut off in order to allow the region around $\Phi = 0$ to be analyzed more easily.

of the tension curve for the crystalline model is nearly symmetric about it minimum while, it is highly asymmetric for the chiral model. In addition, we find that the azimuthal angle at which the force reaches its minimum occurs at

$$\begin{aligned} \Phi^{crys}_{J_{\perp,\min}} &= (0.489 \pm 0.091)\Phi_o \\ \Phi^{chiral}_{J_{\perp,\min}} &= (0.236 \pm 0.043)\Phi_o \end{aligned} \tag{5.65}$$

for each model respectively. Therefore, we predict that one would have to eliminate roughly half of the original helix turns to reach the minimum transverse force in the crystalline model while one would have to unwind nearly three-quarters of the turns in the case of the chiral model. Experimentally, the variable Φ would be controlled by the orientation of the applied field and thus, this measurement would provide a third clear demonstration of whether the chiral or crystalline models were more correct for the helices formed in the quaternary systems. While the evidence presented in Chapter 4 provides a broad and powerful argument for our choice of the crystalline model with an isotropic spontaneous curvature, these experiments would provide further direct, convincing, and very visual proof of our current assumptions.

With these results, we have thus completed our analysis of the winding and unwinding of a low-pitch helix under a pure torque. We have made detailed predictions for the form of the radius and azimuthal angle as a function of the pitch angle which may be compared to future experimental results. In addition, we calculated how the torque will vary with Φ, and found that our model predicts the continuous transition of a right-handed helix into a symmetric left-handed helix upon unwinding. The details and numerical values of these predictions obviously depend upon the values chosen for K_α/K_γ, K_β/K_γ, and $K_s R_o/K_\gamma$, and would therefore provide the first truly independent test of the results presented in section 5.3. Finally, we have detailed three characteristic and easily discernable differences in the response of a helix if the chiral model of Chung *et al.* was correct instead of the crystalline model. Thus, we have shown that, despite the lack of any predicted mechanical instabilities, this type of experiment would still be extremely interesting to perform in that it will provide graphic and unambiguous checks on every aspect of our choice for the free energy

including the isotropic form of the spontaneous curvature and the predicted ratios of the free energy parameters for the helices in CDLC.

Chapter 6

General Conclusions

It this thesis, we have been able to make significant advances in our theoretical and experimental understanding of the helical ribbons formed in the quaternary cholesterol - surfactant - fatty acid / phospholipid - water systems. Combining our latest experimental observations with improvements in the current understanding of the important connections between the phenomenological models that have been proposed for the formation of helical ribbons, we have been able to formulate and fully characterize a model free energy that is capable of self-consistently and quantitatively explaining all of the observed properties of our self-assembled helices. In addition, with this model free energy we have also been able to make a number of detailed predictions for the results of future experiments that may be checked as new tethers are developed.

Our major experimental findings that helped to guide the rest of this work were presented in Chapter 2. These included the first direct measurements of the thickness for low pitch helices in the Chemically Defined Lipid Concentrate (CDLC) system. Using Atomic Force Microscopy (AFM) we were able to image the ribbons under fluid, and found that in two typical samples, the ribbons with widths greater than 3 μm had thicknesses ranging from 33.6 $\pm$ 1.6 nm to 138.0 $\pm$ 0.7 nm. Using the preliminary x-ray diffraction data available at the time of this writing, these thicknesses work out to approximately 10 and 40 layers respectively. While thicker than some previous estimates, these ribbons are found to be composed of a fairly small number

of crystalline layers.

Applying the tethering methodology we have developed for manipulating individual helices, we were able to determine their mechanical response to the application of external stress. There were four major finding from these experiments that strongly influenced our theoretical treatment. The first was the observation that while Devcon 5-Minute Epoxy® epoxy was capable of easily tethering to the low-pitch helices in CDLC and supplying an axial tension without the introduction of a torque, it was very difficult to form such a tether with the high-pitch helices. Along with previous work, this finding indicates that the helices do indeed have functionally different surface properties. Second, we found that that the fractional change in helix radius versus the change in pitch angle under axial tension for a variety of low-pitch structures was statistically equal to zero for small deformations. This result suggests that the pitch angle and the radius are only weakly coupled in the free energy, and turned out to be a sufficient piece of experimental information to uniquely determine the proper form of the spontaneous bending force in our model. Third, by making use of microfabricated silicon-nitride cantilevers as force probes, we were able to develop a methodology for calibrating the elastic properties of low-pitch helical ribbons. We demonstrated this technique on a typical helix in CDLC and found its effective spring constant to be equal to (4.8×10^{-6}) N/m. This value places the force range of this helix on the order of many other interesting biological processes and thus opens up the possibility for the use of these structures themselves as calibrated force transducers (see Appendix A). Fourth, and finally, we discovered a novel type of reversible tension induced straightening transition in both the low and high pitch helical ribbons. This mechanical transition is characterized by the spontaneous separation of a helix into two connected domains beyond a critical extension. In both cases, one domain is straight with a pitch angle of 90°, while the second domain is found to be helical with a pitch angle of $(16.5 \pm 1.3)°$ for the low pitch or $(59.6 \pm 1.7)°$ for the high pitch helices. However, it is important to note that there is some question about our interpretation of this phenomena for the particular high-pitch structure in which it was observed due to the presence of curvature defects we termed "wobbles" in the

straight domain.

In order to analyze our experimental results, we first needed a general theory for the incorporation of tension and torque into the free energy formalism we use to describe the helical ribbons. We presented our derivation of this formalism in Chapter 3 building on simple considerations of the total mechanical energy of the system. This approach is fully general and does not rely on making a thermodynamic analogy as did previous attempts [28]. In addition to the completely general case in which the tension and the torque were considered to be independent, we also worked out the results of our theory for four specific cases of particular experimental importance. These were :

Case 1 no external stress is applied (i.e. the helix is free in solution)

Case 2 the helix is subjected to an axial force in the absence of torque (i.e. freely rotating ends)

Case 3 the helix is subjected to an axial tension and whatever external torque is required to hold Φ constant (i.e. clamped ends)

Case 4 a torque is applied to the helix in the absence of axial tension (i.e. pure winding and unwinding).

In each case we found that the imposed constraint led to the prediction of a relationship between the radius and the axial and contour lengths which could be substituted back into the free energy, reducing it to a function of only two variables (ℓ and s). With this simplification, we were able to work out the conditions of material conservation and domain stability for a helix composed of two distinct regions of different conformations. Most importantly, we were able to express the two stability conditions as a single integral equation directly analogous to the Maxwell equal area construction in the thermodynamic treatment of the gas-liquid phase transition [29].

In order to make use of our general formalism, we first needed to decide on what particular form was appropriate for the model free energy. In Chapter 4, we were able to show that, despite the great success of models that explicitly consider the

effects of molecular or collective chirality in describing other self-assembling systems, our observations on the structures in the quaternary systems were fundamentally incompatible with some of the basic predictions of these models. With this realization, and the preliminary evidence for long-range order in our helical ribbons, we gave the first comprehensive theoretical argument for the use of the new crystalline model with isotropic spontaneous curvature originally proposed by Dr. Lomakin and further developed by the work of Dr. Zastavker [28]. In particular, we showed that the isotropic spontaneous curvature introduced for other reasons in her work, can be shown to be the only possible form capable of self-consistently explaining our determination that the radius does not change to first order under the application of a pure axial tension.

In Chapter 5 we concluded the thesis with a detailed, quantitative analysis of our experimental results making use of the theoretical formalism we developed in the preceding two chapters. From a linearized analysis of the free energy under tension, we were able to predict the theoretical form for the effective spring constant of the helix assuming both the free and clamped end constraints. Interestingly, we found that the difference associated with the two constraints was predicted to be only on the order of $(1 \pm 4)\%$ which would be very difficult to measure with our current calibration techniques. In addition, we found that for small deformations, the transverse force required to maintain the clamped end boundary condition was only $(4.9 \pm 1.5)\%$ of the axial tension, and thus only a weak non-slipping tether would be needed. Finally, by analyzing our spring constant data for the sample measurement, we were able to determine the absolute magnitude of the elastic energy constants in our model free energy. These constants are predicted to be strongly dependent upon the ribbon thickness, but from this measurement we expect that they will have a typical value on the order of 10^{-14} Nm for the low-pitch helices in CDLC.

Turning to a consideration of the tension-induced straightening transition, we were able to show that only the zero-torque boundary condition was capable of sustaining a stable domain separated configuration. We were then able to show that combining the stability condition that defines the pitch angle of the helical domain (ψ_{h}), with the equations for the equilibrium radius (R_{o}) and pitch angle (ψ_{o}) of the helix, we could

find three equations for the three thickness independent ratios of the parameters in our free energy. By fitting these pieces of experimental data to our theory, we found

$$\begin{aligned} \frac{K_\beta}{K_\gamma} &= 0.000 \pm 0.015 \\ \frac{K_\alpha}{K_\gamma} &= 0.038 \pm 0.012 \\ \frac{K_s R_o}{K_\gamma} &= 0.073 \pm 0.022 \end{aligned} \tag{6.1}$$

(see Equation 5.42). This was the first full characterization of the crystalline model free energy in any quaternary system. In addition, we note that (unlike their absolute magnitude) these ratios are expected to be the same for all helices within the CDLC system. Making use of this fact, we were able to predict the limit of metastability for domain separation, and found that our theory ($\nu_{J_{\max}} = 0.418 \pm 0.037$) and our experiments ($\nu_{J_{\max}} = 0.409 \pm 0.029$) agreed remarkably well.

Finally, we were able to use the ratios we determined in order to make detailed predictions for the behavior of a low-pitch helix under the influence of a pure torque. In addition to providing additional quantitative tests of our general formalism and of our predictions for the elastic energy constants, we have shown that this unwinding experiment is capable of providing an unambiguous demonstration of whether the chiral or achiral models for the helical ribbons are correct. This ability of the torque experiments to probe the question of helix handedness makes them likely to be the most interesting mechanical investigations to pursue in the near future.

However, like any good project, we have ended our investigation with as many new questions asked as old ones we answered. In particular there are five areas of great interest that, given the results of this thesis, we now have specific motivation to more fully explore. The first is also the oldest, namely the direct demonstration of three dimensional crystalline order within the ribbons. We have presented a strong theoretical and experimental argument for the need to assume crystalline elasticity, however, we have yet to obtain direct evidence of in-plane ordering. In addition to proving the basis for our theoretical framework, this investigation will allow us to probe whether the helical ribbons formed in all of the various quaternary systems

share a common set of pitch angles (11° and 54°) due to a shared common microscopic structure as we believe, or whether some other mechanism is ultimately responsible.

The second major area for future investigation is the development of new classes of tethering agents to expand the types of mechanical experiments that may be performed on the helical ribbons. This would include the development of tethers for helices in other quaternary systems to check the universality of the domain separation phenomena in both low and high pitch helices, and to repeat the measurements of their effective spring constants. Specifically, we note that given the fact that the equilibrium pitch angle (ψ_o) is common to all systems, it would be reasonable to assume that the pitch angle of the helical domain (ψ_h) would also be constant across the various quaternary systems. In addition, as already mentioned, the development of non-slipping tethers would allow for torque experiments to be carried out that would directly probe the very important question of helix handedness.

A third area of great interest will be in performing a more detailed study of the helices under compression. Given our prediction of a domain separation phenomena for both the free and clamped end boundary conditions upon the application of a negative tension, it will be interesting to look for any signs of this instability in helices that allow for such significant compressions before simple buckling occurs.

Fourth, we expect that an examination of the elastic properties of high-pitch helices under tension will provide a wealth of additional interesting information. Our preliminary findings have already shown the existence of a type of domain separation under extension in a particular helix allowing us to fully characterize its free energy (see Appendix E). In addition, the observation of the curvature defects we dubbed "wobbles" under high tension reminds us that there are still many interesting phenomena likely to yet be discovered.

Finally, as we have pointed out before, the spring constants of these helical ribbons fall within a range that is particularly interesting for a variety of biological systems and processes. Therefore, a very important avenue for future study will be moving towards the use of our helices as force probes in the study of such things as DNA elasticity, protein motors traction, antibody/antigen binding, enzyme/substrate inter-

actions, actin polymerization, and the deformation of natural and synthetic polymers. By investigating the forces involved with these systems, it will possible to extract significant new information about the details of their structure and their functioning. Appendix A will discuss in detail the many unique advantages we feel make it likely that these self-assembling helical ribbons will, in fact, have an important role to play in the investigation of a variety of novel and interesting biomechanics phenomenon.

Appendix A

Strengths and Limitations of Helical Ribbons as Force Probes

The ability to both tether and manipulate individual helical ribbons along with the demonstration that their restoring force varies linearly with displacement over a large range of extensions opens up the real possibility of using these biological springs as force transducers to investigate other systems. In light of this possibility, we will present a brief overview of the strengths and limitations a force probe based on our helical ribbons would have when compared to other modern techniques.

The first advantage to using the helical ribbons is that we would be able to make use of many of the currently existing techniques for tethering to biomolecules developed for use with other systems. In analogy to the biomembrane force probe (BFP) discussed in section 2.4.1, the simplest possible scheme for using a helical ribbon as a force transducer would be to tether a latex bead to one end of the helix, and then bind that bead to the molecule(s) of interest applying methods commonly used in experiments with laser and magnetic trap or the biomembrane force probe. Figure A-1 shows a schematic illustration of the experimental setup we envision in comparison to the typical setup of the BFP, the closest analog among currently used techniques. For simplicity in describing our proposed setup, we will coin the term Helical Spring Scale (HSS) for its configuration.

Once we can tether the helices to biomolecules in this way, we note from our

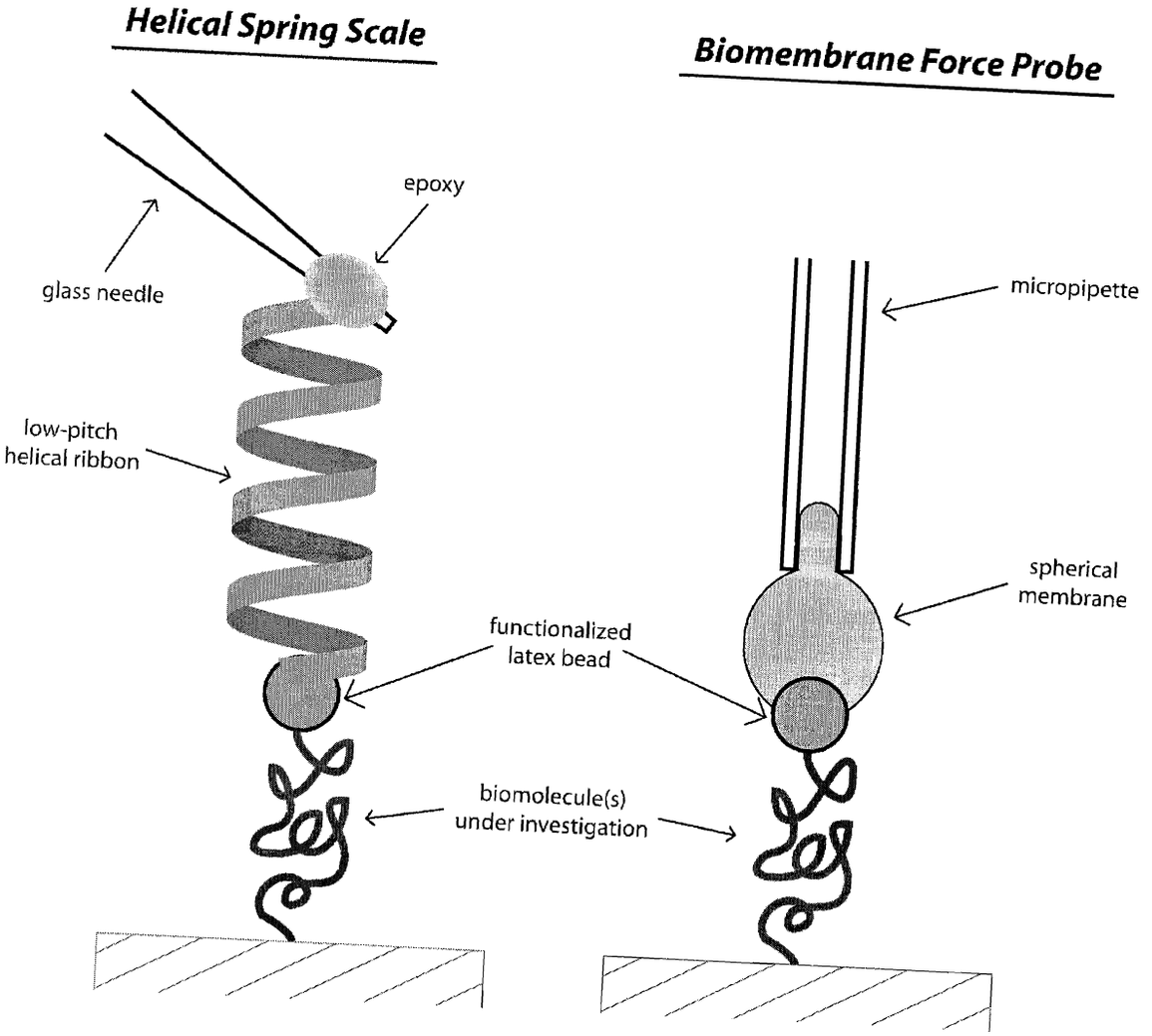

Figure A-1: (a) A cartoon schematic (not drawn to scale) showing the important components that would be associated with using the helical ribbons as force probes. The helix is attached at one end to a glass needle that controls the extension by its connection to a micomanipulator, while the other end is attached to the biomolecule under investigation through the use of a functionalized latex sphere. (b) Shows a similar schematic for the biomembrane force probe developed by Evans *et al.* [103]. In this setup the force is measured by moving the pipette and recording the displacement of the functionalized latex sphere attached to the sample (see section 2.4.1).

measurements of the spring constant that the elasticity of our structures come preset to a scale appropriate for many of the so called "mechanochemical" experiments. In section 5.2 we give a theoretical argument for the expected range of spring constants based upon our calibration data and from this prediction, we expect to find helices with spring constants in the range from 0.1 to 100 pN/μm (10^{-7} to 10^{-4} N/m) depending upon their geometry. For the very stiffest structures, which will tend to be shorter, we expect to be able to probe forces on the range from 0.1 to 1 nN over displacements on the order of 1 to 10 μm. For the very softest structures, however, we predict a dynamic range of roughly 0.1 to 10 pN over displacements up to 100 μm. The lower limit of 1 μm is chosen not only as the limit of resolution for our current microscopy experiments, but also for the typical size of fluctuations due to vibrations in the aqueous solution that tends to make measurements on the helix at a resolution below this much less significant. This range of forces from 0.1 pN to 1 nN is a much larger accessible range than that for optical traps, and is comparable to that which may be achieved with AFM and the BFP. However, we note that the range of accessible deformations is now on a scale more than three orders of magnitude larger than any of these current technique and is, in fact, more comparable to that of the glass needles and microfabricated silicon-nitride cantilevers.

This consideration of the force range, however, also raises a possible limitation to the use of our helical ribbons as force probes, namely the great mismatch between the force and distance scales of interest. The helices are inherently micron scale objects with micron scale displacements, while most other systems of interest having forces on this scale operate over nanometer lengths. Fortunately, data processing techniques have been developed to extract high resolution positional results from even low contrast video images. Such techniques have been demonstrated to achieve precision on the order of 1 to 2 nm when tracking the location of 190 nm latex beads [205] or roughly 5 nm precision when monitoring 600 nm paramagnetic spheres [101], and could be easily adapted to image the bead illustrated in Figure A-1. This type of detection scheme would have the advantage of being able to extract both the high resolution information about the biomolecules extension, and the low resolution

information about the helix extension from the same set of video captures instead of requiring a separate detection scheme for the location of the bead which would require a more complex setup as well as careful temporal alignment with the video images taken of the helix.

The next major advantage our helices would have over most other force probes is that they can, in theory, be calibrated simply by measuring their unstressed radius, width, and total contour length. Relying on theoretical arguments, we found in section 5.2 that the spring constant of a helix may be expressed as some material dependent constant times a function purely of these three geometric parameters. Experimental investigations to explore this prediction are currently underway. It is interesting to note that this simple calibration scheme is similar to that for the BFP, whose stiffness may be determined by measurements of the applied membrane pressure, the inner radius of the pipette, the radius of the spherical vesicle, and the radius of the attached bead. However, it is much easier to measure the macroscopic geometry of a helix than it is to accurately measure these parameters for the micropipette aspiration technique. This makes the helical ribbons likely to be the simplest of all the force probes to calibrate.

Building on this last idea, another major advantage to using these helical ribbons is that they have their own built-in ruler for length, and thus for force. In other words, you do not have to have independent knowledge about the location of a helix before and after a force is applied. All of that information is encoded in the helix pitch angle given that $\psi_o = 11°$. Thus, the helical ribbons could in principle be used to measure forces where real time tracking or manipulation is impossible. For example, imagine adding helices to a gel in the fluid state, and then cooling the system through its transition so that it swelled as the gel networks formed. Taking this system and slicing down through it in thin layers would revel cross sections of the trapped helices. By simply measuring their radius and pitch in this state you could map out the distribution of forces that had been "frozen in" as the gel was formed. This is an idealized thought experiment, but it provides an idea of the potential usefulness to having a force probe that codes absolute force directly in an intensive

geometric parameter like ψ.

Another novel advantage associated with the helical spring scale relies on taking advantage of the domain separation phenomena described experimentally in section 2.5 and theoretically in sections 3.5.2 and 3.5.3. In a domain separated helix, the force applied becomes independent of the displacement while further extensions merely change the relative amount of material in the straight and helical domains. This phenomena provides us a means of creating a simple constant force device without the need for feedback controls used in most constant force devices today. The only drawback to this idea is that the value of the force applied in this state is purely a property of the helix, and thus it can only be changed by changing the helix in use.

The final, and probably most significant, advantage to the HSS system is its ability to apply and easily measure a torque on the attached biomolecule. Currently, the only technique capable of applying a known torque is the magnetic trap (see section 2.4.1). Unfortunately, this device must be re-calibrated experimentally every time it is used due to the variability of magnetic susceptibility between samples, and the analysis required to extract a specific value for the torque is a rather involved process requiring data from highly specialized equipment. In the case of the HSS, however, if the bead is tethered to the helix so that it cannot slide, then rotating the free end of the structure will apply a torque to the sample which can be measured simply from the geometric parameters of the deformed helix. In addition, from Figure 5-8, we can see that the response of the helix is predicted to be linear over a very large range of rotations, deviating from a straight line only very near the fully straight configuration. Finally, we note that the predictions for the torque which may be exerted by a typical low-pitch helix is on the order of 10^{-14} Nm as compared to a maximum of roughly 10^{-18} Nm achieved in the calibrated torque experiments using magnetic traps [95]. As with the axial spring constant, we expect that the value of accessible torques will span a wide range for helices of different dimensions further increasing the advantage to this type of force probe.

Finally, there are two additional limitations to the helical spring scale that must be mentioned. The first is that, just like with the AFM, you have to switch transducers

to change the force range being probed. Each individual helix is predicted to have a one or two order of magnitude force range it can measure, but in order to explore the full four order of magnitude range accessible with this technique, several helices of different dimensions would have to be substituted. This limitation, while important, is also partially an artifact of the very large force range of the helical ribbon system. In fact, of the techniques currently employed, only the BFP has an the ability to measure and apply forces on a range comparable to the helical ribbons without having to replace any components.

The second significant limitation to the helical ribbon force probe is by far the most important discussed in this appendix, namely the question of temporal resolution. The standard measure of the resolution for a force probe is the exponential rise and fall time associated with a sudden step change in the applied force [70, 108, 206]. This is exactly what we measured with the relaxation experiments described in our attempts to use the viscous drag as means of calibrating the helical ribbons (see section 2.4.3). In this case, however, we are now only concerned with the decay times, and thus none of the limitations discussed concerning the calculation of the forces apply. Figures A-2(a) and (b) below show a typical picture of a large and small helix respectively under tension as well as a characteristic plot of their relaxation data showing a slow exponential decays back to their unstressed length.

Table A.1 summarizes our measurements for the characteristic response times of the six helices we measured in the previous work [28].

From the values in Table A.1, it is clear that the temporal resolution of the helical ribbons is quite slow particular compared to AFM ($\sim$ 0.01 ms), optical traps ($\sim$ 0.02 to 1 ms), glass needles ($\sim$ 0.1 to 0.4 ms), or microfabricated silicon-nitride cantilevers ($\sim$ 0.01 to 1 ms). Even the fastest, and therefore stiffest, helical ribbon has a decay time only on the order of video resolution ($\sim$ 1/30 seconds) while the slowest is a full order of magnitude longer than this. These long decay times are a natural and unavoidable result of the softness of the helical ribbons combined with their unusually large hydrodynamic drag compared to other force probes given their size. This fact suggests that the initial uses of the HSS will be primarily quasi-static measurements.

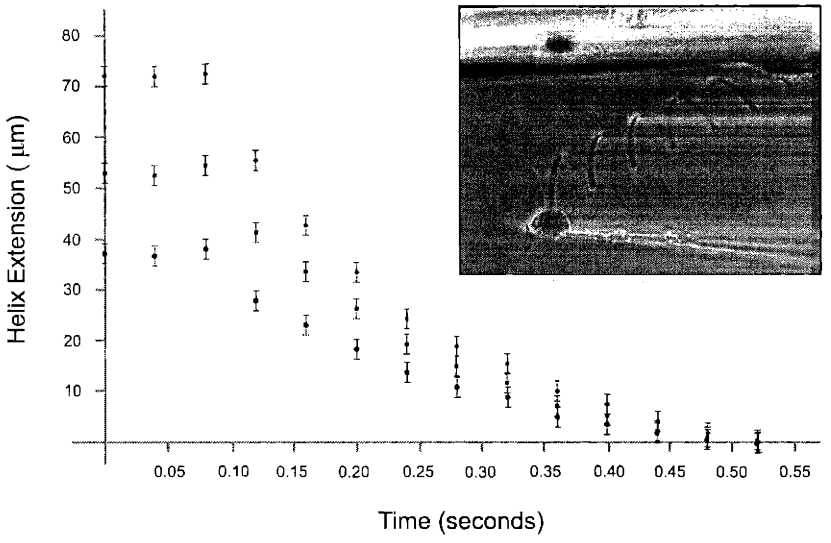

(a)

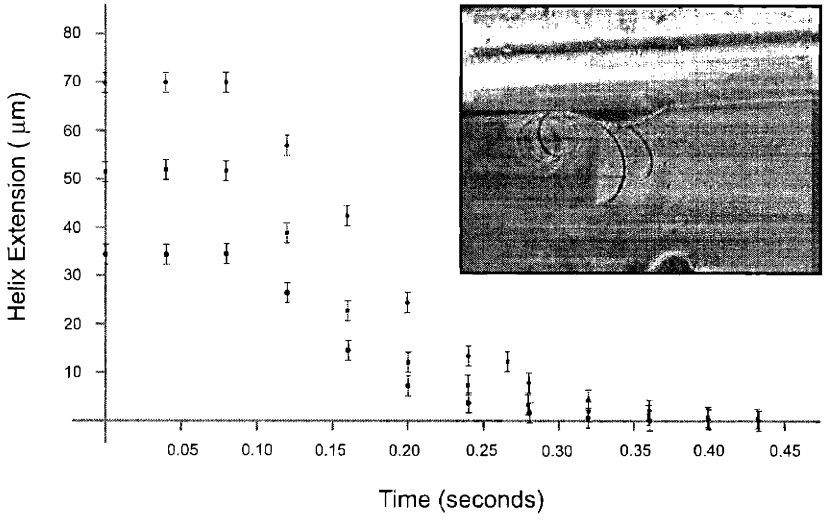

(b)

Figure A-2: A typical example of a characteristically (a) large (radius 24 μm) and (b) small (radius 9 μm) low pitch helix used to determine their response time to a step change in force. The helical ribbons under tension are shown as the inserts on the right-hand side while the plots of their relaxation upon removal of the force approximately 0.08 seconds into the experiment is shown on the left. The large helix (a) corresponds to "Helix Five" in Table A.1 while the small one (b) is the one labeled "Helix Two".

Table A.1: The characteristic decay times of various low-pitch helices in CDLC for relaxation from an extended state upon the sudden removal of the axial tension.

Helix Label	R_o (μm)	w (μm)	ℓ_o (μm)	Time Constant (ms)
One	18 ± 1	8.2 ± 0.5	93 ± 2	34 ± 5
Two	9 ± 1	2.1 ± 0.5	52 ± 2	67 ± 7
Three	21 ± 2	5.2 ± 0.5	77 ± 2	143 ± 16
Four	21 ± 2	2.9 ± 0.5	89 ± 2	174 ± 26
Five	24 ± 1	4.4 ± 0.5	150 ± 2	204 ± 30
Six	50 ± 2	4.6 ± 0.5	117 ± 2	384 ± 31

It is important to note that these long time constants are a further argument for the use of the high-resolution video detection schemes rather than more complex setups. This is because the response time of a helix is fundamentally slower than the video rate, and thus no useful information would be lost by recording the data in this way.

As new tethers are developed, we will gain the ability to study helical ribbons in a wider variety of quaternary systems as well as the ability to construct the type of experiment setup envisioned in Figure A-1. From the predictions presented in this appendix, it is likely that the construction of such a helical spring scale would have many interesting advantages for measuring forces in a variety of systems, and may, in fact, provide a cheap, simple, and readily available alternative force probe. In particular, we find that such a helical ribbon system is likely to have a response similar in many ways to the biomembrane force probe which has already proven itself to be a very useful tool for the study of many interesting phenomena [103, 104], with the added advantage of being able to apply a torque.

Appendix B

Application of the Generalized Energy Formalism to a Classical Spring and Mass

In order to illustrate that the formalism laid out in section 3.3 is the correct way in which to incorporate the effect of an external tension into the theory of helical ribbons, it is instructive to use this technique to examine a very simple and familiar model system involving a classical spring. This comparison will be particularly instructive for two reasons. First, for a simple spring we know that the force versus extension relationship obeys Hooke's Law, and thus we have the ability to compare the equilibrium conditions derived from our considerations of the total energy to those obtained directly from equating the applied and restoring forces. Second, the equations of motion for this spring are simple enough to solve exactly which will allow us to examine the approach to equilibrium as well as the static properties of the combined system.

Figure B-1 shows a simple spring with spring constant K connected at one end to a fixed wall and at the other end to a block of mass m via an inextensible string. The spring is initially at its unstressed length (ℓ_o) when the block is released and the system is allowed to relax to its new equilibrium configuration.

As required by our theoretical treatment, the external axial tension applied to the spring in Figure B-1 is constant, and is given by $J_{\|}^{ext} = mg$. We also know that at

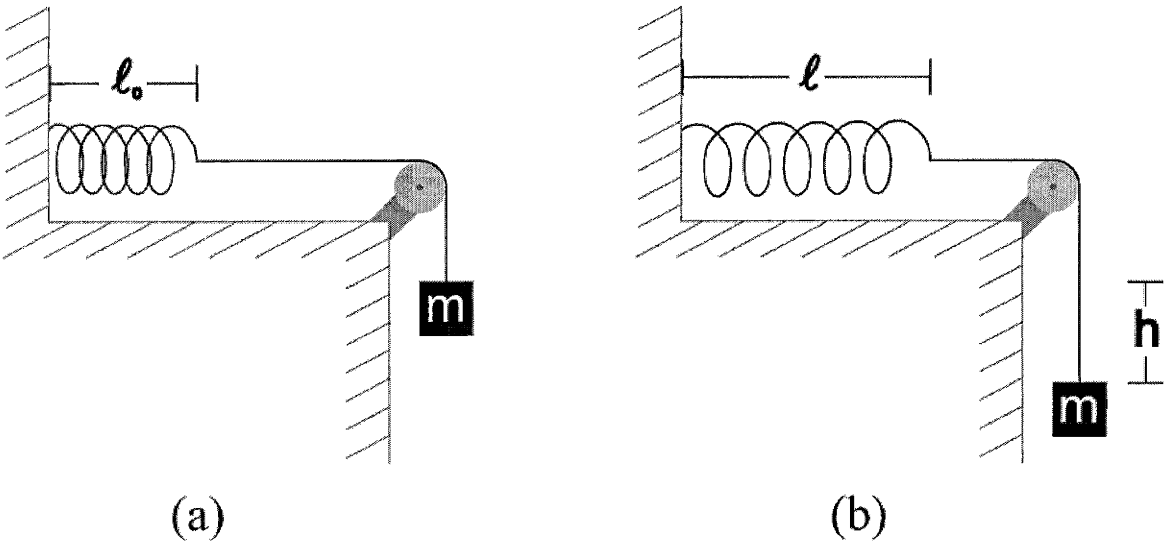

Figure B-1: (a) A classical ideal spring with spring constant K connected to a rigid wall and a mass. The spring is at its unstressed length and the block is held in place by an external force not shown. (b) The block is released and the system is allowed to come into static equilibrium in which the restoring force of the spring just balances the weight of the block.

equilibrium, the restoring force exerted by the helix must be given by $\vec{J}_{\|} = -\vec{J}_{\|}^{ext}$. By construction, there is no applied torque and the spring cannot change its total contour length, which makes the axial length the only variable in this problem. The total amount of work that the block does is equal to the change in its gravitational potential energy between the initial and final states. Thus, the work done by the external tension is given simply by

$$W_{axial} = mgh = mg[\ell - \ell_o] \tag{B.1}$$

which is equal to $-J_{\|}[\ell - \ell_o]$ exactly as we found in section 3.3.2 for the general case.

In order to calculate the restoring force exerted by the spring, and thus the equilibrium value of ℓ, we must minimize the total energy of the system. As for the generalized system, the total energy in this example is equal to the sum of the work done by the block and the change in the internal elastic energy of the spring. In our current notation, the spring potential energy is given by

$$F(\ell) = \frac{1}{2}K(\ell - \ell_o)^2 \tag{B.2}$$

Combining this expression with that for the axial work, we find that the total energy of the system after the extension is given by

$$E^{tot}(\ell) = F(\ell) - J_{\|}[\ell - \ell_o] \tag{B.3}$$

which is exactly Equation 3.11 with $\tau = 0$ and the dependence on the contour length (which is a constant) suppressed for clarity. The condition of mechanical equilibrium may then found by minimizing the total energy with respect to ℓ. Minimizing Equation B.3 yields

$$\frac{dF}{d\ell} = J_{\|} \tag{B.4}$$

just as we found in section 3.4.2 for the case of zero torque extension (Case 2). Plugging the given expressions for F and $J_{\|}$ into Equation B.4 gives us that the condition of mechanical equilibrium is

$$K[\ell - \ell_o] = mg \tag{B.5}$$

The equilibrium described by Equation B.5 is exactly that which is expected from equating the restoring force of the spring as given by Hooke's Law to the weight of the block. Thus our energy formalism succeeds in capturing all of the important static equilibrium physics for this model system in a very simple and direct manner.

In addition to demonstrating that the condition of mechanical equilibrium derived from the total energy predicts the correct force balance, this model system also allows for a direct demonstration of our claim from section 3.3.2 that the difference in the work done by the external force and the work done by the helix is exactly what is "lost" in bringing the combined system into its new static configuration. For completeness, we will demonstrate this fact both by considering the energy dissipated by a typical damping force with no external intervention, and by considering the amount of kinetic energy that an external agent would have to remove in the absence of damping in order to stop the block.

Using the equilibrium condition from Equation B.5 we will first calculate the difference in work done by the block and that done by the spring. From Equation B.1,

the amount of work done in lowering the block is equal to

$$W_{axial} = mg[\ell - \ell_o] = \frac{(mg)^2}{K} \tag{B.6}$$

The amount of work done by the spring in going from ℓ_o to ℓ is equal to the change in its internal elastic free energy and thus we have

$$W_{spring} = \frac{1}{2}K(\ell - \ell_o)^2 = \frac{1}{2}\frac{(mg)^2}{K} \tag{B.7}$$

The difference in these two amounts of work is given by $\Delta W = W_{axial}$ - $W_{spring} = \frac{1}{2}\frac{(mg)^2}{K}$. We will now show that this is exactly the energy that must be removed in order to settle the system in its final equilibrium state.

First, we will consider the case when the spring is over damped and the entire system is left isolated after the block is released. The subsequent equation of motion for the block is simply given by the standard damped harmonic oscillator equation

$$m\frac{d^2\tilde{\ell}}{dt^2} = -K\tilde{\ell} - b\frac{d\tilde{\ell}}{dt} + mg \tag{B.8}$$

where b is the damping coefficient and ℓ_o has been set to zero for convenience. In the end, the damping b will disappear from the final answer, and therefore its introduction will not result in any loss of generality. The solution to Equation B.8 for the over damped case is well known, and when the boundary conditions $\tilde{\ell}(t = 0) = 0$ and $\frac{d\tilde{\ell}}{dt}|_{(t=0)} = 0$ are included it is given by

$$\tilde{\ell}(t) = \frac{mg}{K}\left(\frac{a_-}{a_+ - a_-}e^{-a_+ t} - \frac{a_+}{a_+ - a_-}e^{-a_- t} + 1\right) \tag{B.9}$$

where the decay constants $(a_\pm)$ are given by

$$a_\pm \equiv \frac{b}{2m} \pm \sqrt{\left(\frac{b}{2m}\right)^2 - \frac{K}{m}} \tag{B.10}$$

The amount of energy dissipated by the damping force as the helix approaches its equilibrium conformation is given by

$$W_{diss} = \int_0^\infty b\left(\frac{d\tilde{\ell}}{dt}\right)^2 dt \tag{B.11}$$

Plugging in the solution for $\tilde{\ell}$ into Equation B.11 and performing the integral yields

$$W_{diss} = \frac{b}{2}\frac{(mg)^2}{K^2}\frac{a_+ a_-}{a_+ + a_-} = \frac{1}{2}\frac{(mg)^2}{K} \tag{B.12}$$

which is independent of the damping coefficient b as we claimed. Examining Equations B.9 and B.12 we see that as the time goes to infinity, $\tilde{\ell}$ approaches $\frac{mg}{K}$ and that the energy dissipated in the process goes to $\frac{1}{2}\frac{(mg)^2}{K}$ which is exactly the difference in the work done by the block and by the spring as expected.

Second, we will consider the easier scenario in which the spring is not damped, but an external agent (such as someone's hand) stops the block at the correct equilibrium position by absorbing all of its kinetic energy. The equation of motion for the block in this case is that for the undamped harmonic oscillator, namely

$$m\frac{d^2\tilde{\ell}}{dt^2} = -K\tilde{\ell} + mg \tag{B.13}$$

The solution of the above equation for the same initial boundary conditions considered in the overdamped case above, is found to be

$$\tilde{\ell}(t) = \frac{mg}{K}\Big(1 - \cos(\omega t)\Big) \tag{B.14}$$

where $\omega = \sqrt{\frac{K}{m}}$ is the natural frequency of the spring. Finally, using the solution for $\tilde{\ell}$, we find that the kinetic energy of the block is given simply by

$$KE_{block}(t) = \frac{1}{2}m\left(\frac{d\tilde{\ell}}{dt}\right)^2 = \frac{1}{2}\frac{(mg)^2}{K}\sin^2(\omega t) \tag{B.15}$$

From Equation B.14 it is easy to see that the block passes through the desired point of static equilibrium ($\tilde{\ell} = mg/K$) whenever $\omega\bar{t}$ is an odd multiple of $\frac{\pi}{2}$ (i.e. whenever $\bar{t}$ is an odd multiple of one-quarter period). Finally, Equation B.15 gives us that the kinetic energy of the block at the equilibrium point is $KE_{block}(\bar{t}) = \frac{1}{2}\frac{(mg)^2}{K}$ which is equal to the energy the external agent must remove in order to stop the block. Thus, once again, we have demonstrated that the difference in work done by the applied tension and the internal elastic response of the spring is exactly that which must be removed in order to settle the combined system after the deformation is made.

In the form presented here, it easy to recognize this model experiment as one quite common in introductory mechanics. Our intuition with this classical problem, and the above demonstration of the applicability of our general formalism, provides a simple example that will be useful for establishing a mental framework in which to analyze the more complex deformations and subsequent phenomena of our non-linear biological springs.

Appendix C

Application of Our Indirect Method for Imposing External Constraints to an Ideal Gas

In section 3.4.3, we described a two-step method for finding the torque required to maintain the clamped end boundary condition upon extension of a helix. The first step expanded the helix at zero torque until the desired axial length was reached. During this expansion, the azimuthal angle was allowed to change from Φ_o to $\tilde{\Phi}$ as given by Equation 3.18. The second step then applied a torque to wind the helix holding the axial length fixed until the azimuthal angle was returned to Φ_o. In order to demonstrate the applicability of incorporating an externally imposed constraint in this type of piecewise fashion, we will now discuss the closely analogous problem of the isothermal expansion of a classical ideal gas. This system is particularly useful because it is well established how to both directly and indirectly impose the constant temperature constraint, making it straightforward to compare the two results. In this example, the pressure will be analogous to the torque, the volume is the analog of the axial length, and the temperature is analogous to the angle Φ.

Figure C-1(a) shows the desired path for the expansion of the gas from (P_0, V_0, T) to (P_1^a, V_1, T) along an isotherm. The dashed line in Figure C-1(b) shows the conjugate two step path with an expansion of the gas at constant pressure from (P_0,

V_0, T) to (P_0, V_1, $\tilde{T}$) followed by a cooling of the gas at constant volume to the end point (P_1^b, V_1, T). The initial values P_0 and V_0 are specified, along with the temperature T, and the final volume V_1. Our goal is to determine the end state pressures and the changes in internal energy of the gas, and verify that they are the same in both cases (i.e. that $P_1^a = P_1^b$ and that $\Delta E^a = \Delta E^b$).

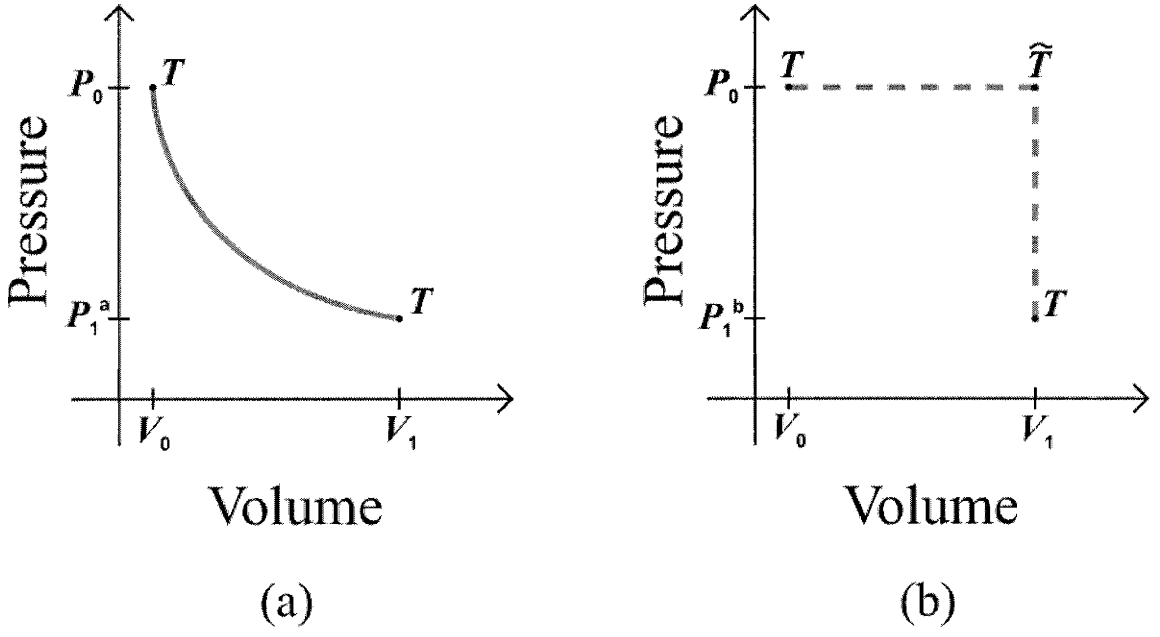

Figure C-1: (a) Schematic pressure-volume diagram of a typical direct isothermal expansion of a classical ideal gas from the initial state (P_0, V_0, T) to the final state (P_1^a, V_1, T). (b) The conjugate two-step path in which the gas is first expanded at constant pressure from (P_0, V_0, T) to (P_0, V_1, $\tilde{T}$) allowing the temperature to change. The gas is then cooled at constant volume until the temperature is returned to its initial value T with a corresponding pressure P_1^b.

At each point along the isothermal path shown in Figure C-1(a), Boyle's Law states that the quantity PV must be equal to a constant [207]. From this, we can directly write down that the desired end state pressure (P_1^a) is equal to

$$P_1^a = P_0 \frac{V_0}{V_1} \tag{C.1}$$

In addition, the work done along the isotherm by the expanding gas is found to be

$$W^a = -\int_{V_0}^{V_1} P(V)dV = -P_0 V_0 \ln\left(\frac{V_1}{V_0}\right) \tag{C.2}$$

Finally, for the gas we must also calculate the amount of heat exchanged with the reservoir during the expansion. This additional means of changing the internal energy of the gas is a degree of freedom that the helices do not possess (i.e. they can only do mechanical work). The entropy of an ideal gas is given by [121]

$$\frac{S}{K_{\mathrm{B}}} = \frac{3}{2}N + N\ln\left(\frac{V}{N}T^{3/2}\right) + \frac{3}{2}N\ln\left(\frac{mK_{\mathrm{B}}}{2\pi\hbar^2}\right) \tag{C.3}$$

where N is the number of gas particles and m is their mass. The heat transferred during the expansion may then be calculated from

$$Q = \int_{\text{initial}}^{\text{final}} T dS \tag{C.4}$$

where dS must be evaluated from Equation C.3 taking into account any imposed constraints on T and V.

Along the isotherm, T is held constant as V changes which reduces Equation C.4 to

$$Q^a = T\int dS = T\int_{V_0}^{V_1} NK_{\mathrm{B}}\frac{dV}{V} = NK_{\mathrm{B}}T\ln\left(\frac{V_1}{V_0}\right) \tag{C.5}$$

From the ideal gas law we know that $NK_{\mathrm{B}}T$ is equal to P_0V_0, and thus we have that the total change in the energy of the gas is equal to

$$\Delta E^a = Q^a + W^a = P_0V_0\ln\left(\frac{V_1}{V_0}\right) - P_0V_0\ln\left(\frac{V_1}{V_0}\right) = 0 \tag{C.6}$$

This result was expected because the internal energy of an ideal gas is only a function of the temperature, and thus it cannot change during an isothermal process.

We must now compare these results to those derived from the two-step expansion. Along the isobaric portion of the path shown in Figure C-1(b), the Law of Charles and Gay-Lussac gives us the condition that V/T must be equal to a constant [207]. Thus the intermediate temperature reached when the volume is increased at constant pressure is found to be

$$\tilde{T} = T\frac{V_1}{V_0} \tag{C.7}$$

Along the second portion of the path corresponding to an isochoric cooling of the gas, the ideal gas law yields the constraint that the quantity P/T is a constant. This

condition results in a value for the end-state pressure given by

$$P_1^b = P_0 \frac{T}{\tilde{T}} \tag{C.8}$$

Substituting Equation C.7 into the above, we find the end state pressure along the two-step path to be

$$P_1^b = P_0 \frac{V_0}{V_1} \tag{C.9}$$

This result is exactly the expression given in Equation C.1 for the direct isothermal path as we claimed it would be.

We must now calculate the change in energy of the gas along this path. The gas can do no work along the constant volume portion of the expansion, and thus the total amount of mechanical work done by this two step expansion yields the simple result that

$$W^b = -\int_{V_0}^{V_1} P_0 dV = -P_0[V_1 - V_0] \tag{C.10}$$

This value, as expected, is larger in magnitude than the work calculated in Equation C.2 for the direct path. Along the isobaric portion of the expansion, $T = \left(\frac{P_0}{NK_B}\right)V$ and thus the amount of heat exchanged is given by

$$Q^{b,1} = \int TdS = \int_{V_0}^{V_1} \left(\frac{P_0 V}{NK_B}\right)\left(\frac{5}{2}NK_B\frac{dV}{V}\right) = \frac{5}{2}P_0[V_1 - V_0] \tag{C.11}$$

Along the isochoric leg, V is held fixed while the temperature changes from $\tilde{T}$ back to T. Inserting this constraint into Equations C.3 and C.4, we have that the heat exchanged along this portion of the expansion is equal to

$$Q^{b,2} = \int TdS = \int_{\tilde{T}}^{T} T'\left(\frac{3}{2}NK_B\frac{dT'}{T'}\right) = \frac{3}{2}NK_B[T - \tilde{T}] \tag{C.12}$$

Substituting Equation C.7 into the above, and using the ideal gas law to replace NK_BT by P_0V_0, we may re-express this result as

$$Q^{b,2} = \frac{3}{2}P_0[V_0 - V_1] \tag{C.13}$$

Finally, combining Equations C.10, C.11, and C.13, we have that the total change in the energy of the gas along the two-step path is

$$\Delta E^b = Q^{b,1} + Q^{b,2} + W^a = \frac{5}{2}P_0[V_1 - V_0] + \frac{3}{2}P_0[V_0 - V_1] - P_0[V_1 - V_0] = 0 \quad \text{(C.14)}$$

Again, exactly as we found for the direct path, the total change in the internal energy is zero because the initial and final temperatures are equal.

We have thus shown that, even though the work done along the two step path is in general greater than the work done in following the isotherm directly, both means of expansion end up predicting the same final pressure and the same total change in the internal energy of the gas. This equivalence guarantees that the end state configuration for the gas is the same regardless of the path chosen. The simple thermodynamic analogy presented in this appendix demonstrates the applicability of our technique for imposing the external constraint, and helps clarify our evaluation of the applied torque required to maintain the clamped end boundary condition given in section 3.4.3.

Appendix D

Derivation of the Energy Due to a Surface-Tension Imbalance

As we described in section 4.3.2, the only choice for the form of the spontaneous bending energy in F that is consistent with our experimental results for the change in radius under extension and compression is an isotropic spontaneous curvature. For cylindrical deformations such as those we are considering, there is a well-defined neutral surface within the ribbon, and thus we know that the outer surface must be stretched whereas the inner surface must be compressed. For the previous models of helix formation, this symmetry was broken by explicitly including the effects of the packing asymmetry due to chirality. Our model, however, requires that the symmetry between the inner and outer surfaces of the ribbon be broken by some other process. In order to discuss one plausible physical model which would lead to the type of bending term we added phenomenologicaly to the crystalline free energy (Equation 4.46), we will examine the consequences of imposing a difference in surface tension between the two ribbon faces. We will then conclude this appendix with a discussion of how such a broken symmetry could occur and show that this picture is at least consistent with our current experimental observations.

The free energy of a surface of area A and constant surface tension σ is given simply by [29]

$$F_{\text{sur}} = A \times \sigma \tag{D.1}$$

Therefore, in order to calculate the contribution to the total energy of a helix from a difference in surface tension between its two faces, we have merely to calculate the difference in area between the stretched outer surface and the compressed inner surface. (We may ignore the contributions from the other four sides because the thickness of the ribbon is assumed to be negligible compared to either its contour length or its width). Figure D-1 below shows a typical section of a ribbon that has been bent into a helix with a pitch angle between zero and ninety degrees.

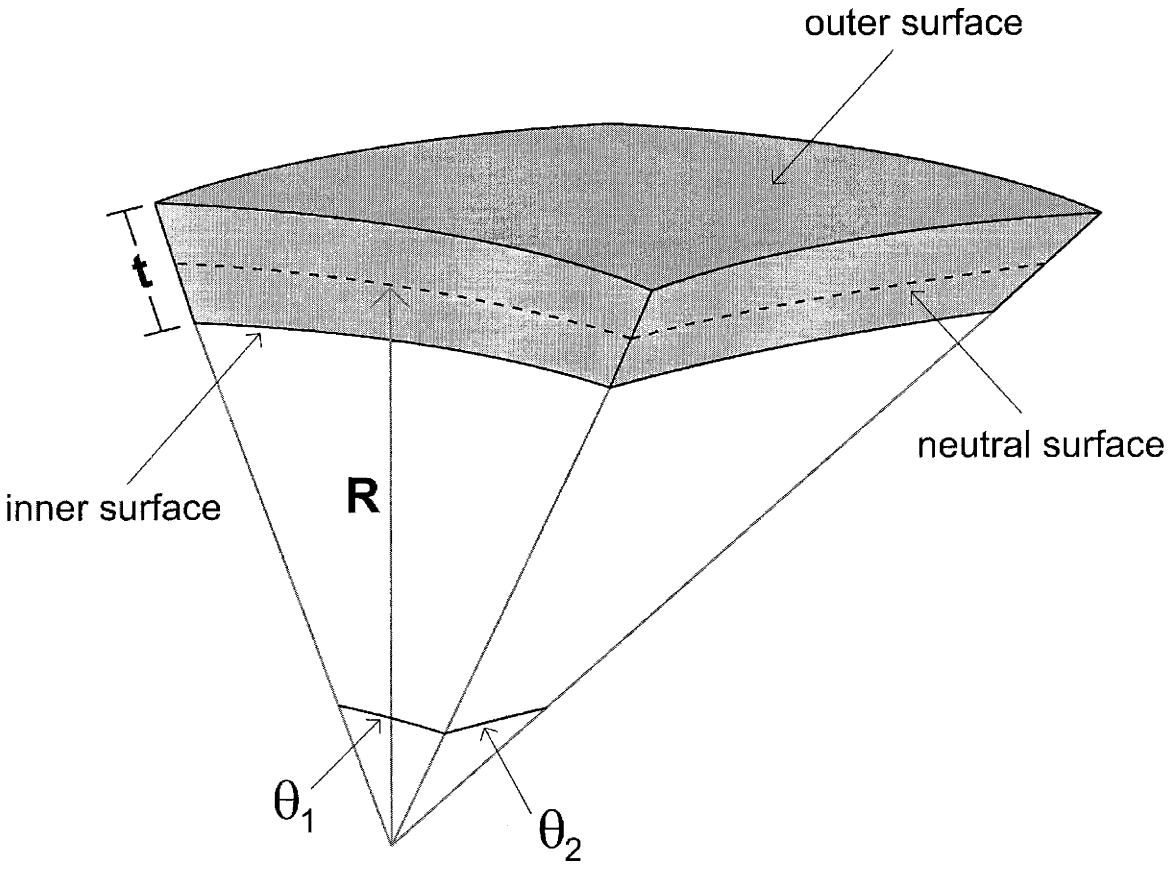

Figure D-1: Schematic illustration of a short section of a ribbon that has been bent into a helix with finite pitch. The figure labels the stretched outer surface (top), the compressed inner surface (bottom), and the neutral surface (dashed line) that separates the two regions. [NOTE: the thickness of the ribbon has been greatly exaggerated for clarity.]

The neutral surface, indicated by the dashed line in Figure D-1, undergoes neither stretching nor compression and thus may be used to relate the two arc angles (θ_1 and θ_2) to the unstressed contour length (s) and width (w) of the ribbon. Upon inspection of the geometry, θ_1 is seen to be the azimuthal angle swept out along the contour length of the ribbon from one end to the other. This is exactly the definition of the angle Φ introduced in section 3.3.2 (see Figure 3-2). Using the expression for Φ given in Equation 3.8 (i.e. $\Phi = s\cos(\psi)/R$) we may immediately write down that

$$s = \frac{R}{\cos(\psi)}\theta_1 \tag{D.2}$$

A simple rotation of our coordinate system by 90° gives us that the width is related to the other desired arc angle by

$$w = \frac{R}{\sin(\psi)}\theta_2 \tag{D.3}$$

With these two relationships, we have everything necessary to determine the difference in area between the two bounding surfaces of the ribbon. In the bent state we know that the two arc angles swept out by the ribbon must be equal for the compressed inner, neutral middle, and stretched outer surfaces. Therefore, in order to calculate the contour length (s_{out}) and width (w_{out}) of the outer surface, we merely have to replace the radius of the neutral surface (R) with the radius of the outer face ($R + \frac{t}{2}$) in Equations D.2 and D.3 respectively. Similarly, we can find s_{in} and w_{in} for the inner surface by replacing the neutral radius with R - $\frac{t}{2}$. Making these substitutions, we find that the area of the outer and inner ribbon faces (i.e. contour length times width) may be written as

$$A_{\text{out}} = \frac{\left(R + \frac{t}{2}\right)^2}{\cos(\psi)\sin(\psi)}\theta_1\theta_2 \tag{D.4}$$

and

$$A_{\text{in}} = \frac{\left(R - \frac{t}{2}\right)^2}{\cos(\psi)\sin(\psi)}\theta_1\theta_2 \tag{D.5}$$

respectively. Some care must be taken, however, when dealing with these two results since we must include only the lowest order changes in the ribbon area. If we were

to keep the terms of order $\left(\frac{t}{R}\right)^2$ we would be describing a deformation that changes the shape of the entire ribbon, and thus we would no longer be able to define a neutral surface (i.e. we would no longer be in the small deformation limit). This type of deformation would correspond to an overall stretching of the ribbon and would require additional terms in order to describe its energy cost which we already ignored in our derivation of the elastic energy (see Equation 4.36 in section 4.3.2). Therefore, we must keep only those terms in Equations D.4 and D.5 that are of first order in $\left(\frac{t}{R}\right)$ in order to remain consistent. Carrying out this expansion, and using Equations D.2 and D.3 to eliminate θ_1 and θ_2 in favor of the more convenient variables s and w, we have

$$A_{\text{out}} \approx sw\left(1 + \frac{t}{R}\right) \tag{D.6}$$

and

$$A_{\text{in}} \approx sw\left(1 - \frac{t}{R}\right) \tag{D.7}$$

Combining these two expressions with Equation D.1, the total contribution to the energy of the ribbon due to surface tension is found to be

$$F_{\text{sur}} = sw\left(\sigma_{\text{out}} + \sigma_{\text{in}}\right) + sw\left(\sigma_{\text{out}} - \sigma_{\text{in}}\right)\frac{t}{R} \tag{D.8}$$

where σ_{out} and σ_{in} are the surface tension of the outer and inner faces respectively. We can simplify this expression by introducing the average $\left(\bar{\sigma} = \frac{\sigma_{\text{in}}+\sigma_{\text{out}}}{2}\right)$ and the difference $(\delta\sigma = \sigma_{\text{in}} - \sigma_{\text{out}})$ surface tensions. We chose the order of the sigmas in the definition of the difference surface tension because we know that the inner surface is compressed relative to the outer surface and thus, as defined, $\delta\sigma$ will be positive to ensure mechanical stability of the helix. With these definitions, the total contribution of the surface energy then takes on the simple form

$$F_{\text{sur}} = 2sw\,\bar{\sigma} - sw\,\delta\sigma\frac{t}{R} \tag{D.9}$$

The first term in Equation D.9 is a constant and has the simple physical interpretation of being the average surface tension of the ribbon times the total area of both faces. The free energy of the helix is only defined up to an overall additive constant, and

therefore without loss of generality we may drop this first term. The second term is easily recognized as being of the exact form that was added by hand to Equation 4.46 with the following definition

$$K_s \equiv t\,\delta\sigma \tag{D.10}$$

Thus we have shown that a difference in surface tension between the inner and outer faces of the ribbon would lead to an energy advantage for bending equivalent to an effective isotropic spontaneous curvature exactly as we argued in section 4.3.2.

We must now examine whether such a surface tension imbalance could reasonably develop for our helical ribbons. Models that explicitly break the top-bottom symmetry of a bilayer have been proposed previously. As discussed in section 4.2.2, the symmetry breaking model proposed Seifert *et al.* improves upon the symmetric bilayer models by allowing for a chiral ground state even for achiral molecules or racemic mixtures of opposite enantiomers [186]. Within this context, it is interesting to note that Konikoff *et al.* found the filament precursors of helical ribbons to be a polymorph of cholesterol monohydrate crystals and anhydrous cholesterol covered by a monolayer of phosphotidylcholine [190, 191]. It is therefore possible that upon the lateral growth of the filament into a thin ribbon, the lipid monolayers on either side of the plate loose their symmetry by developing either a concentration or compositional imbalance. This difference in lipid coating would lead to just the type of difference in surface tension examined here and thus allow the strip to bend into a helix.

In addition to demonstrating a how a particular physically plausible broken symmetry would lead to the spontaneous bending energy given in Equation 4.46, we have also shown explicitly that the curvature modulus K_s will likely have a different thickness dependence than the elastic energy constants K_α, K_β, and K_γ which all scale as the thickness cubed (see section 4.3.2). As we discussed previously, this difference in scaling will lead to a helix radius that is thickness dependent (Equation 4.48). This fact provides one possible explanation of why the radii of the helices formed in the quaternary systems are quite polydisperse whereas the pitch angles (for which the thickness dependence cancels out) are quite monodisperse. There may, however, be factors in addition to varying ribbon thickness that would contribute to the observed

polydispersity of the helix radii. Given the wide variation in radii among the various quaternary systems, it is possible that the detailed microscopic packing of the molecules within the ribbons sets the same value of $\delta\sigma$ for all helices within a particular chemical system. Another possibility, however, is that the ribbon asymmetry is instead controlled dynamically by a difference in the concentration or composition of the fatty acids / phospholipids present on the two surfaces. This imbalance could be set entirely by the local chemical environment of the helix, and thus the K_s modulus may vary between helices even for the same ribbon thickness.

There are, however, two sets of experimental observations available to argue against a variable mechanism for K_s. First, we know from the recent experiments using florescently labeled fatty acids[1] that the low-pitch helices in CDLC are free to continually exchange fatty acids with the surrounding environment. The helices were observed to integrate a significant amount of the florescent fatty acid after less than an hour with no apparent disruption of their structure. We have followed individual helices for up to forty-eight hours at various concentrations of CDLC, and we have observed no change in the radius of the helices. The amount of time we tracked the helices was more than sufficient to have observed any effect if the composition or concentration of the fatty acids was set simply by the local chemical environment. Second, we have (on rare occasions) observed helices that do not have a uniform radius along their length and, in fact, appear to me made up of distinct domains. Maintaining a domain boundary such as this costs elastic energy, and therefore it is unlikely that a helix would retain such a defect for long if it was able to relax by continuously varying the surface tension imbalance. It is more likely that this type of helix configuration is caused by a ribbon that grew with domains of two different thicknesses. This type of thickness defect could relax through the addition of material to the helix as the ribbon grows, which as we argued, is extremely slow compared to the time we have tracked individual helices.

In order to more explicitly probe the possible physical mechanisms for the spontaneous curvature and to determine whether it is fixed or varies among helical ribbons,

[1]Results not shown

a direct measurement of the radius-thickness relationship for a wide variety of low and high pitch helices is needed. As of this writing, an extension of the AFM protocol described in section 2.3.2 is already underway in order to carry out such an experiment.

Appendix E

Domain Separation in a High-Pitch Helix Under Tension

In section 5.3 we presented a detailed theoretical analysis of the tension induced straightening transition for the low-pitch helices in CDLC using our crystalline model free energy. This transition has been explored experimentally in a variety of low-pitch helices, unfortunately the nature of the epoxy tether makes similar experiments very difficult to perform with high-pitch helices (see section 2.4.2). Despite these experimental difficulties, we have been able to observe a reversible transition in a single high-pitch helix that appears to be very similar in characteristics to the type of domain separation observed routinely for low-pitch helices (see the discussion in section 2.5). Although more experiments obviously need to be carried out to confirm our interpretation of this phenomenon and to verify our measurements, it will be instructive to examine the theoretical consequences of our preliminary data, and to compare the results of this analysis for the free energy parameters with those found for the low-pitch helices.

As noted before, we know that the material conservation rules worked out in section 3.5.1 (Equation 3.50) apply equally well to all two domain separations, and thus they may be applied directly to this transition. In addition, the stability constraints discussed in sections 3.5.2 and 3.5.3 (including the forms of the reduced free energies

$\hat{\tilde{F}}(\nu)$ and $\hat{\bar{F}}(\nu)$ and the axial tensions $\tilde{J}_{\|}(\nu)$ and $\bar{J}_{\|}(\nu)\Big)$ apply in exactly the same form in this analysis as they did for the case of the straightening transition in low-pitch helices. This is a necessary requirement since in both cases we are starting from the same underlying model for the form of the free energy $F(R, \ell, s)$. In fact, the only difference between the results in this analysis, and those in section 5.3 will be that the values of the free energy parameters (K_α, K_β, K_γ, and K_s) must now be such that they properly describe the geometry of a high-pitch helix. For example, in section 4.3.3 we found that the unstressed equilibrium pitch angle was related to the three elastic energy constants through

$$\tan^2(\psi_o) = \frac{K_\alpha - K_\beta}{K_\gamma - K_\beta} \tag{E.1}$$

which works out to give a ratio of 0.038 for a low-pitch helix (11°) but 1.89 for a high-pitch helix (54°). Using Equations 5.29 and 5.30 for the tension in the crystalline model, along with the values of the elastic energy constants worked out below (Equation E.11), we may immediately plot the typical force versus extension curves of a high-pitch helix for both the free ($\tilde{J}_{\|}$) and clamped ($\bar{J}_{\|}$) end boundary conditions (Figure E-1).

We see that the clamped end constraint once again leads to a monotonically increasing tension upon extension due to the requirement that the radius shrink to zero as the pitch angle approaches 90°. Thus, we again predict that only for the case of zero torque will we expect to observe any type of stable two domain separation in a high-pitch helical ribbon. Plugging Equation 5.29 for $\tilde{J}_{\|}(\nu)$ into the equal area stability constraint (Equation 3.61), we recover the condition that

$$\begin{aligned} \int_{\nu_1}^{\nu_2} \tilde{J}_{\|}(\nu')d\nu' &= \tilde{J}_{\|}(\nu_1) \times [\nu_2 - \nu_1] \\ \hat{\tilde{F}}(\nu_2) - \hat{\tilde{F}}(\nu_1) &= \tilde{J}_{\|}(\nu_1) \times [\nu_2 - \nu_1] \end{aligned} \tag{E.2}$$

where again $\nu_2 > \nu_1$. In section 2.5.2 we argued that for the high pitch helix shown in Figure 2-17 $\Big(w = (10 \pm 1)\ \mu\text{m}$, $s = (720 \pm 16)\ \mu\text{m}$, $R_o = (16.58 \pm 0.40)\ \mu\text{m}$, and $\psi_0 = (53.9 \pm 1.3)^\circ\Big)$, one domain was straight (i.e. $\nu_2^{\text{expt}} = 1$) while the other domain

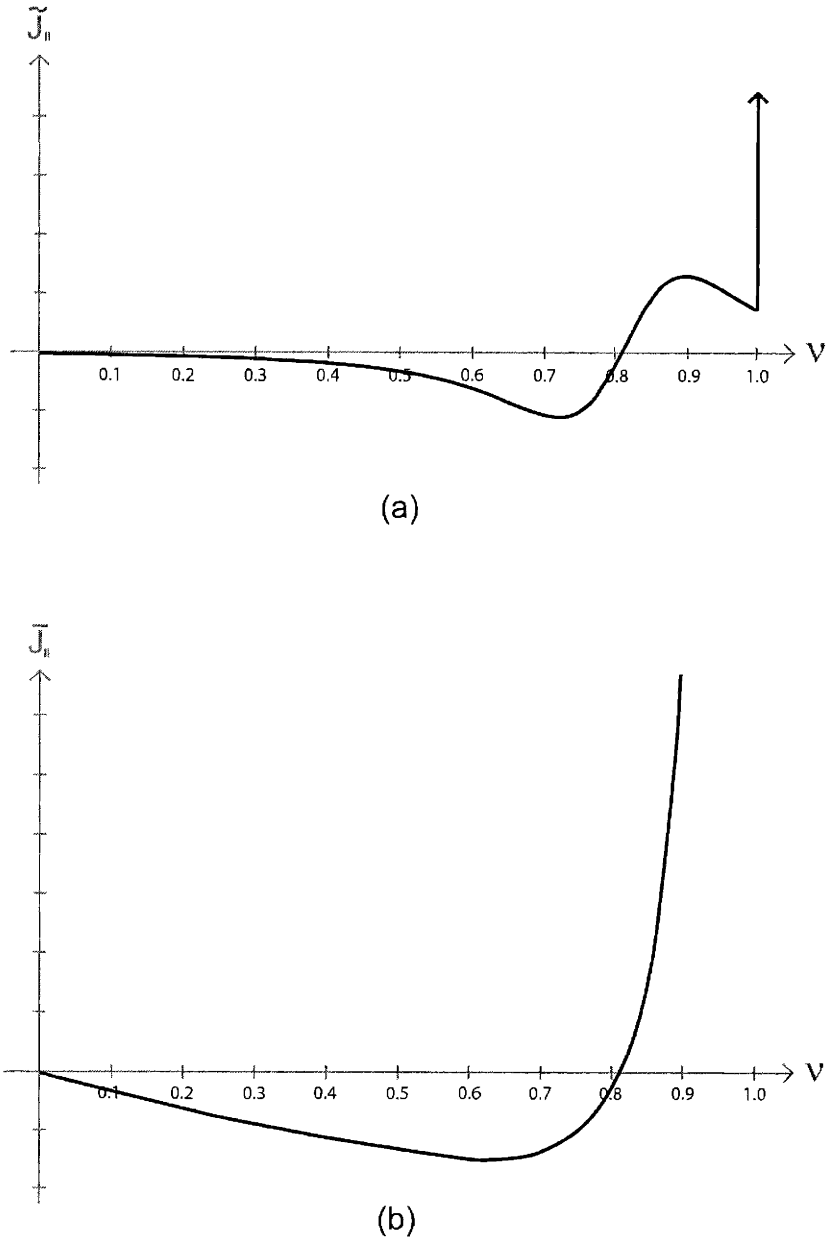

Figure E-1: A typical graph of the theoretical tension vs. inverse axial density curves for the case of extensions with zero external torque (a) and for the case of extensions with clamped ends (b) for a high-pitch helix. For consistency with the results of this section, the elastic energy constants used to generate these plots have been set to the ratios calculated in Equation E.11 while their overall magnitudes have been left arbitrary. The vertical scale in plots (a) and (b) has been set the same in order to allow for more easy comparison of the shape and relative magnitudes of the two functions.

was helical with a pitch angle of $\psi_1^{\text{expt}} = 59.6 \pm 1.7°$ (i.e. $\nu_1^{\text{expt}} = 0.863 \pm 0.015$). We must now attempt to find the values of the parameters in our free energy that will reproduce these values theoretically.

First, in order to verify that $\nu_2 = 1$ is a physically achievable condition in our model, we must examine what the restriction in the allowed range of ν is for a high-pitch helix due to the finite ribbon width. As before, the condition for neighboring turns of a helix to collide and cause the structure to close up into a tubule is given by Equation 3.63 for a pure tension. For the crystalline model, this boundary condition can once again be written as

$$\frac{w}{R_o} = 2\pi\tilde{\nu}_b \frac{f(\tilde{\nu}_b)}{f(\nu_o)} \tag{E.3}$$

where we have used Equation 5.1 for the radius $\left(\tilde{R}(\nu) = (2/K_s)f(\nu)\right)$. As we found in our treatment of the low pitch helices (Equation 5.33), this boundary condition can only be solved numerically in the case of non-zero width. Solving the edge collision condition in Equation E.3 graphically for the high-pitch helices, we find that there is always a lower bound for the inverse axial density (ranging from $\tilde{\nu}_{b,\text{lower}} = 0$ for $w = 0$ to $\tilde{\nu}_{b,\text{lower}} = \nu_o$ for $w = w_{\max} = 2\pi\nu_o R_o$), but that there is no allowed choice of free energy parameters for which an upper bound appears.

This lack of an upper boundary for the pitch angle can be easily understood by examining how the radius changes as ψ approaches 90°. From Equation 5.1, we find that the radius of the straight domain (see Figure 4-7) relative to the unstressed helix radius will scale like

$$\frac{\tilde{R}(\psi = 90°)}{R_o} = \frac{K_\gamma(K_\alpha - 2K_\beta + K_\gamma)}{K_\alpha K_\gamma - K_\beta^2} \tag{E.4}$$

which works out to 2.92 ± 0.75 using the values of the elastic energy constants summarized in Equation E.11. Thus, in this case, the straight domain is predicted to have a radius of curvature which is only about three times that of the unstressed radius (as compared to 27 times for a low pitch helix). However, this non-zero radius for a straight ribbon will once again allow the helix to completely unwind and eliminate all of its turns as it is extended, which obviously removes the possibility of two neighboring turns colliding for $\nu > \nu_o$.

Now that we have verified that $\nu_2 = 1$ is a theoretically allowed solution for real helices, we may substitute it into Equation E.2 to find the following equation for ν_1 in terms of K_α, K_β, and K_γ

$$\left(\frac{1}{K_\gamma} - \frac{1}{f(\nu_1)}\right) = -\nu_1\left(\frac{(K_\alpha - 2K_\beta + K_\gamma)\nu_1^2 - (K_\alpha - K_\beta)}{f(\nu_1)^2}\right)[1 - \nu_1] \tag{E.5}$$

This equation cannot be solved analytically, however (as discussed in section 5.3), we may rearrange the stability condition to be viewed instead as an equation for the ratios of the elastic energy constants (K_α/K_γ and K_β/K_γ) given the measured value of ν_1. For consistency with our previous work on the straightening transition in low-pitch helices, we will again define ν_1 to be a constant given by $\nu_\mathrm{h} = \nu_1^{\mathrm{expt}} = 0.863 \pm 0.015$. Using Equation 5.28) to replace the ratio K_α/K_γ by

$$\frac{K_\alpha}{K_\gamma} = \frac{\nu_\mathrm{o}^2}{1 - \nu_\mathrm{o}^2} + \left(1 - \frac{\nu_\mathrm{o}^2}{1 - \nu_\mathrm{o}^2}\right)\frac{K_\beta}{K_\gamma} \tag{E.6}$$

we find that the stability constraint may be reduced to the following simple quadratic equation for K_β/K_γ

$$a_\mathrm{oh}^2\left(\frac{K_\beta}{K_\gamma}\right)^2 - [a_\mathrm{oh}(2a_\mathrm{oh} + 1) - b_\mathrm{oh}]\left(\frac{K_\beta}{K_\gamma}\right) + a_\mathrm{oh}(a_\mathrm{oh} + 1) - b_\mathrm{oh} = 0 \tag{E.7}$$

where the two phenomenological parameters a_oh and b_oh are given by

$$\begin{aligned} a_\mathrm{oh} &\equiv (2\nu_\mathrm{o}^2 - \nu_\mathrm{h}^2 - 1)\frac{1 - \nu_\mathrm{h}^2}{1 - \nu_\mathrm{o}^2} = -(0.323 \pm 0.016) \\ b_\mathrm{oh} &\equiv 4\nu_\mathrm{h}(1 - \nu_\mathrm{h})\frac{\nu_\mathrm{o}^2 - \nu_\mathrm{h}^2}{1 - \nu_\mathrm{o}^2} = -(0.125 \pm 0.024) \end{aligned} \tag{E.8}$$

Finally, Equation E.7 may be factored analytically, to yield the single physically allowed solution

$$\frac{K_\beta}{K_\gamma} = 1 - \left((b_\mathrm{oh} - a_\mathrm{oh})/a_\mathrm{oh}^2\right) \tag{E.9}$$

just as we found in section 5.3.

We may now substitute this solution for K_β/K_γ along with the unstressed inverse axial density (ν_o) back into Equation E.6 in order to find the value of the elastic anisotropy (K_α/K_γ) for the high-pitch helical ribbons. In addition, we may rearrange Equation 5.1 in order to find K_s/K_γ given the previously determined ratios of the

elastic energy constants and the measured value of the unstressed helix radius (R_o). Thus, we now have three equations for the three ratios of the parameters in our model free energy. Solving these relationships given the measured values of $\nu_o = 0.808 \pm 0.014$, $\nu_h = 0.863 \pm 0.015$, and $R_o = (16.58 \pm 0.40)\mu$m, we find that the three thickness independent ratios for the high pitch helix under investigation are

$$\begin{aligned} \frac{K_\beta}{K_\gamma} &= -0.90 \pm 0.26 \\ \frac{K_\alpha}{K_\gamma} &= 2.67 \pm 0.56 \\ \frac{K_s R_o}{K_\gamma} &= 0.68 \pm 0.14 \end{aligned} \tag{E.10}$$

From these results we note that our model predicts very different microscopic elastic properties for the high-pitch helices compared to those for the low-pitch helices in CDLC (assuming that our observation is of a true tension induced straightening transition). The first thing to note about the above results is that the ratio of the coupling between the two bending modes (K_β) is negative and close to K_γ in magnitude. In order to explain the differences in the unstressed pitch angle between the two types of helices (i.e. 11° versus 54°), we have always assumed that the elastic anisotropy (K_α/K_γ) of a low-pitch ribbon was different than that of a high-pitch ribbon. It is therefore not entirely surprising that we should require the ratio of the other elastic energy constants to also be different. However, the fact that the coupling constant is negative requires some careful consideration. Examining the definition of K_β in terms of the components of the elastic modulus tensor (λ_{ijkl}), we note that a negative value for this constant cannot immediately be ruled out theoretically [28], and thus we will continue to examine the consequences of our current predictions. In addition to a large negative value of K_β, we also note that the spontaneous curvature ratio (K_s/K_γ) is roughly one order of magnitude greater for the high-pitch helix than for the typical low-pitch helices. This difference is particularly interesting given the other experimental evidence for differences in the surface properties of the two types of helical ribbons. In particular, section 2.4.2 notes the difference in tethering between the high and low-pitch helices in CDLC and section 2.4.2 in [28] details the qualitatively

different fluorescent signatures of the helices in a related model bile system.

Turning to the limit of metastability for this transition, we must now attempt to find the extremum of the tension from the following equation

$$5(K_\alpha - 2K_\beta + K_\gamma)^2\left(\nu_{J_{\max}}^2\right)^3 - 9(K_\alpha - K_\beta)(K_\alpha - 2K_\beta + K_\gamma)\left(\nu_{J_{\max}}^2\right)^2$$
$$-3[K_\alpha(K_\alpha - 2K_\beta + K_\gamma) - 2(K_\alpha - K_\beta)^2]\left(\nu_{J_{\max}}^2\right) + K_\alpha(K_\alpha - K_\beta) = 0 \quad \text{(E.11)}$$

which was derived by setting the derivative of $\tilde{J}_{\|}(\nu)$ equal to zero. Solving this equation given the ratios of the elastic energy constants in Equation E.11, we find a theoretical prediction of $\nu_{J_{\max}} = 0.898 \pm 0.018$ which corresponds to a pitch angle of $\psi_{J_{\max}} = (63.9 \pm 2.5)^\circ$. While we were not been able to probe this limit as closely as we were for the low pitch helices due to the larger ambient vibrations occurring in the sample during this particular experiment, we can note that the largest pitch angle achieved for the high-pitch helix under extension was $\psi_{\max}^{\text{expt}} = (60.8 \pm 1.6)^\circ$ corresponding to an inverse axial density of $\nu_{\max}^{\text{expt}} = 0.873 \pm 0.013$. As required, this maximum observed pitch angle is close to, but less than, the theoretical limit we predict. Thus, overall our experimental results are again seen to be consistent with our interpretation and theoretical treatment of this mechanical transition. With this determination, we can finally plot in Figure E-2 a more detailed graph of our theoretical prediction for the axial tension of this typical high-pitch helix in CDLC in order to make explicit the various features of its equal area construction.

As we did for our treatment of the low-pitch helices in section 5.3, we will conclude this appendix with a brief discussion of our predictions for the response of a high-pitch helix under axial compression. Examining Figures E-1(a) and (b) above, we see again that the tension for both constraints have a minimum value below which a helix becomes mechanically unstable. For the free end boundary condition, this minimum occurs at $\tilde{\nu}_{J_{\min}} = 0.722 \pm 0.017$ corresponding to a pitch angle of $(46.2 \pm 1.4)^\circ$, while for the clamped end constraint, the minimum occurs at $\bar{\nu}_{J_{\min}} = 0.613 \pm 0.052$ $\left(\bar{\psi}_{J_{\min}} = (37.8 \pm 3.9)^\circ\right)$. Both of these values are sufficiently far from the unstressed equilibrium to allow for accurate measurements in principle, and it is interesting to note that unlike the low-pitch case where the results for the clamped and free end

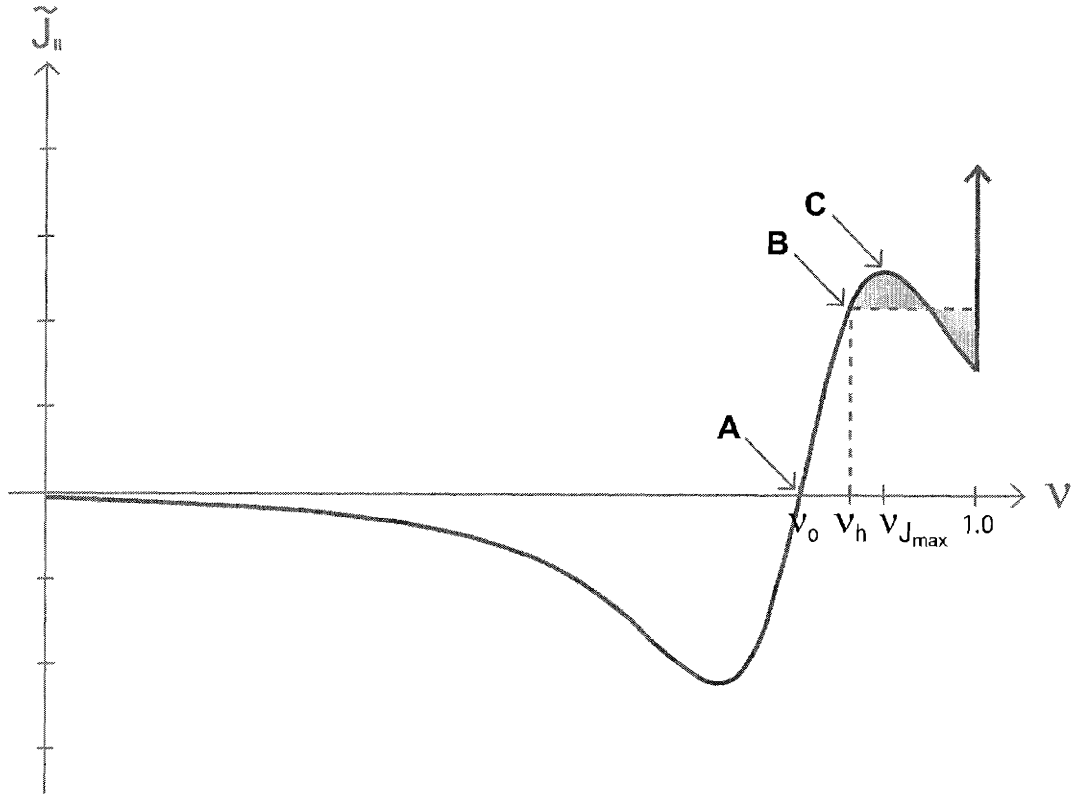

Figure E-2: A plot of the theoretical tension in arbitrary units vs. ν for the high-pitch helix showing the appropriate equal area stability condition. The figure also labels the free equilibrium value of ν (Point A: $\nu_o = 0.808$), the value of the order parameter in the helical phase (Point B: $\nu_h = 0.863$), and the limit of metastability with respect to the straightening transition (Point C: $\nu_{J_{max}} = 0.898$).

constraints were always within our uncertainty of one another, the results for the high-pitch case are easily distinguishable for the two conditions.

As noted throughout this work, the material conservation (Equation 3.50) and domain stability (Equation 3.61) conditions worked out in Chapter 3 are applicable to any type of two domain transition under tension, and thus they may be applied directly to the current problem. For consistency we will again define the helical region of the separated ribbon to be domain 1, while the tubule region will be labeled as domain 2. As before, the tubule domain will form when $\nu = \tilde{\nu}_{\mathrm{b,lower}}$ or $\bar{\nu}_{\mathrm{b,lower}}$ depending upon the constraint imposed on the deformation. The value of this limit obviously depends upon the ratio of the width to the radius of the helix chosen making a general treatment of the transition impossible. Therefore, in order to examine the typical features of our predictions for domain separation under compression, we will choose to analyze the case when $w/R_{\mathrm{o}} = 0.603 \pm 0.075$ which is the value appropriate for the high-pitch helix we have been considering (see Figure 2-17). With this width ratio, we may use the graphical solution to Equation E.3 above to find that the lower bound for the inverse axial density under the free end constraint is given by $\tilde{\nu}_{\mathrm{b,lower}} = 0.0122 \pm 0.0036$. For the clamped end case, we know from Equation 3.66 that the lower boundary of ν is given by

$$\bar{\nu}^2_{\mathrm{b,lower}} = \frac{1}{2} - \frac{1}{2}\sqrt{1 - \left(\frac{1-\nu_{\mathrm{o}}^2}{\pi^2}\right)\frac{w^2}{R_{\mathrm{o}}^2}} \tag{E.12}$$

which works out to $\bar{\nu}_{\mathrm{b,lower}} = 0.0566 \pm 0.0088$ for the given width ratio. These values for the inverse axial density will thus define ν_2 for the tubule domain.

In order to determine pitch angle of the helical domain, we must now substitute the values determined for $\tilde{\nu}_{\mathrm{b,lower}}$ and $\bar{\nu}_{\mathrm{b,lower}}$, as well as those determined for the ratios of the elastic energy constants (Equation E.11) into the domain stability condition. With these substitutions, the equal area construction in Equation E.2 can be written as

$$\begin{aligned}
\hat{\tilde{F}}(\tilde{\nu}_{\mathrm{b,lower}}) - \hat{\tilde{F}}(\tilde{\nu}_1) &= \tilde{J}_{\|}(\tilde{\nu}_1) \times [\tilde{\nu}_{\mathrm{b,lower}} - \tilde{\nu}_1] \\
\hat{\bar{F}}(\bar{\nu}_{\mathrm{b,lower}}) - \hat{\bar{F}}(\bar{\nu}_1) &= \bar{J}_{\|}(\bar{\nu}_1) \times [\bar{\nu}_{\mathrm{b,lower}} - \bar{\nu}_1]
\end{aligned} \tag{E.13}$$

where $\tilde{\hat{F}}(\nu)$ and $\tilde{J}_{\|}(\nu)$ are given by Equations 5.25 and 5.29 and $\bar{\hat{F}}(\nu)$ and $\bar{J}_{\|}(\nu)$ are given by Equations 5.26 and 5.30 respectively. Neither of these two equations can be solved analytically for ν_1, but as usual they may easily be solved numerically. Plugging in the numerical values we have calculated for the constants in Equation E.13, we find

$$\begin{aligned} \tilde{\nu}_1 &= 0.794 \pm 0.017 \qquad & \tilde{\nu}_2 &= 0.0122 \pm 0.0047 \\ \bar{\nu}_1 &= 0.748 \pm 0.016 \qquad & \bar{\nu}_2 &= 0.0566 \pm 0.0088 \end{aligned} \tag{E.14}$$

respectively for the free and clamped end conditions. For comparison, these values for the inverse axial density of the two domains correspond to pitch angles of

$$\begin{aligned} \tilde{\psi}_1 &= (52.6 \pm 1.6)^\circ \qquad & \tilde{\psi}_2 &= (0.70 \pm 0.27)^\circ \\ \bar{\psi}_1 &= (48.4 \pm 1.4)^\circ \qquad & \bar{\psi}_2 &= (3.24 \pm 0.50)^\circ \end{aligned} \tag{E.15}$$

The value of the pitch angle for the helical domain is significantly larger than that of the tubule domain that it would, in principle, be possible to clearly resolve the two regions experimentally. Figure E-3 shows a typical plot of our theoretical predictions for the axial tension upon compression including the equal-area constructions for a high-pitch helix with $w/R_o = 0.603 \pm 0.075$.

Finally, we must discuss the experimental limitations that will once again tend to inhibit the observation of this transition in real systems. For this particular high-pitch helix, we find that the concern of having the two phases coalesce around the minimum of the tension is typically not as serious a concern as it was for the low-pitch helices. This is due primarily to the much longer range of compressions possible for a high-pitch helix relative to a low-pitch helix guaranteeing a large separation of the two domains in general. However, we expect that buckling will be an even greater problem for these structures than it is for the low-pitch variety. This increased susceptibility to buckling is due to the fact that high-pitch helices are typically much longer than low-pitch helices, while their radii are usually on the same order of magnitude. This leads to a much larger slenderness ratio (ℓ_o/R_o) for the high-pitch structures. In particular, the helix that we have been considering has a slenderness ratio of $35.1 \pm$

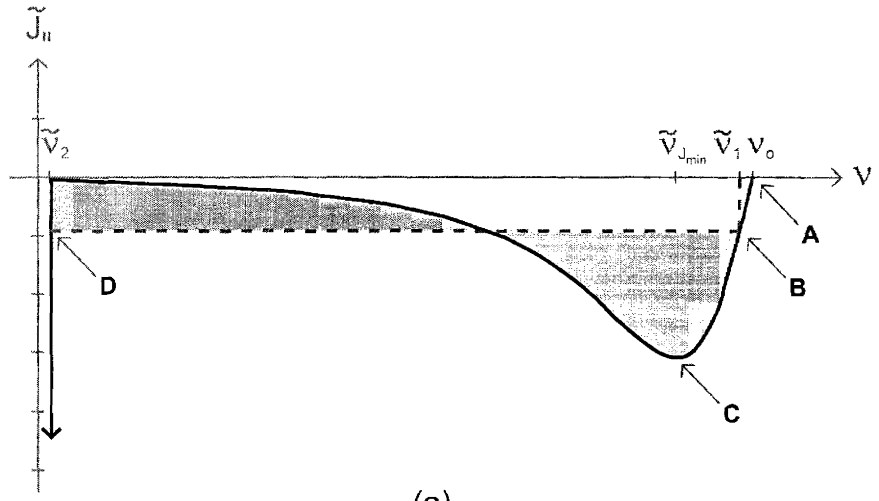

(a)

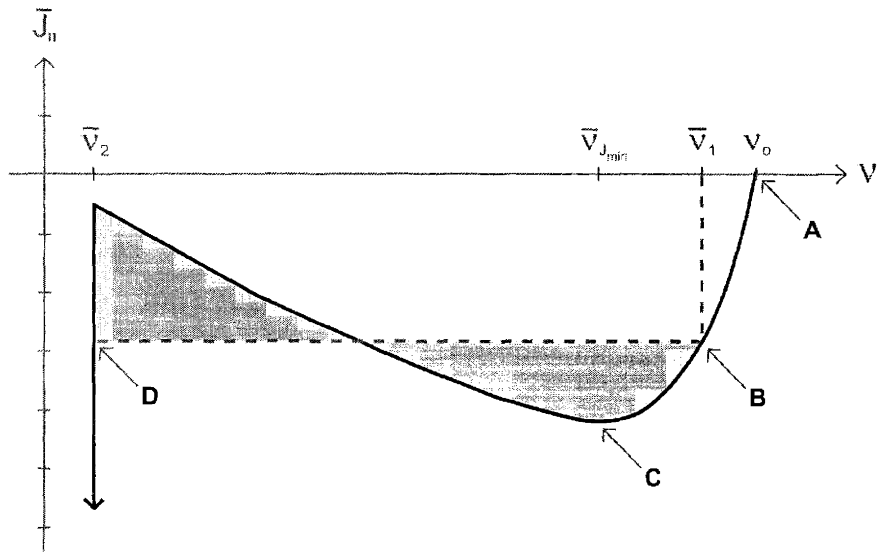

(b)

Figure E-3: A plot of the theoretical tension in arbitrary units vs. ν for a typical high-pitch helix in CDLC with $w/R_o = 0.603 \pm 0.075$ showing the appropriate equal area stability condition upon compression for the free (a) and clamped (b) end constraints. The figure also labels the unstressed equilibrium value of ν (Point A: $\nu_o = 0.808$), the value of the order parameter in the helical phase (Point B: $\tilde{\nu}_1 = 0.794$ / $\bar{\nu}_1 = 0.748$), the limit of metastability (Point C: $\tilde{\nu}_{J_{min}} = 0.722$ / $\bar{\nu}_{J_{min}} = 0.613$), and the lower boundary of ν at which point the helix closes up into a tubule (Point D: $\tilde{\nu}_2 = 0.0122$ / $\bar{\nu}_2 = 0.0566$).

2.3 with only 4.07 $\pm$ 0.47 turns. For comparison, a low pitch helix with this number of turns would have a slenderness ratio of just 4.97 $\pm$ 0.57. In general, we typically want to work with helices of greater than 5 turns, which would correspond to an ℓ_o/R_o of over 40, in order to guarantee that we are correct in ignoring the finite size of the helix in our calculations. At such high aspect ratios, the helix can be expected to buckle under even extremely minor compression forces [199, 200, 201] making most of the region below ν_o, and thus all of the interesting phenomena discussed above, totally inaccessible in real experiments.

There is still clearly much work that needs to be done in order to more fully explore these possible transitions in high-pitch helices under tension, as well as to determine whether or not we have actually observed the type of stable two domain separation clearly seen in low-pitch helices. As new tethers are developed, it will become possible to more easily and routinely deform high-pitch structures, and thus to perform these experiments for many other structures. For now, however, we can note that our preliminary results for the helix pictured in Figure 2-17 strongly suggests the existence of some type of interesting mechanical instability upon extension. In addition, under the assumption that it is a zero torque straightening transition, the data collected has allowed us to determine the three thickness independent ratios of the free energy parameters for the high-pitch helices in CDLC. These values are quite different from those calculated for the low-pitch helices, and indicate a very different microscopic structure for the two types of ribbons. However, the large and negative value predicted above for K_β is quite surprising, and could indicate that our assumptions about the phenomena are incorrect. If the high-pitch helices do, in fact, undergo a new and different type of reversible domain separation, it could possibly offer a more satisfying explanation of the unusual kinks or "wobbles" observed in the straight domain we discussed at the end of section 2.5.2. Either way, this phenomena should be a focus of future experiments looking to explore the mechanisms by which more than 20 chemically distinct quaternary systems end up forming helices of either 11 or 54 degrees.

Bibliography

[1] P. Yager and P.E. Schoen. Formation of Tubules by a Polymerizable Surfactant. *Mol. Cryst. Liq. Cryst.*, **106**: 371-381 (1984)

[2] J.M. Schnur. Lipid Tubules: A Paradigm for Molecularly Engineered Structures. *Science*, 262: 1669-1676 (1993)

[3] M.S. Spector, R.R. Price, and J.M. Schnur. Chiral Lipid Tubules. *Adv. Mater.*, **11** (1999)

[4] D.T. Bong, T.D. Clark, J.R. Granja, and M.R. Ghadiri. Organic Nanotubules. *Angew. Chem. Int. Ed.*, **40**: 988-1011 (2001)

[5] J.M. Schnur, R. Price, P. Schoen, P. Yager, J.M. Calvert, J. Georger, and A. Singh. Lipid-Based Tubule Microstructures. *Thin Solid Films*, **152**: 181-206 (1987)

[6] W. Stockton, J. Lodge, F. Rachford, M. Orman, F. Falco, and P. Schoen. Artificial Dielectric-Properties Of Microscopic Metallized Filaments In Composites. *J. Appl. Phys.*, **70**: 4679-4686 (1991)

[7] F. Behroozi, M. Orman, R. Reese, W. Stockton, J. Calvert, F. Rachford, and P. Schoen. Interaction Of Metallized Tubules With Electromagnetic-Radiation. *J. Appl. Phys.*, **68**: 3688-3693 (1990)

[8] N.J. Meilander , X. Yu , N.P. Ziats , and R.V. Bellamkonda. Lipid-based microtubular drug delivery vehicles. *J. Controlled Release*, **71**: 141-152 (2001)

[9] R.L. Cleek, A.A. Rege, L.A. Dennerm, S.G. Eskin, A.G. Mikos. Inhibition of smooth muscle cell growth in vitro by an antisense oligodeoxynucleotide release from poly(DL−lactic-co-glycolic acid) microparticles. *J. Biomed. Mater. Res.*, **35**: 525-530 (1997)

[10] A.J.S. Jones and J.L. Cleland. Technical and regulatory hurdles in delivery and aspects of macromolecular drugs. *J. Control. Release*, **41**: 147-155 (1996)

[11] A.S. Goldstein, J.K. Amory, S.M. Martin, C. Vernon, A. Matsumoto, and P. Yager. Testosterone delivery using glutamide-based complex high axial ratio microstructures. *Bioorg. Med. Chem.*, **9**: 2819-2825 (2001)

[12] R. Price and M. Patchan. Controlled release from cylindrical microstructures. *J. Microencapsulation*, **8**: 301-306 (1991)

[13] R. Price, M. Patchan, A. Clare, D. Rittschof, and J. Bonaventura. Performance Enhancement of Natural Antifouling Compounds and Their Analogs Through Microencapsulation and Controlled Release. *Biofouling*, **6**: 207-216 (1992)

[14] R. Price and M. Patchan. Entrapment and release characteristics of 2-methoxynaphthalene from cylindrical microstructures formed from phospholipids. *J. Microencapsulation*, **10**: 215-222 (1993)

[15] P. Ringler, W. Muller, H. Ringsdorf, and A. Brisson. Functionalized lipid tubules as tools for helical crystallization of proteins. *Chem. Eur. J.*, **3**: 620-625 (1997)

[16] E.M. Wilson-Kubalek, R.E. Brown, H. Celia, and R.A. Milligan. Lipid nanotubes as substrates for helical crystallization of macromolecules. *Proc. Natl. Acad. Sci. USA*, **95**: 8040-8045 (1998)

[17] J.M. Donovan and M.C. Carey. Physical-Chemical Basis Of Gallstone Formation. *Gastroenterol. Clin. North Am.*, **20**: 47-66 (1991)

[18] F.M. Konikoff, D.S. Chung, J.M. Donovan, D.M. Small, and M.C. Carey. Filamentous, Helical, And Tubular Microstructures During Cholesterol Crystallization From Bile - Evidence That Cholesterol Does Not Nucleate Classic Monohydrate Plates. *Journal Of Clinical Investigation*, **90**: 1155-1160 (1992)

[19] L. Barbara, C. Sama, A.M.M. Labate, and M. Malavolti. Epidemiology and Natural-History of Gallstones. *Problems In General Surgery*, **8**: 525-540 (1991)

[20] D.S. Chung, G.B. Benedek, F.M. Konikoff, and J.M. Donovan. Elastic free energy of anisotropic helical ribbons as metastable intermediates in the crystallization of cholesterol. *Proc. Natl. Acad. Sci. USA*, **90**: 11341-11345 (1993)

[21] N. Nakashima, S. Asakuma, and T. Kunitake. Optical Microscopic Study of Helical Superstructures of Chiral Bilayer Membranes. *J. Am. Chem. Soc.*, **107**: 509-510 (1985)

[22] J.H. Georger, A. Singh, R.R. Price, J.M. Schnur, P. Yager, and P.E. Schoen. Helical and Tubular Microstructures Formed by Polymerizable Phosphatidylcholines. *J. Am. Chem. Soc.*, **109**: 6169-6175 (1987)

[23] J.H. Fuhrhop, P. Schnieder, E. Boekema, and W. Helfrich. Lipid Bilayer Fibers from Diastereomeric and Enantiomeric $N-$Octylaldonamides. *J. Am. Chem. Soc.*, **110**: 2861-2867 (1988)

[24] R.M. Servuss. Helical ribbons of lecithin. *Chem. Phys. Lipids*, **46**: 37-41 (1988)

[25] J.V. Selinger, M.S. Spector, and J.M. Schnur. Theory of Self-Assembled Tubules and Helical Ribbons. *J. Phys. Chem. B*, **105**: 7157-7169 (2001)

[26] K. Shigeyuki and Z.C. Ou-Yang. High- and Low-Pitch Helical Structures of Tilted Chiral Lipid Bilayers. *Phys. Rev. Lett.*, **81**: 473-476 (1998)

[27] Y.V. Zastavker, N. Asherie, A. Lomakin, J. Oande, J.M. Donovan, J.M. Schnur, and G.B. Benedek. Self-assembly of helical ribbons. *Proc. Natl. Acad. Sci. USA*, **96**: 7883-7887 (1999)

[28] Y.V. Zastavker. *Ph.D. Thesis: Self-Assembly of Helical Ribbons From Chiral Amphiphiles.* Massachusetts Institute of Technology, Cambridge (2001).

[29] L.D. Landau and E.M. Lifshitz, *Statistical Physics: Part One.* Pergamon Press, Oxford (1980)

[30] T.T. Perkins, D.E. Smith, and S. Chu. Direct Observation of the Tube-Like Motion of a Single Polymer Chain. *Science*, **264**: 819-822 (1994)

[31] T.T. Perkins, S.R. Quake, D.E. Smith, and S. Chu. Relaxation of a Single DNA Molecule Observed by Optical Microscopy. *Science*, **264**: 822-826 (1994)

[32] N. Nakashima, S. Asakuma, J.M. Kim, and T. Kunitake. Helical Superstructures are Formed from Chiral Ammonium Bilayers. *Chem. Lett.*, **10**: 1709-1712 (1984)

[33] K. Yamada, H. Ihara, T. Ide, and T. Fukumoto. Formation of Helical Super Structure from Single-Walled Bilayers by Amphiphiles with Oligo-L-Glutamic Acid-Head Group. *Chem. Lett.*, **10**: 1713-1716 (1984)

[34] P. Yager, P.E. Schoen, C. Davies, R. Price, and A. Singh. Structure of Lipid Tubules Formed from a Polymerizable Lecithin. *Biophys. J.*, **48**: 899-906 (1985)

[35] R. Oda, I. Huc, M. Schmutz, S.J. Candau, and F.C. MacKintosh. Tuning bilayer twist using chiral counterions. *Nature*, **399**: 566-569 (1999)

[36] J.J.L.M. Cornelissen, M. Fischer, N.A.J.M. Sommerdijk, and R.J.M. Nolte. Helical superstructures from charged poly(styrene)-poly(isocyanodipeptide) block copolymers. *Science*, **280**: 1427-1430 (1998)

[37] F.M. Konikoff, D.S. Chung, J.M. Donovan, D.M. Small, and M.C. Carey. Filamentous, Helical, and Tubular Microstructures During Cholesterol Crystallization From Bile - Evidence That Cholesterol Does Not Nucleate Classic Monohydrate Plates. *J. Clin. Invest.*, **90**: 1155-1160 (1992)

[38] H. Ochi, S. Tazuma, and G. Kajiyama. Lecithin hydrophobicity modulates the process of cholesterol crystal nucleation and growth in supersaturated model bile systems. *Biochem. J.*, **318**: 139-144 (1996)

[39] S. Tazuma, H. Ochi, K. Teramen, Y. Yamashita, K. Horikawa, H. Miura, N. Hirano, M. Sasaki, N. Aihara, S. Hatsushika, S. Tao, T. Ohya, and G. Kajiyama. Degree of Fatty Acyl-Chain Unsaturation in Biliary Lecithin Dictates Cholesterol Nucleation and Crystal-Growth. *Biochim. Biophys. Acta*, **1215**: 74-78 (1994)

[40] Y. Ringel, G.J. Somjen, F.M. Konikoff, R. Rosenberg, and T. Gilat. Increased saturation of the fatty acids in the sn-2 position of phospholipids reduces cholesterol crystallization in model biles. *Biochim. Biophys. Acta*, **1390**: 293-300 (1998)

[41] F.M. Konikoff, D.E. Cohen, and M.C. Carey. Filamentous Crystallization of Cholesterol and Its Dependence on Lecithin Species in Bile. *Mol. Cryst. Liq. Cryst. A*, **248**: 291-296 (1994)

[42] D. Jungst, T. Lang, P. Huber, V. Lange, and G. Paumgartner. Effect of Phospholipids and Bile-Acids on Cholesterol Nucleation Time and Vesicular Micellar Cholesterol in Gallbladder Bile of Patients With Cholesterol Stones. *J. Lipid. Res.*, **34**: 1457-1464 (1993)

[43] J.J. Collins and M.C. Phillips. The Stability and Structure of Cholesterol-Rich Co-Dispersions of Cholesterol and Phosphatidylcholine. *J. Lipid Res.*, **23**: 291-298 (1982)

[44] J.V. Selinger, F.C. MacKintosh, and J.M. Schnur. Theory of cylindrical tubules and helical ribbons of chiral lipid membranes. *Phys. Rev. E*, **53**: 3804-3818 (1996)

[45] B. Smith, Y.V. Zastavker, and G.B. Benedek. Tension-Induced Straightening Transition of Self-Assembled Helical Ribbons. *Phys. Rev. Lett.*, **87**: 278101−1 - 278101−4 (2001)

[46] F. Gunstone, *Fatty Acid and Lipid Chemistry.* Blackie Academic and Professional, Glasgow (1996)

[47] A.A. Spector, S.N. Mathur, and T.L. Kaduce. Lipid nutrition and metabolism of cultured mammalian cells. *Prog. Lip. Res.*, **19**: 155-186 (1981)

[48] G. Rothblat and D. Kritchevsky. *Lipid Metabolism in Tissue Culture Cells.* The Wistar Institute Press, Philadelphia (1967)

[49] T.E. Mittler and R.H. Dadd. *Metabolic Aspects of Lipid Nutrition in Insects.* Westwood Press Incorporated, New York (1983).

[50] R.H. Goodwin. *Cell Biology.* Elsevier Scientific Publications Ltd., London (1985)

[51] B.N. Thomas, R.C. Corcoran, C.L. Cotant, C.M. Lindemann, J.E. Kirsch, and P.J. Persichini. Phosphonate Lipid Tubules 1. *J. Am. Chem. Soc.*, **120**: 12178-12186 (1998)

[52] B.N. Thomas, C.M. Lindemann, and N.A. Clark. Left- and right-handed helical tubule intermediates from a pure chiral phospholipid, *Phys. Rev. E*, **59**: 3040-3047 (1999)

[53] M.S. Spector, A. Singh, P.B. Messersmith, and J.M. Schnur. Chiral Self-Assembly of Nanotubules and Ribbons from Phospholipid Mixtures. *Nano Lett.*, **1**: 375-378 (2001)

[54] Research Services Branch (RSB) of the National Institute of Mental Health (NIMH), Bethesda, MD. *NIH Image V1.61*, available on the Internet at <http://rsb.info.nih.gov/nih-image/>

[55] T.C. Lubensky and J. Prost. Orientational order and vesicle shape. *J. Phys. II France*, **2**: 371-382 (1992)

[56] G. Binnig, C.F. Quate, and C. Gerber. Atomic force microscope. *Phys. Rev. Lett.*, **56**: 930-933 (1986)

[57] S. Alexander, L. Hellemans, O. Marti, J. Schneir, V. Elings, and P.K. Hansma. An atomic resolution atomic force microscope implemented using an optical lever. *J. Appl. Phys.*, **65**:164-167 (1989)

[58] G. Meyer and N.M. Amer. Novel approach to atomic force microscopy. *Appl. Phys. Lett.*, **53**: 1045-1-47 (1988)

[59] Y.L. Lyubchenko, B.L. Jacobs, S.M. Lindsay, and K.A. Dunker. Atomic force microscopy of reovirus dsRNA: a routine technique for length measurements. *Nucl. Acids Res.*, **20**: 3983-3986 (1992)

[60] Y.L. Lyubchenko, P.I. Oden, D. Lampner, S.M. Lindsay, and K.A. Dunker. Atomic force microscopy of DNA and bacteriophage in air, water, and propanol: the role of adhesion forces. *Nucl. Acids Res.*, **21**: 1117-1123 (1993).

[61] B.M. Craven. Crystal structure of cholesterol monohydrate. *Nature*, **260**: 727-730 (1976)

[62] D.A. Kessler and Y. Rabin. Stretching Instability of Helical Springs. *Phys. Rev. Lett.*, **90**: 024301-1 – 024301-4 (2003)

[63] C. Bustamante, J.C. Macosko, and G.L.Wuite. Grabbing the Cat by the Tail: Manipulating Molecules One by One. *Nature Rev. Mol. Cell Bio.*, **1**: 130-136 (2000)

[64] A. Chilkoti, T. Boland, B.D. Ratner, and P.S. Stayton. The relationship between ligand-binding thermodynamics and protein-ligand interaction forces measured by atomic force microscopy. *Biophys. J.*, **69**:2125-2130 (1995)

[65] V.T. Moy., E.L. Florin, and H.E. Gaub. Intermolecular forces and energies between ligands and receptors. *Science*, **266**: 257-259 (1994)

[66] M. Carrion-Vazquez. Mechanical and chemical unfolding of a single protein: a comparison. *Proc. Natl. Acad. Sci. USA*, **96**: 3694-3699 (1999)

[67] A. Kishino and T. Yanagida. Force measurements by micromanipulation of a single actin filament by glass needles. *Nature*, **334**: 74-76 (1988)

[68] J. Howard, A.J. Hudspet, and R.D. Vale. Movement of microtubules by single kinesin molecules. *Nature*, **342**: 154-158 (1989)

[69] K. Svoboda, C.F. Schmidt, B.J. Schnapp, and S.M. Block. Direct observation of kinesin stepping by optical trapping interferometry. *Nature*, **365**: 721-727 (1993)

[70] A. Ishijima, T. Doi, K. Sakurada, and T. Yanagida. Sub-piconewton force fluctuations of actomyosin *in vitro*. *Nature*, **352**: 301-306 (1991)

[71] G.J. Wuite, S.B. Smith, M. Young, D. Keller, and C. Bustamante. Single-molecule studies of the effect of template tension on T7 DNA polymerase activity. *Nature*, **404**: 103-106 (2000)

[72] C. bustamante, J.F. Marko, E.D. Siggia, and S. Smith. Entropic elasticity of lambda-phage DNA. *Science*, **265**: 1599-1600 (1994)

[73] S.B. Smith, L. Finzi, and C. Bustamante. Direct mechanical measurements of the elasticity of single DNA molecules by using magnetic beads. *Science*, **258**: 1122-1126 (1992)

[74] J.F. Marko and E.D. Siggia. Stretching DNA. *Macromolecules*, **28**: 8759-8770 (1995)

[75] A. Ashkin, K. Schutze, J.M. Dziedzic, U. Euteneuer, and M. Schliwa. Force generation of organelle transport measured in vivo by an infrared laser trap. *Nature*, **348**: 346-348 (1990)

[76] S.C. Kuo and M.P. Sheetz. Force of single kinesin molecules measured with optical tweezers. *Science*, **260**:232-234

[77] J. Wong, A. Chilkoti, and V.T. Moy. Direct force measurements of the streptavidin-biotin interaction. *Biomol. Eng.*, **16**: 45-55 (1999)

[78] M. Rief, M. Gautel, F. Oesterhelt, J.M. Fernandez, and H.E. Gaub. Reversible unfolding of individual titin immunoglobulin domains by afm. *Science*, **276**: 1109-1112 (1997)

[79] R. Merkel, P. Nassoy, A. Leung, K. Ritchie, and E. Evans. Energy landscapes of receptor-ligand bonds explored with dynamic force spectroscopy. *Nature*, **397**: 50-53 (1999)

[80] P.K. Hansma, V.B. Elings, O. Marti, and C.E. Bracker. Scanning tunneling microscopy and atomic force microscopy: Application to biology and technology. *Science*, **242**: 209-242 (1988)

[81] J.Y. Shao. Measuring Piconewton Forces and Its Application in Cellular and Molecular Biomechanics. *Advances in Biomechanics: Proceedings of the First International Young Investigator Workshop on Biomechanics*, CHEP Bejing and Springer-Verlag, Berlin (2001)

[82] M. Tokunaga, T. Aoki, M. Hiroshima, K. Kitamura, and T. Yanagida. Subpiconewton intermolecular force microscopy. *Biochem. Biophys. Res. Commun.*, **231**: 566-569 (1997)

[83] J.H. Hoh, J.P. Cleveland, C.B. Prater, J.-P Revel, and P.K. Hansma. Quantized adhesion detected by atomic force microscope. *J. Am. Chem. Soc.*, **114**: 4917-4918 (1992)

[84] H. Clausen-Schaumann, M. Seitz, R. Krautbauer, and H.E. Gaub. Force Spectroscopy with Single Bio-Molecules. *Curr. Opin. Chem. Bio.*, **4**: 524-530 (2000)

[85] J.P. Cleveland, S. Manne, D. Bocek, and P.K. Hansma. A nondestructive method for determining the spring constant of cantilevers for scanning force microscopy. *Rev. Sci. Instr.*, **64**:403-405 (1993)

[86] J.L. Hutter, and J. Bechhoefer. Calibration of atomic-force microscope tips. *Rev. Sci. Instr.*, **64**: 1868-1873 (1993)

[87] H.-J Butt and M. Jaschke. Calculation of thermal noise in atomic force microscopy. *Nanotechnology*, **6**: 1-7 (1995)

[88] A. Ashkin. Applications of laser-radiation pressure. *Science*, **210**: 1081-1088 (1980)

[89] A. Ashkin, J.M. Dziedzic, J.E. Bjorkholm, and S. Chu. Observation of a single-beam gradient force optical trap for dielectric particles. *Opt. Lett.*, **11** 288-290 (1986)

[90] A. Ashkin. Forces of a single-beam gradient laser trap on a dielectric sphere in the ray optics regime. *Biophys. J.*, **61**:569-582 (1992)

[91] K. Svoboda and S.M. Block. Biological applications of optical forces. In: *R.M. Stroud, C.R. Cantor, and T.D. Pollard (Eds.), Annual Reviews of Biophysics and Biomolecular Structures*, **23**. Annual Reviews, Inc. Palo Alto, CA pp. 247-285

[92] J.C. Meiners and S.R. Quake. Direct Measurements of Hydrodynamics Cross Correlations between Two Particles in an External Potential. *Am. Phys. Soc.*, **82**: 2211-2214 (1999)

[93] J.C. Meiners and S.R. Quake. Femtonewton Force Spectroscopy of Single Extended DNA Molecules. *The American Physical Society*, **84**: 5014-5017 (2000)

[94] F. Gittes and C.F. Schmidt. Signals and noise in micromechanical measurements. *Methods Cell Biol.*, **55**: 129-156 (1998)

[95] G. Romano, L. Sacconi, M. Capitanio, and F.S. Pavone. Force and torque measurements using magnetic micro beads for single molecule biophysics. *Opt. Commun.*, **215**: 323-331 (2003)

[96] S.C. Kuo. A simple assay for local heating by optical tweezers. In: *Sheetz, M.P. (Ed.), Methods in Cell Biology*, **55** Academic Press, San Diego, pp. 43-45

[97] H. Yin, M.D. Wang, K. Svoboda, R. Landick, S.M. Block, and J. Gelles. Transcription against an applied force. *Science*, **270**: 1653-1657 (1995)

[98] S.B. Smith, L. Finzi, and C. Bustamante. Direct Mechanical Measurements of the Elasticity of Single DNA Molecules by Using Magnetic Beads. *Science*, **258**: 1122-1126 (1992)

[99] T.R. Strick, J.F. Allemand, D. Bensimon, A. Bensimon, and V. Croquette. The Elasticity of a Single Supercoiled DNA Molecule. *Science*, **271**: 1835-1837 (1996)

[100] G. Romano, L. Sacconi, M. Capitanio, and F.S. Pavone. Force and torque measurements using magnetic micro beads for single molecules biophysics. *Opt. Commun.*, **215**: 323-331 (2003)

[101] D.A. Simson, F. Ziemann, M. Strigl, and R. Merkel. Micropipet-Based Pico Force Transducer: In depth Analysis and Experimental Verification. *Biophys. J.*, **74**: 2080-2088 (1998)

[102] T. Strick, J.-F. Allemand, V. Croquette, and D. Bensimon. Physical approaches to the study of DNA. *J. Stat. Phys.*, **93**: 647-672 (1998)

[103] E. Evans, K. Ritchie, and R. Merkel. Sensitive Force Technique to Probe Molecular Adhesion and Structural Linkages at Biological Interfaces. *Biophys. J.*, **68**: 2580-2587 (1995)

[104] V. Heinrich, K. Ritchie, N. Mohandas, and E. Evans. Elastic Thickness Compressibility of the Red Cell Membrane. *Biophys. J.*, **81**: 1452-1463 (2001)

[105] U. Bockelmann, B. Essevaz-Roulet, and F. Heslot. DNA strand separation studied by single molecule force measurements. *Phys. Rev. E*, **58**: 2386-2394 (1998)

[106] D. Dunaway, M. Fauver, and G. Pollack. Direct Measurement of Single Synthetic Vertebrate Thick Filament Elasticity Using Nanofabricated Cantilevers. *Biophys. J.*, **82**: 3128-3133 (2002)

[107] A. Ishijima, H. Kojima, H. Higuchi, Y. Harada, T. Funatsu, and T. Yanagida. Multiple- and Single- Molecule Analysis of the Actomosin Motor by Nanometer-Piconewton Manipulation with a Microneedle: Unitary Steps and Forces. *Biophys. J.*, **70**: 383-400 (1996)

[108] M.E. Fauver, D.L. Dunaway, D.H. Lilienfeld, H.G. Craighead, and G.H. Pollack. Microfabricated Cantilevers for Measurement of Subcellular and Molecular Forces. *IEEE Transa. Biomed. Eng.*, **45**: 891-898 (1998)

[109] T. Neumann, M. Fauver, and G.H. Pollack. Elastic Properties of Isolated Thick Filaments Measured by Nanofabricated Cantilevers. *Biophys. J.*, **75**: 938-947 (1998)

[110] S. Tha, J. Shuster, and H.L. Goldsmith. Interaction Forces Between Red Cells Agglutinated by Antibody. II. Measurement of Hydrodynamic Force of Breakup *Biophys. J.*, **50**: 1117-1126 (1986)

[111] D.F.J. Tees, O. Coenen, and H. Goldsmith. Interaction Forces Between Red Cells Agglutinated by Antibody. IV. Time and Force Dependence of Break-up. *Biophys. J.*, **65**: 1318-1334 (1993)

[112] S.C. Kuo and D.A. Lauffenburger. Relationship between Receptor/Ligand Binding Affinity and Adhesion Strength. *Biophys. J.*, **65**: 2191-2200 (1993)

[113] L.A. Faern, M.L. Bartoo, J.A. Meyers, and G.H. Pollack. An optical fiber transducer for single myofibril force measurement. *IEEE Trans. Biomed. Eng*, **40**:1127-1132 (1993)

[114] T. Iwazumi. High-speed ultrasensitive instrumentation for myofibril mechanics measurements. *Amer. J. Physiol.*, **252**:C253-C262 (1987)

[115] C.A. Mirkin. Tweezers for the Nanotool Kit. *Science*, **286**: 2095-2150 (1999)

[116] P. Kim and C.M. Lieber. Nanotube nanotweezers. *Science*, **286**: 2148-2150 (1999)

[117] P.G. de Gennes. Coil-stretch transition of dilute flexible polymers under ultra-high velocity gradients. *J. Chem. Phys.*, **60**: 5030-5042 (1974)

[118] F. Brochard-Wyart. Polymer Chains under Strong Flows: Stems and Flowers. *Europhys. Lett.*, **30**: 387-392 (1995)

[119] A. Buguin and F. Brochard-Wyart. Unwinding of Globular Polymers under Strong Flows. *Macromolecules*, **29**: 4937-4943 (1996)

[120] P.S. Doyle, B. Ladoux, and J.L. Viovy. Dynamics of a Tethered Polymer in Shear Flow. *Phys. Rev. Lett.*, **84**: 4769-4772 (2000)

[121] R.K. Pathria, *Statistical Mechanics*. Butterword-Heinemann, Oxford (1996)

[122] A.V. Vologodskii and N.R. Cozzarelli. Supercoiling, Knotting, Looping and Other Large-Scale Conformational Properties of DNA. *Curr. Opin. Struc. Biol.*, **4**: 372-375 (1994)

[123] A.L. Lehninger, D.L. Nelson, and M.M. Cox, *Principles of Biochemistry*. Worth Publishers, New York (1982)

[124] W. Helfrich. Elastic properties of lipid bilayers: theory and possible experiments. *Z. Naturforsch*, **28C**: 693-703 (1973)

[125] D. Nelson, T. Piran, and S. Weinberg. *Statistical Mechanics of Membranes and Surfaces*. World Science, Singapore (1994)

[126] R. Lipowsky. The Conformation of Membranes. *Nature (London)*, **349**: 475-481 (1991)

[127] R. Lipowsky, D. Richter, and K. Kremer. *The Structure and Conformation of Amphiphilic Membranes.* Springer, Berlin (1992)

[128] J.R. Murphy. Erythrocyte metabolism. VI. Cell Shape and the Location of Cholesterol in the Erythrocyte Membrane. *J. Lab. Clin. Med.*, **65**: 756-774 (1965)

[129] P. Seeman, D. Cheng, and G.H. Iles. Structure of Membrane Holes In Osmotic and Saponin Hemolysis. *J. Cell Biol.*, **56**: 519-527 (1973)

[130] Y.C.B. Fung and P. Tong. Theory of the Sphering of Red Blood Cells. *Biophys. J.*, **8**: 175-198 (1968)

[131] L. Lopez, I.M. Duck, and W.A. Hunt. On the Shape of the Erythrocyte. *Biophys. J.*, **8**: 1228-1235 (1968)

[132] M.A. Greer and R.F. Baker. *Congr. Int. Microsc. Electron.*, **7th edition**: 31 (Paris 1970)

[133] F.C. Frank. On the theory of liquid crystals. *Discuss. Faraday Soc.*, **25**: 19-28 (1958)

[134] Z.C. Ou-Yang and W. Helfrich. Instability and Deformation of a Spherical Vesicle by Pressure. *Phys. Rev. Lett.*, **59**: 2486-2488 (1987)

[135] Z.C. Ou-Yang and W. Helfrich. Bending Energy of Vesicle Membranes - General Expressions for the 1st, 2nd, and 3rd Variation of the Shape Energy and Applications to Spheres and Cylinders. *Phys. Rev. A*, **39**: 5280-5288 (1989)

[136] Z.C. Ou-Yang. Correction. *Phys. Rev. Lett.*, **60**: 1209-1209 (1988)

[137] Z.C. Ou-Yang. Anchor Ring-Vesicle Membranes. *Phys. Rev. A*, **41**: 4517-4520 (1990)

[138] M. Mutz and D. Bensimon. Observation of Toroidal Vesicles. *Phys. Rev. A*, **43**: 4525-4527 (1991)

[139] H. Naito, M. Okuda, and Z.C. Ou-Yang. Counterexample to Some Shape Equations for Axisymmetrical Vesicles. *Phys. Rev. E*, **48**: 2304-2307 (1993)

[140] H. Naito and M. Okuda. Polygonal shape transformation of a circular biconcave vesicle induced by osmotic pressure. *Phys. Rev. E*, **54**: 2816-2826 (1996)

[141] P.G. de Gennes. *The Physics of Liquid Crystals*. Oxford University Press, London (1975)

[142] P.G. de Gennes. Electrostatic buckling chiral lipid bilayers. *C.R. Acad. Sci. II Paris*, **304**: 259-263 (1987)

[143] J.S. Chappell and P. Yager. Electrostatic interactions within helical structures of chiral lipid bilayers. *Chem. Phys.*, **150**: 73-79 (1991)

[144] J.S. Chappell and P. Yager. Electrolyte effects on bilayer tubule formation by diacetylenic phospholipid. *BioPhys. J.*, **60**: 952-965 (1991)

[145] M.A. Markowitz, J.M. Schnur, and A. Singh. The influence of the polar headgroups of acidic diacetylenic phospholipids on tubule formation, microstructure morphology and Langmuir film behavior. *Chem. Phys. Lipids*, **62**: 193-204 (1992)

[146] B.N. Thomas, C.R. Safinya, R.J. Plano, and N.A. Clark. Lipid Tubule Self-Assembly: Length Dependence on Cooling Rate Through a First-Order Phase Transition, *Science*, **267**: 1635-1638 (1995)

[147] J.M. Schnur, B.R. Ratna, J.V. Selinger, A. Singh, G. Jyothi, and K.R.K. Easwaran. Diacetylenic Lipid Tubules: Experimental Evidence for a Chiral Molecular Architecture. *Science*, **264**: 945-947 (1994)

[148] C.M. Chen. Theory for the bending anisotropy of lipid membranes and tubule formation. *Phys. Rev. E*, **59**: 6192-6195 (1999)

[149] S.B. Dierker, R. Pindak, and R.B. Meyer. Consequences of Bond-Orientational Order on the Macroscopic Orientation Patterns of Thin Tilted Hexatic Liquid-Crystal Films. *Phys. Rev. Lett.*, **56**: 1819-1822 (1986)

[150] W. Helfrich. Helical bilayer structures due to spontaneous torsion of the edges. *J. Chem. Phys.*, **85**: 1085-1087 (1986)

[151] W. Helfrich and J. Prost. Intrinsic bending force in anisotropic membranes of chiral molecules. *Phys. Rev. A*, **38**: 3065-3068 (1988)

[152] Z.C. Ou-Yang and J.X. Liu. Helical Structures of Tilted Chiral Bilayers Viewed as Cholesteric Crystals. *Phys. Rev. Lett.*, **65**: 1679-1682 (1990)

[153] Z.C. Ou-Yang and J.X. Liu. Theory of helical structures of tilted chiral lipid bilayers. *Phys. Rev. A*, **43**: 6826-6836 (1991)

[154] I. Dahl and S.T. Langerwall. Elastic and Flexoelectric Properties of Chiral Smectic-C Phase and Symmetry Considerations on Ferroelectric Liquid-Crystal Cells. *Ferroelectrics*, **58**: 215-243 (1984)

[155] J.V. Selinger and J.M. Schnur. Theory of Chiral Lipid Tubules. *Phys. Rev. Lett.*, **71**: 4091-4094 (1993)

[156] P. Nelson and T. Powers. Rigid Chiral Membranes. *Phys. Rev. Lett.*, **69**: 3409-3412 (1992)

[157] A. Tardieu, V. Luzzati, and F.C. Reman. Structure and Polymorphism of the Hydrocarbon Chains of Lipids: A Study of Lecithin-Water Phases. *J. Mol. Biol.*, **75**: 711-733 (1973)

[158] M.J. Janiak, D.M. Small, and G.G. Shipley. Nature of the Thermal Pretransition of Synthetic Phospholipids: Dimyristoyl- and Dipalmitoyl lecithin. *Biochem.*, **15**: 4575-4580 (1976)

[159] D.C. Wack and W.W. Webb. Measurements of Modulated Lamellar P-Beta' Phases Of Interacting Lipid-Membranes. *Phys. Rev. Lett.*, **61**: 1210-1213 (1988)

[160] T.C. Lubensky and F.C. MacKintosh. Theory of "Ripple" Phases of Lipid Bilayers. *Phys. Rev. Lett.*, **71**: 1565-1568 (1993)

[161] D.R. Nelson and L. Peliti. Fluctuations in membranes with crystalline and hexatic order. *J. Physique*, **48**: 1085-1092 (1987)

[162] R. Treanor and M.D. Pace. Microstructure, Order and Fluidity of 1,2-Bis(Tricosa-10,12-Diynoyl)-sn-Glycero-3-Phosphocholine (Dc8,9pc), A Polymerizable Lipid, By ESR and NMR. *Biochim. Biophys. Acta*, **1046**: 1-11 (1990)

[163] S.L. Brandow, D.C. Turner, B.R. Ratna, and B.P. Gaber. Modification of Supported Lipid-Membranes by Atomic Force Microscopy. *Biophys. J.*, **64**: 898-902 (1993)

[164] D.G. Rhodes, S.L. Blechner, P. Yager, and P.E. Schoen. Structure of Polymerizable Lipid Bilayers .1. 1,2-Bis(10,12-Tricosadiynoyl)-sn-Glycero-3-Phosphocholine, A Tubule-Forming Phosphatidylcholine. *Chem. Phys. Lipids*, **49**: 39-47 (1988)

[165] J.B. Lando and R.V. Sudiwala. Structural Investigation of Langmuir-Blodgett-Films and Tubules Of 1,2-Bis(10,12-Tricosadiynol)-sn-Glycerol-3-Phosphocholine (Dc8,9pc) Using Electron-Diffraction Techniques. *Chem. Mater.*, **2**: 594-599 (1990)

[166] M. Caffrey, J. Hogan, and A.S. Rudolph. Diacetylenic Lipid Microstructures - Structural Characterization by X-Ray-Diffraction and Comparison with the Saturated Phosphatidylcholine Analog. *Biochemistry*, **30**: 2134-2146 (1991)

[167] A. Singh, T.G. Burke, J.M. Calvert, J.H. Georger, B. Herendeen, R.R. Price, P.E. Schoen, and P. Yager. Lateral Phase-Separation Based on Chirality in a Polymerizable Lipid and its Influence on Formation of Tubular Microstructures. *Chem. Phys. Lipids*, **47**: 135-148 (1988)

[168] B.R. Ratna, S. Baraltosh, B. Kahn, J.M. Schnur, A.S. Rudolph. Effect of Alcohol Chain-Length on Tubule Formation in 1,2-Bis(10,12-Tricosadiynoyl)-sn-Glycero-3-Phosphocholine. *Chem. Phys. Lipids*, **63**: 47-53 (1992)

[169] M.S. Spector, J.V. Selinger, A. Singh, J.M. Rodriguez, R.R. Price, and J.M. Schnur. Controlling the Morphology of Chiral Lipid Tubules. *Langmuir*, **14**: 3493-3500 (1998)

[170] P.A. Pramod, Y. Hatwalne, and N.V. Madhusudana. Chiral symmetry breaking in three-dimensional smectic-C liquid-crystal domains. *Phys. Rev. E*, **56**: R4935-R4938 (1997)

[171] J.H. Pang and N.A. Clark. Observation of a Chiral-Symmetry-Breaking Twist-Bend Instability in Achiral Freely Suspended Liquid-Crystal Films. *Phys. Rev. Lett.*, **73**: 2332-2335 (1994)

[172] D.R. Link, G. Natale, R. Shao, J.E. Maclennan, N.A. Clark, E. Korblova, and D.M Walba. Spontaneous formation of macroscopic chiral domains in a fluid smectic phase of achiral molecules. *Science*, **278**: 1924-1927 (1997)

[173] J. Maclennan and M. Seul. Novel Stripe Textures in Nonchiral Hexatic Liquid-Crystal Films. *Phys. Rev. Lett.*, **69**: 2082-2085 (1992)

[174] J.E. Maclennan, U. Sohling, N.A. Clark, and M. Seul. Textures in Hexatic Films of Nonchiral Liquid-Crystals - Symmetry-Breaking and Modulated Phases. *Phys. Rev. E*, **49**: 3207-3224 (1994)

[175] X. Qiu, J. Ruizgarcia, K.J. Stine, C.M. Knobler, and J.V. Selinger. Direct Observation of Domain-Structure in Condensed Monolayer Phases. *Phys. Rev. Lett.*, **67**: 703-706 (1991)

[176] J. Ruiz-Garcia, X. Qiu, M.W. Tsao, G. Marshall, C.M. Knobler, G.A. Overbeck, and D. Mobius. Splay Stripe Textures in Langmuir Monolayers. *J. Phys. Chem.*, **97**: 6955-6957 (1993)

[177] D.K. Schwartz, J. Ruiz-Garcia, X. Qiu, J.V. Selinger, and C.M. Knobler. Tilt Stripe Textures in Langmuir Monolayers of Fatty-Acids. *Physica A*, **204**: 606-615 (1994)

[178] Y. Tabe, N. Shen, E. Mazur, and H. Yokoyama. Simultaneous observation of molecular tilt and azimuthal angle distributions in spontaneously modulated liquid-crystalline Langmuir monolayers. *Phys. Rev. Lett.*, **82**: 759-762 (1999)

[179] W.E. Lindsell, P.N. Preston, J.M. Seddon, G.M. Rosair, and T.A.J. Woodman. Macroscopic Helical and Cylindrical Morphologies from Achiral 1,3-Diynes. *Chem. Mater.*, **12**: 1572-1576 (2000)

[180] A. Singh, P.E. Schoen, and J.M. Schnur. Self-assembled Microstructures from a Polymerizable Ammonium Surfactant: Di(Hexacosa-12,14-diynyl)dimethylammonium Bromide. *J. Chem. Soc., Chem, Commun.*, 1222-1223 (1988)

[181] J. Katsaras and V.A. Raghunathan. Molecular Chirality and the "Ripple" Phase of Phosphotidylcholine Multibilayers. *Phys. Rev. Lett.*, **74**: 2022-2025 (1995)

[182] J. Katsaras, R.F. Epand, and R.M. Epand. Absence of chiral domains in mixtures of dipalmitoylphosphotidylcholine molecules of opposite chirality. *Phys. Rev. E*, **55**: 3751-3753 (1997)

[183] J. Katsaras, S. Tristram-Nagle, Y. Liu, R.L. Headrick, E. Fontes, P.C. Mason, and J.F. Nagle. Clarification of the ripple phase of lecithin bilayers using fully hydrated, aligned samples. *Phys. Rev. E*, **61**: 5668-5677 (2000)

[184] B.N. Thomas, C.M. Lindemann, R.C. Corcoran, C.L. Cotant, J.E. Kirsch, and P.J. Persichini. Phosphonate Lipid Tubules II. *J. Am. Chem. Soc.*, **124**: 1227-1233 (2002)

[185] J.V. Selinger, Z.G. Wang, R.F. Bruinsma, and C.M. Knobler. Chiral Symmetry Breaking in Langmuir Monolayers and Smectic Films. *Phys. Rev. Lett.*, **70**: 1139-1142 (1993)

[186] U. Seifert, J. Shillcock, and P. Nelson. Role of Bilayer Tilt Difference in Equilibrium Membrane Shapes. *Phys. Rev. Lett.*, **77**: 5237-5240 (1996)

[187] M.S. Spector, K.R.K. Easwaran, G. Jyothi, J.V. Selinger, A. Singh, and J.M. Schnur. Chiral molecular self-assembly of phospholipid tubules: A circular dichroism study. *Proc. Natl. Acad. Sci. USA*, **93**:12943-12946 (1996)

[188] T. Tachibana and H. Kambara. Studies of Helical Aggregates of Molecules. I. Enantiomorphism in the Helical Aggregates of Optically Active 12-Hydroxystearic Acid and its Lithium Salt. *Bull. Chem. Soc. Jpn.*, **42**: 3422-3424 (1969)

[189] N. Nandi and B. Bagchi. Prediction of Senses of Helical Amphiphilic Assemblies from Effective Intermolecular Pair Potential: Studies on Chiral Monolayers and Bilayers. *J. Phys. Chem. A*, **101**: 1343-1351 (1997)

[190] F.M. Konikoff, D.S. Chung, J.M. Donovan, D.M. Small, and M.C. Carey. Filamentous, Helical, And Tubular Microstructures During Cholesterol Crystallization From Bile - Evidence That Cholesterol Does Not Nucleate Classic Monohydrate Plates. *J. Clin. Invest.*, bf 90: 1155-1160 (1992)

[191] F.M. Konikoff, D.E. Cohen, and M.C. Carey. Filamentous Crystallization Of Cholesterol And Its Dependence On Lecithin Species In Bile. *Mol. Cryst. Liq. Cryst. -A* , **248**: 291-296 (1994)

[192] H.S. Seung and D.R. Nelson. Defects in flexible membranes with crystalline order. *Phys. Rev. A*, **38**: 1005-1018 (1988)

[193] J.S. Chappell and P. Yager. A model for cystalline order within helical and tubular structures of chiral bilayers. *Chem. Phys. Lipids*, **58**: 253-258 (1991)

[194] L.D. Landau and E.M. Lifshitz, *Theory of Elasticity.* Pergamon Press, Oxford (1959)

[195] Y.M.M. Bishop, S.E. Fienberg, and P.W. Holland, *Discrete Multivariate Analysis*. MIT Press, Cambridge (1975)

[196] W.R. Bowen, N. Hilal, R.W. Lovitt, and C.J. Wright. An atomic force microscopy study of the adhesion of a silica sphere to a silica surface-effects of surface cleaning. *Colloid Surf. A*, **157**: 117-125 (1999)

[197] M. Benoit and H.E. Gaub. Measuring cell adhesion forces with the atomic force microscope at the molecular level. *Cells Tissues Organs*, **172**: 174-189 (2002)

[198] D. Fotiadis, S. Scheuring, S.A. Muller, A. Engel, and D.J. Muller. Imaging and manipulation of biological structures with the AFM. *Micron*, **33**: 385-397 (2002)

[199] A.M. Wahl, *Mechanical Springs*. McGraw-Hill, New York (1963)

[200] L.E. Becker and W.L. Cleghorn. On the buckling of helical compression springs. *Int. J. Mech. Sci.*, **34**: 275-282 (1992)

[201] G.G. Chassie, L.E. Becker, and W.L. Cleghorn. On the buckling of helical springs under combined compression and torsion. *Int. J. Mech. Sci.*, **39**: 697-704 (1997)

[202] L.E. Reichl, *A Modern Course in Statistical Physics*. John Wiley and Sons, Inc., New York (1998)

[203] A. Goriely and M. Tabor. Spontaneous Helix Hand Reversal and Tendril Perversion in Climbing Plants. *Phys. Rev. Lett.*, **80**: 1564-1567 (1998)

[204] R.E. Goldstein, A. Goriely, G. Huber, and C.W. Wolgemuth. Bistable Helices. *Phys. Rev. Lett.*, **84**: 1631-1634 (2000)

[205] J. Gelles, B. Schnapp, and M.P. Sheetz. Tracking kinesin-driven movements with nanometer-scale precision. *Nature*, **331**: 450-453 (1988)

[206] J. Howard, and A.J. Hudspeth. Mechanical relaxation of the hair bundle mediates adaptation in mechanoelectrical transduction by the bullfrog's saccular hair cell. *Proc. Natl. Acad. Sci. USA*, **84**: 3064-3068 (1987)

[207] N.T. Porile, *Modern University Chemistry.* McGraw-Hill Inc., New York (1993)